Ordering of Organic Molecules on Templated Surfaces

A thesis for the degree of

PHILOSOPHIAE DOCTOR

Presented to

DUBLIN CITY UNIVERSITY

By

Gráinne Sheerin B.Sc.
School of Physical Sciences
Dublin City University

Research Supervisor:
Dr. A. A. Cafolla

External Examiner: Prof. S. P. Wilks
Internal Examiner: Dr. E. McLoughlin

July 2006

Declaration

I hereby certify that this material which I now submit for assessment on the programme of study leading to the award of Philosophiae Doctor is entirely my own work and has not been taken from the work of others save and to the extent that such work has been cited and acknowledged within the text of this work.

Gráinne Sheerin, July 2006

ID No.: 98392808

Acknowledgements

I wish to acknowledge all the academics who have generously shared their time and expertise with me, my supervisor Tony Cafolla, Eilish McLoughlin, Enda McGlynn, James Fryer, Don Walko, Alastair McLean, Richard Woolley, Philip Moriarty, Rob Jones, Thorsten Wagner, Lorenz Kampschulte, Markus Lackinger, Mick Philips, Zheshen Li and at the Daresbury SRS, George Miller and Vin Dhanak.

This work was funded by the Irish Research Council for Science, Engineering and Technology, IRCSET-Embark Initiative.

蠔油叉燒包
越南春卷
馄饨汤
乾炒牛河

To all my friends and among them the many other PhD students I encountered over the years, for their friendship and camaraderie.

And finally to my family, especially Mum, without whom
I would never have made it.

Contents

List of Figures

List of Tables

List of Publications

G. Sheerin and A. A. Cafolla,
Self-assembled structures of trimesic acid on the Ag/Si(111)-$(\sqrt{3} \times \sqrt{3})R30°$ surface,
Surface Science 577, (2005), pp.211-219.

O. McDonald, A. A. Cafolla, D. Carty, G. Sheerin and G. Hughes,
Photoemission, NEXAFS and STM studies of pentacene thin films on Au(100),
Surface Science, In Press, doi:10.1016/j.susc.2006.06.007

A. A. Cafolla, E. McLoughlin, G. Sheerin, E. AlShamaileh, Ph. Guaino, D. Carty, T. McEvoy, C. Barnes, V. Dhanak, A. Santoni,
Observation of an anti-phase domain structure in the Cu{100}/Sn surface alloy system,
Surface Science 544, (2003), pp. 121-133.

Ph. Guaino, A. A. Cafolla, D. Carty, G. Sheerin and G. Hughes,
An STM investigation of the interaction and ordering of pentacene molecules on the Ag/Si(111)-$(\sqrt{3} \times \sqrt{3})R30°$ surface,
Surface Science 540, (2003), p.107.

Ph. Guaino, A. A. Cafolla, O. McDonald, D. Carty,
G. Sheerin and G. Hughes,
Scanning tunnelling spectroscopy of low pentacene coverage on the Ag/Si(111)-$(\sqrt{3} \times \sqrt{3})R30°$ surface,
Journal of Physics-Condensed Matter 15 (2003) pp.S2693-S2698.

List of Poster Presentations

STM03

International Conference on Scanning Tunnelling Microscopy, July 2003,

A structural study of the Sn/Cu{100} surface alloy system.

ECOSS 22

European Conference on Surface Science, September 2003

Structural phases of pentacene molecules on the Ag/Si(111)-($\sqrt{3}\times\sqrt{3}$)R30° surface.

ICSS-12

International Conference on Surface Science 12, June 2004,

A Structural Study of Mg,Bi/Cu(100) Ordered Surface Alloys

NCSS-5

Fifth Nordic conference on surface science, September 2004,

An STM study of organic molecules on a metallic film. The case of trimesic acid on Si(111)-($\sqrt{3}\times\sqrt{3}$)R30°-Ag.

ECOSS 23

European Conference on Surface Science, September 2005,

A study of the Bi/Si(100) system as a template for the growth of organic structures.

Abstract

This thesis describes the controlled growth of molecular nanostructures using modified metallic and semiconductor surfaces. The Ag/Si(111)-($\sqrt{3} \times \sqrt{3}$), the Sn/Cu(100) surface alloy system and the Bi/Si(100) nanolines and (2×n) surfaces were all investigated as suitable substrates for the controlled growth of pentacene, ($C_{22}H_{14}$) or trimesic acid, ($C_6H_3(COOH)_3$) organic molecules. The following techniques were used in this study; Scanning Tunnelling Microscopy (STM), Low Energy Electron Diffraction (LEED), Normal Incident X-Ray Standing Waves (NIXSW) and Temperature Programmed Desorption (TPD).

The room temperature growth and ordering of trimesic acid on the Ag/Si(111)-($\sqrt{3} \times \sqrt{3}$) surface was investigated. An oblique unit cell was determined and a model proposed for the highly ordered close-packed domains.

The discovery of a new submonolayer phase on Sn/Cu(100) and the re-examined known phase are discussed. New models for these reconstructions are proposed. Adsorption of trimesic acid at room temperature on the clean substrate the lowest Sn coverage phase were studied. Two new Sn coverage dependent structures were discovered and bonding schemes in upright and flat orientations are discussed.

Bi/Si(100)-(2×n) surface was exploited as a template for the ordered growth of pentacene, which exhibited orientation specific adsorption. The Bi/Si(100)-(2×n) single domain surface created on vicinal silicon was used to test the suitable of Daresbury 4.2 beamline for NIXSW Imaging experiments and the quality of the results are discussed.

Chapter 1

Introduction

The development of instruments such as the Scanning Tunnelling Microscope [1] and Atomic Force Microscope [2] by the physics community has reached a point that enables visualisation and manipulation of matter down to the atomic level and has opened the way to nanoscale research.

Nanotechnology aims to contribute to a range of different areas; the pursuit of further miniaturisation in the microelectronics industry, the growth of stable nanowires, the growth and selected electronic properties of organic thin films and the improved efficiency of catalysis to name but a few.

Surface science research aspires to provide a fundamental understanding and intuition about interactions on the atomic scale. Although research is performed in strictly controlled environments, this aspect of surface sciences plays a central role in the development of nanotechnology and helps in the development of new industrial applications.

Supramolecular chemistry, the chemistry of the intermolecular non-covalent bond, is the science involved in creating a desired supramolecular crystal or supramolecular compound. Organic molecules are used for this purpose because they can be synthesised with specific properties [3]. Researchers are now aiming to create tailor-made nanostructures. These organic-inorganic heterostructures can have tailored properties including reactivity, ultra-fast optical response, chemical sensing, and biocompatibility [4] [5] [6].

Understanding the forces governing the ordering of organic molecules is key to the control and the construction of these organic structures [7]. The knowledge of supramolecular chemistry can only guide researchers in the assembly of adsorbed molecules on surface. Consideration must be given to the influence of the substrates' atomic and electronic structure on adsorbed molecules before these forces can be

mediated by appropriate choices of substrate and organic molecule. Within the last five years there have been many publications in relation to the issue of choosing a suitable organic molecule and templated substrate ([8] and references therein).

Templating these substrates covers a wide range of surface modifications and the type of template used will depend on the structures one desires to create. Templates can be created directly from the substrate with no additional adsorbate required. For example with a judicious choice of vicinal silicon surface double row Au quantum wires were created on the Si(553) surface [9]. Other researchers have successfully created supramolecular nanostructures using hydrogen bonding [10] [11]. Most notably the creation of nanoporous organic honeycomb layers fabricated on the hexagonal Ag-passivated Si(111) substrate [11]. The repeat unit gives rise to the regular nanoporous honeycomb layers into which guest C_{60} molecules can be accommodated. In this case the organic molecules form the template on the passivated surface and control the position of the C_{60} molecules. In a less complex structure an organic molecule $C_{90}H_{98}$ act as templates accommodating Cu atoms at the step edges of the Cu(110) surface, forming metallic nanostructures that are adapted to the dimensions of the molecules [12]. A recent success of surface templating is "nanoline templating" [13], in which Bi nanolines are used as a template and the surrounding silicon substrate is passivated by hydrogen. For example, Bi nanolines have been exploited by Owen et al. [14] as a template to create one-dimensional epitaxial growth of indium on bismuth nanolines. Research is currently in progress to create nanowires out of other species by depositing them on top of the Bi nanoline to form a wire. In this way it is hoped that wires with different properties can be made. These continuing efforts have lead to the successful creation of two-dimensional assemblies stabilised by hydrogen bonding and metal coordination and self-assembled films of organic molecules on modified semiconductor and metallic surfaces.

In this thesis three different surfaces were modified with the adsorption of a metal and the resulting reconstructions were then investigated as suitable templates upon which the orientation of an organic molecule could be controlled. The organic molecules pentacene and trimesic acid were chosen as the focus of this research because of their relatively simple structures and the body of published research with which accurate comparisons could be made.

In chapter 2 the different experimental techniques used in this thesis along with their theoretical bases are presented. Specifically, low energy electron diffraction (LEED), normal incidence X-ray standing wave (NIXSW), scanning tunnelling spectroscopy (STM) and temperature programmed desorption (TPD) are discussed. For each technique the basic concept is discussed before a review of the theory is given.

The components and operating procedures are then addressed including the ultra high vacuum (UHV) chambers. Any software which aided the analysis of data is detailed in the relevant technique section. This chapter also includes an introduction to synchrotron radiation which is used for NIXSW studies. Finally the two organic molecules studied in this work are discussed. A review of recent relevant publications for both molecules is included.

In chapter 3 the Sn/Cu(100) surface alloy is examined and five submonolayer surface structures are discussed. The possibility of using the Sn/Cu(100) surface alloy as a template is motivated by the observation that molecules with carboxyl end-groups will bond to Cu atoms but not to Sn atoms [15]. The adsorption of trimesic acid (TMA) on clean Cu(100) and the Sn/Cu(100) surface alloy structure is described in chapter 4. The motivation for the work arose out of the possibility of selectively adsorbing TMA molecules onto exposed Cu atoms within the surface alloy structure and in this manner order the molecules on the surface.

An overview of the structures formed by bismuth on the Si(100) surface is presented in chapter 5. The study of the Bi/Si(100)-(2×n) structure is motivated by the comparable width of a bismuth dimer row (1.416 nm), within the (2×6) structure, with the length of the pentacene molecule (1.41 nm). It was hoped to control the ordering of the pentacene molecules using the comparable dimensions of the Bi passivated surface. The following chapter continues the Bi/Si(100) surface investigations. A vicinal surface is used to create a single domain structure. A new analysis method [16] was applied to the NIXSW Bragg reflections to explore the possibility of constructing real-space images of the single domain structure from atomic-density maps derived from the different reflections.

Chapter 7 discusses the adsorption of trimesic acid on the silver passivated Si(111) surface. This surface provides a substrate upon which the TMA molecular interaction dominates and could be investigated. Both the surface and the molecule possess a high degree of symmetry and the motivation is to produce a network of cyclic hexamers in a commensurate structure with respect to the substrate.

Finally chapter 8 is dedicated to the conclusions that emerged from these studies. Some suggestions as to the possible directions that future work could take are also outlined.

Chapter 2

Theoretical and Experimental Detail

2.1 Low Energy Electron Diffraction (LEED)

In this section the origin and basic experimental setup for LEED is discussed. The Ewald construction, in relation to the analysis of a diffraction pattern is presented. The symmetry elements required to describe the symmetry properties of two-dimensional structures are introduced. An overview of the LEEDpat [17] program which is used to simulate various diffraction patterns is included.

LEED was first observed in 1927, by Davisson and Germer, who noted that by firing electrons with energies between 15 and 200 eV at a nickel crystal, variations in angular reflected fluxes consistent with electron diffraction were observed [18]. Refinement of these early electron diffraction experiments led to the development of the modern LEED system, see figure 2.1. A LEED apparatus typically consists of a hemispherical phosphorescent screen with an electron gun aligned along the central axis of the screen. The sample is positioned at the centre of curvature of the screen. A beam of low energy electrons are thermionically emitted by the heated filament. The Wehnelt, which has a small negative charge with respect to the filament, collimates the beam. The lenses are then used to focus the beam. When the beam is incident on a crystalline sample the electrons are scattered both elastically and inelastically by the surface atoms. The distances between the surface atoms are of the same order of magnitude as the electron wavelength so the elastically scattered electron waves interfere and reflect the periodicity of the sample surface. The electrons backscatter from the sample and pass through a number of grids positioned in

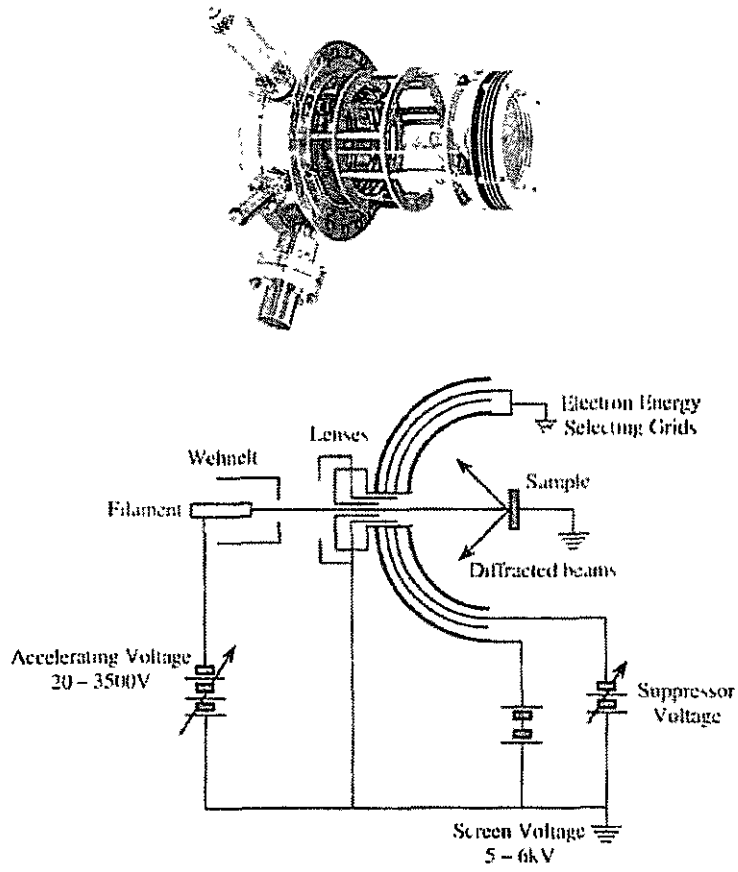

Figure 2.1: The Omicron LEED system and schematic diagram of LEED optics [20].

front of the screen. The first grid, closest to the sample, is earthed so the diffracted electrons follow a linear trajectory in the field free region between the sample and the grid. Subsequent grids are held at negative potentials to reject inelastically scattered electrons that would otherwise result in a high diffuse background on the screen [19]. The interference pattern is visible when the remaining electrons impinge on the phosphorescent screen biased at 5-6 kV.

All diffraction patterns presented in this thesis were measured with a rear view Omicron Spectraleed system. It is fitted with a lanthanum hexaboride filament (LaB_6), which has good emission characteristics at low power inputs, and higher emission currents with lower energy spread than the traditional thoriated tungsten filament. These characteristics are advantageous for investigating organic layers and help minimise desorption of the molecules from the sample surface by electron bombardment.

Miller indices (h, k, l) are a convenient label for planes within a crystal structure. They are obtained by calculating the intercepts of the plane as a fraction of the real

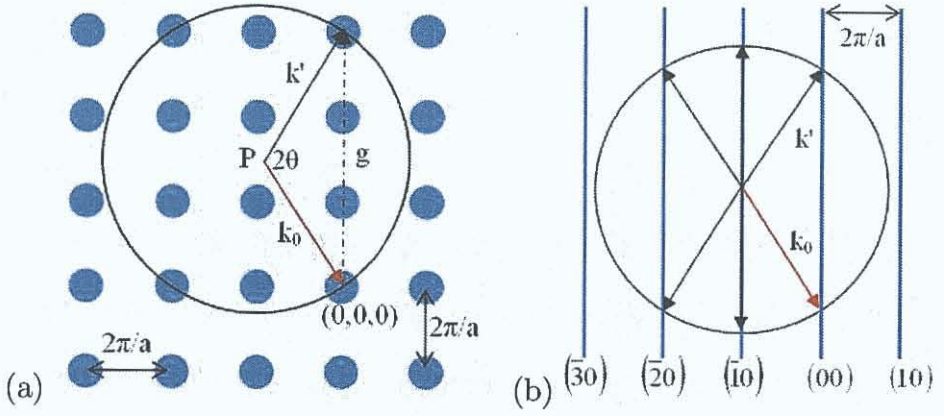

Figure 2.2: Ewald geometric constructions (a) 3D and (b) 2D. Increasing the energy increases the radius of the Ewald sphere.

space a, b and c axes, taking the reciprocal of each of these numbers. The Miller indices of a plane have a reciprocal relationship to the real intercepts of the plane with the axes of the crystal.

From the de Broglie equation ($p = h/\lambda$), the momentum p of a particle is related to its wavelength λ, similarly the wavelength of light, a real space distance has a reciprocal relationship to the wavevector $k = 2\pi/\lambda$. In reciprocal space, distance is a direct measure of k, and for this reason it is often referred to as k-space. The advantage of working in k-space means one can determine when constructive interference will occur by applying the law of conservation of momentum. This means the wavevector is an important quantity, as a measure of the momentum of an incident and diffracted photon or X-ray from a crystalline sample.

2.1.1 Ewald Construction as related to LEED

The condition for elastic scattering can be visualised using the Ewald geometric construction [19][21], shown for a cubic lattice in figure 2.2(a) in 3D and (b) in 2D. The distance between adjacent points is $2\pi/a$, where a is the real space lattice constant. The incident wavevector k_0 is drawn to scale with its tip pointing towards the origin of reciprocal space $(0, 0, 0)$. The Ewald sphere maps the magnitude of the incident wavevector to the reciprocal space lattice centred at point P. If any of the reciprocal lattice points are intersected by the sphere then the condition for elastic scattering is satisfied (i.e. a change in momentum of the beam but no change in energy) by the scattered wavevector $|k'|$. The condition for constructive interference for the elastically scattered electron is that the change in the electron wavevector

must be equal to a reciprocal lattice vector given by g_{hkl}

$$|k^{'}| - |k_0| = g_{hkl} \tag{2.1}$$

It can be seen from the figure 2.2(a) that

$$\sin\theta = \frac{|g|/2}{|k_0|} \text{ and } |g| = \sqrt{h^2 + k^2 + l^2}2\pi/a \tag{2.2}$$

by Pythagoras. These can then be substituted and rearranged to form the Bragg condition

$$n\lambda = 2a\sin\theta, \text{ where } n = \sqrt{h^2 + k^2 + l^2} \tag{2.3}$$

where n is known as the order of diffraction.

LEED is a direct representation of the surface reciprocal lattice and is a simplified 2D version of the 3D case just presented. This means the requirements are much less stringent for only the component of the wavevector parallel to the surface must be conserved when the periodic 2D sample surface is investigated. This is reflected in a change in the Ewald construction figure 2.2(b). The period normal to the sample surface is infinite. This means that the points in reciprocal space have a separation of zero and are represented by lattice rods. The Bragg condition, equation (2.3), can now be satisfied over a wide energy range and geometries. Diffraction occurs at all energies provided the corresponding rod lies within the Ewald Sphere.

2.1.2 LEED analysis

LEED is routinely employed when checking the surface for cleanliness and ordering. Adsorbed species will influence the diffraction spots and from a qualitative analysis of the spot positions in the diffraction pattern the symmetry and alignment of the adsorbate with respect to the substrate structure may be determined. There are two types of symmetry operators required to discuss the symmetry properties of two-dimensional structures, point symmetries and line symmetries. Point symmetry refers to the rotational symmetry which may exist about some point or points in the unit cell. Line symmetry indicate the existence of lines or planes about which the cell has mirror-reflection symmetry or glide-reflection symmetry [19]. Mirror-reflection symmetry occurs when the mirror image of the initial geometrical configuration of the unit cell is regenerated on the opposite side of the plane. Glide-reflection symmetry requires both reflection and translation along the mirror plane to be combined to bring the unit cell into coincidence with an initial geometrical configuration of the

unit cell. These glide-reflection symmetries results in systematic absences of Bragg spots in the LEED pattern [22].

The arrangement of adsorbates in a particular domain or phase can have at most the symmetry indicated by the LEED pattern. This is because the diffraction pattern is a composition of the individual patterns from different surface arrangements within the coherence length of the electrons. The coherence length, typically 50-100 Å, is limited by the energy spread of the incident beam and its angular divergence [21]. It also sets the maximum long range order of the surface that can be probed on the surface. Only structures ordered over lengths comparable to the coherence length contribute to the LEED pattern. This means that if there is a preferential formation of a particular domain or phase the Bragg spots associated with that structure will have a greater intensity. Ordered domains or phases at length below the coherence length will produce weaker Bragg spots and a higher background over the diffraction pattern.

The arrangement of the adsorbed molecules on a surface relative to the underlying substrate can be categorised as either commensurate or incommensurate. A commensurate overlayer forms when each adsorbate adopts an inter-adsorbate separation that is either equal to that of the substrate atoms or an integer multiple of the substrate spacing. This can be due to either the size of the molecule or the domination of substrate-adsorbate interactions over any lateral adsorbate-adsorbate interactions. Alternatively in the case of an incommensurate overlayer, the spacing adopted is irrationally related to the substrate lattice spacing. Diffraction patterns from more complicated structures where the overlayer is incommensurate result in weaker diffuse spots, making analysis more challenging. This is especially true for organic layers where larger unit cells and surface damage due to the incident electrons mean LEED patterns must be taken at low beam energy, ≤ 30 eV. At these low energies however the diffracted electrons forming the pattern are more susceptible to stray magnetic fields.

All modelling of LEED diffraction patterns were carried out using a LEED pattern simulator, LEEDpat [17]. It is designed to help interpret experimentally observed LEED spot patterns for well-ordered surfaces especially in the presence of superlattices. In particular it allows one to tell which 2D surface lattices are compatible with an observed LEED pattern. Providing extensive 2D symmetry information, it can show all rotational, mirror and glide symmetries that are compatible with the observed pattern. Rotational domains and glide plane extinction of spots are taken into account. This allows the user to narrow down possible structural models of the surface and to propose atomic positions in the actual structure. Simulations

made with the LEEDpat are included in this work, two figures are shown on each occasion. The first figure is a real-space sketch of basic 2D lattice and superlattice (for one domain orientation only). The basic 2D lattice is shown as a green grid, while the superlattice is shown with a lattice of dots. Basis vectors are included for both lattices (thick green and black lines, respectively). The second figure is the diffraction pattern for the basic 2D lattice is shown as white spots surrounded by circles. The additional white or coloured spots represent the "fractional-order" spots of the superlayer (white, single domain or coloured, several symmetry induced domains). It is noted that LEEDpat does not itself predict structural models or determine atomic positions.

2.2 Normal Incidence X-ray Standing Wave (NIXSW)

In this section the important parameters involved in the analysis of NIXSW profiles are discussed, and the theory underlying the XSW imaging technique is outlined. Many standard texts contain an introduction to the key aspects underlying XSW which evolved with the dynamic theory of X-ray diffraction [23]. Recent reviews which deal specifically with XSW theory and contain experimental examples should be consulted to provide a more detailed discussion [24] [25].

2.2.1 Basic theory of XSW

Standing waves are produced by a superposition of two or more coherent waves travelling in opposite directions. Synchrotron radiation which offers a high flux and a tuneable wavelength is used for this technique. When the sufficiently intense and monochromatic X-rays are incident on a sample, constructive interference at the Bragg condition, $n\lambda = 2d\sin\theta$ between the incident and the back-scattered waves produces an X-ray standing wave. It extends both above and below the semiconductor or metal crystal surface, figure 2.3. The phase of the backscattered wave, in the region of total reflectivity about the Bragg condition, is a strong function of the angle of incidence θ and the photon energy hc/λ. This makes it possible to tune the nodes and antinodes of the standing wave relative to the atomic scattering planes by scanning either the angle of incidence or the photon energy.

Due to instrumentation considerations scanning through the Bragg condition, by rocking the crystal to scan the angle of incidence θ, is a non-trivial task. Woodruff et al. [26] introduced a modification to the XSW technique. Rather than rocking the

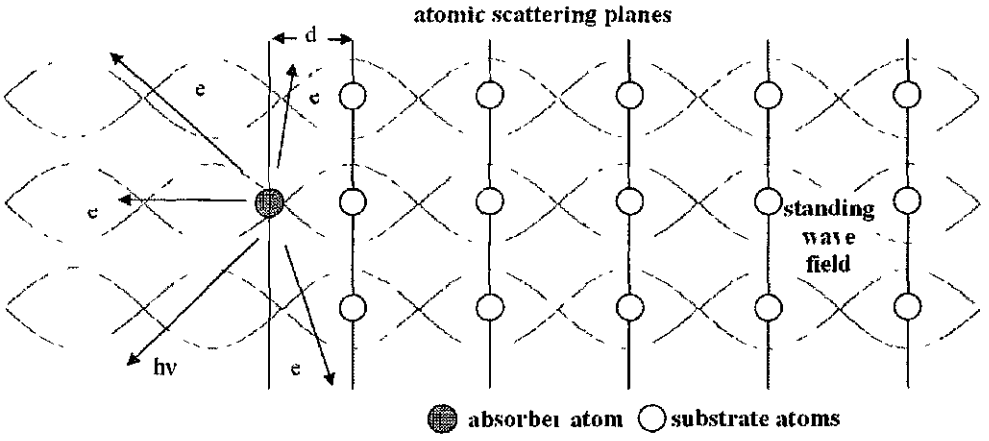

Figure 2.3: A schematic diagram of a standing wave field set up in a crystal. Adsorption is proportional to intensity is measured by monitoring the emission from the absorber atom. The distance d of the absorber atom from the scattering planes is determined by scanning the phase of the standing wave.

crystal it was preformed by scanning the photon energy. This is referred to Normal Incidence X-ray Standing Wave, (NIXSW), where normal refers to the angle between the Bragg plane under investigation and the incident radiation. The popularity of NIXSW as a surface science technique is due to (i) the wide range of crystals it can elucidate, including metals and oxides with mosaicities[1] up to tenths of a degree, (ii) the less stringent collimation of the incident X-ray beams compared to X-ray standing wave spectroscopy, and to a lesser extent, (iii) the wider availability of synchrotron radiation.

Any atom placed in the standing wave will adsorb radiation in proportion to the intensity of the standing wave field. Since the position of nodes in the standing wave field is known, it is possible to locate the absorber atom relative to the crystal scattering planes by monitoring the photoexcitation as a function of the incident energy This position can only be determined as a fraction of the distance between the Bragg planes due to the limitation imposed by the periodicity of the standing wave field. This is the basic theory behind the X-ray standing wave technique.

The XSW technique allows one to determine the amplitude and phase of the individual Fourier components of the real-space structure in the direction normal to the Bragg plane under investigation[2]. When the XSW technique in used in combination with spectroscopy e.g. photoelectrons, X-ray fluorescence, Auger electrons (or other element specific signals), one can also record an atomic distribution in an

[1]The degree of long-range order of the unit cells within a crystal

[2]While real-space reconstructions are also possible to produce with just the X-ray diffraction results [27], it is only with the phase information that it is straight forward.

element specific way. In recent studies [28] [29] it was noted that applying XSW to a range of Bragg planes, allows one to obtain the real-space structure directly from a Fourier transform of the diffracted beam intensities without any trial and error or assumptions. Thus, if one can measure a sufficient number of different XSW absorption profiles, then, with a direct inversion, it is possible to produce an element-specific image of the real-space structure. It is noted however that no information on the length scale beyond the unit cell size of the substrate crystal is obtained, and the adsorbate position is found relative to the bulk extended planes of the substrate.

2.2.2 NIXSW Theory

The intensity of the X-ray standing wave in the crystal is simply the modulus squared of the sum of the incident and reflected X-ray amplitudes. Taking the incident amplitude to be unity, and assuming σ-polarisation synchrotron radiation (electric vectors of incident and scattered X-rays are parallel), the intensity in the crystal at a real space vector position r can be written as

$$I/I_0 = \mid 1 + (E_H/E_0)e^{-2\pi\imath H.r}\mid^2 \tag{2.4}$$

where E_H and E_0 are the amplitude of the reflected and incident X-rays respectively, and H is the reciprocal lattice vector of the relevant Bragg reflection under study. The scalar product of $H.r$ may be expressed in terms of the interlayer spacing d_H, and the perpendicular distance of the absorber from the scattering planes z as $H.r = z/d_H$, then

$$I/I_0 = \mid 1 + (E_H/E_0)e^{-2\pi\imath z/d_H}\mid^2 \tag{2.5}$$

The amplitude of the scattered X-ray is determined, from the scan parameter η, and the geometrical structure factors F_H and $F_{\bar{H}}$ of the reflections defined by H and $\bar{H}$, as

$$(E_H/E_0) = -\sqrt{F_H/F_{\bar{H}}}(\eta \pm \sqrt{\eta^2 - 1}) \tag{2.6}$$

The structure factor is a complex number, its real part corresponds to the scattering strength of the plane and its imaginary part corresponds to any absorption and phase shift that takes place during the scattering. For a scattering plane with the reciprocal lattice vector H the structure factor can be expressed as

$$F_H = \sum_{\imath=1}^{n} f_\imath e^{2\pi\imath H\, r_\imath} \tag{2.7}$$

where f_i is the atomic scattering factor of atom number i at the point r_i in the unit cell and n is the number of atoms in the unit cell. Thermal vibration caused the atoms to move about their equilibrium positions, and so the atomic scattering factor f_i of atom i is reduce by the Debye-Waller factor e^{-M_i}, where $M = {}^1/_3\langle U_{H^2}\rangle H^2$ and $\langle U_{H^2}\rangle$ is the mean square displacement of the atoms in the H direction [23].

The scan parameter η is a measure of how far the scattering conditions are from the midpoint of the reflectivity curve. Traditionally for XSW technique this parameter was written in terms of an angular displacement. In the case of the NIXSW technique the scattering angle is held fixed and one scans through the X-ray energy (E) or wavelength (λ), because of this it is convenient to express η in terms of the deviation in X-ray energy, ΔE, from the value at the Bragg condition.

$$\eta = \frac{-2(\Delta E/E)\sin^2\theta_B + \Gamma F_0}{|P|\Gamma\sqrt{F_H F_{\bar{H}}}} \tag{2.8}$$

where $\Delta E/E$ is the instrumental resolution of the monochromator and analyser, the Bragg angle θ_B (defined as the grazing incidence angle to the scatterer planes such that normal incidence corresponds to a value of 90 °), P is a polarisation factor (σ-polarisation), F_0 is the structure factor for the (000) reflection and Γ is

$$\Gamma = \frac{e^2}{4\pi\varepsilon_0 mc^2}\cdot\frac{\lambda^2}{\pi V} \tag{2.9}$$

where V is the volume of the unit cell, e and m the charge and mass of an electron, ε_0 the permittivity of free space and c the speed of light.

Simple kinematical theory predicts a peak in the reflectivity ($|E_H/E_0|^2$) is of infinitesimal width at the exact Bragg condition. For dynamical theory of X-ray diffraction two important differences are highlighted by the previous equations. For a non-absorbing crystal (for which F_0 and $F_H F_{\bar{H}}$ are real) one has a finite range of total reflectivity corresponding to the range of η between -1 and +1. This energy range,

$$\Delta E = \pm\frac{E|P|\Gamma\sqrt{F_H F_{\bar{H}}}}{2\pi\sin^2\theta_B} \tag{2.10}$$

is obtained by inverting equation (2.8). The second important difference is that this total reflectivity range is not centred around the kinematical Bragg condition, but is offset by the ΓF_0 term in equation (2.8) which is independent of ΔE.

In summary the phase of the term E_H/E_0 varies as one scans through the reflectivity range and causes η to vary. Further manipulation is required before this

fact can be utilised by the NIXSW technique. The amplitude of the electromagnetic field is related to the reflectivity R as

$$E_H/E_0 = \sqrt{R}e^{i\phi} \tag{2.11}$$

with the phase ϕ, varying by π across the reflectivity range in a fashion wholly predictable from the equations given above. Using this form, equation (2.5) can be written as

$$I = \mid 1 + \sqrt{R}e^{\phi i - 2\pi i z/d_H} \mid^2 \tag{2.12}$$

$\Leftrightarrow$

$$I = 1 + R + 2\sqrt{R}\cos(\phi - 2\pi z/d_H) \tag{2.13}$$

This holds if one assumes that all absorber atoms are in the same site. Due to the disorder of imperfect reconstructions, thermal vibrations and the possibility of several atomic sites, this is never the case Some probability distribution for discrete sites must be included in the equation. This is done by including the distribution term $f(z).dz$, which defines the fraction of absorbers at a spacing z within the range dz,

$$I = 1 + R + 2\sqrt{R}\int_0^{d_H} f(z)\cos(\phi - (2\pi z/d_H))dz \tag{2.14}$$

Two structural fitting parameters used in the analysis of XSW profiles, the coherent position, D, and the coherent fraction f_{co} are introduced,

$$I = 1 + R + 2f_{co}\sqrt{R}\cos(\phi - (2\pi D/d_H)) \tag{2.15}$$

The distribution term $f(z).dz$ is normalised to one which simply means that the absorber atom must be somewhere between the two adjacent Bragg planes and so the coherent fraction and coherent position are both numbers between 0 and 1. The coherent fraction defines the homogeneity of the adsorbates position. When $f_{co} = 1$ it implies that all the atoms are in the same position relative to the scatterer planes When $f_{co} = 0$ it generally implies a random height distribution for that particular plane. The coherent fraction is lowered when affected by the relative heights of the multiple positions. It is possible to have two discrete position that interfere and result in an ordered surface with $f_{co} = 0$. The coherent position defines the average height of the absorbed atoms as a fraction of the spacing (d_H) of scattering planes. $D \approx 0.5(\equiv 1.5)$ places the absorber atoms half-way between the scattering planes, and implies a distance of half the lattice spacing above the surface.

These two parameters define the structural dependence of the measured absorp-

tion profile, and are the parameters which emerge from the analysis of the experimental data. Evidently for the idealised case of a singly occupied layer spacing with no disorder (i.e. $f(z)$ is a delta function at a particular value of z) the coherent fraction is unity and the coherent position is simply the actual layer spacing. Rewriting equation (2.15) in the form

$$I = f_{co}(1 + R + 2\sqrt{R}\cos(\phi - (2\pi D/d_H))) + (1 - f_{co})(1 + R) \tag{2.16}$$

reveals the relation between these parameters more clearly. The first bracketed term is now the right-hand side of equation (2.13) (the ideal single-site absorption in a perfectly coherent standing wave-field) multiplied by f_{co}. The second term $(1 - f_{co})$ is (i.e. the "incoherent fraction") multiplied by $(1+R)$, that is the wavefield intensity sum of the incident and reflected waves in the absence of coherent interference. The simplest way of relating these parameters to the actual position distribution is

$$f_{co}e^{2\pi iD/d_H} = \int_0^{d_H} f(z)e^{2\pi iz/d_H}dz \tag{2.17}$$

from which it is clear that f_{co} and D define the amplitude and phase of one Fourier component of the absorber site distribution projected along a direction perpendicular to the relevant Bragg scatterer plane.

2.2.3 XSW analysis

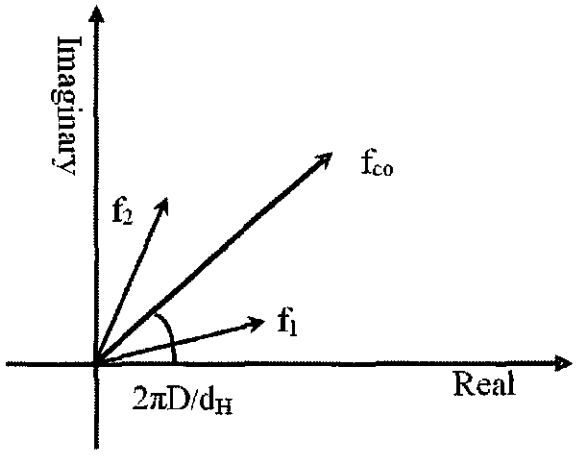

Figure 2.4: The Argand diagram representation of the vector sum of XSW contributions from two distinct absorber heights, z_1 and z_2.

An Argand diagram is useful as a simple graphical representation of how the measured quantities f_{co} and D relate to the integral over a real spatial distribution

function [24]. It can also be exploited to calculate the distribution of atoms between two distinct sites on the surface.

For some arbitrary Bragg reflection a coherent position and coherent fraction would be recorded experimental in the NIXSW profile. They can be represented on the Argand diagram, figure 2.4. From the centre (0,0), i.e. (coherent position, coherent fraction) a vector can be drawn with length equal to f_{co} and an angle calculated from the coherent position, where the phase angle is equal to $2\pi z/d_H$ is relative to the positive x-axis. In the case where there are two distinct absorber heights at z_1 and z_2 with a fractional occupancy of f_1 and f_2 (with $f_1 + f_2 = 1$). The vector sum of these components would give a resultant vector of length f_{co} and phase angle $2\pi D/d_H$. The integral on the right hand side of equation (2.17) would then reduce to a sum over two terms:

$$f_{co}e^{2\pi\imath D/d_H} = f_1 e^{2\pi\imath z_1/d_H} + f_2 e^{2\pi\imath z_2/d_H} \tag{2.18}$$

In the formalism of crystallography, the geometrical structure factors (including the Debye-Waller factor) are the measured Fourier coefficients [23],

$$F_H = f_{co}e^{2\pi\imath D/d_H} \tag{2.19}$$

where the D/d_H coherent position and the f_{co} coherent fraction define the amplitude and phase of one Fourier component of the absorber site distribution. The imaging of the real-space surface [28] requires one to measure a sufficient range of adsorption profiles, apply certain symmetry rules and sum the Fourier terms. One can define an element specific distribution within the unit cell, $\rho(r)$, as

$$\rho(r) = \sum_H F_H e^{-2\pi\imath(H.r)} \tag{2.20}$$

which expands to

$$\rho(r) = \sum_H f_{co}e^{2\pi\imath(D/d_H)}e^{-2\pi\imath(H.r)} \tag{2.21}$$

which implies

$$\rho(r) = 1 + 2\sum_{H\neq -H\neq 0} f_{co}\cos\left(2\pi(D_H - H.r)\right) \tag{2.22}$$

where f_{co} and $D_H = D/d_H$ are the coherent fractions and the coherent positions for the Bragg reflections denoted by the reciprocal lattice vector H.

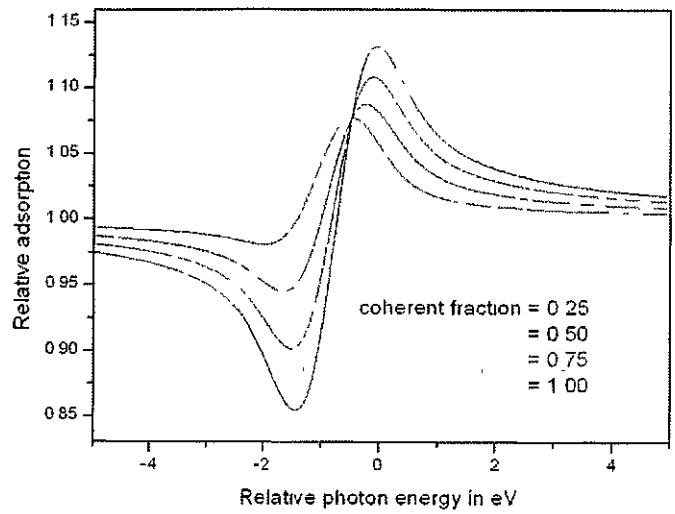

Figure 2.5: NIXSW profiles calculated for a range of coherent fractions. A reduction in the coherent fraction reduces the height of the XSW profile but does not broaden it.

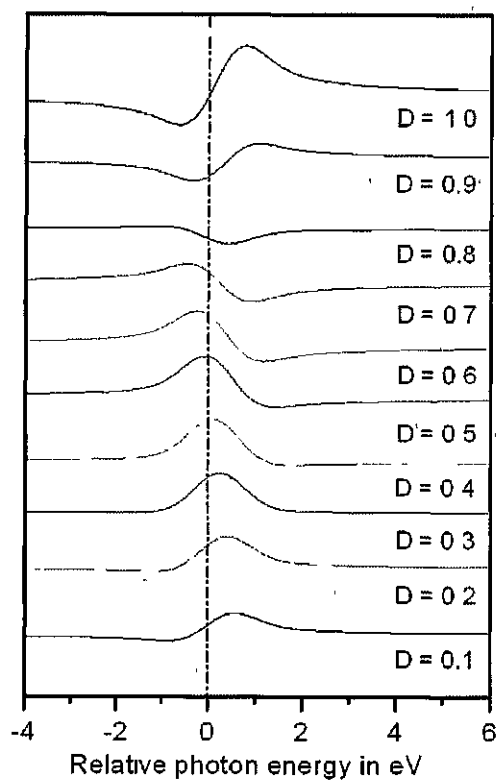

Figure 2.6: NIXSW profile calculated for coherent positions from 0 to 1 with an instrumental resolution of 1 eV.

The coherent position and coherent fraction have a dramatic influence on the shape of the Bragg profile and depend on the adsorbate position relative to the Bragg planes. In order to appreciate this, it is important to recall that scanning through the Bragg energy results in a variation in the phase of the standing wave. When the nodes of the standing wave coincide with the Bragg planes, the intensity is at a minimum, and a dip is produced in the profile curve. When the antinodes of the standing wave coincide with the Bragg planes the maximum intensity is reached and this produces a peak in the profile. This produces an XSW profile with the characteristic shape of a dip before and a peak behind the Bragg condition.

When monitoring the adsorbate signal the absorber atom will encounter the nodes and antinodes of the standing wave, depending on its position between the Bragg planes. The influence of the coherent fraction on the shape of the XSW profile is shown in figure 2.5. A reduction in the height of the XSW profile is observed for a reduction in the coherent fraction. The calculated profiles in figure 2.6 show the effect of different coherent positions relative to the Bragg planes on the profiles. For example, for a coherent position is 0.5, the absorber atom will encounter the antinodes before and the nodes after the Bragg energy, and the XSW profile appears as the inverse of the profile for coherent position of 0. All profiles were plotted with an instrumental resolution of 1 eV, if the resolution decreases the profiles broaden.

2.2.4 Synchrotron Radiation

When a charged particle is forced to follow a curved trajectory at relativistic velocity synchrotron radiation is emitted. This radiation has a continuous spectrum extending from the infrared (IR) to the hard X-ray region of the electromagnetic spectrum, it is very intense over a wide range of photon energies, and it is linearly polarised in the plane of the ring [30]. In order to exploit the synchrotron radiation, high-energy electrons are contained under UHV conditions in a storage ring. At the Daresbury Synchrotron Radiation Source (SRS) [31], a pulsed beam of 600 MeV electrons is injected tangentially into the main storage ring (approximately 32 m in diameter) and RF power (from klystron cavities) is used to raise the electron energy to 2 GeV. Bending magnets around the ring are used to accelerate and direct the electrons along a curved path. The energy lost to synchrotron radiation emission is replaced by RF power however, the beam current decays appreciably over a 24 hour period and a new beam is injected atleast once in every 24 hours during normal operation at the Daresbury SRS [31].

The synchrotron radiation is directed down a beamline, which incorporates var-

ious mirrors to direct and focus the light onto the sample. The required photon energy is selected using a monochromator. A ruled Bragg diffraction grating can be used for photon energies up to ~1500 eV however, at higher energies the wavelengths are so small that crystals (e.g. InSb(111), Ge(111)) are used to diffract out the required photon energy. The broad range of energies allows a variety of different techniques to be used to investigate the sample [21] [30].

2.2.5 Daresbury beamline 4.2

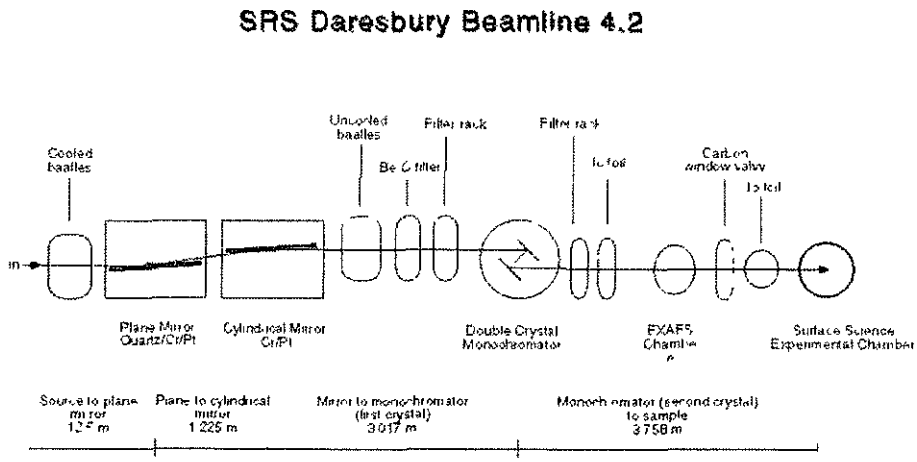

Figure 2.7: Schematic of beamline 4.2 at the Daresbury SRS facility, UK.

All NIXSW experiments presented in this thesis were carried out at the Daresbury SRS facility. The results obtained from studies of Sn/Cu(100) and Bi/Si(100) surfaces are presented in section 3.5 and 6.3.1 respectively.

Beamline 4.2, figure 2.7, is situated on bending magnet 4 and has a double crystal monochromator that consists of pairs of single crystals. The photon energy range covered is 1800 eV to 6000 eV. The beamline employs a chromatic pre-mirror system, which allows the high-energy cut-off to be selected in situ. The InSb(111) crystal pair cover the photon energy range from 1780 eV to 5200 eV and the Ge(111) crystal pair has a photon energy range from 2010 eV to 6000 eV. and a resolution of less than 1 eV at 2450 eV and less than 3 eV at 4000 eV photon energy. The photon flux exhibit sharp dips at some energies, referred to as glitches, and have an overall drop-off at the extremes of the energy range. The glitches in the flux are an intrinsic property of the crystals and are caused by interference of the directly reflected beam with a multiply reflected beam in the crystal [32].

The beamline was equipped with a permanent UHV chamber shown schematically in figure 2.8. A vacuum of 2×10^{-10} mbar could be achieved after a 24 hour bake

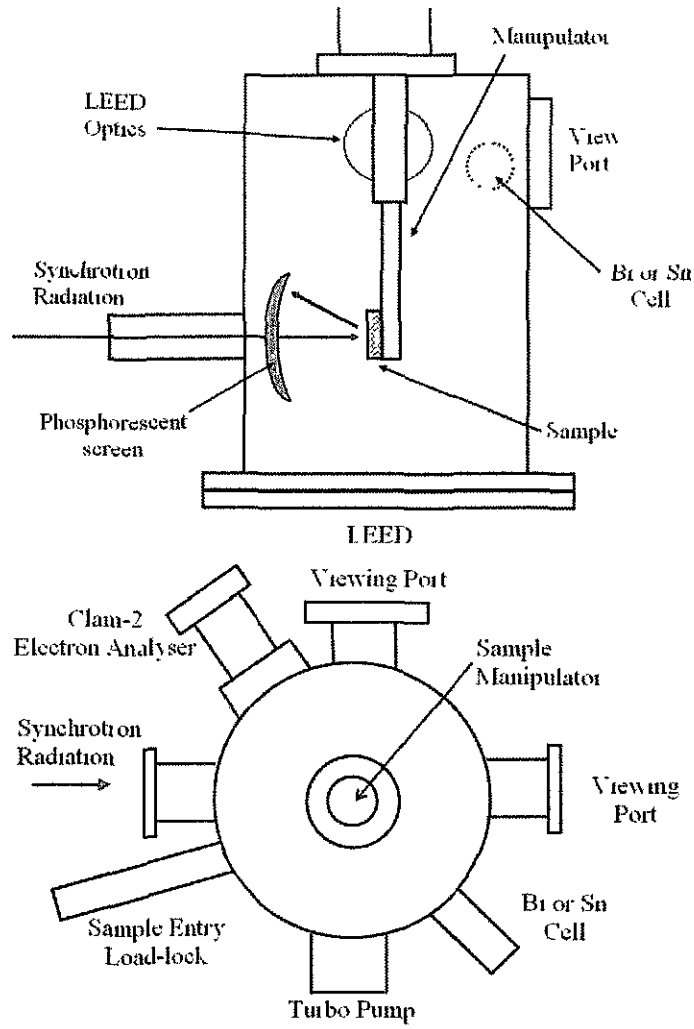

Figure 2.8: Schematic of vacuum chamber on beamline 4.2 in Daresbury SRS.

at ~450K. The vacuum was maintained by a turbo molecular pump and a titanium sublimation pump (TSP). The analysis chamber contained a Vacuum Generators sample manipulator, a Clam-2 electron energy analyser, an Omicron 4-grid LEED, and a fast entry load lock for sample entry. The chamber contained two levels; the upper level accessed the LEED and a window to monitor sample heating/material deposition, the lower level accessed the synchrotron radiation where the NIXSW measurements were performed.

The samples were mounted on a high precision manipulator with sample translation in the x, y, z directions, 360° rotation about the vertical axis and almost ± 90° azimuthal rotation. The Cu(100) crystal was mounted on a tantalum spade using tantalum clips to secure it in place. For the Cu crystal, argon ion bombardment at 2kV and annealing cycles at 800K readily produced a clean surface. The silicon samples were mounted on a tantalum holder that permitted direct current

heating of the sample to 1370K, required for removal of the oxide and obtaining a (2×1) reconstruction. Each sample was cleaned with the appropriate cleaning procedure (as described here for the Cu crystal and in section 5.1 for the Si(100) sample). All sample temperatures were measured using a pyrometer. The X-ray standing wave experiments were carried out with the relevant scattering planes of the crystal aligned at normal incidence to the photon beam. In order to locate the Bragg plane the monochromator energy is set to ~5-10 eV above the Bragg condition. The reflected beam could then be observed on a phosphor coated screen surrounding the photon entry port see figure 2.8. By alternately varying the sample angle and reducing the monochromator energy the diffracted beam was aligned so it was reflected back into the beamline. The diffracted beam is then aligned at normal incidence. Final tuning is done by observing the increase in flux on the I_0 monitor, figure 2.7. Once a good reflectivity is observed the diffracted beam was moved off normal incidence by ~1°. This means the reflected intensity does not show in the recorded normalisation spectra.

2.2.6 NIXSW analysis

The NIXSW profiles of the adsorbate and the substrate atoms are measured by recording two separate data files; (i) the intensity of a photoemission or Auger peak, the on-peak and (ii) the background spectra at an energy ~10 eV higher than the photoemission or Auger peak position, this is referred to as the off-peak [33]. The on-peak and off-peak spectra are then normalised to the beam intensity. The background spectrum, which includes the contribution due to inelastically scattered electrons, was then subtracted from the on-peak to give the X-ray standing wave contribution.

The recording and analysis of the NIXSW profiles was performed using a program written by Prof. R. Jones [34] in Igor Pro [35]. This program requires a procedure file with certain parameters for each new substrate. These parameters include the volume of the unit cell, the layer spacing, the structure factors (F_{000} and F_{hkl}) and the Debye-Waller factor (DW). The structure factors for the Bragg reflection for all substrates were calculated using the XOP program [36]. The crystal geometry, the Bragg planes and the real part of the atomic scattering factors for the different atoms in the crystal are supplied by the user as an input file. The program then calculates the real and imaginary part of the structure factor. The other parameters such as the interplanar distances, the photon energy, the instrumental resolution, etc. are either known or can be calculated in a straightforward manner. The Igor

program [34] uses these values to fit a profile to the normalised absorption curve and to determine the coherent position (D) and the coherence fraction (f_{co}) and a Q-factor. The Q-factor is a correction factor for the backward-forward asymmetry in the photoemission signal due to non-dipole [37] transitions.

2.3 Scanning Tunnelling Microscopy (STM)

In this section the basic theory underlying the quantum-tunnelling of the STM is reviewed. The components of the Omicron VT STM unit are described. The electronics that control the tip movement and tunnelling current are discussed. The tools provided by the analysis software WXsM [38] which are used in this work are introduced. Finally, the vacuum chamber which contains the STM is presented.

The STM is a practical application of the principle of quantum-tunnelling, which describe how electrons can tunnel through a potential energy barrier. In this context, the barrier is the vacuum gap between two conductors; an atomically sharp tip and the sample surface. When the two conductors are brought to within a few Ångströms under an appropriate bias, electrons will flow between them as a result of quantum mechanical tunnelling.

The tunnel current depends exponentially on the size of the vacuum gap. By measuring this current and rastering the tip over the surface, a contour map of the surface electron density is recorded. This gives a good two dimensional representation of the surface topography with atomic resolution. From these images the cleanliness and structure of the surface can be investigated on the atomic scale. The simplicity of the concept however belies the complexity of the technique and data analysis.

2.3.1 Basic Theory of STM

A simple one-dimensional model is adequate to illustrate the basic concepts of the technique. To begin; the classical momentum p of an electron with mass m, energy E, travelling in a potential $U(z)$ is given by

$$p = \sqrt{(E - U(z))/2m)} \tag{2.23}$$

Provided the electron has a nonzero momentum it can move within the region but it cannot penetrate a potential barrier if its energy is smaller than the potential

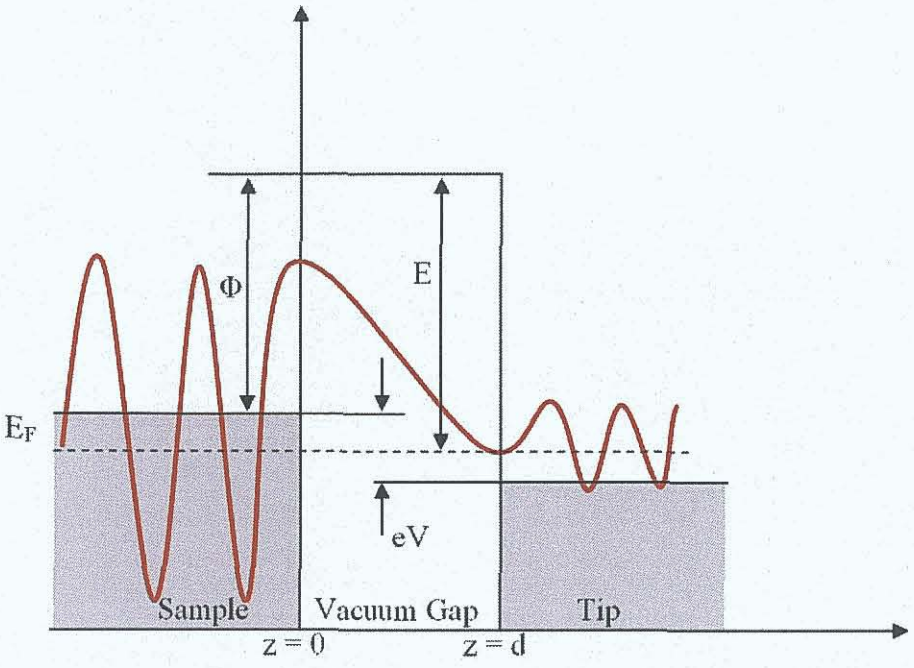

Figure 2.9: Schematic diagram of a one dimensional tunnel junction under an applied bias voltage V. The work function Φ of a metal is the minimum energy required to remove an electron from the metal to the vacuum level. An identical Φ is used for both conductors so vacuum level is effectively the same for both.

energy U of the barrier. By exploiting the quantum nature of electrons, the concept can be extended, the same electron can now be described by a wavefunction $\Psi(z)$ which satisfies Schrödinger wave equation [39],

$$-\frac{\hbar^2}{2m}\frac{d^2}{dz^2}\Psi(z) + U(z)\Psi(z) = E\Psi(z) \tag{2.24}$$

where h is Planck's constant and $\hbar = h/2\pi$. The vacuum gap forms a potential barrier between the two conducting surfaces, when they are sufficiently close together as illustrated in figure 2.9. In this case the two conductors, are the tip and the sample surface. A rectangular potential barrier is used to elucidate the interaction of an electron with the barrier. By solving Schrödinger wave equation, an electron can be described as a travelling wave outside and within the vacuum gap potential barrier. In the region outside the potential barrier

$$\Psi(d) = \Psi(0)e^{\pm\kappa d} \quad \text{where} \quad \kappa = \frac{\sqrt{2mE}}{\hbar} \tag{2.25}$$

and within the barrier

$$\Psi(d) = \Psi(0)e^{-\kappa d} \quad \text{where} \quad \kappa = \frac{\sqrt{2m(\Phi - E)}}{\hbar} \tag{2.26}$$

This predicts an exponential decaying solution for the electron wave function within the classically impenetrable barrier [39]. A solution of the form depicted in figure 2.9 (red line), shows that there is a finite probability of finding the electron both outside and within the barrier. This phenomenon is called quantum mechanical tunnelling and it depends exponentially on the thickness of the barrier [40]. The probability of tunnelling is proportional to the ratio of the probabilities of finding the particle on either side of the barrier, i.e. the ratio of the squares of the wave function at these points.

$$|\Psi(d)|^2 = |\Psi(0)|^2 e^{-2\kappa d} \tag{2.27}$$

The height of the potential barrier is determined by the work function of the tip and sample, (here assumed to be equal). Fermi energy $E_F = -\Phi$ if the vacuum level is taken as the zero point for energy. In the absence of an applied bias voltage, electrons can tunnel through the barrier in either direction so there is no net tunnel current. In the STM a bias voltage V can be applied, electrons within the energy range $E_F - eV \leq E \leq E_F$ produce a net tunnelling current. For small bias voltages $eV \ll \Phi$ only electrons about the Fermi energy are probed. The probability of an electron in the n^{th} energy state tunnelling through a barrier of width z is

$$P \propto |\Psi_n(0)|^2 e^{-2\kappa z} \quad \text{where} \quad \kappa = \frac{\sqrt{2m\Phi}}{\hbar} \tag{2.28}$$

is the inverse decay length for all tunnelling electrons [39] [41]. The total tunnel current I, which is proportional to the probability of electrons tunnelling through the barrier, from the sample to the tip is calculated by summing over all the possible states in the energy range, $E_F - eV \leq E \leq E_F$ [41]

$$I(v) \propto \sum_{E_n = E-\varepsilon}^{E} |\Psi_n(0)|^2 e^{-2\kappa z} \tag{2.29}$$

For small bias voltages the density of states of a metal is constant over the energy range. The current can then be written in terms of the local density of states (LDOS) of the sample at the Fermi energy where $\rho(z = 0, E = E_F)$. The LDOS is defined

as [42] [43]

$$\rho(z,E) \equiv \lim_{\varepsilon \to 0} \frac{1}{\varepsilon} \sum_{E_n = E-\varepsilon}^{E} |\Psi_n(z)|^2 \tag{2.30}$$

for sufficiently small energy, ε. The tunnel current at the tip can then be written in terms of the LDOS of the sample [41]

$$I(V) \propto V \rho_s(0, E_F) e^{-2\kappa z} \tag{2.31}$$

The sensitivity of the tunnel current to any change in z of the tip to the sample, results in the very sensitive normal resolution. This can be demonstrated by a quick back of the envelope calculation. Transmission probability and thus tunnel current is about equal to $e^{-2\kappa Z}, \kappa \sim 1.6 \times 10^{10}$ m^{-1} for electrons of energy 1 eV meeting a potential barrier of 10 eV. The difference in the tunnel probability between a 0.5 nm and 1 nm vacuum gap, varies between $1.1{\times}10^{-7}$ and $1.3{\times}10^{-14}$ respectively. For future reading and more comprehensive reviews of the current theoretical approaches the reader is directed to dedicated texts [41] [44] [45].

2.3.2 Scanning Tunnelling Microscope: Omicron unit

The STM unit consists of an atomically sharp tip, a piezoelectric scanner tube, a vibration isolation platform, and tunnelling current feedback controller. It is housed under UHV conditions to maintain the atomic cleanliness of the samples. The tip is made with wire usually tungsten (W) or platinum iridium alloy (Pt/Ir). The wire is electronically etched in an electrochemical bath, for example sodium hydroxide (NaOH), to produce the atomically sharp tip [46] [47]. The Pt/Ir alloy tip is more malleable than W, it is easier to sharpen and can be formed by simple mechanical means. The W tips build up an oxide layer in air but they can be cleaned and reformed in situ by nanostructuring. This involves placing the tip in a high electric field or the controlled crashing of the tip into sample surface.

A cylindrical piezoelectric transducer allows the controlled vertical and lateral positioning of the tip and for rastering of the tip over the sample surface, figure 2.10. The tip is placed in a magnetic holder at the top of this piezoelectric transducer tube. The tube is hollow with the outer surface divided into four electrodes and a single inner electrode. Lateral motion (x or y direction) can be achieved by applying equal and opposite voltages to the two opposing vertical outer electrodes while keeping the other two outer electrodes grounded or at constant voltage. The vertical motion (z direction) can be controlled by applying the same voltage to the four outer electrodes

as [42] [43]

$$\rho(z,E) \equiv \lim_{\varepsilon \to 0} \frac{1}{\varepsilon} \sum_{E_n=E-\varepsilon}^{E} |\Psi_n(z)|^2 \tag{2.30}$$

for sufficiently small energy, ε. The tunnel current at the tip can then be written in terms of the LDOS of the sample [41]

$$I(V) \propto V\rho_s(0,E_F)e^{-2\kappa z} \tag{2.31}$$

The sensitivity of the tunnel current to any change in z of the tip to the sample, results in the very sensitive normal resolution. This can be demonstrated by a quick back of the envelope calculation. Transmission probability and thus tunnel current is about equal to $e^{-2\kappa Z}, \kappa \sim 1.6 \times 10^{10}$ m^{-1} for electrons of energy 1 eV meeting a potential barrier of 10 eV. The difference in the tunnel probability between a 0.5 nm and 1 nm vacuum gap, varies between 1.1×10^{-7} and 1.3×10^{-14} respectively. For future reading and more comprehensive reviews of the current theoretical approaches the reader is directed to dedicated texts [41] [44] [45].

2.3.2 Scanning Tunnelling Microscope: Omicron unit

The STM unit consists of an atomically sharp tip, a piezoelectric scanner tube, a vibration isolation platform, and tunnelling current feedback controller. It is housed under UHV conditions to maintain the atomic cleanliness of the samples. The tip is made with wire usually tungsten (W) or platinum iridium alloy (Pt/Ir). The wire is electronically etched in an electrochemical bath, for example sodium hydroxide (NaOH), to produce the atomically sharp tip [46] [47]. The Pt/Ir alloy tip is more malleable than W, it is easier to sharpen and can be formed by simple mechanical means. The W tips build up an oxide layer in air but they can be cleaned and reformed in situ by nanostructuring. This involves placing the tip in a high electric field or the controlled crashing of the tip into sample surface.

A cylindrical piezoelectric transducer allows the controlled vertical and lateral positioning of the tip and for rastering of the tip over the sample surface, figure 2.10. The tip is placed in a magnetic holder at the top of this piezoelectric transducer tube. The tube is hollow with the outer surface divided into four electrodes and a single inner electrode. Lateral motion (x or y direction) can be achieved by applying equal and opposite voltages to the two opposing vertical outer electrodes while keeping the other two outer electrodes grounded or at constant voltage. The vertical motion (z direction) can be controlled by applying the same voltage to the four outer electrodes

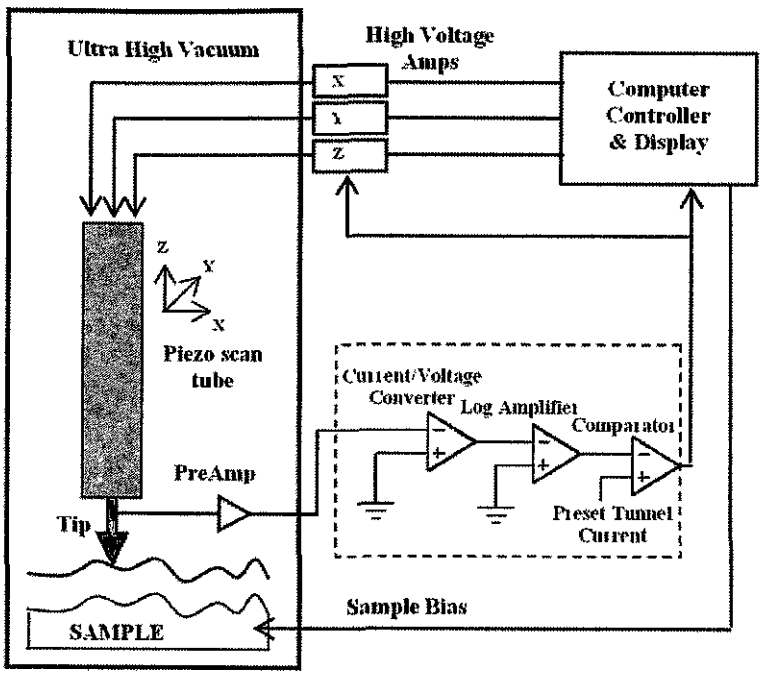

Figure 2.10: Schematic diagram of electronic feedback in dashed box contains feedback loop for STM operating in constant current mode.

and grounding the inner electrode.

The typical corrugation amplitude on an atomic surface is on the order of Angstroms or less. Considering that typical floor vibrations are at least six orders of magnitude greater than the surface corrugation any disturbance from external vibrations is detrimental to atomic resolution and so the vibration isolation system for the STM is critical. Passive damping of the STM is achieved through viscoelastic materials between the system and the floor and metal springs combined with an eddy-current damping system consisting of copper elements and permanent magnets, see figure 2.11 of the Omicron VT-STM.

During operation the tip height is controlled by an electronic feedback system. The tunnel current is amplified when passing through an amplifier placed as close as possible to the tip inside the vacuum system. The amplified current is then converted into a voltage which is linearised in a logarithmic amplifier (an op-amp with a diode) in the feedback loop to improve the dynamic range of the feedback and extract the distance dependence. This output signal from the log-amp is compared with the preset tunnelling current, in the comparator. The difference signal is fed back into the z-piezo high voltage amplifier and the tip is moved accordingly to bring the tunnelling current back to the preset value thus maintaining a constant tunnelling current. The time constant of the feedback loop slows down the scan

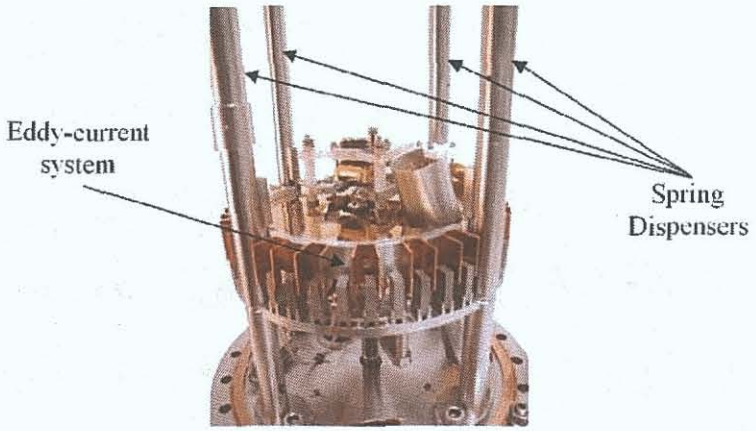

Figure 2.11: Omicron damping system consisting of eddy-current system combined with four springs [20].

rate. This mode of operation, know as constant current mode, is used when imaging rough surfaces to avoid crashing the tip into the surface.

The alternative mode of operation does not require a feedback loop resulting in a faster scan rate, is known as constant height mode. It is performed on atomically flat surfaces, a constant voltage is applied to the z-piezo and the tip is scanned across the surface at a constant height while the tunnelling current varying with tip-sample separation is recorded.

2.3.3 STM analysis

The analysis of STM results requires careful consideration. The contour map of the surface it produces is both electronic and topographic in origin as it depends on the overlap of the tip and surface wavefunctions and follows a height contour of constant electron density. Simple interpretation in terms of atomic height is seductively intuitive but can be extremely misleading [48].

The STM data was analysed with the software package WSxM (version 4.0, development 7.6) [38]. The fast Fourier transform filtered images and the line profiles were all prepared using this software. There are three types of line profile options, (i) the profile, (ii) the multiple profiles and (iii) the Y average profile. These tools produce a profile curve in a new window of a 1D path over the 2D image. The multiple profiles allows the same 1D path to be taken from exactly the same positions over multiple image windows. Finally the Y average profile averages all horizontal lines of the image and displays a single curve, in a new window. Horizontal and vertical measurements are taken from these line profile curves.

The Fourier transform tool performs a fast Fourier transform of the image, and

produces the filtered image in a new window. The previously mentioned profile tools may then be used to make measurements. These Fourier transform filtered images represent the reciprocal space features of the structures present in the STM images. These filtered images are comparable to the LEED diffraction patterns of the same surfaces as both represent the reciprocal space features of the structures. They are an excellent way to measure the periodicities present in an image. This is a major advantage over single line profiles which are prone to spurious results as they are not representative of the entire image.

It is noted however that both measurements will be prone to drift and creep effects due to the nature of STM images. Special consideration should be given to STM images recorded at different tunnelling currents. Surfaces can have current dependent features and the Fourier transform filter will only display the periodicities present in the image and not those of the real surface. Other absences in the Fourier transform filtered images can include periodicities greater than the STM image window size, and multiple domains or multiple phases.

2.3.4 The vacuum chamber and sample holders

The Omicron vacuum system consists of three different chambers, figure 2.12. The entire system is mounted on Viton© blocks under each corner. The preparation and anaylsis chambers are pumped by ion getter pumps with titanium sublimation pumps. The analysis chamber can be isolated from the preparation chamber with a manual gate valve. All experiments were conducted at base pressures of 1×10^{-10} mbar and 5×10^{-11} mbar in the preparation and analysis chambers respectively. Samples and STM tips are loaded through a fast entry load lock attached with a manual gate valve to the preparation chamber. This is pumped with a turbo molecular pump before samples are brought into the preparation chamber on the magnetic transfer system.

Two types of holders, figure 2.13 where used to mount the samples, (a) a tantalum (Ta) spade and (b) an Omicron (CP VT MC) holder [20]. The single crystal metal samples were mounted on the Ta spade. Ta strips were folded into incisions along two sides of the crystal and spot welded to the spade to secure the sample. The Omicron holders were used for the semiconductor samples. They allow both resistive heating and direct current heating of the samples. Basically they consisted of four Mo rods screwed into a base plate, two clamping foils which run parallel between two of the rods and a metal coated ceramic top plate with four holes for the rods to protrude and a window to access the sample. The semiconductor samples (30

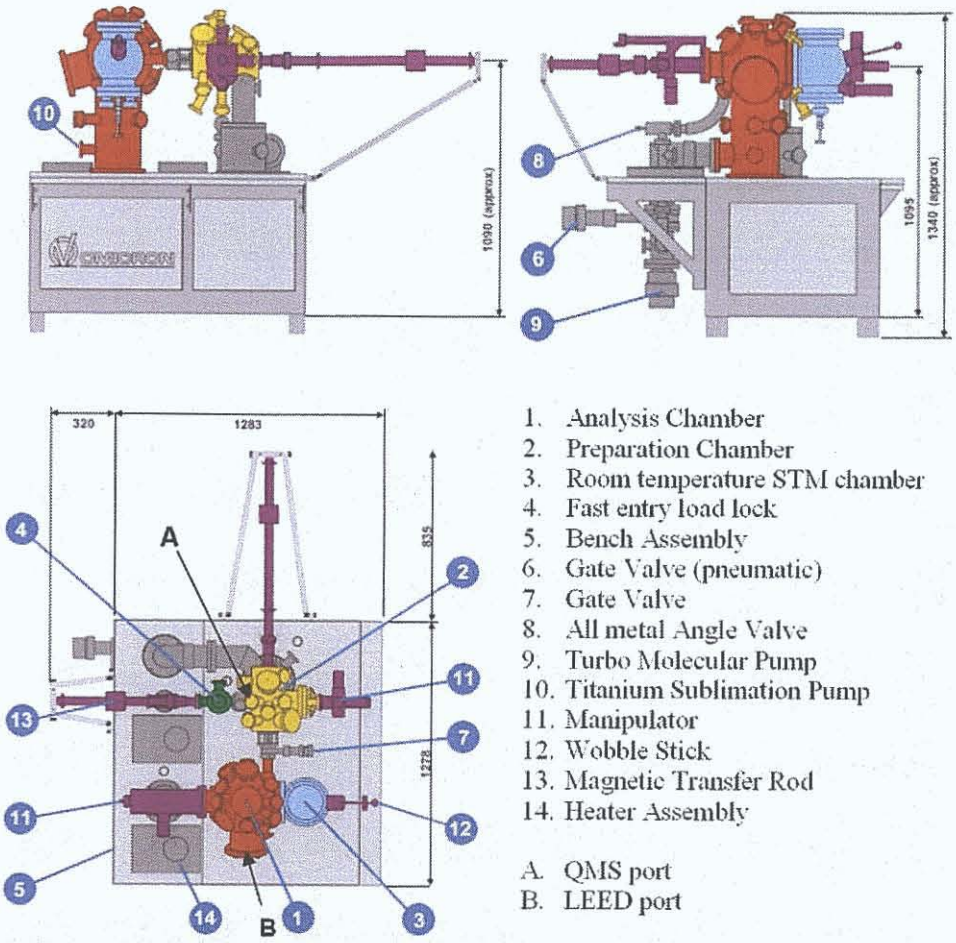

Figure 2.12: The Omicron UHV system shown in plan and elevation [20] : the preparation chamber (yellow), the anaylsis chamber (red) the fast entry load lock (green) and the STM chamber (light blue).

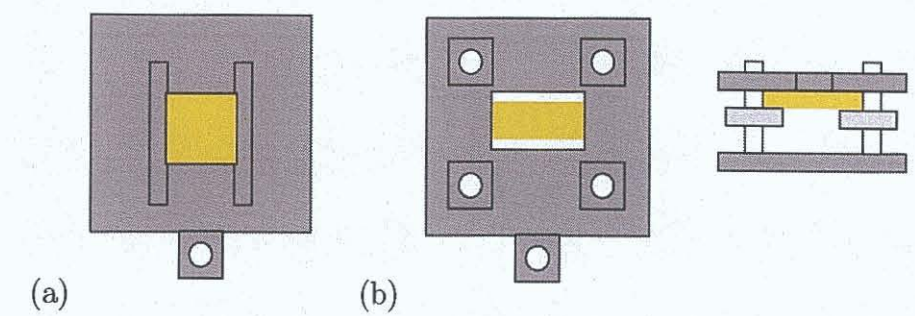

Figure 2.13: Schematics diagram of samples holders. From left to right, (a) a tantalum (Ta) spade with metal crystal sample, (b) the Omicron holder holder for silicon samples in plan and front elevation [20].

mm × 100 mm) were cut from a wafer using a diamond scribe and rested upon the Ta foils. The top plate, secured with four Mo nuts was then used to hold the sample in place. Both types of holders have a keyhole arrangement to allow secure transfers through the system on a magnetic transfer system. The final transfer from the analysis chamber to the STM sample stage is performed using a wobble stick.

2.4 Temperature Programmed Desorption (TPD)

In this section the basic theory behind the TPD technique is discussed. The equipment required and experimental set up to record a TPD spectrum is described.

Temperature programmed desorption (TPD) provides information concerning the strength of the interaction between a substrate and an adsorbed species. The desorption of adsorbed atoms and molecules is a fundamental elementary surface kinetic process. Apker introduced TPD as a surface analysis technique in 1948 [49]. The sample is prepared by adsorbing one or more molecular species at a temperature that is low compared to the desorption temperature, usually ambient. A temperature ramp, preferably linear, is then applied while monitoring the amount of adsorbate desorbed into the gas phase as a function of temperature.

2.4.1 TPD theory

As the sample is heated the temperature increase provides sufficient thermal energy to break surface bonds and desorption occurs. The partial pressure increases as the molecules start to desorb from the surface. The rate of desorption reaches a maximum at the so-called desorption peak temperature T_p, and then falls off as quantity of molecules left to desorb drops. A graph of the rate of desorption versus temperature, for first order kinetics, is shown in figure 2.14.

The rate of desorption per unit surface area may be expressed as [50]

$$-\frac{dN}{dt} = k_d N^m \tag{2.32}$$

where

$$k_d = Ae^{-E_d/RT} \tag{2.33}$$

m is the order of the reaction and N is the number of adsorbed molecules. The des-

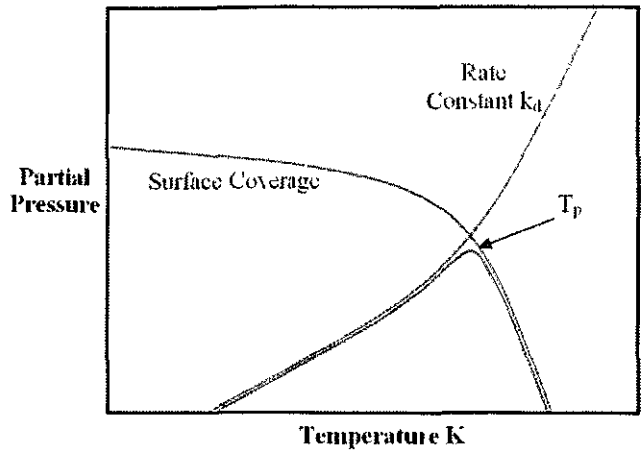

Figure 2.14: The rate of desorption (black curve) as a convolution of changes in surface coverage and rate constant as a function of temperature is shown for first-order desorption. T_p the maximum thermal desorption peak.

orption rate constant k_d, obeys an Arrhenius dependency and shows an exponential increase with temperature. E_d is defined as the activation energy for desorption, A is the pre-exponential factor and R is the gas constant 8.314 $mol^{-1}K^{-1}$. For first order desorption ($m = 1$), A is assumed to be of the same order of magnitude as the molecular vibration frequency and is usually accepted to be about $10^{13}s^{-1}$ [50]. Substituting the heating rate $\beta = dT/dt$ into equation (2.32) for k_d yields

$$-\frac{dN}{dT} = N^m \frac{A}{\beta} e^{-E_d/RT} \tag{2.34}$$

When $T = T_p$ the rate of desorption reaches a maximum, (i.e. $d^2N/dT^2 = 0$), shown in figure 2.14. By differentiating equation (2.34) with respect to T and equating to zero, an equation relating T_p, E_d and N, is found:

$$\frac{E_d}{RT_p^2} = \frac{A}{\beta} m N^{m-1} e^{-E_d/RT_p} \tag{2.35}$$

Since β and T_p are experimentally measured parameters, the activation energy E_d may be evaluated and conclusions drawn about the binding energies of different adsorbates.

Important characteristics of the surface reactivity can be obtained from studying the rate of desorption curve. The position of the peak temperature, T_p, is related to the enthalpy of adsorption, i.e. to the binding energy of the adsorbate to the surface. The existence of multiple desorption peaks and coverage-dependent shifts in peak maxima may indicated the presence of more than one distinct binding site

(e.g. atop, hollow, bridge) and coverage-dependent lateral interactions between adsorbates. The kinetics of desorption (obtained from the peak profile and the coverage dependence of the desorption characteristics) give information on the state of aggregation of the adsorbed species, e.g. molecular versus dissociative. Finally providing the pumping speed of the vacuum remains constant during desorption, the area under the peak is proportional to the surface coverage and the simple operation of integrating of the area under two TPD curves can yield the relative coverage.

2.4.2 Experimental detail

The temperature programmed desorption studies are carried out under UHV conditions. The sample temperature is monitored using a thermocouple (TC). The heating should ideally be linear and restricted to the sample, thus avoiding desorption from other surfaces such as a sample holder. A Vacuum Generators Quasar quadrupole mass spectrometer (QMS) detects the desorption flux by measuring the partial pressures of different ions. It consists of four parallel rods, two opposing rods have either an applied dc voltage or an ac voltage. The applied voltages affect the trajectory of ions travelling longitudinally between the four rods. For given applied voltages, only ions of a certain mass-to-charge ratio will reach the channeltron detector, other ions will have an unstable oscillation and collide with the rods. A mass spectrum is obtained by monitoring the ions passing through the quadrupole filter as the voltages on the rods are varied. The atomic mass unit (amu) was the unit used to compare the mass of particles (atoms, fragments, molecules) recorded by the mass spectrometery, 1 amu = 1.66055×10^{-27}kg.

Ideally the QMS is orientated in line of sight and close to the sample, typical separation of 2-5 cm. This ensures maximum detecting efficiency and is kept fixed to ensure that the integrated areas of different TPD spectra can be compared quantitatively. The TPD spectrum is obtained by plotting the temperature reading from the thermocouple against the signal from the QMS. Since a QMS detector is used in TPD the sensitivity of the technique is high, with attainable detection limits below 0.1 % of a monolayer of adsorbate [51].

In practice, it is not always possible to have the ideal experiments conditions and consideration of the following limitations should be made. These TPD experiments were carried out in the Omicron UHV preparation chamber, figure 2.12 and because of the need to have sample transfer between chambers certain restrictions could not be strictly adhered to: the samples were heated resistively by ceramic heaters on the manipulator head located beneath the sample; the TC was positioned on the

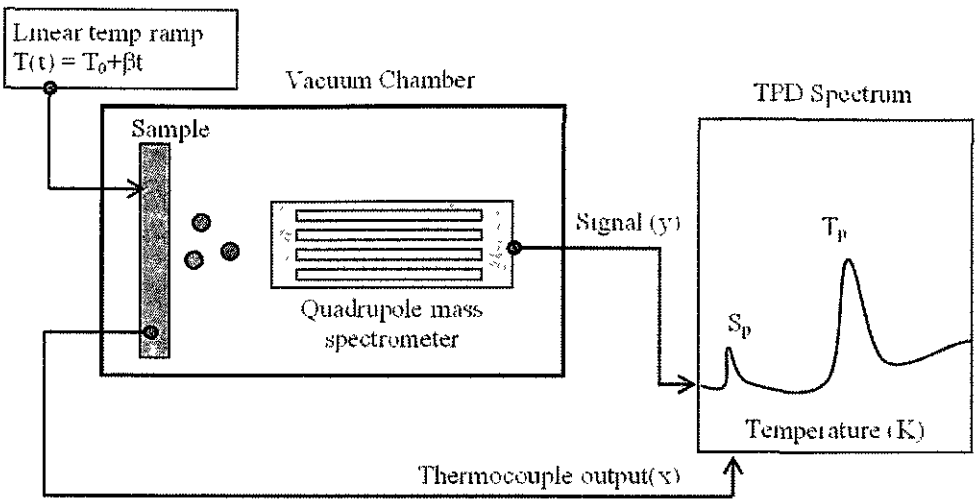

Figure 2.15: A schematic diagram of the experimental setup for TPD. T_p is the peak desorption temperature and S_p a support peak due to desorption from heaters.

manipulator head close to but not in contact with the sample and the position of the QMS was close to the sample, at 80 mm but outside the recommended distance to avoid extraneous signal from surfaces other than the sample. Finally as adsorbate molecules may decompose into a range of products of different masses, this experiment requires monitoring several masses simultaneously. Truly simultaneous monitoring of assorted desorbing species on different channels of the QMS is not possible however a quasi-continuous output can be obtained. The mass spectrometer achieves this by switching between several detected masses as the temperature of the system is increased.

2.5 Organic Molecules

2.5.1 Pentacene

The microelectronics industry has recently taken a significant interest in the application of organic semiconductors in microelectronic devices, a change from the almost exclusive work with inorganic materials such as silicon and gallium arsenide. Pentacene is an organic semiconductor of particular promise as it has been successfully used in organic thin film transistors[3] with field-effect mobilities matching or even surpassing those of amorphous silicon [52].

Pentacene thin films are relatively easy to grow on a wide range of substrates, from oxides [53] and semiconductors [54] to metallic surfaces [55] [56] [57]. The

[3]organic thin film transistors are a type of field effect transistor

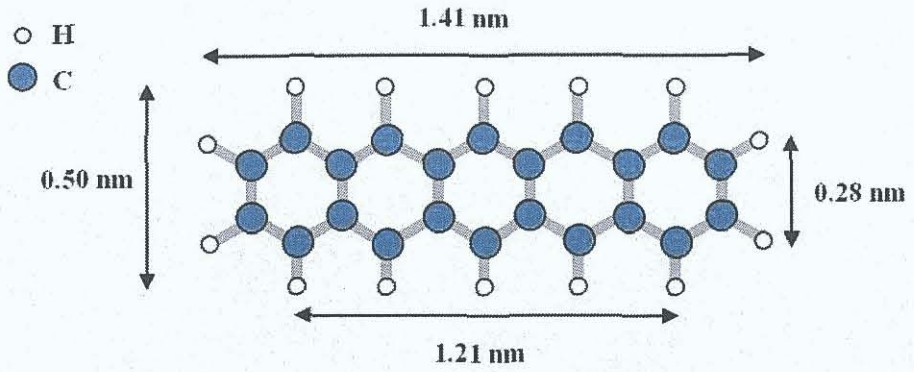

Figure 2.16: Ball and stick model of the pentacene molecule with element legend.

pentacene molecule ($C_{22}H_{14}$) is an planar aromatic molecule. It is one in a series of acenes, consisting of five fused benzene rings. Molecules in the acene group share the common characteristics of σ-bonds in the plane of the molecule and π-bonds perpendicular to the plane of the molecule. Crystalline pentacene has a triclinic structure with lattice parameters of $a = 0.79$ nm, $b = 0.606$ nm, $c = 1.601$ nm, $\alpha = 101.9\,°$, $\beta = 112.6\,°$, $\gamma = 85.8\,°$ in which the molecules are aligned with the ac plane [58].

2.5.2 Trimesic acid

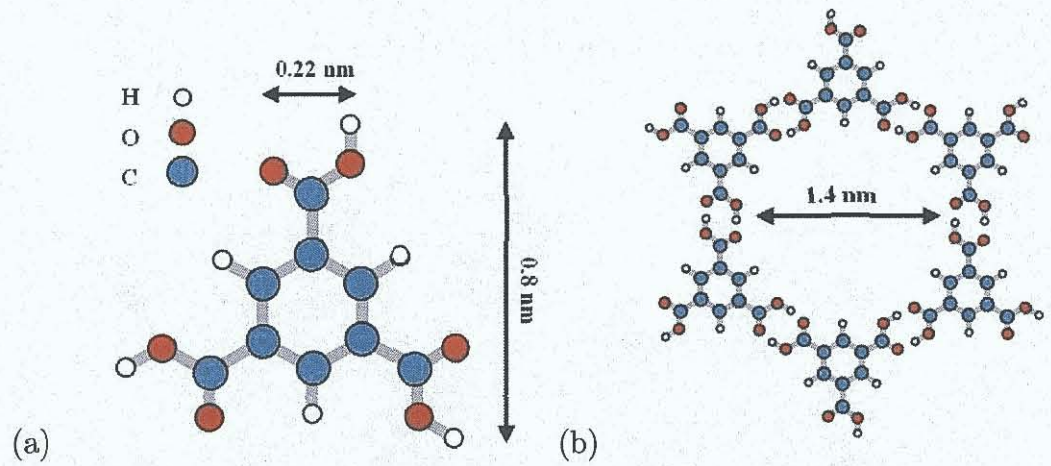

Figure 2.17: (a) Ball and stick model of the TMA molecule with element legend. The distance between the two oxygen atoms on an end-group is 0.22nm. (b) Cyclic hexamer crystal structure observed within the bulk motif [59].

Trimesic acid, (1,3,5-benzenetricarboxylic acid, $C_6H_3(COOH)_3$), abbreviated to TMA, is a polyfunctional carboxylic acid with 3-fold symmetry comprising a phenyl ring and three identical carboxyl end-groups lying in the same plane. Initial research

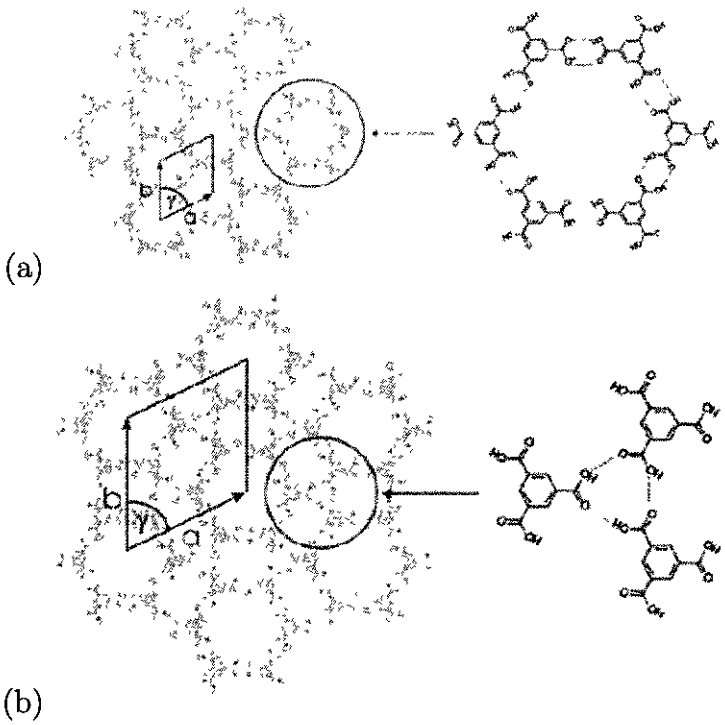

Figure 2.18: Schematic image of (a) the "chicken-wire" structure (a = b = 1.72 ± 0.1 nm, $\gamma = 60\,°$) and (b) the "flower" structure (a = 27.0 ± 0.1 nm, $\gamma = 60\,°$) [10].

on this molecule has concentrated on bulk growth for fabrication of clathrates and the design of organic porous solids [60] [61] [62].

TMA can assemble into a diverse range of structures due to the trigonal exodenate functionality. The crystal structure of the α-polymorph of trimesic acid, reported by Duchamp and Marsh in 1969 [59], is an infinite planar honeycomb network structure with holes diameters of approximately 1.4 nm.

This molecule has recently attracted wider attention as a promising candidate for forming supramolecular structures, because of the two-dimensional hexagonal networks formed by the exploitation of hydrogen bonding. Interaction with a surface can take place though the lone electron pairs of the deprotonated carboxylate groups in either a tilted or perpendicular orientation, or with the π-electrons of the phenyl ring in a planar orientation parallel to the surface. Scanning tunnelling microscopy (STM) has been used in studies of TMA on Cu(100) [63], Au(111) [64] and graphite [10] surfaces.

TMA has been shown to form self-assembled two-dimensional molecular caves on single crystal graphite surfaces [10]. At 25K two stable hydrogen bonded structures exist on the graphite substrate forming a "chicken wire" or "flower" motif, figure 2.18. The former is composed of six-fold rings of TMA with perfect arrangement

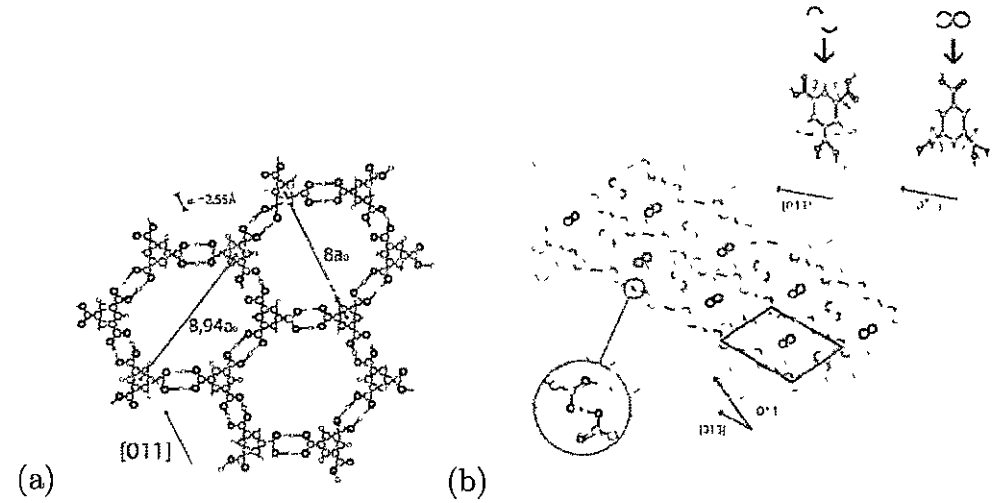

Figure 2.19: Schematic model of Cu(100)-TMA for (a) low temperature and (b) room temperature structure. Two possible bonding geometries (top right) for room temperature model included [65].

of the hydrogen bonds in which each molecule is part of three neighbouring rings. The latter is again 6-fold but a close packing of the rings forms a denser inner ring structure. The rings can accept single TMA guest molecules in different positions. The guest molecules are contained within these rings and they provide an elementary way of preferentially nucleating nanoscale structures on a surface.

Dmitriev et al. [63] have recently reported the ordering of TMA on the Cu(100) surface, figure 2.19. There are two distinct phases formed by the balance between adsorbate-substrate and intermolecular interactions. At low temperatures the molecules lie flat, π-bonding to the copper surface and forming islands of two dimensional hexagonal networks over the surface with diameters of $\sim$2 nm. This structure, similar to that identified in the 3D supramolecular structures, transforms irreversibly into a striped structure at room temperature. These striped supramolecular structures have an ordered upright adsorption geometry with either one or two end-groups chemisorbed to the substrate copper through a deprotonation of the COOH groups leading to carboxylate formation.

2.5.3 The Evaporators

A separate organic evaporator was built to deposit each of the different organic molecules onto the sample surface, figure 2.20(a). A pouch which contained the molecules was fashioned from a small rectangular sheet (1.25 mm $\times$ 3 mm) of tantalum foil of thickness 0.25 mm. The tantalum rectangle is folded into a cylindrical shape and one end is pinched closed with a double fold. The bottom and side

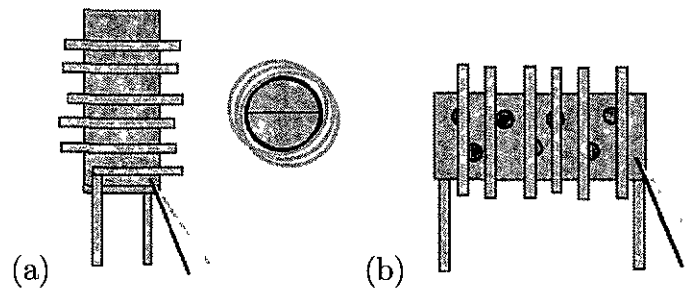

Figure 2.20: (a) A schematic side elevation and plan of the organic evaporator. Theromocouple wires are shown in red and yellow. (b) Schematic of bismuth evaporator.

seams are spot-welded to form a seal. This leaves a single circular orifice of 5 mm in diameter. A 0.5 mm tungsten wire is then coiled about the pouch leaving two trailing wires, from the bottom of the pouch, across which the heating current can be applied. An alumel/chromel theromocouple was then spot welded to the bottom of a pouch for accurate temperature control. The tantalum wires and thermocouple wires were attached to a UHV compatible feedthrough flange.

All organic molecules are initially degassed at 423K for 24 hours to remove water before being used. The coverage on the samples has been stated in Langmuirs, as calculated from the deposition pressure multiplied by the deposition time. The quoted coverages are only an indication of the amount of material deposited and not an absolute coverage since it does not take account of the sticking coefficient, which strongly depends on the substrate in question, the step density, and the cleanliness of the substrate as regards defect sites.

The bismuth was evaporated from a homemade Ta cell, figure 2.20(b). The cell was formed in a similar fashion to the organic evaporators. In this case, the bismuth shot was then poured into the pouch and the end was then sealed closed with a double fold and spot-welded in place. In order for the bismuth to exit the package pinholes where made in the surface of the package. Tungsten wire was then coiled about the pouch leaving two trailing wires, from either side of the package. The heating current could then be applied to heat the package. An alumel/chromel theromocouple was again spot welded to the cell for accurate temperature control.

Chapter 3

The Sn/Cu(100) surface alloy

In this chapter a review of previous research on bimetallic alloys formed on the Cu{100} surface is presented. The Sn/Cu(100) system is examined by LEED, STM and NIXSW, providing further insight into Sn adsorption on the Cu(100) surface. The submonolayer phases which are consistent with adsorbate induced reconstruction/surface alloy formation are presented. Previously proposed models based on LEED IV, for each of the phases, are reviewed in light of the new LEED, STM and NIXSW results. The discovery of an entirely new submonolayer phase is presented and discussed.

3.1 Bimetallic Alloys

The two main structures for alloy films have been reported (i) a surface alloy with a mixed adsorbate/substrate top layer or (ii) a top layer consisting of substrate atoms with the adsorbate atoms subsurface occupying the second layer. A theoretical study based on surface energy, interface energy and strain energy showed that surface alloy formation is generally expected in systems that are dominated by an atomic size mismatch [66] [67].

Tersoff et al. [66] inferred that the ratio of the metallic radii of the adsorbate and substrate atoms can be used to predict surface alloy formation. The different observed behaviours of adsorbates grown on Cu{100} are in good agreement with that conclusion. For elements with an atomic radii ratio < 1.25, there are two types of behaviour dependent on whether the element is miscible or immiscible in the bulk phase with copper. For immiscible elements such as Ni and Ir, alloy formation occurs at low coverages, <1ML, with the elements located subsurface. For miscible

Ni	Mn	Ir	Pd	Pt	Au	Ag
0.98	0.99	1.06	1.08	1.09	1.13	1.13
Sn	In	Bi	Te	Pb	Na	K
1.27	1.3	1.33	1.33	1.37	1.5	1.86

Table 3.1: Table of metal adsorbates on Cu{100} listed in order of increasing ratio of their 12-fold coordinate metallic radii to the radius of Cu =1.278 Å. These results are adapted from [15] and references therein.

elements Mn, Pd, Pt and Au, surface alloys form over a coverage range, 0-0.6ML. These alloy structures are based on a 1:2 ratio of adsorbate atoms to topmost layer atoms of the substrate. For elements, Ag, In, Bi and Pb where the ratio of atomic radii is between 1.13 and 1.37 surface alloy structures form at coverages < 0.4ML. Increasing the coverage causes the adsorbate atoms to dealloy to form overlayer structures. The atomic radii ratio for Sn/Cu of 1.27 is within this range. Finally for adsorbates with larger atomic radii ratios, > 1 37, for example Na and K, overlayer structures are reported for all coverages [15].

There are numerous publications in this area from early an publication by Argile and Rhead [68] who wrote a general review of some 440 investigations of 220 adsorbate/substrate systems, to more a recent review by Bardi [69] of 34 different surface alloy systems reported in 1994. Two books containing reviews of the more recent material published on adsorbate/substrate systems were released in 1994 [70] and 2002 [71]. As evident from these reviews, there is a wealth of knowledge in relation to the complex bimetallic systems in the literature which could be exploited to provide templates for organic growth on the nanoscale.

3.2 Clean Cu{100} crystal

The structure of the bulk copper crystal is face centred cubic (fcc). The $p(1 \times 1)$ unit cell is shown in figure 3.1 with copper to copper interatomic spacings of 0.255 nm along the [011] and [01$\bar{1}$] directions respectively. The interplanar distance for copper {100} planes is 0.181 nm, half of the lattice constant 0.361 nm of the face centred crystal. The Cu(100) crystal was mounted on a tantalum spade using tantalum clips to secure it in place. Cycles of argon ion bombardment at 2kV and annealing to 800K readily produced a clean surface.

Faults on the clean surface such as dislocations and steps do not appear to be ordered or straight in STM images and instead appear as ragged edge, figure 3.2.

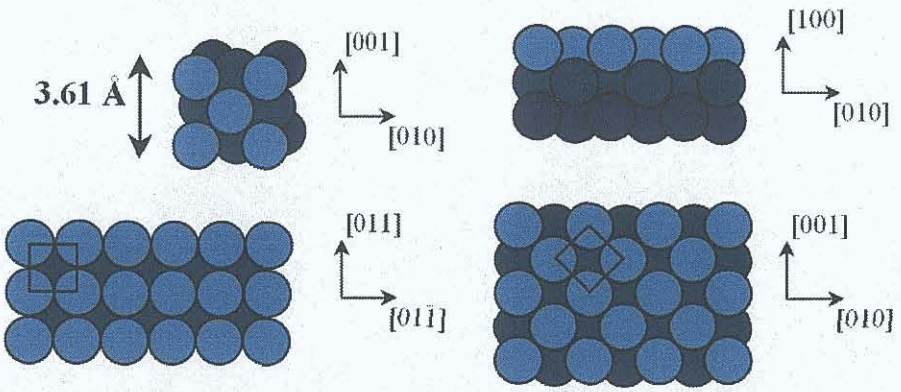

Figure 3.1: The Cu(100) fcc crystal structures and directions, with unit cells as marked.

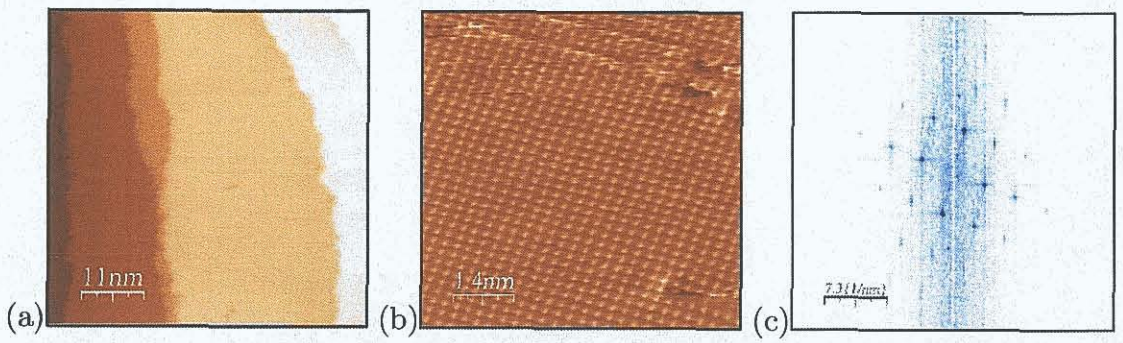

Figure 3.2: STM images (a) and (b) of the clean Cu surface atoms as imaged at room temperature by the STM, (b) reveals real space lattice of 0.265 nm and 0.206 nm in the [011] and [01$\bar{1}$] directions (c) Fourier transform of STM image. (a) $V_s = 1.0$ V, $I_t = 0.5$ nA, 55 nm^2 (b) $V_s = 0.01$ V, $I_t = 3.0$ nA, 7 nm^2.

This apparent roughness is due to the high mobility of kinks along the edges, making the edges move between consecutive STM line-scans [72]. The terrace shown in figure 3.2(b) reveals the Cu atoms at room temperature with an interatomic spacing of 0.206 ± 0.03 nm and 0.265 ± 0.03 nm in the [011] and [01$\bar{1}$] directions. Drift in the image accounts for the difference to the accepted 0.255 nm value [48].

3.3 Previous Studies of the Cu(100)/Sn surface

The Sn/Cu{100} surface was first investigated by Argile and Rhead [68] [73] using Auger Electron Spectroscopy (AES) and Low Energy Electron Diffraction (LEED). Four ordered phases were reported in the submonolayer regime. Phase I: a "complex" pattern with unidentified unit cell; phase II: a rotated domain p(2 × 6) structure, at a tin coverage of $\theta_{Sn} = 0.42$ ML; phase III: a rotated domain p($3\sqrt{2} \times \sqrt{2}$)R45° structure at $\theta_{Sn} = 0.5$ ML and phase IV: a p($2\sqrt{2} \times 2\sqrt{2}$)R45° structure at a

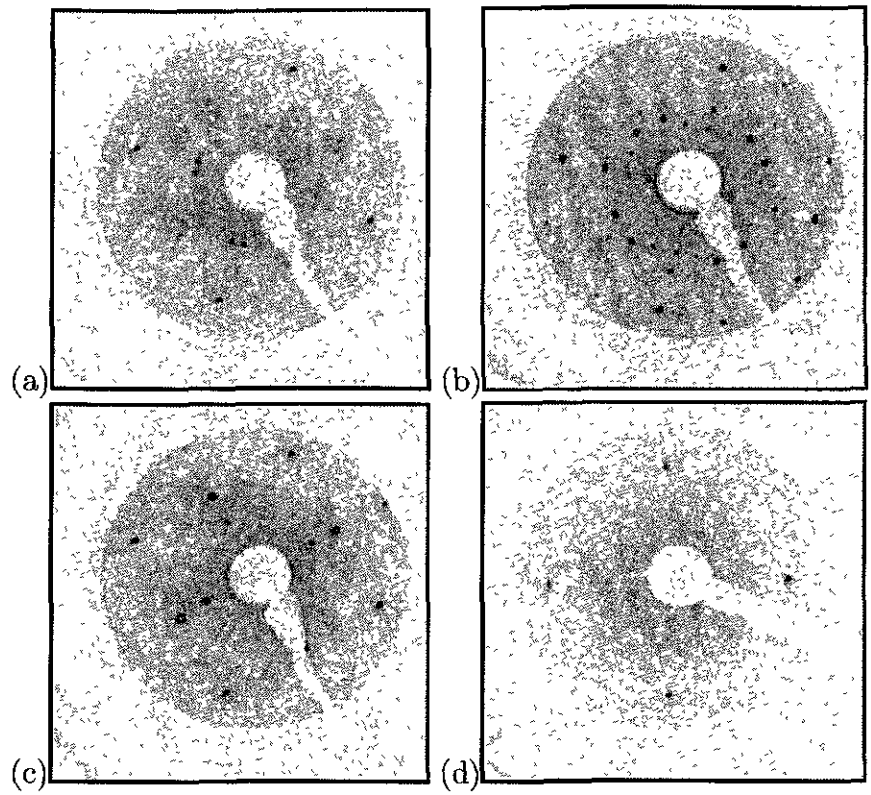

Figure 3.3: LEED diffraction patterns for phases (a) I (b) II (c) III (d) IV, were collected at 60 eV beam energy. These images are in excellent agreement with the literature [15] [68] [73].

tin coverage of $\theta_{Sn} = 0.625$ ML with respect to the Cu{100}-(1 × 1) density of 1.538×10^{15} atoms cm^{-2}.

Auger spectroscopy indicates that further Sn depositions on phase IV results in an overlayer structure with a Stranski Krastanov growth mode. Figure 3.3 present typical LEED diffraction patterns recorded for phase I-IV respectively and are in excellent agreement with previous studies of Argile and Rhead [68] [73] and McLoughlin [15]. No model was proposed for phase I by Argile and Rhead however, phases II-IV were described in terms of overlayer structures consistent with the determined Sn coverage and the symmetry/periodicity of the LEED patterns. For phases II and III it was observed that the LEED beams in the c(2 × 2) positions, i.e. the $(^1/_2, ^1/_2)$, spots, were significantly brighter over a wider energy range than the other superlattice reflexes. This suggests either multiple phase formation or alternatively, phases II and III originate from a c(2 × 2) superstructure with additional weaker reflexes arising from a longer range modulation in the c(2 × 2) structure due for example, to strain in the adlayer-substrate combination. This suggestion however is not consistent with the structural models presented by Argile and Rhead [68] [73].

Evidence of surface alloy formation was presented in work carried out by Able et al. [74] using Rutherford backscattering spectroscopy (RBS). Submonolayer Sn deposition was found to lead to an increase in the Cu RBS surface peak. If overlayer tin atoms covered the copper atoms, the backscattered peak would be attenuated. The results are explained by each Sn atom displacing one Cu atom from their four-fold hollow lattice site.

The latest results in the literature are presented by McLoughlin et al. [75]. Building on these initial studies [68] [73] the different Sn phases were re-examined using AES, LEED and double scattering LEED pattern simulations [15]. Eight new models for the submonolayer phases based on both overlayer and surface alloy structures were introduced. The Sn coverage assignments were made by AES and monitoring the LEED spot profiles as a function of Sn deposition time. This analysis indicated that phase I, II, III and IV reached maximal perfection at Sn coverages of 0.21 $\pm$ 0.05 , 0.37 $\pm$ 0.05, 0.5 $\pm$ 0.05 and 0.70 $\pm$ 0.05 ML respectively, assuming phase III reached maximum perfect at 0.50 ML, i.e. c(2 $\times$ 2). These surface alloy models will be the focus of the rest of this section.

Phase I

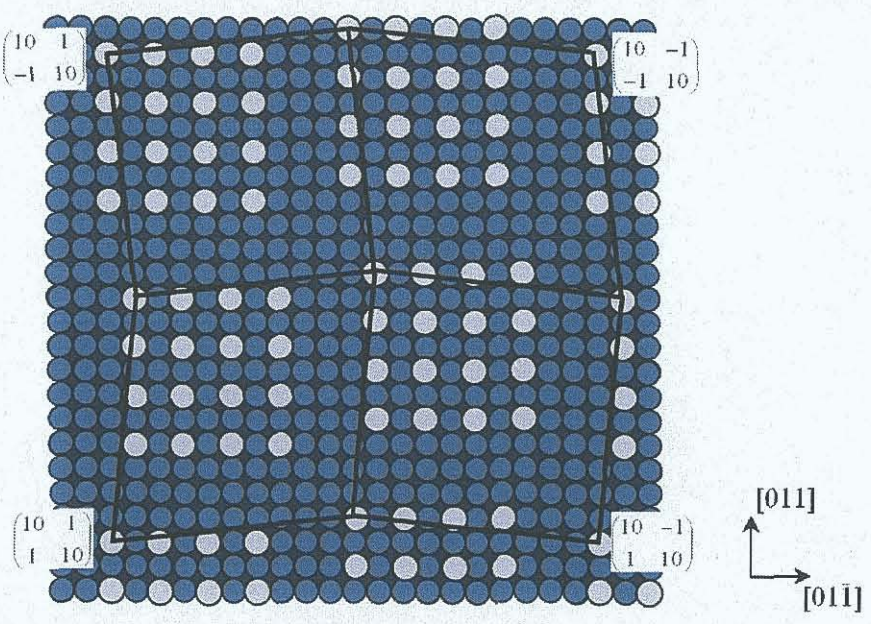

Figure 3.4: The McLoughlin [15] surface alloy model of phase I is illustrated, superlattice outlined in black. No model was proposed by Argile and Rhead.

Phase I, was described by Argile et al. [73] as a "complex" diffraction pattern, and although a model was not presented, they proposed that existence of antiphase

domain wall boundaries based on the observed spot splitting. The existence of several subdomains of the same structure within an area smaller than the coherence length of the electron beam produces spot splitting. When the subdomains form antiphase boundaries which are parallel and regularly spaced, a splitting of beams will take place in a direction determined by the orientation of the boundaries [22]. Beginning from this point McLoughlin et al. [75] noted the following about the diffraction pattern: the pattern was based on a modified p(2 × 2) structure; the half order spots are split along the a_1 and a_2 reciprocal lattice vectors of the (1 × 1) substrate in the [011] and [01$\bar{1}$] directions; the four equivalent $(^1/_2, ^1/_2)$ reflexes are split into four satellite spots while the $(\pm^1/_2, n)$ and $(n, \pm^1/_2)$ spots are split into two spots. Measurements were made from the LEED images of the splitting of all beams relative to the reciprocal lattice vectors of the substrate. These indicate that the domain wall structure adopts a periodicity of $1/11^{\text{th}}$ (0.09 ± 0.01) of the reciprocal space lattice. This splitting was independent of the beam energy and Sn coverage up to completion of phase I. The observed splitting in the LEED pattern for the $(^1/_2, ^1/_2)$ spots was simulated by rectangular domains of p(2 × 2) cells separated by anti-phase domain walls in both the [011] and [01$\bar{1}$] directions. Such a superlattice structure $\begin{pmatrix} n & 1 \\ 1 & n \end{pmatrix}$ reconstruction, where $n = 10$, is shown in figure 3.4. An anti-phase domain wall structure has also been observed by surface X-ray diffraction [76] and by STM [77] for the Bi/Cu{100} system at 0.6 ML coverage, as shown in figure 3.5.

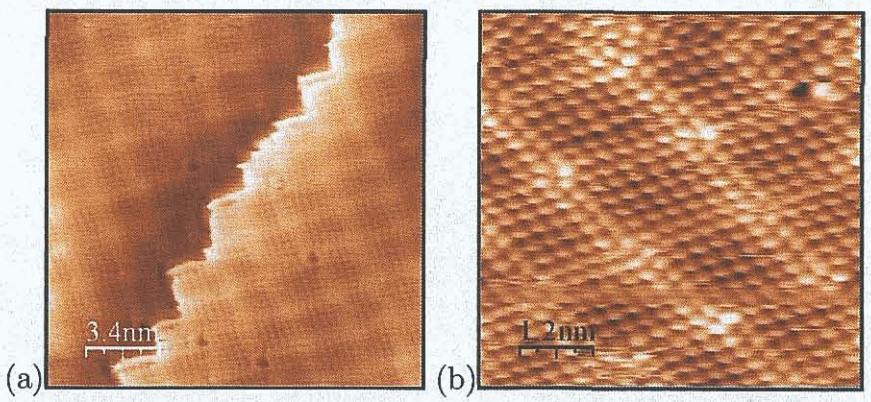

Figure 3.5: STM images of the Bi/Cu(100) p(10 × 10) structure at $\theta_{Bi} = 0.6 \pm 0.02$ ML. Shown is a two-dimensional dislocation array of heavy anti-phase domain walls. (a)$V_s = 0.6$ V, $I_t = 2.0$ nA, 17.1 nm^2 (b)$V_s = -1.0$ V, $I_t = 2.8$ nA, 6 nm^2.

Phase II

Phase II has a comparatively simpler p(2 × 6) diffraction pattern, ($^1/_2$,$^1/_2$) beams with considerably higher intensity than other superlattice beams are observed. The Argile and Rhead model for phase II consists of a coincidence mesh with five Sn atoms fitting into six copper interatomic spacings along the [01$\bar{1}$] direction, figure 3.6(a). While this model is entirely consistent with the p(2 × 6) periodicity it did not produce the higher intensity of the ($^1/_2$,$^1/_2$) beams when simulated.

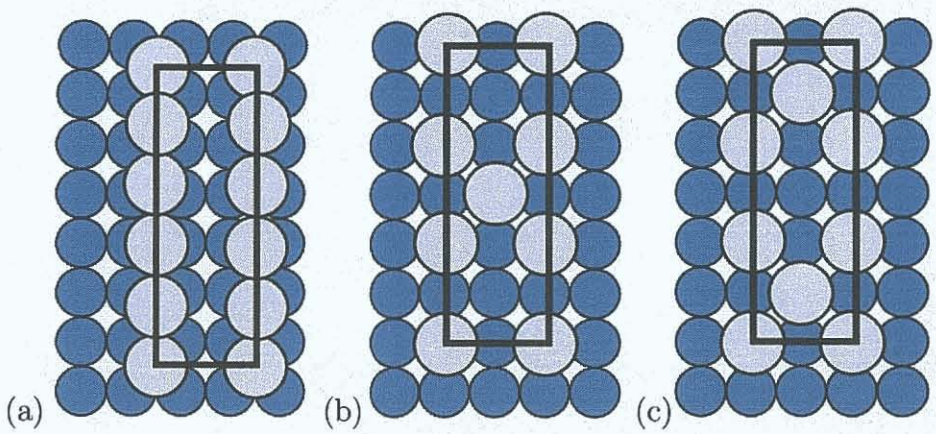

Figure 3.6: The structure models of phase II (a)Argile and Rhead (b) and (c) McLoughlin surface alloy models. Unit cells outlined in black.

A new model was suggested by McLoughlin et al. [75] which reproduced the correct intensities and has its origin in a mix of c(2 × 2)/p(2 × 2) structures, see figure 3.6(b) and (c). The first (b) contains domains of c(2 × 2) separated by p(2 × 2) unit cells, and the second (c) contains p(2 × 2) domains separated by c(2 × 2) unit cells.

Phase III

Phase III is described in all publications as a rotated domain p($3\sqrt{2} \times \sqrt{2}$)$R45°$ reconstruction with intense ($^1/_2$,$^1/_2$) beams. The Argile and Rhead model, figure 3.7(a), generated the correct symmetry and periodicity but not the intensity of the ($^1/_2$,$^1/_2$) beams. McLoughlin [15] considered the addition of Sn atoms to the phase II structure, shown in figure 3.6(b) and (c), filling the vacancy in the centre of the p(2 × 2) to form a complete c(2 × 2) surface. This would however lead to significant strain along the [010] direction to accommodate the larger metallic radius of the Sn atoms (0.162 nm). Relief of this strain by a buckling and/or small lateral displacements of the Sn and Cu atoms was proposed. If every second and third Sn row are compressed as in figure 3.7(b) the intense ($^1/_2$,$^1/_2$) beams were observed

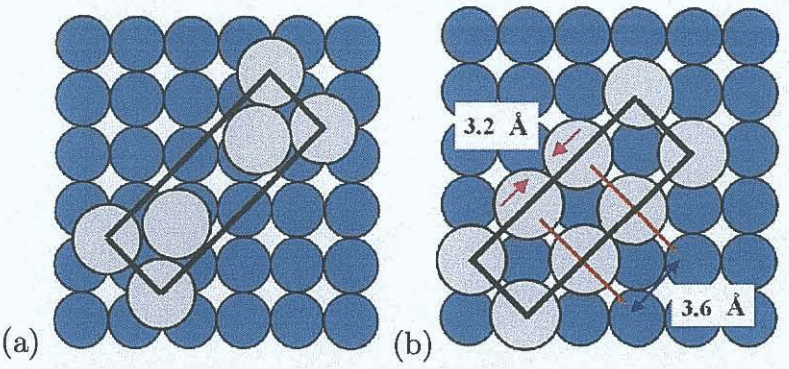

Figure 3.7: The structure models of phase III (a)Argile and Rhead (b)McLoughlin surface alloy model.

in the simulated LEED pattern in agreement with experimental observations. Best agreement was found with a lateral shift of approximately 0.04 nm along the [010] direction resulting in a Sn-Sn spacing of 0.32 nm. This theory was later tested by K. Pussi et al. [78] using dynamical LEED calculations prepared using the Barbieri/Von Hove Symmetrized Automated Tensor LEED package [79]. Pendry reliability factors were used to evaluate the theory-experiment agreement. It was concluded that the strain in the topmost layers was released by both lateral relaxation and buckling within the Cu layers. The favoured structure was a surface alloy that included a missing Cu row and a buckled Sn-Sn atoms spacing of 0.31 ± 0.01 nm.

Phase IV

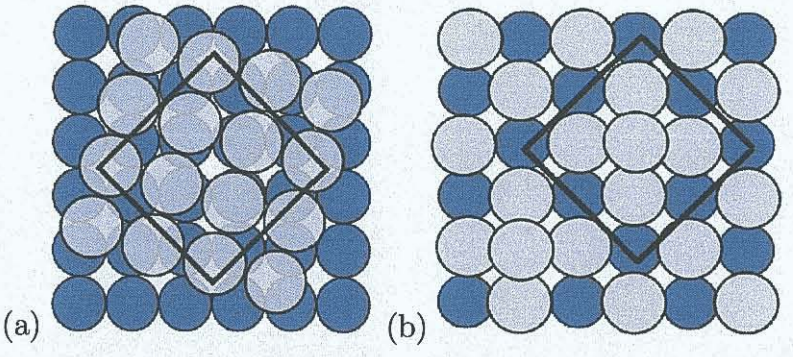

Figure 3.8: The structure models of phase IV (a)Argile and Rhead overlayer model, (b)McLoughlin surface alloy model.

Phase IV is described as a $p(2\sqrt{2} \times 2\sqrt{2})R45°$ structure and forms a complete monolayer. Models for this structure suggested by Argile and Rhead [68] [73] and McLoughlin et al. [75] are illustrated in figure 3.8 (a) and (b). It is observed from the diffraction pattern that the $(^1/_4, ^1/_4)$ beam is more intense than the $(^1/_2, ^1/_2)$

beam. This is not reflected in any of the simulations of the three models. The model suggested by Argile and Rhead gives the best agreement between the observed diffraction pattern and the simulated pattern, but the difference between the intensity ratios would indicate that phase IV is not correctly modeled and further strain relief should be considered.

Previous studies indicated four submonolayer phases. The spectral structure recorded in the IV LEED experiments [75], are consistent with a Sn induced reconstruction supporting surface alloy formation and indicate that local geometry surrounding Sn adsorbates varies significantly for all coverage dependent phases of the Sn/Cu{100} system [80]. Double scattering LEED pattern simulations based on the McLoughlin surface overlayer and alloy models were preformed for each phase [15]. The results gave good agreement with the available experimental data for all phases except phase IV. The available data was not sufficient to differentiate between surface alloy and overlayer models but the atomic radii ratio for Sn/Cu of 1.27 is within the coverage range which causes the adsorbate atoms to dealloy to form overlayer structures.

3.4 Experimental Results

The Cu(100) sample of dimensions $10 \times 10 \times 2$ mm^3 (Metal Crystals and Oxides, Ltd.) was mechanically polished to a mirror finish. It was mounted on a molybdenum sample plate prior to loading into the vacuum system. A clean Cu(100) surface with large terraces was obtained by repeated cycles of Ar ion sputtering and annealing (800 K). The cleanliness of the Cu(100) surface was assessed by the appearance of a sharp p(1×1) LEED pattern over an energy range of 45 eV to 400 eV, and by comparison to the IV LEED spectra with those reported in the literature [81] [82].

All LEED and STM experiments were preformed in an Omircon VT-STM system operated in a ultra high vacuum chamber with a base pressure of 5×10^{-11} mbar, discussed in section 2.3.4. The LEED diffraction patterns and simulations presented in this section were collected for each phase concurrently with the STM experiments. The LEED was used to ascertain the phase and the STM was then used to investigate the local structures and the local coverage. LEED diffraction pattern simulations contain two images, (i) a real-space sketch of a basic 2D lattice with green lines and a superlattice with a lattice of dots, (ii) the diffraction pattern for the basic 2D lattice of white spots surrounded by circles and additional white or coloured spots to represent the spots of the superlayer, more detail can be found in section 2.1.2. The STM measurements were made at room temperature using W tips. Depositions

Bragg Reflection	Polar angle to (100) plane	Interplanar distance Å $d_H = \frac{a}{\sqrt{h^2+k^2+l^2}}$	E_{Bragg} eV $E = \frac{hc}{2d_H}$
(111)	54 73°	a/√3 = 2 084	2970
(200)	0°	a/2 = 1.805	3430

Table 3.2: Bragg energies and angles relative to the (100) plane for the reflection planes discussed.

Bragg Reflection	Structure Factors			
	$F_{(000)}$		$F_{(hkl)}$	
	Re	Im	Re	Im
(111)	116.14	13 57	88 47	13 57
(200)	115 6	10 71	82.49	10.71

Table 3.3: Calculated structure factors for the Bragg reflection planes (111) and (200) of the Cu crystal.

of Sn made on room temperature Cu(100) were carried out using a water cooled Knudsen cell evaporator (WA Technology).

The Sn/Cu(100) normal incidence X-ray standing wave (NIXSW) studies were performed on beamline 4.2 of the SRS at Daresbury Laboratory, UK. The experimental set-up for NIXSW is described in section 2.2. NIXSW measurements from two inequivalent sets of reflecting planes can be used to determine the local registry of an atom by real space triangulation. This facilitates the ability to distinguish between Sn adsorption sites. X-ray absorption profiles were collected from all four phases at 300 K, using the (111) and (200) planes at 2970 eV and 3430 eV respectively. Each NIXSW profile monitors an element specific emission from the sample. The Sn profiles were collected by monitoring the Sn MNN (421 eV) Auger electron emission. The substrate profiles were collected from the Cu LMM (918 eV) Auger electron emission. All the profiles were fitted using a program written by Prof. R. Jones [34] in Igor Pro [35]. This program requires a procedure file with certain set parameters which are discussed in section 2.2.6. The main parameters are included in tables 3.2 and table 3.3. From fitting the substrate coper profiles the energy resolution of the incident beam was determined, this was subsequently used as a non-adjustable parameter in fits for the Sn Bragg profiles.

For the case of adsorption in a well defined high symmetry adsorption site, it is straightforward to triangulate the position from the coherent positions $d_{(200)}$

and $d_{(111)}$. The angle between the (111) and (200) planes is $\cos^{-1}(\sqrt{3})$ or 54.73° and $D_{(111)} = 2D_{(200)}/\sqrt{3}$ is the bulk layer spacing of the (111) scattering planes. If the tin adsorbs atop of an outermost layer Cu atom one would expect $d_{(111)} = d_{(200)}/\sqrt{3} + D_{(111)}/2$. For adsorption in a four-fold symmetric hollow site the expected (111) coherent position is $d_{(111)} = d_{(200)}/\sqrt{3}$.

There are two different bridge sites for the Sn atoms, with respect to the (111) planes, and they are expected to be occupied with equal probability. One of these leads to a (111) coherent position that is the same as that of the atop site, and the other, the same as for the hollow site. This would result in a (111) coherent position which is the mean of these sites and a reduced coherent fraction relative to that expected for either one of the two bridge sites in isolation. A fourth possibility is that the tin substitutes into the first layer of the substrate, displacing a copper atom and thus forming a surface alloy. In this case one would expect that $d_{(111)} = d_{(200)}/\sqrt{3}$. These four adsorption sites are illustrates schematically in figure 3.9 and based on the reasoning just discussed the predicted heights for each of the sites is shown in table 3.4.

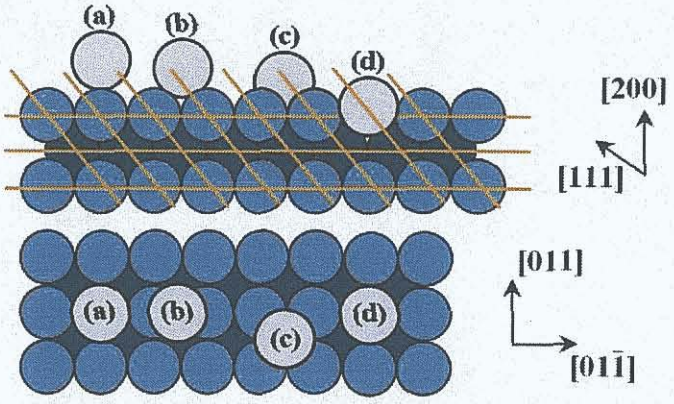

Figure 3.9: Model of Cu substrate atoms with Sn atoms in the following positions: (a) atop site, (b) bridge site, (c) 4-fold hollow site and (d) 4-fold substitutional site. The 1.805 Å and 2.08 Å spacing of the (200) and (111) planes are included (yellow).

Predicted Values ± 0.05 Å	Atop	Bridge Site I	Bridge Site II	Substitutional Alloy	4-Fold Hollow
$d_{(111)}$	1.26	1.26	0.22	0.22	0.22

Table 3.4: The predicted heights of $d_{(111)}$ for NIXSW results.

By comparing these predicted values of $d_{(111)}$ for all phases to the values calculated from the measured coherent positions it will be possible to distinguish between certain adsorption sites. Distinguishing between a four-fold hollow or substitutional alloy adsorption sites however is not possible based on the NIXSW results alone.

Each of the techniques, NIXSW, LEED and STM compliment one another with the information they provide. Upon completion of the analysis, all available experimental data are drawn on to create models for each of the five different Sn/Cu(100) phases in the following sections.

3.4.1 Phase I

LEED

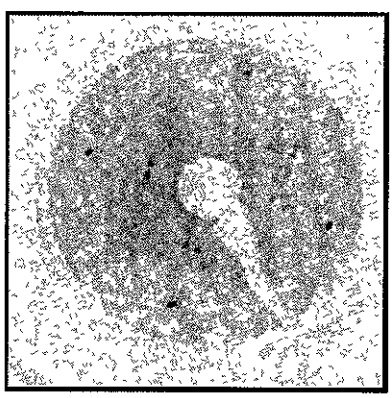

Figure 3.10: Phase I diffraction pattern recorded at 60 eV.

The phase I diffraction pattern at a tin coverage of $\theta_{Sn} = 0.21$ ML is shown in figure 3.10. The characteristic pattern of four equivalent $(^1/_2, ^1/_2)$ reflexes split into four satellite spots and the $(\pm^1/_2, n)$ and $(n, \pm^1/_2)$ Bragg spots split into two Bragg spots, is apparent. The splitting of the fractional order beams and not the integer order beams suggests anti-phase domain boundaries.

STM

Figures 3.11, 3.12 and 3.13 show STM images of the Cu(100)/Sn phase I surface recorded at room temperature. Figure 3.11(a) displays a 25 nm^2 area of the Cu(100) surface, recorded at a sample bias of -5.0 mV and a high tunnelling current of 3.0 nA, after room temperature deposition of 0.22 ± 0.02 ML of Sn. This coverage is slightly greater than that required for the formation of an optimal phase I structure, as determined from line profiles of the diffraction spots in the LEED data. Figures 3.12, 3.13 show 16.5 nm^2 and 8.2 nm^2 regions respectively recorded at a sample bias

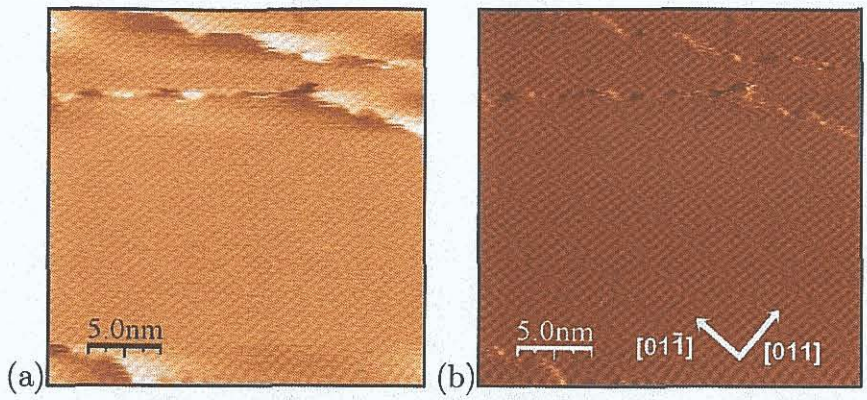

Figure 3.11: (a) STM image of the Cu(100)/Sn surface at a tin coverage of 0.22 ± 0.02 ML showing small domains of p(2 × 2) structure separated by light anti-phase domain walls. In this image only the Sn atoms are resolved. $V_s = -5.0$ V, $I_t = 3.0$ nA, 25 nm^2. (b) Derivative of image (a).

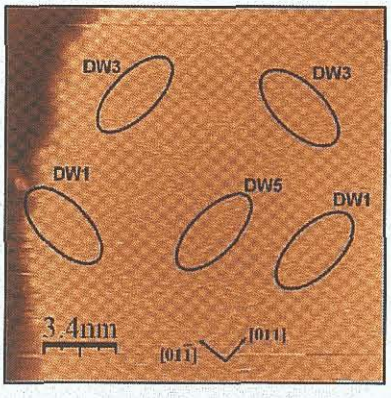

Figure 3.12: STM image of the Cu(100)/Sn surface at a tin coverage of 0.18 ± 0.02 ML. Domain walls with one, three and five rows of copper atoms are indicated by the regions marked DW1, DW3 and DW5 respectively. $V_s = -20.0$ V, $I_t = 1.3$ nA, 16.5 nm^2.

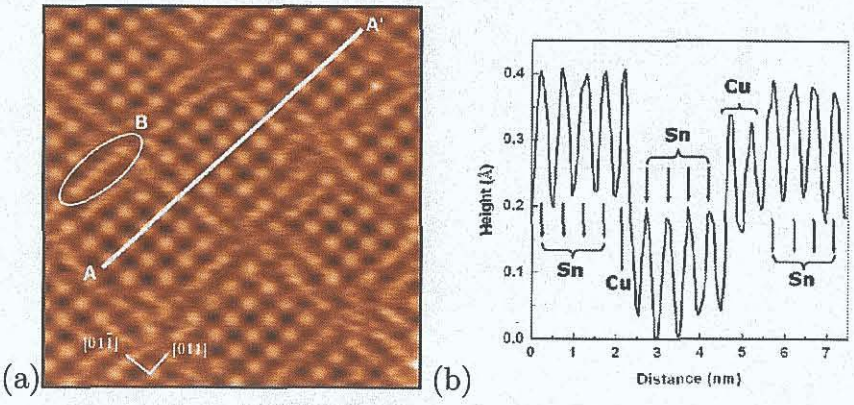

Figure 3.13: (a) High resolution STM image of the Cu(100)/Sn surface at a tin coverage of 0.18 ± 0.02 ML. The region marked B shows six copper atoms. $V_s = -20.0$ V, $I_t = 1.3$ nA, 8.2 nm^2. Line profile (b) measured along the line AA'.

of -20.0 mV and tunnelling current of 1.3 nA after deposition of 0.18 ± 0.02 ML of Sn. The apparent height of the step edges is measured to be 0.176 ± 0.015 nm.

Care must be taken when assigning the bright features in the STM images to atoms, as they only reflect variations in the electronic charge density, but for metals it is generally accepted that the maxima observed in an image correspond to the atomic positions [83]. Being mindful of this the p(2 × 2) arrangement of the Sn atoms is readily distinguished in these images. The structure in figure 3.11(a) may be further enhanced by taking a derivative of the image shown in figure 3.11(b).

The distance between the Sn atoms have an average value of 0.51 ± 0.005 nm. The small p(2 × 2) domains typically contain sixteen tin atoms in a 4×4 array, however, larger and smaller domains are also observed with sides consisting of 3, 5 and sometimes 6 tin atoms. The p(2 × 2) regions are separated by domain walls of different widths as indicated in figure 3.12. Three types of domain wall are observed: a "heavy" domain wall, indicated by the areas labelled DW1 in figure 3.12 with an average width of 0.54 ± 0.02 nm and "light" domain walls indicated by the areas labelled DW3 and DW5 with average widths of 0.97 ± 0.02 nm and 1.54 ± 0.02 nm respectively. The p(2 × 2) domains are laterally shifted relative to each other in the [011] and [01$\bar{1}$] directions with the magnitude of the lateral shift corresponding to a unit lattice vector of the copper substrate (0.255 nm). This shift results in an anti-phase alignment of the Sn atoms in neighbouring domains. This anti-phase alignment of the domains can be seen along the line AA' in figure 3.13(a). A height profile along the line AA' is shown in figure 3.13(b). The vertical corrugation is approximately 0.04 ± 0.01 nm as calibrated from the step height on the (100) plane. The atomic structure within most of the domain walls remains unresolved but occasionally copper atoms within a domain wall are clearly resolved. An example of this is labelled B in figure 3.13(a), where six copper atoms are clearly resolved in a line. The atomic spacing along this row of atoms is measured to be 0.26 ± 0.01 nm in good agreement with the copper unit cell length of 0.255 nm.

Protrusions without atomic structure are also observed within, and parallel to, the domain walls along the [011] and [01$\bar{1}$] directions. A single protrusion is observed in the domain walls containing three copper rows, such as those indicated as DW3 in figure 3.12, while in the wider domain walls with five copper rows (DW5 in figure 3.12) two protrusions are observed. This structure is attributed to elastic strain in the outer layer(s) associated with the large metallic radius of the Sn atoms relative to the Cu resulting in vertical, and possibly lateral, displacements of the copper rows within the domain walls as shown schematically in figure 3.15.

NIXSW

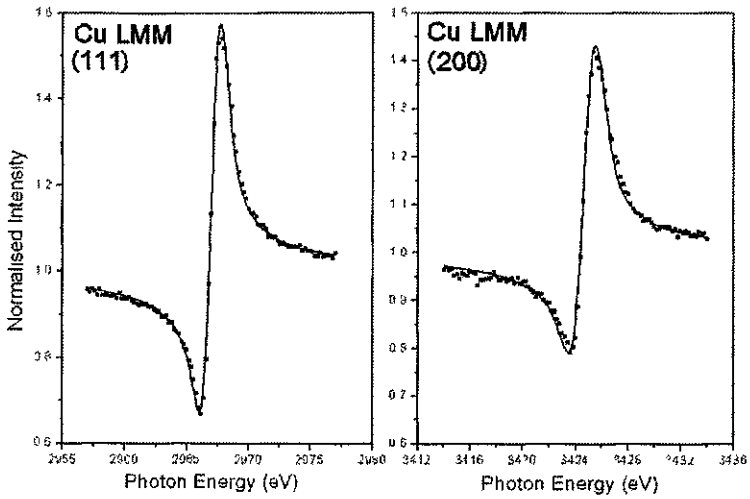

Phase	Plane	E_{Bragg} eV	$f_{(hkl)}$	$p_{(hkl)}$	$d_{(hkl)}$ Å	ΔE eV
I	111	2966 6	0.76	0.13	0.27	0.56
	200	3424 3	0.74	0.22	0.38	0.72

Figure 3.14: NIXSW profiles for phase I: Sn $p_{111} = 0.13 \pm 0.05$ and $f_{111} = 0.76 \pm 0.05$. Sn $p_{200} = 0.22 \pm 0.05$ and $f_{200} = 0.74 \pm 0.05$. The solid lines show theoretical fits.

The Bragg profiles and parameters of phase I are shown in figure 3.14. In this case the coherent fractions (f_{hkl})for phase I as measured for both the Sn Bragg profiles of the (200) and (111) planes confirm the Sn atoms adopt a single well-defined adsorption site on the surface.

Phase I model

The model for phase I, (shown in figure 3.4, page 41) deduced from IV LEED experiments by McLoughlin et al. [75] is based on a substitutional alloy. This structure, further elucidated by STM measurements, is similar to a (10×10) superstructure based on a $p(2 \times 2)$ cell but with some notable differences. First, the $p(2 \times 2)$ domains observed in the STM images do not all have the same size as proposed in figure 3.4. Domains with sides containing three, four, five and six tin atoms are observed. Nevertheless, in all cases, the domains have anti-phase boundaries in both the [011] and [01$\bar{1}$] directions.

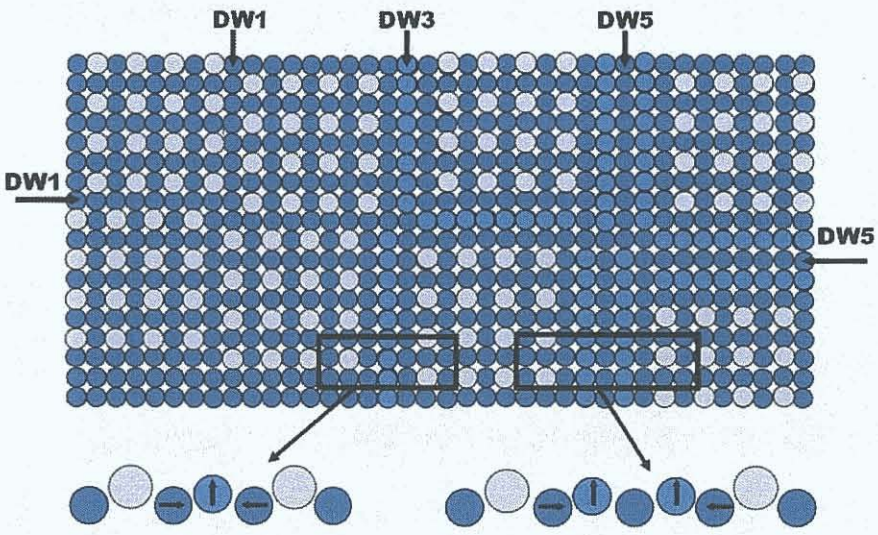

Figure 3.15: Schematic diagram of the different domain wall structures observed in the STM images. Cu atoms are shown in green, Sn atoms in grey. The regions DW1, DW3 and DW5 show domain walls comprised of one, three and five copper rows respectively. Side-view of the DW3 and DW5 "light" domain walls showing proposed lateral and vertical displacements of the Cu rows.

The model presented in figure 3.4 shows the four possible superstructures forming a larger superstructure, this implies that the surface is successfully tiled using this larger structure as the repeat unit cell. The STM data shows that this is clearly not the case. Examples of all four superstructures may be found in the STM images however they do not tile in the ordered manner. The domains form a "randomly ordered" structure, where the Sn atoms within each domain are ordered but the anti-phase alignment of the domains with respect to each other is random. A consequence of this random ordering is that the width of the domain wall varies, as shown in figure 3.15. In figure 3.4 the domain walls all have the same width corresponding to that of three copper rows separating the $p(2 \times 2)$ regions, in the STM data domain

walls containing one and five copper rows are also observed. The average width of the domain walls measured from the STM data are 0.53 ± 0.02 nm, 0.97 ± 0.02 nm and 1.54 ± 0.02 nm respectively. These measurements are in good agreement with the predicted widths of 0.51 nm, 1.02 nm and 1.53 nm respectively, based on the copper unit cell size of 0.255 nm. A model based on the "heavy" domain wall structure with a single row of copper atoms separating the domains would have a Sn coverage of $\theta_{Sn} = 0.25$ ML. The structures with "light" domain walls consisting entirely of three or five copper have ideal coverages of $\theta_{Sn} = 0.11$ ML and $\theta_{Sn} = 0.16$ ML respectively. The fact that the LEED Bragg spots are sharpest at a tin coverage of $\theta_{Sn} = 0.21 \pm 0.02$ ML indicates that the optimal structure predominantly consists of light domain walls with three or five copper rows. Measurements of the average value of the magnitudes of the vectors connecting equivalent atoms in two adjacent domains are 2.0 ± 0.2 nm, 2.6 ± 0.2 nm and 3.0 ± 0.2 nm, for domains having one, three and five copper rows respectively. The relative splitting of the fractional order diffraction spots predicted for these domain sizes are 0.127, 0.098 and 0.085 respectively. Compared to the measured value of the spot splitting of 0.091 again shows that the structure consists of light domain walls with three or five copper rows as shown schematically in figure 3.15.

Combining the results of the LEED and the NIXSW analysis above leads to the conclusion that the Sn atoms occupy a site with four-fold symmetry at submonolayer coverages, however these techniques fail to distinguish between overlayer and a surface alloy structures. Further information is obtained from the STM data. Line profiles similar to those shown in figure 3.13(b) show a small vertical corrugation of 0.04 ± 0.01 nm for the Sn atoms in the p(2 × 2) structures. This value is close to the difference in the 12-fold coordinate metallic radii of the Sn (0.162 nm) and Cu (0.128 nm) atoms and indicates that they lie in, or close to, the same atomic plane in the crystal with the tin forming a substitutional alloy. Furthermore, STM measurements on overlayer systems in general show much larger modulations, for example the Cu(111)/Sb overlayer system has a vertical corrugation of approximately 0.25 nm [84], in contrast to the Cu(100)/Ir surface alloy which has a stripe structure with a corrugation of 0.03 nm [85].

3.4.2 Phase II

LEED

Phase II p(2 × 6) diffraction patterns taken at 60 eV and 40 eV beam energy at θ_{Sn}≈0.33 ML are shown in figure 3.16(a). A higher intensity is noted in the $(^2/_3, ^1/_2)$

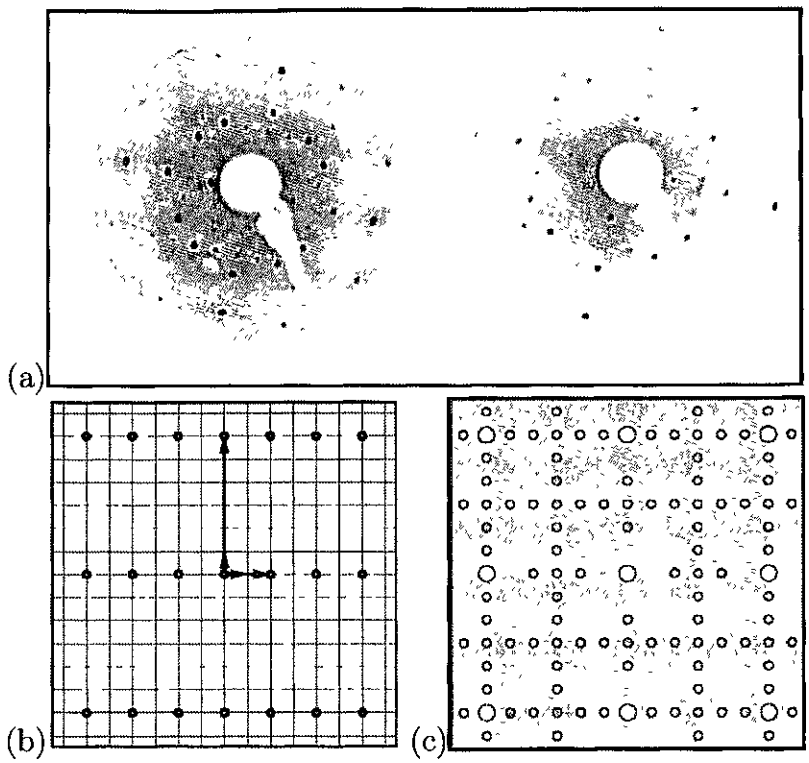

Figure 3.16: (a) Phase II diffraction pattern at 60 eV (left) and 40 eV (right). (b) and (c) LEEDpat simulated diffraction pattern. Cu substrate (p4mm): $a_1 = 2.55, a_2 = 2.55, \theta = 90°$, Sn (p2mg): p(2 × 6) $1 = 5.1, b_2 = 15.3, \theta = 90°$. Two unique domains are indicated in red and blue.

and equivalent symmetry beams at 60 eV beam energy. The absence of the $(0, {}^5/_6)$ $(0, -{}^5/_6)$ $({}^5/_6, 0)$ $(-{}^5/_6, 0)$ Bragg spots is also noted. These reflections are absent over the energy range 40 eV to 200 eV, outside of which the spots are either off screen or too close together to individually discern. Missing Bragg spots in diffraction patterns are attributed to the presence of glide-reflection symmetry [22]. No glide plane was every mentioned for this phase in any of the previous studies described in the literature.

Glide-reflection symmetry requires both reflection and translation along the mirror plane to be combined to bring the unit cell into coincidence with an initial geometrical configuration of the unit cell. In order to confirm the presents of these glide-reflection symmetries the LEEDpat program [17] was used to simulate the substrate symmetry constrained glide and mirror planes. Two different glide plane space groups, p2gg and p2mg are possible for a square p4mm substrate. Agreement with the experimental results was found with a p2mg space group showing systematic Bragg spot absences in the $(0, {}^5/_6)$ $(0, -{}^5/_6)$ $({}^5/_6, 0)$ $(-{}^5/_6, 0)$ and $(0, {}^1/_6)$ $(0, -{}^1/_6)$ $({}^1/_6, 0)$ $(-{}^1/_6, 0)$ positions. The p2gg revealed additional absences in the $(0, {}^1/_2)$

$(0, -^1/_2)$ $(^1/_2, 0)$ $(-^1/_2, 0)$ which is inconsistent with the experimental diffraction pattern and so dismissed.

STM

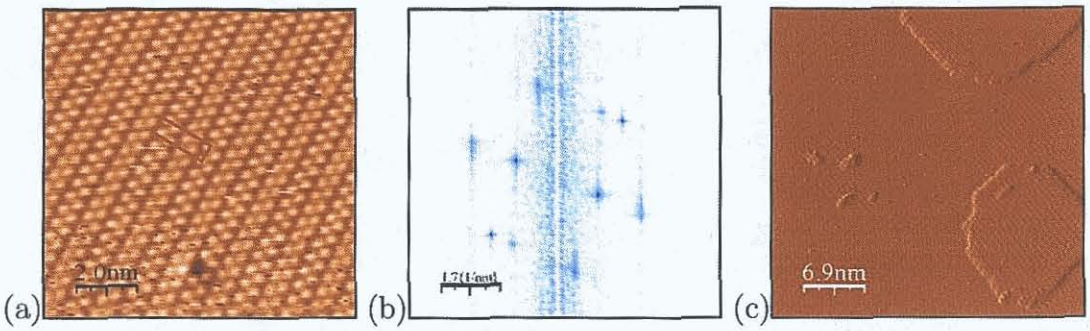

Figure 3.17: (a) STM image of the phase II Cu(100)/Sn surface at $\theta_{Sn} = 0.33 \pm 0.02$ ML. $V_s = -0.2$ V, $I_t = 0.9$ nA, 10 nm^2. (b) Fourier transform with spot spacings of 0.666 nm^{-1} and 2.216 nm^{-1} in the [011] and [01$\bar{1}$] directions. (c) Derivative enhanced STM image of islands, $V_s = 0.06$ V, $I_t = 1.32$ nA, 34.7 nm^2.

As more Sn is deposited on to the previous phase the copper domain walls begin to fill and the p(2×2) domains begin to extend in either the [01$\bar{1}$] or the [011] direction. The second phase appears as double rows of Sn atoms with a dark spacing between each double row. Neighbouring double rows form misaligned chevrons and exhibit a p(2×6) unit cell as in figure 3.17(a). Islands are noted on the surface in this phase, figure 3.17(c) while their sides are straight and well ordered their corners tend to be rough and rounded and they are usually surrounded by areas of phase I. There is a possibility that the Cu atoms displaced from the domain walls in phase I can diffuse across the surface to add to the step edges and also provide the

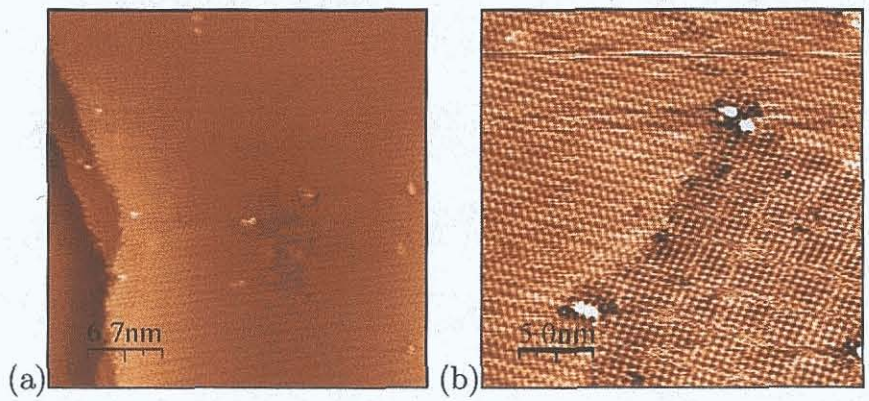

Figure 3.18: STM images of phase I to phase II transition at step edges, (a) $V_s = -0.007$ V, $I_t = 1.61$ nA, 33 nm^2, (b) $V_s = -0.027$ V, $I_t = 1.71$ nA, 25 nm^2.

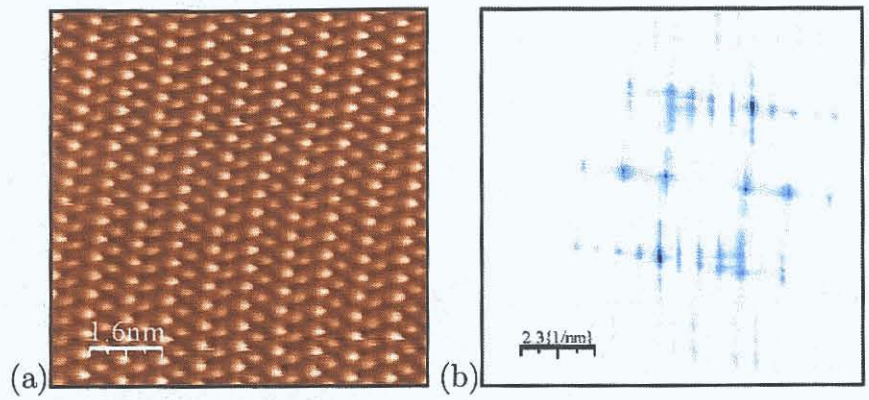

Figure 3.19: STM image of phase II,(a) $V_s = -0.055$ V, $I_t = 0.8$ nA, 15 nm^2, (b) associated Fourier transform, 0.637 $\pm$ 0.005 nm^{-1} and 2.530 $\pm$ 0.005 nm^{-1} along the [011] and [01$\bar{1}$] directions.

additional Cu to form theses islands [72]. The step edges are always the last areas on the surface to complete the transition to the next phase, as shown in figure 3.18 (a) and (b).

To understand the origin of the p(2 $\times$ 6) periodicity observed in the LEED diffraction patterns, Fourier transforms of the STM images were calculated [38]. Figure 3.17(a) and (b) shows an STM image, -0.2 mV sample bias, 0.9 nA tunnel current, and its corresponding Fourier transform. The Fourier transform exhibits a distorted unit cell as a consequence of the drift in the STM image. An angle of 84 $^\circ$ $\pm$ 1 $^\circ$ between reciprocal lengths of 0.666 $\pm$ 0.005 nm^{-1} and 2.216 $\pm$ 0.005 nm^{-1} are recorded along the [011] and [01$\bar{1}$] directions respectively. These reciprocal lengths correspond to lattice spacings of 5.888 and 1.769 units respectively.

Surface structures imaged at different tunnel currents, can often appear quite different as evident when figure 3.19(a) and figure 3.17(a) are compared. The images are taken from the same sample surface but figure 3.19(a) is taken at a higher tunnelling current of 2.0 nA. Measurements from the corresponding Fourier transform, figure 3.19(b) give an angle of 85 $^\circ$ $\pm$ 1 $^\circ$ between the [011] and [01$\bar{1}$] directions and reciprocal lengths of 0.637 $\pm$ 0.005 nm^{-1} and 2.530 $\pm$ 0.005 nm^{-1} for the unit cell. These measurements correspond to substrate lattice spacings of 6.161 and 1.550 units. In both sets of results from the Fourier transform the lengths determined compare favourable to the expected 2 and 6 lattice spacing of the unit cell when drift of the local structure is taken into consideration.

NIXSW

The Bragg profiles and parameters of phase II are shown in figure 3.20. The coherent fractions, 0.66 and 0.68 are lower when compared to phase I, this result would support the theory of two adsorption sites at slightly different heights resulting in a coherent position which reflects the average of the two heights. Dealloying is easily dismissed as a possible cause as phase III has already been determined to be a surface alloy [78].

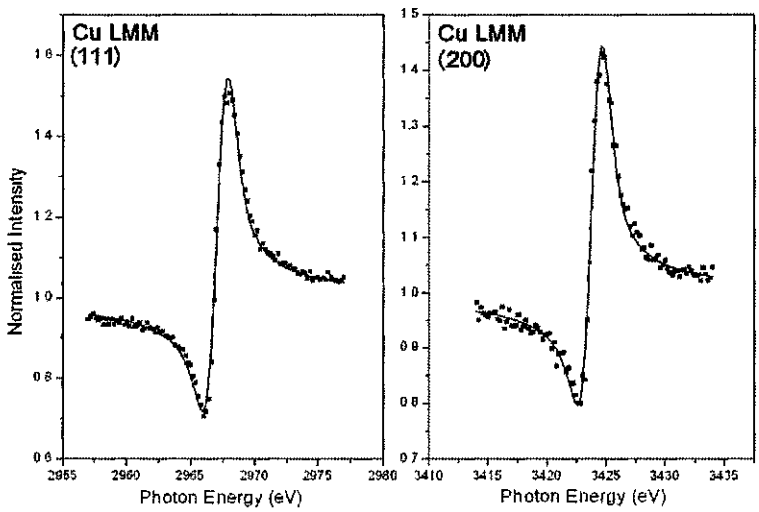

Phase	Plane	E_{Bragg} eV	$f_{(hkl)}$	$p_{(hkl)}$	$d_{(hkl)}$ Å	ΔE eV
II	111	2966.6	0.66	0.11	0.23	0.65
	200	3423 9	0.68	0.21	0.38	0.66

Figure 3.20: NIXSW profiles for phase II: Sn $p_{(111)} = 0.11 \pm 0.05$ and $f_{(111)} = 0.66 \pm 0.05$. Sn $p_{(200)} = 0.21 \pm 0.05$ and $f_{(200)} = 0.68 \pm 0.05$. The solid lines show theoretical fits.

Phase II model

The optimum coverage for this phase is reached at $\theta_{Sn} = 0.33$ ML, with 4 Sn atoms per 12 Cu atoms in the unit cell, indicated in black on the figure 3.21. STM images of phase II reveals the Sn atoms positions in relation to a p(2 × 6) unit cell and a low density of island formation which are suggestive of displaced copper. The LEED data revealed a p2mg space group. The newly discovered glide plane symmetries are distinguished by the telltale missing spots at $^1/_6$ and $^5/_6$ positions in the diffraction pattern. The p2mg space group restricts the positions of the Sn atoms in this model to conform to the mirror and glide plane symmetry which have been overlaid on the model in white, figure 3.21. These restrictions were not applied to previous models and explain why they were unsuccessful in modelling the experimental data.

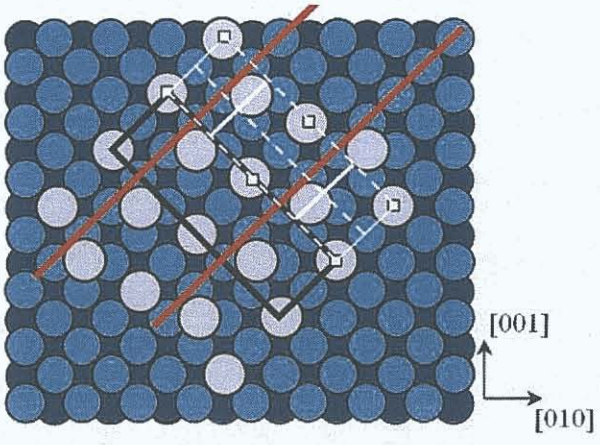

Figure 3.21: Proposed model for phase II, red lines indicate darker gaps present in STM images. The p(2 × 6) unit cell outlined in black. The p2mg symmetry is indicated with a white cell, mirror planes as solid lines, glide planes as dashed lines and 4-fold rotation as squares.

Finally the NIXSW analysis exhibits slightly low coherent fractions of $f_{(111)} = 0.66$ and $f_{(200)} = 0.68$. This is an indication of slightly different bonding environments for the Sn atoms as illustrated in the model of the p(2 × 6) unit cell for this phase shown in figure 3.21. A uniform Cu substrate top layer is shown in the model. It is noted that not all Sn atoms are situated in the substitutional alloy sites in the model but some are in four-fold hollow sites. The position and spacing of the dark rows noted in the STM images coincides with the position and spacing of the red lines in the model. This spacing and the island formation suggest an adjustment in the top Cu substrate layers does take place and further suggests the Sn atoms could be accommodated into substitutional surface alloy site at these positions.

3.4.3 Phase IIH

LEED

The diffraction patterns recorded for the transition between phase II and phase III at a coverage of $\theta_{Sn} = 0.45 \pm 0.5$ ML are displayed in figure 3.22(a) and (b). They show evidence for the new phase. The diffraction spots appearing in the transition between these two phases, marked with red circles on the LEED image, are not consistent with spots present in either phase II or III. This is a new phase, unreported in the literature. It has been designated phase IIH, or higher phase II because it co-exists between phase II and phase III.

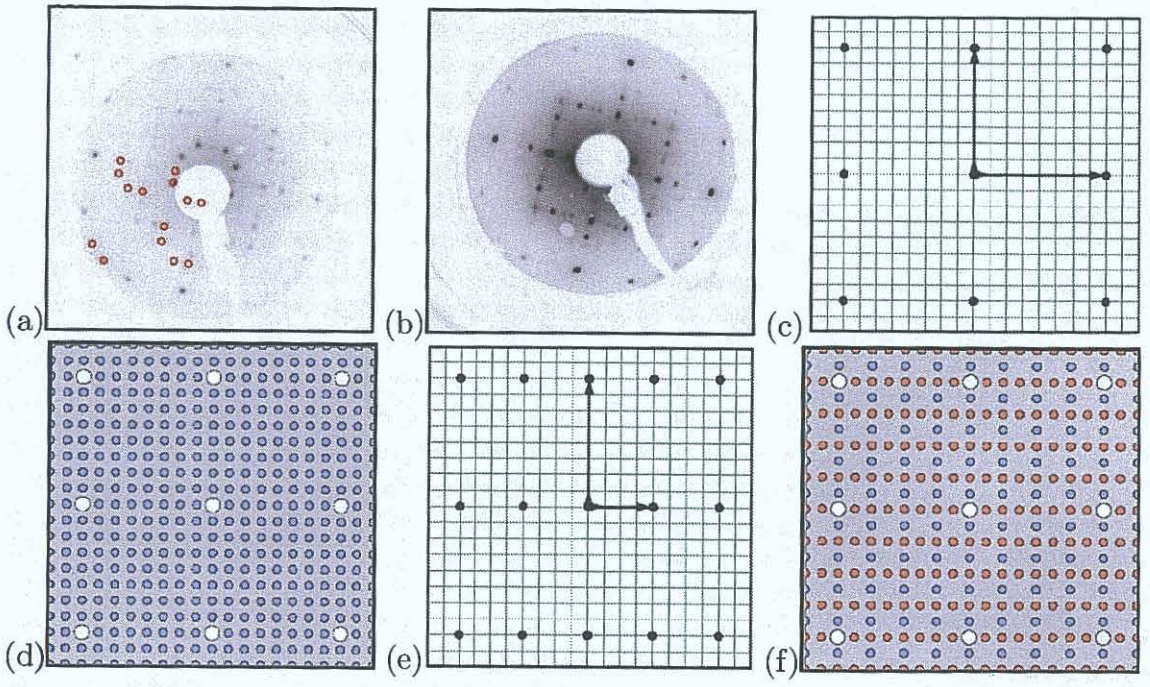

Figure 3.22: Evidence for new phase occurring between phase II and phase III is observed in the diffraction patterns, both recorded at 60 eV. Red circles indicate the additional Bragg spots. LEEDpat simulated diffraction patterns. (c) and (d) single domain, Sn : p(8×8) $b_1 = 20.4, b_2 = 20.4, \theta = 90°$. (e) and (f) double domain, Sn : p(4×8) $b_1 = 10.2$, $b_2 = 20.4$, $\theta = 90°$.

In the LEED diffraction pattern for phase IIH a greater intensity is noted in the $(^1/_8, ^1/_2)$ beams and those with equivalent symmetry. Figure 3.22(a) and (b) LEED diffraction patterns taken at 60 eV beam energy illustrate this point. The real space distances between the Cu p(1×1) bulk diffraction beams were measured. This allows one to calculate the interatomic spacing of the copper atoms. These measurements were taken from all the symmetry equivalent positions in the LEED images of this new phase in order to ascertain the periodicity of the new beams in

the diffraction pattern. Then measurements were averaged to reduce the effects of distortion. Calculating the ratio between the real space Cu p(1 × 1) bulk diffraction beams and the nearest distance between the beams of the new phase in the [011] and [01$\bar{1}$] directions gives a ratio of 8:1 for the new phase to the copper interatomic spacing. It is also noted that the $(^1/_2, 1)$ and symmetrical equivalent beams are beginning to appear, supporting an 8:1 ratio. This indicates that the new phase IIH can be described by a p(8 × 8) single domain or a p(4 × 8) double domain structure, figure 3.22(c) and (d).

A large number of beams are absent from the LEED images for both of the proposed structures, this could be attributed to low intensity in these spots or the possibility of glide plane symmetries. This investigation of the new phase is hampered by the concurrent formation of the phase III and high background intensity.

STM

Phase IIH develops from the phase II structure with additional Sn atoms inserting themselves between the double Sn atom rows, the boundary between the phase II and phase II structures is evident in figure 3.23(a) and (b). The STM tip often looses resolution along the boundary, as manifested by the streaking in these images and is attributed to loose atoms on the surface interacting with the STM tip. Phase IIH maintains the same alignment as phase II with the bulk Cu as noted by the alignment of the Bragg spots in the LEED.

Stripes of the phase III structure begin to appear on the surface rotated by 45° to the lower coverage phase II structure before any large domains of the phase IIH are formed. As phase III domains continue to grow, islands begin to form on the surface and even as phase III begins to dominate the LEED patterns, phase II and phase IIH continue to co-exist on the surface, figure 3.23(c).

Figure 3.24(a) shows two domains of phase IIH rotated at 90° to one another. The phase is completed out to the step edges, although some phase II still remains as seen on the left hand side of the image. The insert highlights the stripes of phase III enclosed in blue lines, which are forming within the phase IIH domains.

The three phases II, IIH and III are imaged in figure 3.23(b), 3.23(c) and figure 3.24(a) co-existing in areas as small as 15 nm^2 which is well within the coherence length of the electrons from the LEED. Figure 3.24(b) show an area of phase IIH with rows of two Sn atoms orientated along the [011] direction, they are a remnant of the phase II rows and they are interspaced from one another by widely spaced single Sn atoms aligned in rows along the [01$\bar{1}$] direction. These periodicities are reflected

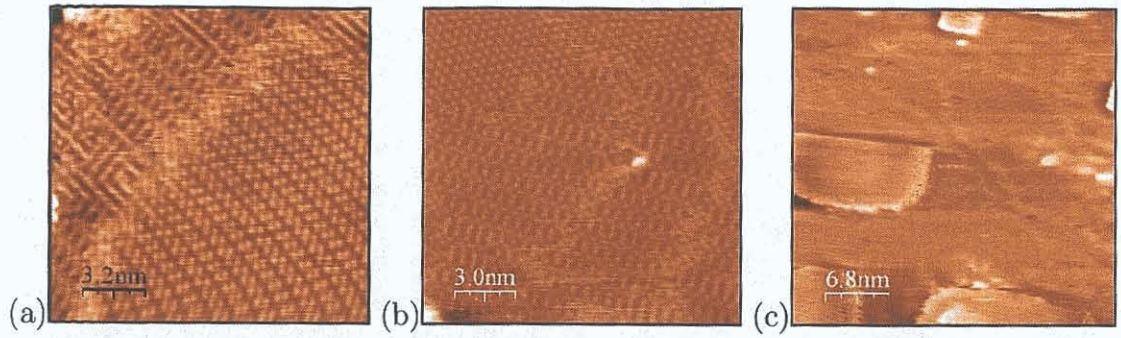

Figure 3.23: STM images of the domain boundaries between phase II and phase IIH. (a) phase IIH beginning to form in top left, $V_s = -0.2$ V, $I_t = 1.07$ nA, 15.9 nm^2, (b) first indication of transition to phase III, $V_s = -0.09$ V, $I_t = 2.0$ nA, 15 nm^2. (c) islands of phase III existing with regions of phase II and phase IIH, $V_s = -0.13$ V, $I_t = 1.14$ nA, 34.5 nm^2.

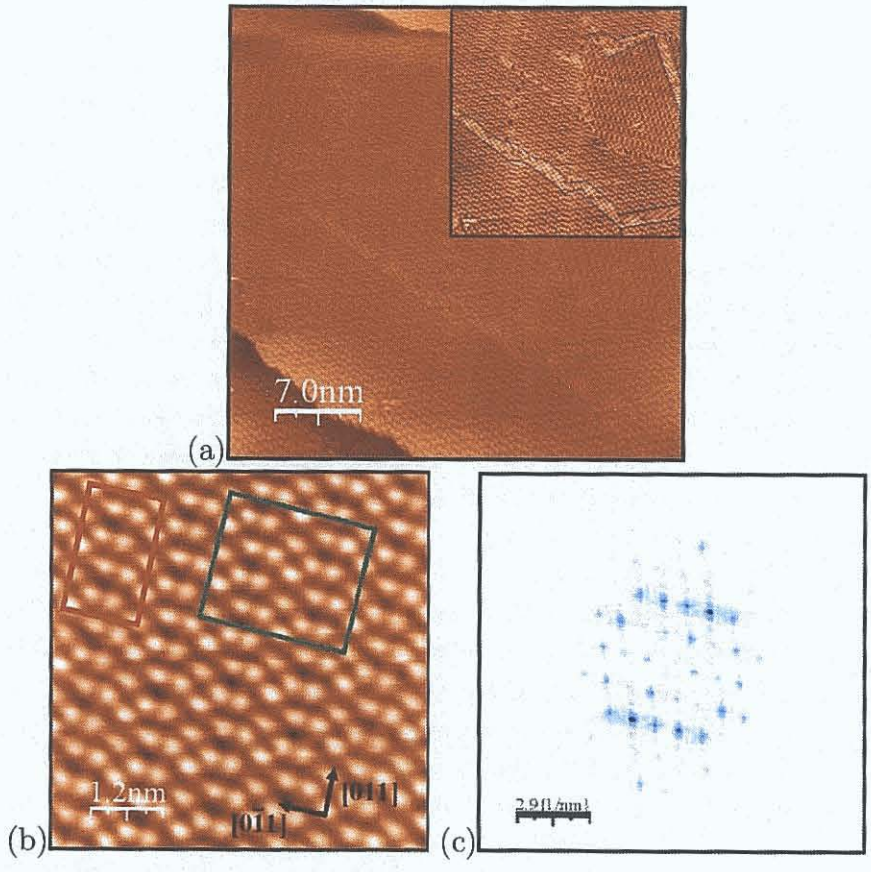

Figure 3.24: STM images of (a) the two different domains of phase IIH. Insert shows beginning of phase III, $V_s = -0.05$ V, $I_t = 0.78$ nA, 35 nm^2, (b) high resolution phase IIH image overlaid with (8×8) or (4×8) unit cells, $V_s = -0.05$ V, $I_t = 0.78$ nA, 6.1 nm^2,(c) Fourier transform, $0.882 \pm 0.05\text{nm}^{-1}$ and $2.378 \pm 0.05\text{nm}^{-1}$ along the [011] and [01$\bar{1}$] directions.

in the Fourier transform of this STM image. The distances measured between the bright spots in the Fourier transform correspond to two periodic lengths of 1.12 ± 0.03 nm and 0.42 ± 0.03 nm aligned with the Cu substrate. This suggests a unit cell of 4.40 ± 0.1 units by 1.65 ± 0.1 units of the substrate lattice for phase IIH.

The Fourier transforms of the STM images do not reflect the same periodicities observed in the LEED diffraction studies, of a p(8 × 8) or p(4 × 8) unit cell. The dimensions of the p(4 × 8) unit cell are 1.02 nm × 2.24 nm. It is assumed that the 1.02 nm from the LEED and 1 12 ± 0.03 nm from the STM relate to the same periodic unit cell length of the surface structure. The 2.24 nm from the LEED diffraction pattern would compare favourably with a total length of five times the 0.42 ± 0.03 nm periodicity (2.10 nm) as noted in the Fourier transform. This unit cell is marked in red on figure 3.24(b). Comparing the p(8×8) unit cell, real space lengths of 2.24 nm × 2.24 nm, with the Fourier transform, with twice the 1.12 ± 0.03 nm periodicity (2.24 nm) and five times the 0.42 ± 0.03 nm periodicity (2.10 nm) then good agreement is obtained. This unit cell is marked in green on figure 3.24(b). The Fourier transform of an STM image will by its very nature only exhibit the periodicities in the recorded STM image and not the true surface periodicity. Bearing this and the drift associated with STM imaging in mind, the LEED and Fourier transform results equally support a p(8×8) or p(4×8) unit cell for phase IIH.

No NIXSW results were recorded for this transition phase because of the co-existing phase II and phase III make it impossible to record meaningful results based solely on phase IIH.

Phase IIH model

This previously unreported phase, designated phase IIH, was discovered in the sub-monolayer Sn coverage range. A model based on LEED and STM is illustrated figure 3.25(b). STM images of the boundary between phase II and phase IIH were used to construct an initial model of phase IIH, figure 3.25(a). The Sn atoms in phase IIH are shown in black and the previous phase II is shown in grey. Yellow lines are drawn along the middle of the double row structure and short black lines guide the eye to show the chevron structure of the rows as evident in the STM images. This produced an initial guess for the Sn atom positions in this new structure. Measurements from the LEED images suggested a p(4 × 8) or p(8 × 8) unit cell. Theses unit cells where then overlaid on this model figure 3.25(b) in light and dark purple respectively. The STM images and the Fourier transforms of these images

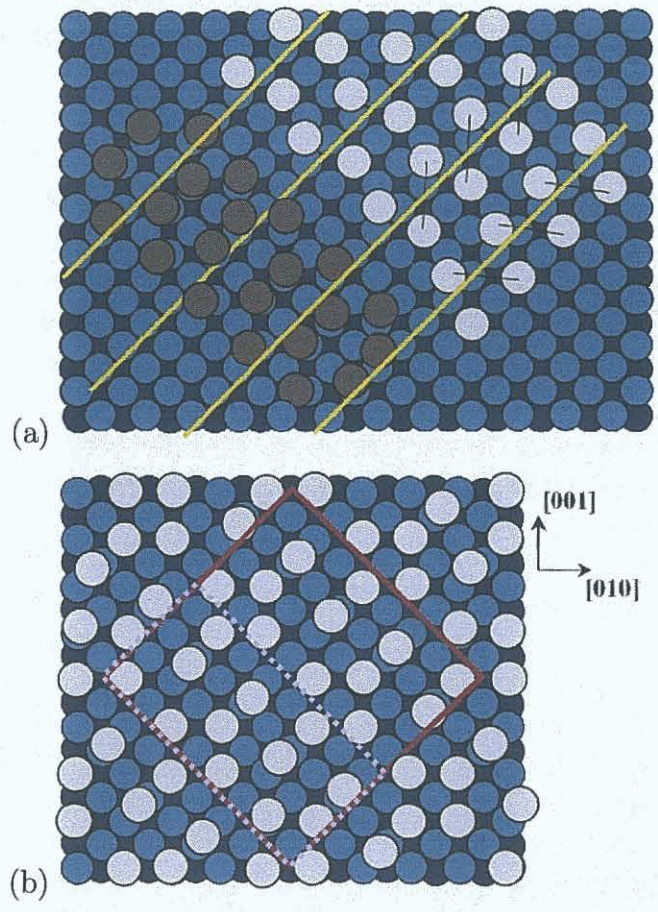

Figure 3.25: (a) Initial positioning of Sn atoms (black), and phase II structure with Sn atoms (grey). (b) Proposed phase IIH model, Sn atoms (grey), p(4 × 8) and p(8 × 8) unit cells outlined in dashed light and solid dark purple.

do not fully agree with the LEED data and so they could support either unit cell structure. The reason for the uncertainty noted between the techniques is attributed to differences in the positions of the substrate copper top layers which is reflected in the LEED diffraction pattern but not accessible to the STM.

The coverage of phase II is reported as $\theta_{Sn} = 0.37$ ML [75] and $\theta_{Sn} = 0.42$ ML [68] [73] [86]. This inconsistency can be attributed to this new phase. Optimum coverage for phase IIH as based on the proposed model is $\theta_{Sn} = 0.375$ML, with 12 Sn atoms per 32 Cu atoms in the unit cell. This is only marginally more than phase II, $\theta_{Sn} = 0.33$ ML and explains the short coverage range over which phase IIH is observed. The early appearance of phase III co-existing with the phase IIH domains can be qualified by low packing efficiency of the phase IIH structure where the need to accommodate the additional Sn is best served in the stable phase III modified c(2 × 2) reconstruction.

3.4.4 Phase III

LEED

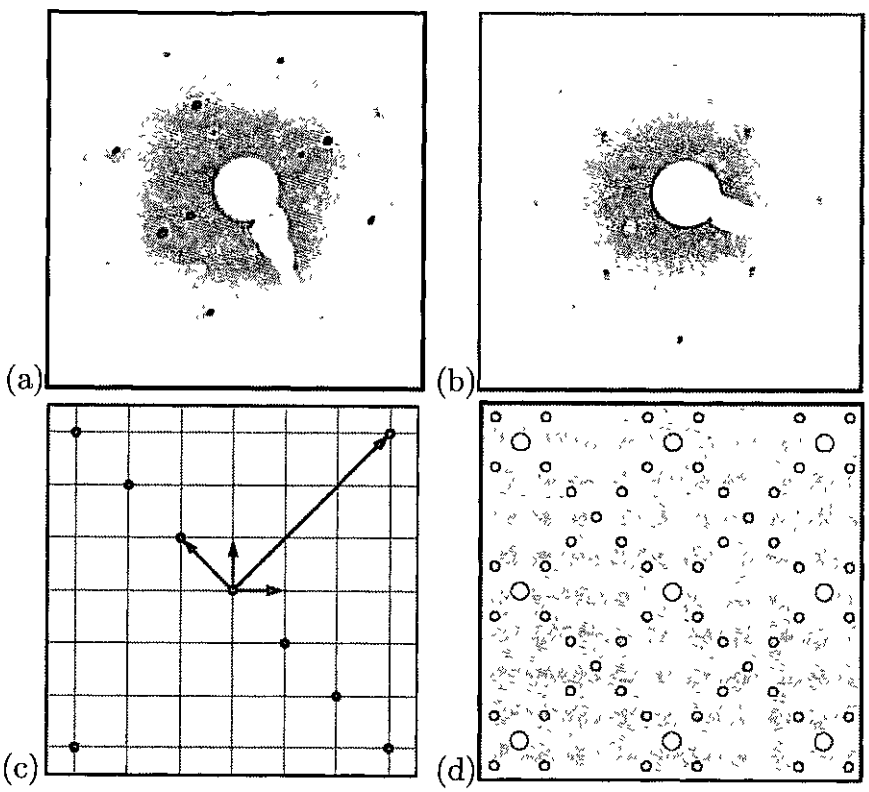

Figure 3.26: Phase III LEED diffraction patterns (a) and (b) recorded at 60 eV. LEEDpat simulation, (c) and (d) Sn : $b_1 = 10.8, b_2 = 3.6, \theta = 90\,°$.

A Sn deposition of $\theta_{Sn} = 0.5$ ML at room temperature on the Cu(100) surface results in the p($3\sqrt{2} \times \sqrt{2}$)R45 ° structure, designated phase III. This structure originates in a distorted c(2 × 2) structure due to the significant strain induced by accommodating the larger metallic radius of Sn (1.64 Å) within a layer of Cu (1.275 Å) atoms. The diffraction pattern appears, as shown in figure 3.26(a) with intense ($^1/_2, ^1/_2$) beams. The higher intensity in the ($^1/_3, ^1/_3$) and equivalent beams in the diffraction pattern is noted, this is in excellent agreement with all previous publications [68] [73] [75]. The LEEDpat simulation of phase III is included as a guide 3.26(c) and (d). The addition or extra Sn to this surface causes Bragg spots in the ($0, ^1/_2$) and symmetry equivalent positions to appear, indicating the transition to the next phase, as shown in figure 3.26(b).

STM

Double domains of phase III, orientated along the [001] and [010] directions, as shown in figure 3.27(a) and (b), rotated by 90 ° to one another. The interface between any two domains occurs at the island corners or at defect sites on the surface. A single domain of phase III covers each island.

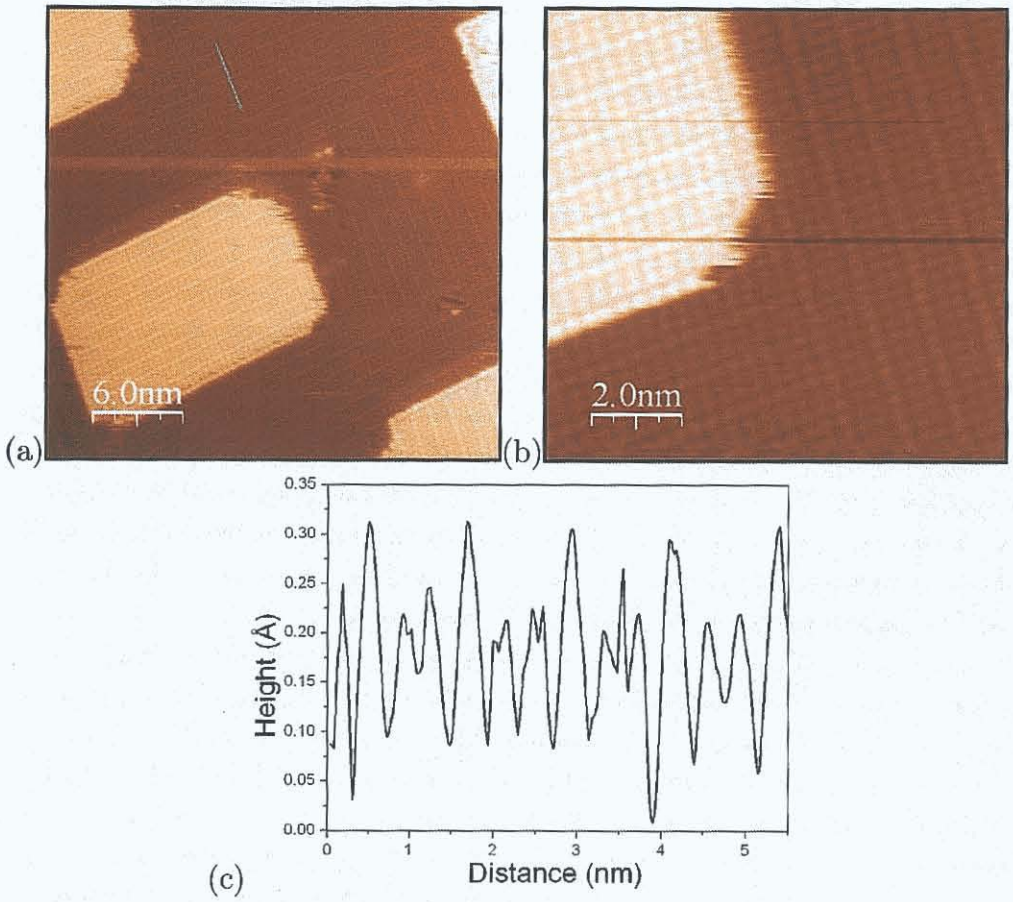

Figure 3.27: STM images of phase III and regular island formations, (a)$V_s = -0.1$ V, $I_t = 1.0$ nA, 30 nm^2, (b) $V_s = -0.01$ V, $I_t = 3.0$ nA, 10.2 nm^2. (c) Line profile as indicated in STM image (a).

Vertical and horizontal corrugations of the surface are observed and can be accounted for by the surface strain in the [010] direction. The STM image in figure 3.27(c) shows a line profile of a small area of the phase III where the surface modulation is clearly visible. It is observed that every third tin row is higher and the two tin rows between are compressed laterally. Measurements from this and similar profiles determine a distance of 0.32 $\pm$ 0.02 nm between the atoms of the compressed rows. This result is in excellent agreement with the separation of 0.32 nm proposed in model based on the previous LEED studies [75] and the 0.31 $\pm$ 0.01 nm spacing determined from IV LEED calculations [78], as listed in table 3.5. The vertical cor-

rugation of 0.008 ± 0.002 nm measured from the STM images compared favourable with 0.012 ± 0.007 nm from the same IV LEED study [78].

Researcher	Corrugation nm	Compression nm
McLoughlin	N/A	0.32
Pussi	0.012 ± 0.007	0.31 ± 0.01
Sheerin	0.008 ± 0.002	0.32 ± 0.02

Table 3.5: Vertical corrugation and lateral row compression reported by McLoughlin [15], Pussi et al. [78] and the present work.

Depicted in figure 3.28(a) are several of these well ordered rectangular islands, all of which are aligned parallel or perpendicular to the [001] and [010] directions. A Fourier transform of figure 3.28(a) is shown in figure 3.28(b), the observed pattern is in agreement with the LEED pattern shown in figure 3.26(a). Measurements made from this Fourier transform indicate 1.106 nm ($0.255 \times 3\sqrt{2} = 1.0818$ nm) and 0.37 nm ($0.255 \times \sqrt{2} = 0.36$ nm) unit cell lengths in good agreement with the p($3\sqrt{2} \times \sqrt{2}$)R45 ° structure.

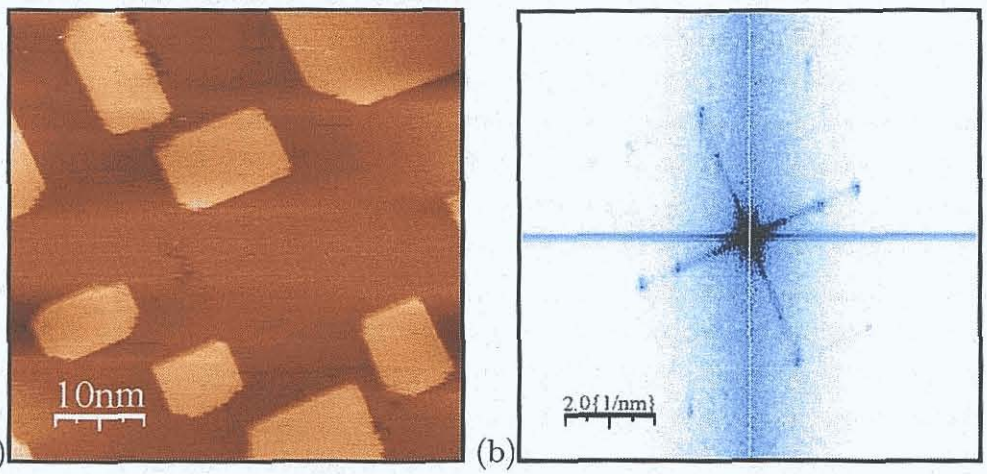

(a) (b)

Figure 3.28: (a) STM image of phase III islands aligned along the [001] and [010] directions, $V_s = -0.01$ V, $I_t = 3.0$ nA, 50 nm^2 and corresponding (b) Fourier transform, $0.904 \pm 0.05\text{nm}^{-1}$ and $5.344 \pm 0.05\text{nm}^{-1}$ along the [001] and [010] directions.

NIXSW

The Bragg profiles and parameters of phase III are shown in figure 3.29. The coherent fractions improve for phase III over the previous phase II results, for both the (111) and (200) planes. This indicates a single adsorption site for the Sn atoms

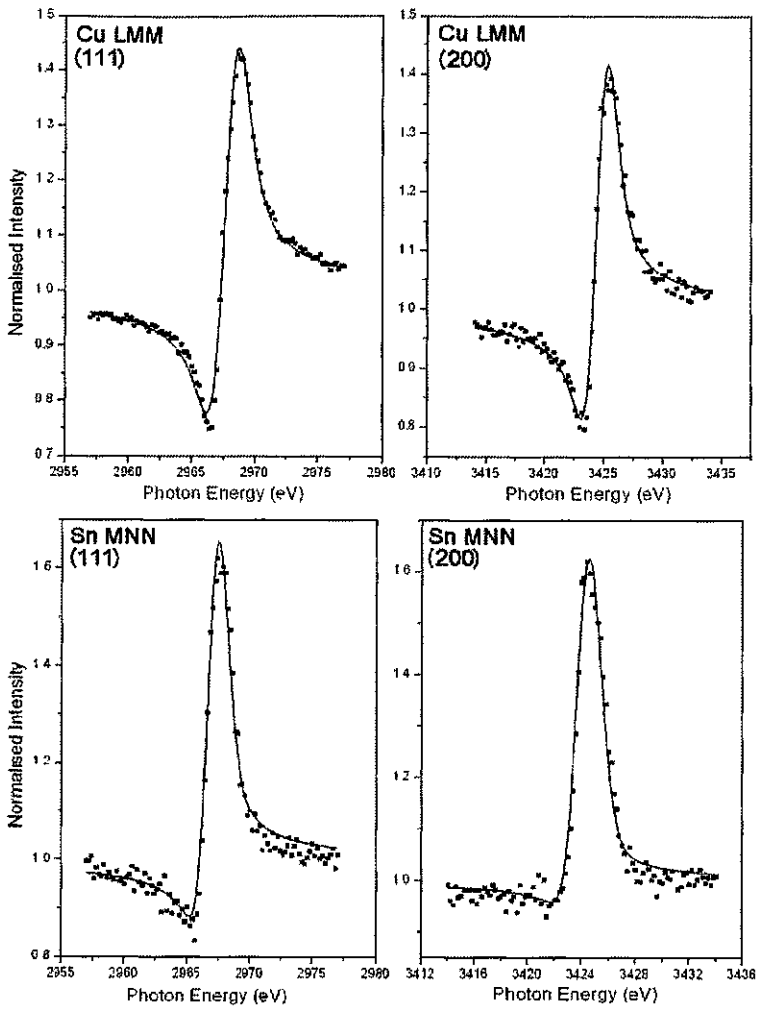

Phase	Plane	E_{Bragg} eV	$f_{(hkl)}$	$p_{(hkl)}$	$d_{(hkl)}$ Å	ΔE eV
III	111	2966.5	0.73	0.09	0.19	0.73
	200	3424.2	0.77	0.21	0.38	0.76

Figure 3.29: NIXSW profiles for phase III: Sn $p_{(111)} = 0.09 \pm 0.05$ and $f_{(111)} = 0.73 \pm 0.05$. Sn $p_{(200)} = 0.21 \pm 0.05$ and $f_{(200)} = 0.77 \pm 0.05$. The solid lines show theoretical fits.

as the values are slightly lower than the ~0.8 expected from a well ordered single high symmetry adsorption site. The continuing trend of a compression of Sn atom positions towards the (111) plane is also noted.

Phase III model

The surface alloy model proposed for phase III by McLoughlin et al. [75] and further developed by Pussi et al. [78] is illustrated in figure 3.30(a) and (b). This model agreed with the recorded STM and NIXSW results. The unit cell is outlined in

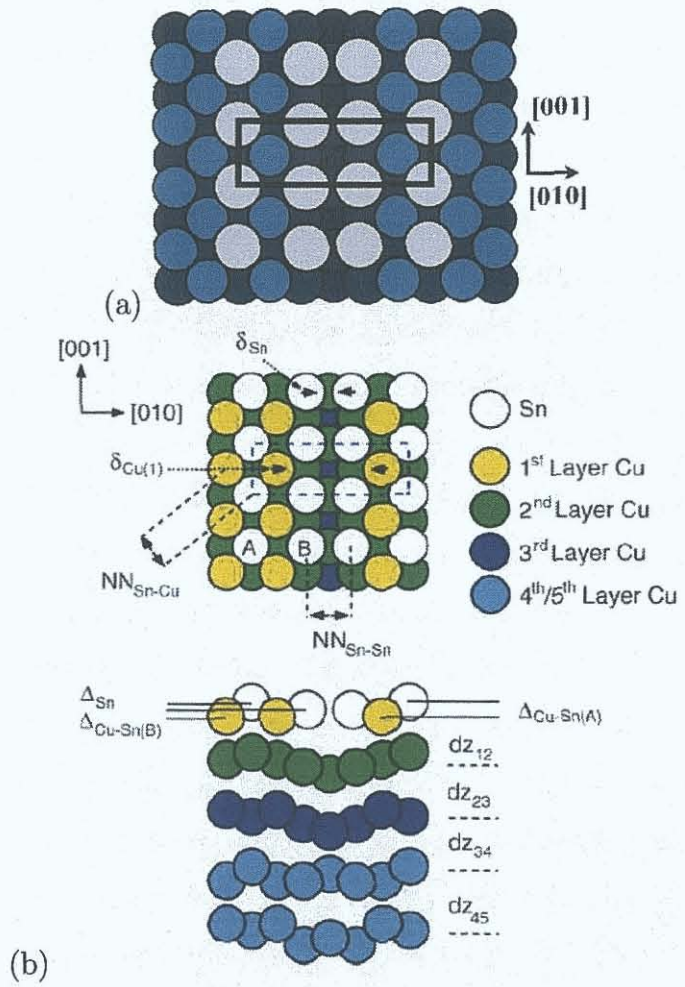

Figure 3.30: (a) Proposed phase III model, Sn atoms (grey), unit cell outlined in black, distance of 0.32 ± 0.02 nm between Sn atoms above missing copper row. (b) Model developed by Pussi et al. [78] included with permission.

black and a missing Cu row below the compressed Sn row is noted. These expelled Cu atoms form islands on the surface as evident from recorded STM images of the phase. The distance of 0.32 ± 0.02 nm between the centres of the compressed rows of Sn atoms as measured from the STM images compares well to the value of 0.32 nm proposed in the model based on the previous LEED studies [75] and the 0.31 ± 0.01 nm based on the IV LEED study of phase III [78]. From the same IV LEED study, positions of 0.039 ± 0.007 nm and 0.027 ± 0.007 nm were calculated for the two Sn positions above the buckled Cu surface [78]. The vertical corrugation of the Sn rows is then $\Delta_{Sn} = 0.012 \pm 0.007$ nm. The vertical corrugation of 0.008 ± 0.002 nm from the STM measurements compares favourable with this result. Pussi et al. [78] also notes an expansion of the first interlayer spacing of 0.187 ± 0.004 nm, from the 0.181 nm bulk spacing. This relaxation and the perpendicular

relaxation considered within the top five layers, lead to the Sn atoms positions being an additional 0.006 nm above the extended (200) bulk planes. From the calculated positions of the Sn atoms with respect to the bulk extended planes at 0.033 nm and 0.045 nm, the average position of the Sn atoms at the surface is 0.039 nm. This result is in excellent agreement with the result of the NIXSW for the (200) extended bulk planes, which place the Sn atoms at an average height of 0.38 ± 0.02 nm.

3.4.5 Phase IV

LEED

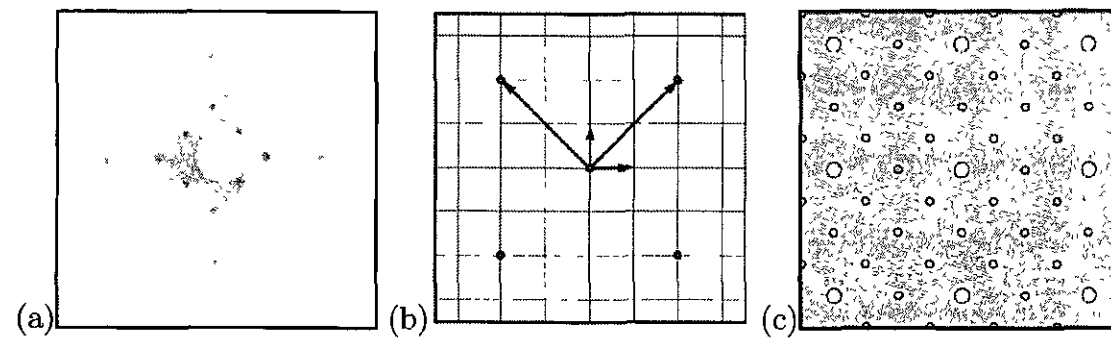

Figure 3.31: Phase IV diffraction pattern (a) taken at 60 eV. LEEDpat simulation (b) and (c) Sn : $b_1 = 7.212, b_2 = 7.212, \theta = 90°$.

As the Sn coverage is increased from 0.5 ML the p($2\sqrt{2} \times 2\sqrt{2}$)R45° diffraction pattern of phase IV is formed, figure 3.31(a). The LEEDpat simulation is included as a guide. No extraneous Bragg spots are observed and all spots are accounted for by either the phase III or the emerging phase IV structure. Any extra Sn on this phase IV surface results in an increase in the background intensity and the loss of the diffraction pattern, indicating a disordered surface.

STM

The p($2\sqrt{2} \times 2\sqrt{2}$)R45° surface at a tin coverage of $\theta_{Sn} = 0.625$ ML is revealed by STM imaging as a network arrangement, figure 3.32. Dark holes in the surface are observed between crossing rows consisting of bright spots which are attributed to the Sn atom positions. Two separate sets of line profiles were taken from multiple STM images of the phase IV surface. Those along the bright rows and those along the dark holes both, as indicated in figure 3.32(b). The height corrugation along the bright and dark rows is 0.029 ± 0.005 nm and 0.050 ± 0.005 nm respectively.

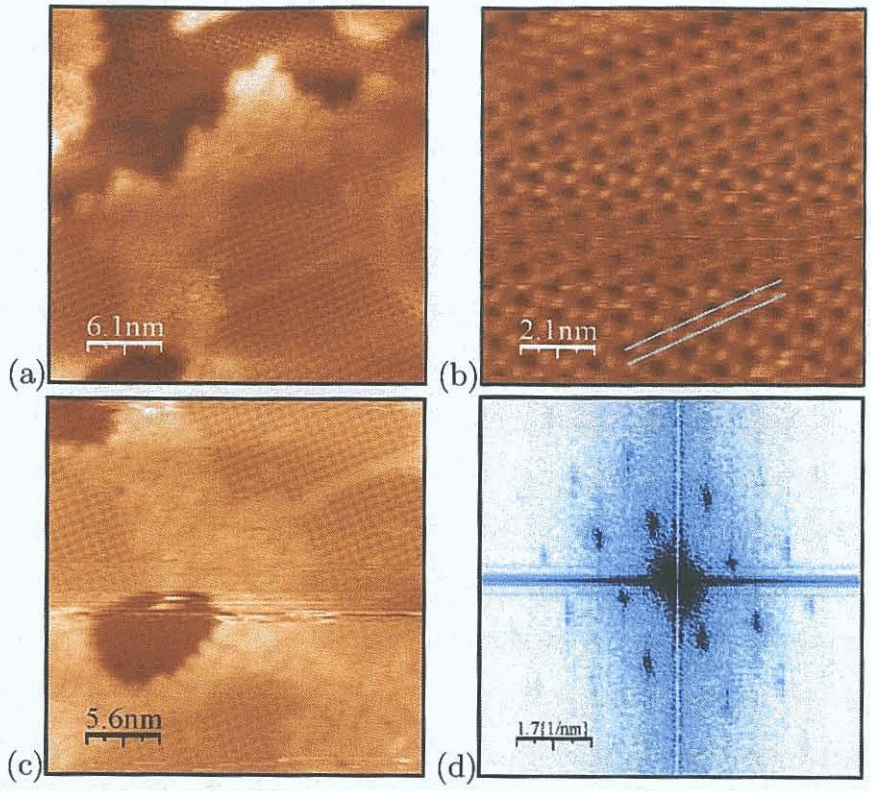

Figure 3.32: STM images of of the same area phase IV, $V_s = -0.1$ V, $I_t = 0.5$ nA, (a) 30.5 nm^2, (b) 10.3 nm^2. (c) STM image resolving Stranski Krastanov growth, $V_s = 1.0$ V, $I_t = 1.0$ nA, 27.9 nm^2, (d) Fourier transform 1.295 ± 0.03 nm^{-1} and 1.473 ± 0.03 nm^{-1} along the [001] and [010] directions.

From the hard sphere model calculations used in the NIXSW analysis the bridge site model is used to calculate a height different between the two Sn layers of 0.21 nm which is greater than the STM measurement. The dark area should coincide with the copper substrate and results in a height difference of 0.46 nm which is again much greater than the STM measurements. Given the finite radius of the STM tip it is not surprising that the ideal calculated height difference is greater than measurements taken from the STM images.

A Fourier transform is shown in figure 3.32(d). Calculations from the Fourier transform record lengths of 0.772 ± 0.03 nm and 0.679 ± 0.03 nm with a relative angle of 91 °. These measurements are in agreement with the LEED diffraction pattern $2\sqrt{2}$, 0.72 nm, length with a relative angle of $90\,° \pm 1\,°$.

In a large area image, figure 3.32(a) the step edges are no longer visible and strips of growth above the monolayer coverage are starting to form. The Stranski Krastanov growth mode predicted by the Auger signal versus time plots of Argile and Rhead [68] [73] is exhibited in the short range order observed in the higher Sn coverage areas, figure 3.32(c).

NIXSW

For phase IV there is a stark contrast between the coherent fractions of both planes shown in figure 3.33.

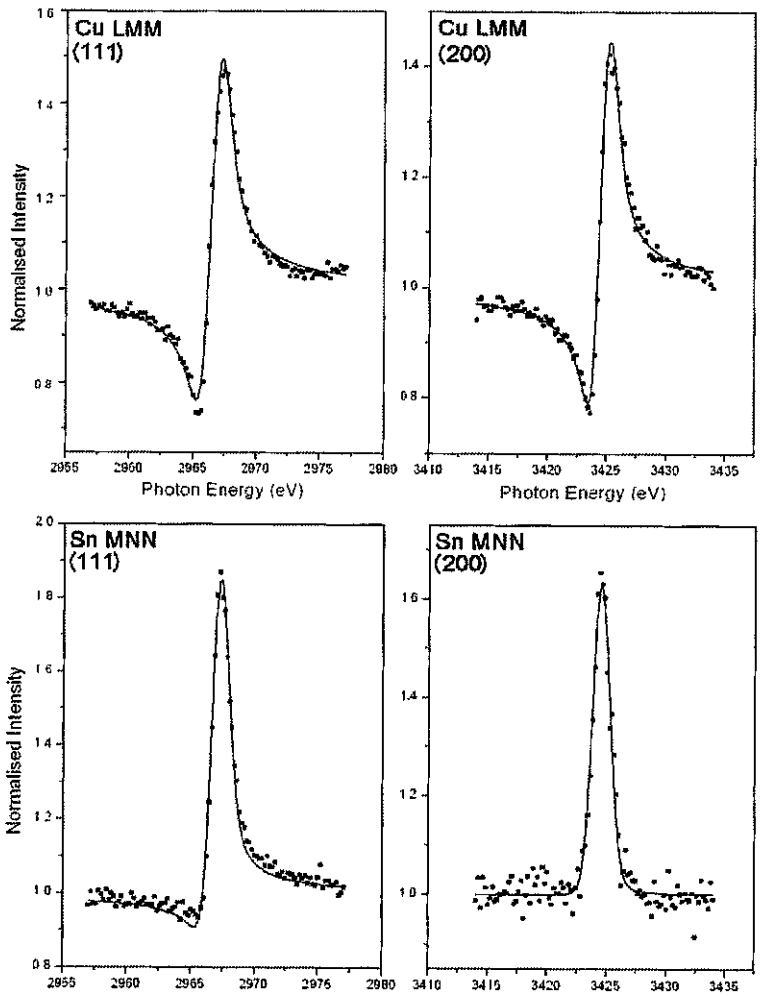

Phase	Plane	E_{Bragg} eV	$f_{(hkl)}$	$p_{(hkl)}$	$d_{(hkl)}$ Å	ΔE eV
IV	111	2966.51	0.65	0.13	0.27	0.58
	200	3424.06	0.48	0.25	0.45	0.69

Figure 3.33: NIXSW profiles for phase IV: Sn $p_{(111)} = 0.13 \pm 0.05$ and $f_{(111)} = 0.65 \pm 0.05$. Sn $p_{(200)} = 0.25 \pm 0.05$ and $f_{(200)} = 0.48 \pm 0.05$. The solid lines show theoretical fits.

These results suggest the possibility of two bonding sites which are close to equivalent with respect to the (111) planes but are inequivalent with respect to the (200) planes as suggested by a double Sn layer for phase IV [15] and the possibility that the Sn has begun to dealloy out of the surface.

Phase IV may be explored by assuming a double layer of Sn is responsible for

the dramatic drop in the coherent fraction for the (200) plane. From the phase IV McLoughlin model [15] a double layer of Sn is expected, four atoms in the first layer supporting a fifth atom between them. This results in two different heights for the Sn atoms relative to the copper substrate.

In order to explain the NIXSW results for phase IV, four different adsorption sites for the first Sn layer are used to calculate the height of the first and second layer of Sn above the Cu substrate extended (200) bulk planes. The height of the Sn atoms layers were calculated from hard sphere constructions using the 12-fold coordination radii of Sn and Cu atoms [87]. The four different Sn adsorption sites for the first layer, the atop site, the short bridge site, the 4-fold hollow site and the 4-fold substitutional site are illustrated in figure 3.34.

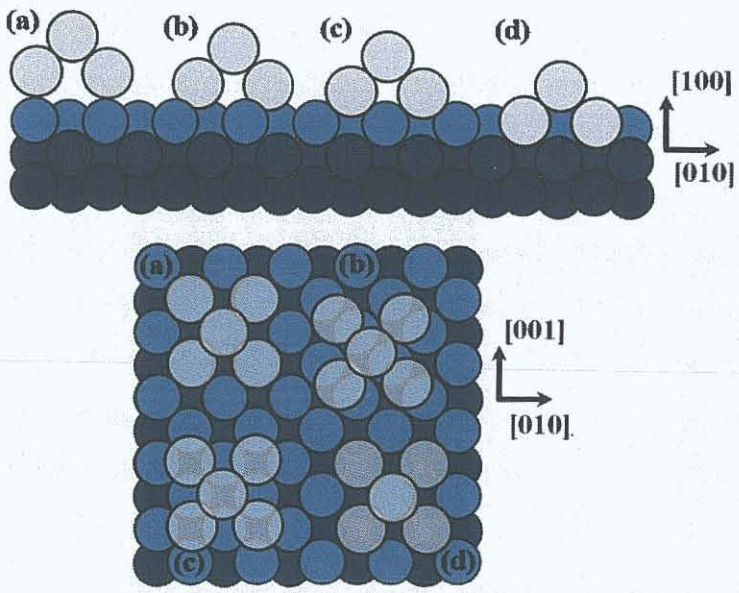

Figure 3.34: The scaled hard sphere schematic diagrams in plan and elevation illustrate the Cu substrate atoms (blue) with Sn atoms (grey) in the following positions: (a) atop site, (b) bridge site, (c) 4-fold hollow site and (d) 4-fold substitutional site.

The first of four models is the atop model. In this model the four atoms in the first layer were all positioned at a nearest neighbour atop site, and the second layer Sn atom was positions between the four Sn atoms of the first layer. The second model is the bridge model here the second layer atom rest on top of four neighbouring, first layer, bridge site atoms. The heights of the first and second layer Sn atoms are all straight forward to calculate and convert to coherent positions relative to the (111) planes. To illustrate this consider the third model, which places four Sn atoms at four-fold hollow sites in the Cu substrate. This results in two coherent positions for the two Sn layers of 0.88 and 0.99 with respect to the (200) plane. These spacings

can easily be converted to the (111) plane spacings by $d_{(111)} = d_{(200)}/\sqrt{3}$, to give coherent positions of 0.45 and 0.5 for the (111) planes. The fourth model considered was a substitutional alloy (SA) model. For this model the heights of the first layer Sn atoms was set at 0.038 nm or the average height of the Sn atoms above the (200) planes as calculated from the NIXSW results for phase III. The Sn atom in the second layer rests on top of the four first layer Sn atoms in the 4-fold hollow site.

The phase IV models differ in the position of the first layer Sn atoms relative to the Cu substrate extended (200) bulk planes just as their names suggest. The heights of the Sn atoms for both layer were calculated as coherent positions relative to the (200) planes for all the models. These two heights were then converted to coherent positions relative to the (111) planes. The results for each model are presented in table 3.6.

MODEL	Plane	Layer I	Layer II	*Calculated Layer II*	$\pm\chi^2$
Atop	200	0.60	0.70	0.20	0.25
	111	0.30	0.35	0.57	0.04
Bridge	200	0.55	0.33	0.18	0.02
	111	0.28	0.17	0.03	0.02
4-Fold Hollow	200	0.88	0.99	0.29	0.49
	111	0.45	0.5	0.09	0.17
SA	200	0.21	0.32	0.58	0.07
	111	0.11	0.16	0.36	0.04

Table 3.6: The calculated layer I and layer II heights of the Sn atoms layers for each of the four models. The experimental coherent fraction ($f_{200} = 0.48$ and $f_{111} = 0.65$) and the calculated [88] layer II heights for each model. (Surface Alloy model - SA).

These models can be tested for agreement with the experimental results by exploiting the Argand diagram construction, discussed in section 2.2.3, and implemented in an Excel program written by B. C. Cowie [88]. An example screenshot for the bridge site is shown in figure 3.35. In each case the experimentally obtained coherent fraction and coherent position, are the initial settings for the program. They are represented by a single vector of length f_{co} and phase angle $2\pi D/d_H$, (coherent position, coherent fraction) The height of the first layer Sn position dictated by the models along with the 4:1 ratio with respect to the number of Sn atoms in each of the layers set the system constraints. The two fractional occupancy vectors of f_1 and f_2 represent the individual contributions from the two different Sn layers

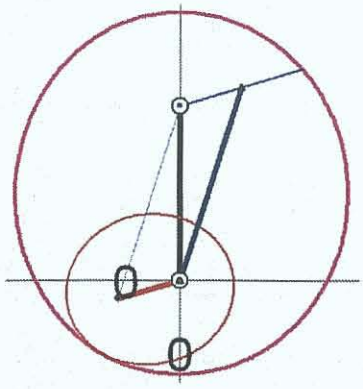

Figure 3.35: Argand diagram construction [88], for the bridge site is shown. Measured f_{co} and $2\pi D/d_H$ shown in black, all possible solutions generate the pink ellipse. f_1 and f_2 represented by green and red vectors respectively. Red ellipse is generated by 4:1 ratio.

of the recorded results. The coherent positions in layer I (*Layer I* input by the users) and layer II (*Calculated Layer II* calculated by the program) are represented by the f_1 and f_2 vectors on the Argand diagram. As the system is constrained to a 4:1 ratio, so too are the magnitudes of the vectors. This allows the second Sn layer position to be calculated for each model. The calculated positions (*Calculated Layer II*) were then compared to the positions calculated by the hard sphere models (*Layer II*). Best agreement was obtained between the experimental NIXSW positions and the positions calculated for the bridge site model. This suggests the Sn atoms dealloy and move out of the Cu surface to the bridge sites to form the phase IV structure.

A bridge site position for the Sn atoms in the first layer was shown to have the best agreement with the NIXSW results for the phase IV. This bridge site position is not unexpected because as previously noted in the introduction (section 3.1) the atomic radii ratio for Sn/Cu of 1.27 is within the range where coverages >0.4 ML causes the adsorbate atoms to dealloy to form an overlayer structure.

Phase IV model

No clear model for phase IV has emerged from any of the previous studies of the p($2\sqrt{2}\times 2\sqrt{2}$)R45° diffraction pattern, figure 3.8(a) and (b). The coverage for phase IV has been reported as $\theta_{Sn} = 0.70$ML [75] and $\theta_{Sn} = 0.625$ ML [68] [73].

Fourier transforms of the STM images are in excellent agreement with a p($2\sqrt{2}\times 2\sqrt{2}$)R45° structure. It is generally accepted for metals that the maxima observed in the STM images correspond effectively to the atomic positions [83]. Accepting this assumption it is possible to evaluate the two different models [68] [73] [75] proposed

for this structure by comparing the position of the maximum intensity in the STM images with the Sn atom positions in the models. Best agreement was reached with the surface alloy model of McLoughlin [15], because the maximum intensity coincide with the Sn atom positions in the model and it accounts for the square dark holes noted in the STM images.

The McLoughlin surface alloy model [15] was altered to reflect the bridge site adsorption of the Sn atoms concluded from the NIXSW analysis, resulting in the new phase IV model, figure 3.36. This new model has an optimum coverage for phase IV of $\theta_{Sn} = 0.625$ ML, with 5 Sn atoms per 8 Cu atoms in the unit cell. Four of the Sn atoms occupy the first layer and are positioned at the bridge site in each unit cell. A single Sn atom occupies a second layer and is positioned between neighbouring Sn atoms of the first layer.

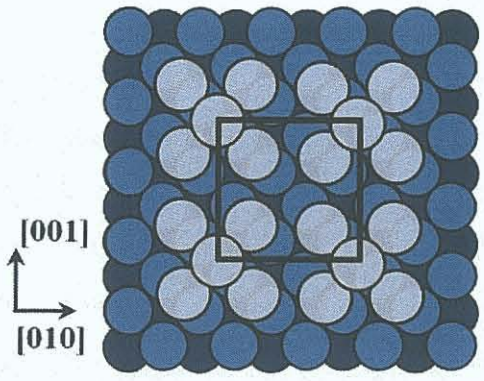

Figure 3.36: Proposed phase IV model, unit cell outlined in black, first Sn layer of atoms positioned at bridge site.

3.5 Discussion

From the results presented in the previous section the surface alloy formation of the four submonolayer phases I, II, IIH and III have been confirmed. From the NIXSW results, shown in table 3.7 for the first three phases I, II and III there is no change in the height of the Sn atoms above the (200) planes, and only a small compression towards the (111) plane which increases with increasing Sn coverage. The relatively high values for the coherent fraction for both the (111) and (200) planes is also noted. This meant the atop site and the bridge site are readily dismissed for phase I, II and III. The greatest changes in the NIXSW results are for phase IV where the heights above both planes and coherent fractions change significantly as shown in table 3.7.

Phase	Plane	E_{Bragg} eV	$f_{(hkl)}$	$p_{(hkl)}$	$d_{(hkl)}$ Å	ΔE eV
I	111	2966.6	0.76	0.13	0.27	0.56
	200	3424.3	0.74	0.22	0.38	0.72
II	111	2966.6	0.66	0.11	0.23	0.65
	200	3423.9	0.68	0.21	0.38	0.66
III	111	2966.5	0.73	0.09	0.19	0.73
	200	3424.2	0.77	0.21	0.38	0.76
IV	111	2966.51	0.65	0.13	0.27	0.58
	200	3424.06	0.48	0.25	0.45	0.69

Table 3.7: NIXSW coherent positions and coherent fractions for four Sn/Cu(100) phases.

The new STM and NIXSW results for phase I confirmed the surface alloy model proposed by McLoughlin et al. [75] and revealed a modulation and varying widths of the atoms within the Cu channels. New LEED analysis reveals glide plane symmetries in the phase II structure and in combination with STM results, a new model for the phase was proposed. The NIXSW results confirmed the different bonding environments of the Sn atoms as a result of the glide plane restrictions on Sn atom positions within the unit cell. The new submonolayer phase IIH was reported for the first time. LEED and STM results were used to propose a surface alloy model of the structure, and calculate the Sn coverage. Two different unit cells were suggested for the phase IIH structure. The surface alloy model of Pussi et al. [78] for the phase III reconstruction remains unaltered and gave excellent agreement with the new experimental results presented in this work, in regard to both the Sn rows compression and the surface corrugation. The growth of a second Sn layer and the dealloyed structure of phase IV have been confirmed with both STM and NIXSW results. The phase IV surface alloy model of McLoughlin [15] was altered to reflect the dealloyed Sn atoms positions in bridge sites between substrate copper atoms.

As a result of these investigations and the greater insight into the surface structures gained, the submonolayer phases may now be considered as candidates to act as templates to control the ordering of organic molecules.

Chapter 4

The adsorption of TMA on Cu(100) and Sn/Cu(100)

An initial experiment to ascertain the structures that are formed by the TMA molecules on the clean Cu(100) surface was conducted before TMA adsorption on the bimetallic Sn/Cu(100) surface was explored. The room temperature deposition of TMA on phase I of the Sn/Cu(100) surface alloy was investigated. The studies were conducted using the LEED, STM and TPD techniques. A comparison between the structures formed in the presence of Sn and those in its absence are presented.

4.1 Cu(100)-TMA

The structure of TMA on Cu(100) was investigated with STM by Dmitriev et al. [65]. It was found to form two different temperature dependent supermolecular assemblies. The two structures are shown in figure 2.19. The first is a low temperature (~200K) two-dimensional honeycomb motif, which evolves from extensive hydrogen bonding in a flat-lying formation. With increasing temperature this phase transforms into a second structure, a densely packed stripe structure that can also be formed by depositing the molecule at room temperature These stripes consist exclusively of an odd number of rows orientated along the [013] direction.

These structures are associated with a bonding transition leading to an upright geometry due to carboxylate formation with the copper substrate. The difference in height of the molecules within the rows as imaged by the STM is presumed to be related to different bonding configurations of the TMA molecules with the substrate, where bonding occurs through either one or two of the deprotonated carboxyl groups. The room temperature (300K) stripe phase is noted to have no

long-term stability. Over time it destabilises and eventually well-defined complexes are formed. No detail on the form of these complexes are given in the publication [65] but it was indicated that deprotonation of carboxyl groups occurs and the TMA molecules change their orientation with respect to the substrate to switch back to a flat-lying geometry forming metal-organic complexes with copper adatoms. Details of the complexes have not yet been published but the co-deposition of Fe atoms and TMA on a Cu(100) surface which creates thermally stable structures on the surface has [89].

In order to make a comparison between the structures formed in the presence of Sn and those in its absence the Cu(100)-TMA surface was investigated. The experimental results for these metal-organic complexes with copper adatoms are now presented.

4.1.1 LEED

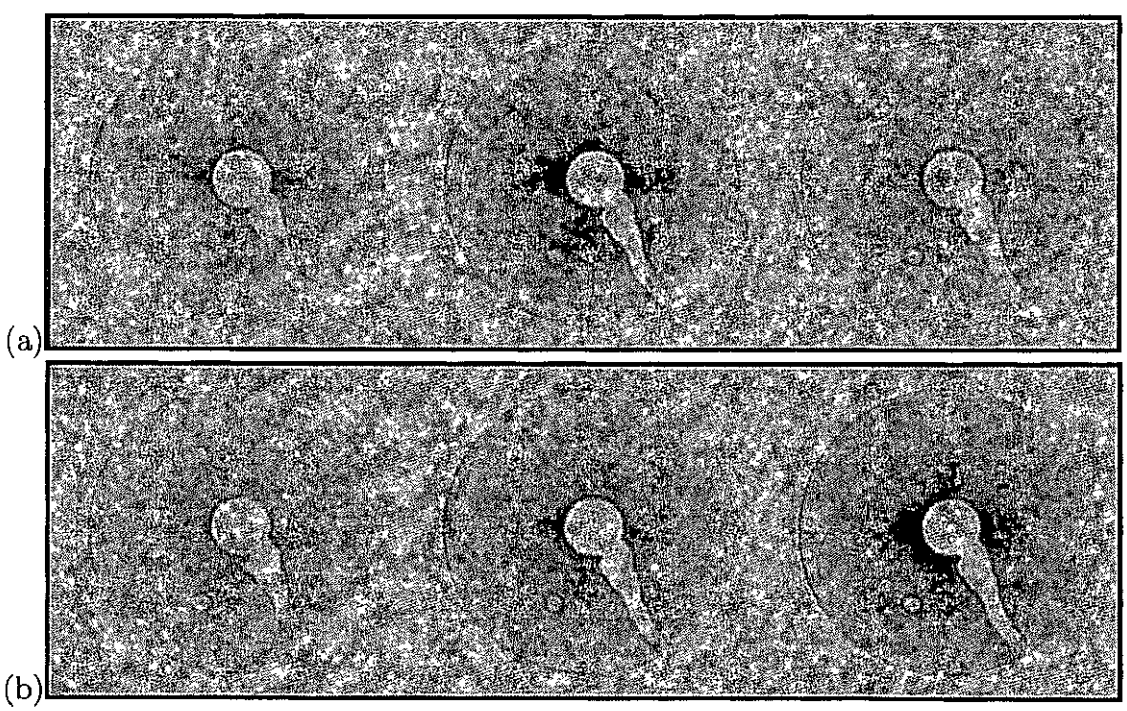

Figure 4.1: LEED diffraction patterns at a TMA coverage of 8.1 $\times 10^{-3}$L on Cu(100) taken at beam energies of (a) left to right 12, 18, 30 eV and (b) left to right 39, 46, 52 eV, respectively. The bulk Bragg spots p(1 $\times$ 1) are only visible at 46 and 52 eV.

The Cu(100) forms a simple p(1×1) diffraction pattern. The bulk Bragg spots only become visible on the screen for primary electron energies of 46 eV and above. Any diffraction spots present in the diffraction pattern below this beam energy can be attributed to a structured adsorbate layer. In the case of TMA adsorbed on

Cu(100), such additional Bragg spots are observed for incident electron energies as low as 12 eV. The diffraction pattern[1] produced by TMA structures formed at a monolayer coverage are clearly discernible in figure 4.1. The TMA structures produce both sharp and diffuse Bragg spots in the diffraction pattern.

The largest repeating unit for the structure was calculated by comparing the distance between the bulk Cu Bragg spots and the smallest distance between the shaper more distinct spots from the new TMA surface structure. Good agreement was made to a (10×10) double domain diffraction pattern, aligned along the high symmetry directions [011] and [01$\bar{1}$] of the bulk Cu. Two concentric diffuse boxes appear in the diffraction pattern, aligned with the Cu symmetry directions. The inner box is best resolved at 18 eV and the outer at 30 eV and correspond to the $^{5}/_{10}$ and $^{6}/_{10}$ Bragg spots of the (10×10) cell respectively. This diffuse intensity is usually attributed to small domain sizes [22] which agrees with the STM images.

4.1.2 STM

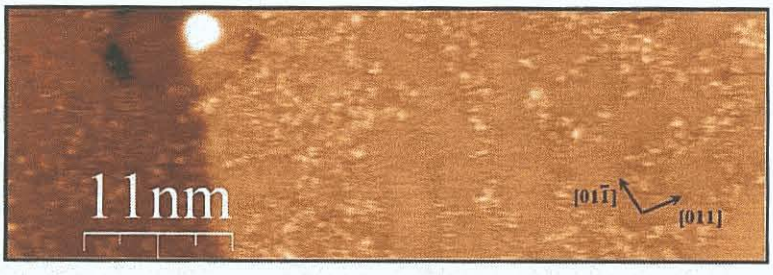

Figure 4.2: The TMA modulated row structure surrounded by disordered TMA molecules at a coverage of 8.1×10^{-3}L. $V_s = -0.75$ V, $I_t = 0.5$ nA, 54.7 × 18.3 nm.

After the room temperature deposition of TMA on the Cu(100) crystal, the molecules change from the stripe formation described above [65] into a new structure previously unreported. During this transition the STM images a disordered surface and no resolution is attained until the new structure has formed as shown in figure 4.2. The structure consists of short segmented rows along the [011] direction and long modulated rows along the [01$\bar{1}$] direction. Two domains orientated at 90° relative to one another are visible in the image. Disordered TMA molecules are imaged in the areas surrounding these segmented rows. There is a 0.50 ± 0.04 nm separation lengthwise between the rows, i.e. two lattice spacings of the clean Cu(100)-(1 × 1) termination. These rough row edges make it difficult to attribute a specific width to the stripes however, by taking multiple measurements across the rows an average

[1]Contrast was altered to enhance images.

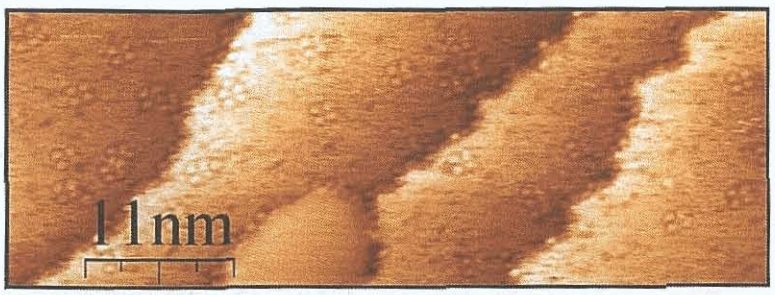

Figure 4.3: STM image of the TMA quad structure which always aligns with the substrate along the [011] and [01$\bar{1}$] directions, $V_s = 1.0$ V, $I_t = 0.5$ nA, 54.8 × 20.2 nm.

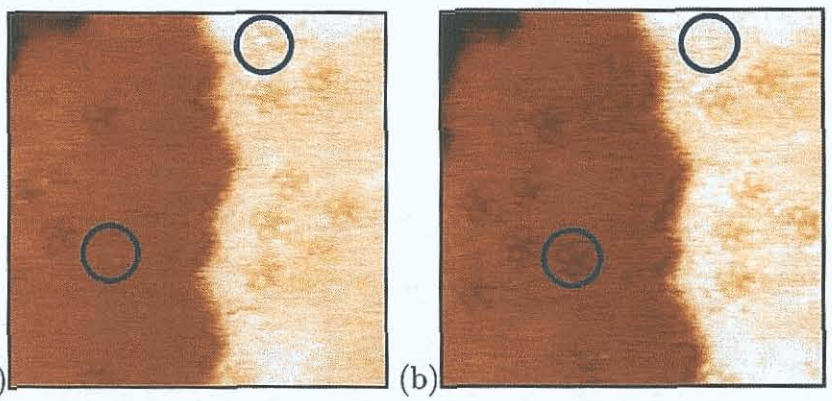

Figure 4.4: STM images (a) and (b) are taken four mins apart, the circles highlight a quad which destabilised and a new quad which formed during that time frame, $V_s = -0.085$ V, $I_t = 0.12$ nA, 22 nm^2.

width of 2.69 ± 0.4 nm was determined. The 0.5 ± 0.04 nm and 2.69 ± 0.4 nm measurements suggest a unit cell within the range (2×9) to (2×12) for the TMA structure.

The modulated row structure shown in figure 4.2 is short lived and within one hour of having formed it has completely destabilised. The molecules reorganise by exploiting metal-ligand coordinated interactions. Cu-carboxylate compounds with four molecular ligands are coordinated in a planar fashion by the central metal adatom. They are best described as a four-member "flower" structure or quad structure, figure 4.3, where four TMA molecules are attached to a central Cu adatom. In these structures the molecules are always aligned with the substrate along the [011] and [01$\bar{1}$] directions. They exhibit a rectangular shape, of dimensions 1.59 ± 0.05 nm by 2.09 ± 0.1 nm, which is partially attributed to drift in the image. The molecules are also seen to decorate the step edges forming non-uniform unstable groups.

The instability of the quad structures at room temperature is illustrated in figure

4.4. New quads form and others disperse on the surface during the four minute time frame between the two consecutive STM images. Two changes are highlighted by the coloured circles. Eventually the only detectable presence of TMA on the surface is at the step edges.

4.2 TMA on Sn/Cu sub-monolayer phases

4.2.1 LEED

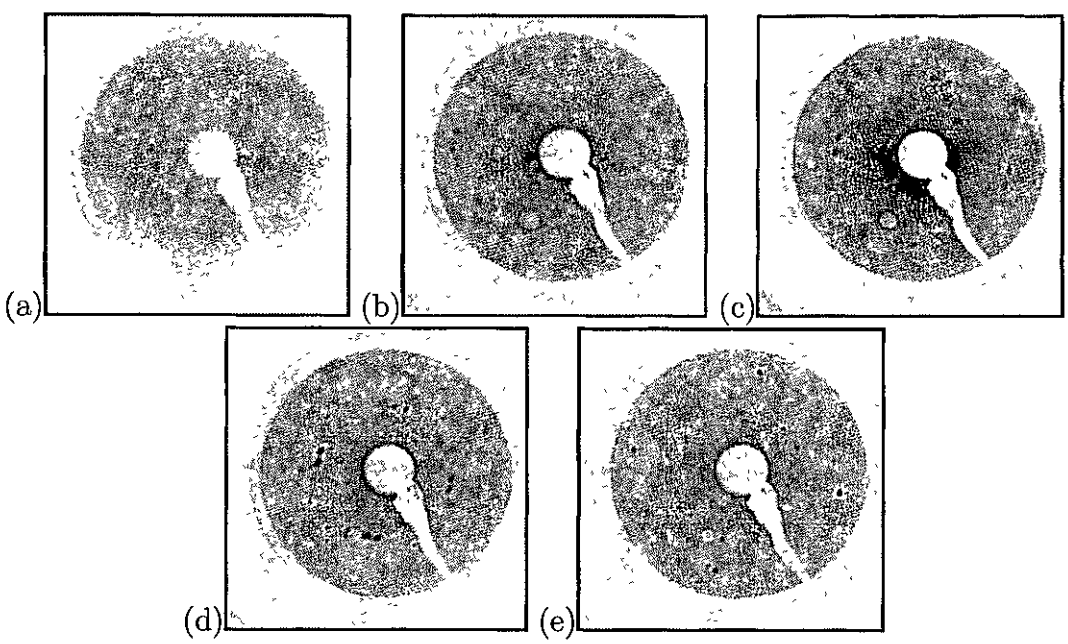

Figure 4.5: LEED diffraction patterns taken at (a) 10 eV, (b) 15 eV, (c) 23 eV, (d) 36 eV and (e) 60 eV at a TMA coverage of 8.1×10^{-3}L on the Sn/Cu(100) phase I surface.

The LEED diffraction pattern for the Sn/Cu(100) phase I structure was discussed in detail in section 3.4.1. As previously noted no Bragg spots are observed within the ($^1/_2$,0) and equivalent beam positions in the phase I diffraction pattern. Figure 4.5(a)-(e) shows the diffraction pattern[2] for TMA deposited on Sn/Cu(100) phase I which were recorded at the following beam energies; 10, 15, 23, 36, and 60 eV. The adsorption of TMA on phase I creates two new features in the LEED pattern; (i) two diffuse rings about the (0,0) origin and (ii) the appearance of additional spots associated with the phase II structure within the phase I diffraction pattern. The diffuse rings were affected by high beam energies and began fade if exposed to beam energies above 70 eV.

[2]Contrast was altered to enhance images.

The reciprocal space distance between the $(\pm^1/_2, 0)$ beams equates to the 0.255 nm lattice spacing of the substrate Cn atoms. Using this relationship the radius of the rings created by the TMA structure equates to lengths of 0.76 $\pm$ 0.03 nm and 1.39 $\pm$ 0.03 nm respectively.

The TMA induced a repeatable change from a clean phase I diffraction pattern to the appearance of phase II Bragg spots within the diffraction pattern. No post-deposition anneal was required for the additional Bragg spots to appear. The only conclusion is that TMA modifies the surface and in doing so assists in the formation of the phase II structure.

Subsequent annealing of the TMA modified sample up to 450K removes the double ring diffraction pattern completely with an accompanying reduction in the background intensity. These changes are associated with the removal of the TMA molecules from the surface. However it is noted that the TMA induced phase II Bragg spots remain.

4.2.2 STM

A low coverage of TMA on the Sn/Cu phase I structure results in the formation of phase II p(2×6) domains on the surface as seen in figure 4.6. The expected disordered adsorption of molecules at defect sites and step edges where Sn coverage is usually lowest, is noted. The TMA molecules are clearly visible as bright protrusions along the double rows within the induced phase II p(2×6) domains. The phase II structure appears to have been stabilised by the adsorption of the molecules as each of the rows begin and end with a TMA molecule. This is also evident at the border between the phase I and TMA induced phase II domains. This change in phase observed in the STM images is in agreement with the observed changes in the diffraction patterns.

For high flux TMA depositions, two structures were observed to form on the phase I Sn/Cu surface, figure 4.7(a). The first is a modulated row structure which is shown as an insert in the same figure. This structure is very similar to a modulated row TMA structure previously observed on the clean Cu(100) substrate, section 4.1.2. The second structure, imaged on the right hand side of the STM image shown in figure 4.7(a), shares many similarities with the cyclic hexamer motif present in the crystal structure of the α-polymorph of TMA [59].

The modulated row structure on the Sn/Cu(100) surface shares the same molecular spacing perpendicular to the width of the rows as the similar structure on the Cu(100)-TMA surface. A spacing of 0.505 $\pm$ 0.003 nm along the rows is calculated

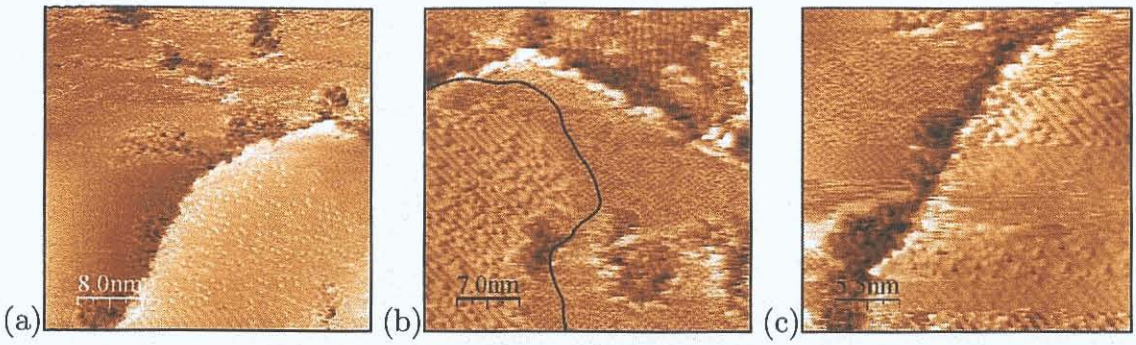

Figure 4.6: STM images of the Sn/Cu(100) phase I surface after a low TMA deposition of 8.1 $\times 10^{-9}$ L, $V_s = -1.6$ V, $I_t = 0.8$ nA, (a) 40 nm^2, (b) 35 nm^2 and (c) 27.5 nm^2.

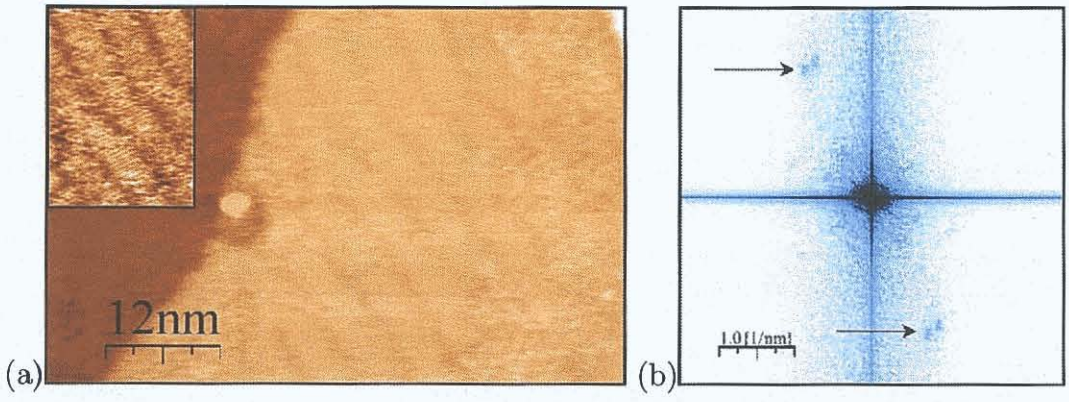

Figure 4.7: STM image (a) is of the Sn/Cu(100) phase I surface after TMA deposition of 8.1 $\times 10^{-3}$ L, $V_s = 0.6$ V, $I_t = 1.0$ nA, 60 $\times$ 39 nm and insert of 17.6 $\times$ 18.2 nm. Row structure aligned along the [011] and [01$\bar{1}$]. (b) Fourier transform exhibits spot splitting as indicated.

from the Fourier transform of the STM image. These similar structures formed on the different substrates are both double domain and aligned along the [011], [01$\bar{1}$] directions of the Cu surface. The only different noted between the two structures is that disordered TMA molecules are imaged in the gaps between the modulated rows on the clean Cu surface. These cleaner row edges make it easier to calculate the average width. Spot splitting is observed in the Fourier transform of the STM image, figure 4.7(b) as indicated. The width of this splitting can be attributed to the width of the molecular rows in the same manner that regular steps on a surface cause splitting of the Bragg spots [22]. The measured splitting of the spots equates to an average row width of 5.58 $\pm$ 0.05 nm.

The second structure present on the surface is a cyclic hexamer arrangement made up of six characteristically triangular shaped flat lying TMA molecules [90]. These structures are observed to form at step edges and to grow out across the

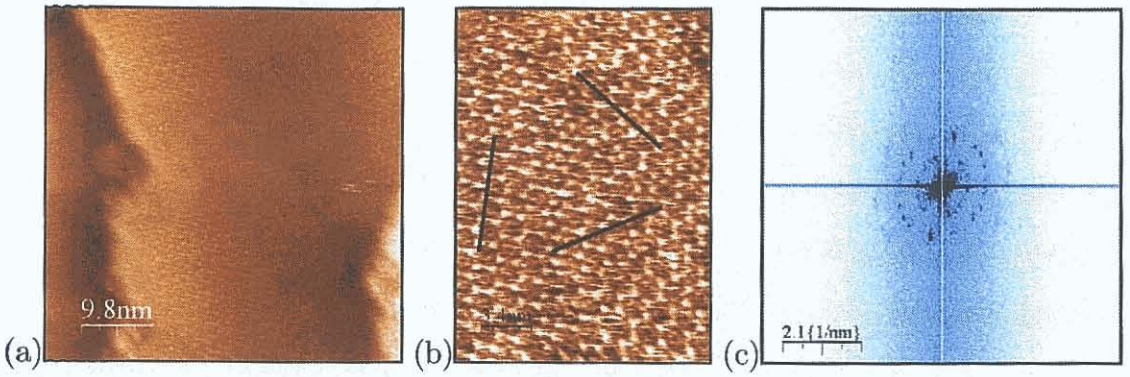

Figure 4.8: STM images of the cyclic hexamer arrangements (a) and (b)enlarged section which contains three different domains. V_s = 1.3 V, I_t = 0.3 nA, (a)49 nm^2,(b) 17 × 24 nm. (c) Fourier transform after a TMA deposition of 0.71 L.

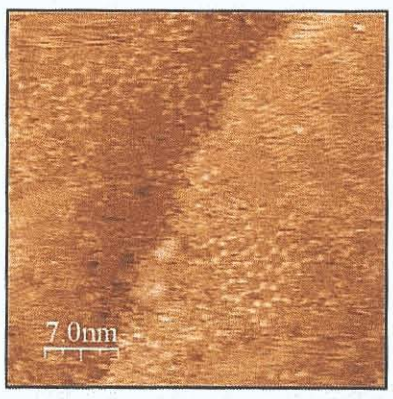

Figure 4.9: STM image of Sn/Cu phase I surface after a TMA deposition of 0.71 LV_s = 1.3 V, I_t = 1.0 nA, 35 nm^2.

surface, figure 4.8(a) and (b). Large areas of the surface can be covered with this hydrogen bonded hexamer structure. TMA molecules, imaged in the areas between the cyclic hexamer domains, coalesce at the domain edges. The enlarged area, figure 4.8(b), shows the boundary between three different domains. Black lines are overlaid on the image to show angles of 60° between the domains.

The Fourier transforms of the STM image exhibits a double ring pattern, figure 4.8(c), which is similar to that noted in the LEED, figure 4.5(a). Each ring consists of 12 spots of higher intensity. The Fourier transform of single domain STM images confirm the spots in the rings are formed by the existence of six rotated domains. There are two periodicities present in the cyclic hexamer structure, 1.38 ± 0.07 nm resulting in the inner ring and 0.76 ± 0.05 nm resulting in the outer ring. Neither the modulated row nor the cyclic hexamer structures are stable at room temperature, and over time they destabilise with fragments of both structures co-existing as shown in figure 4.9.

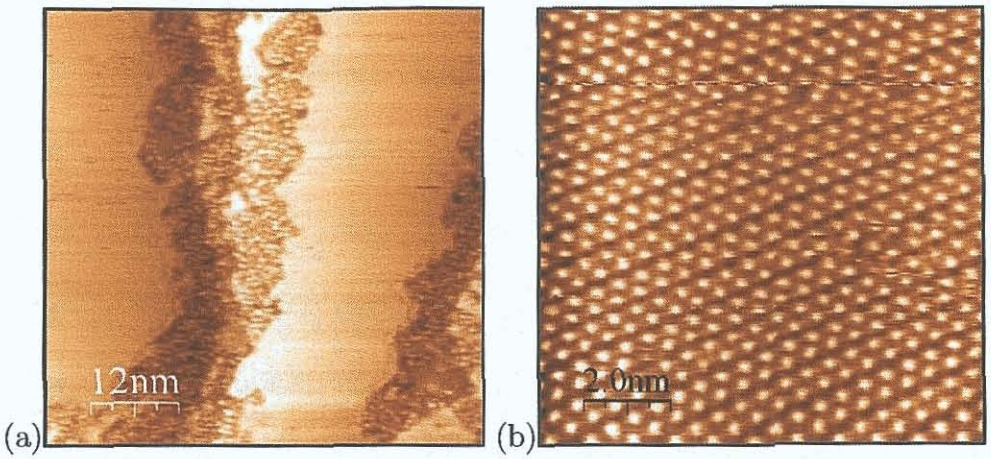

Figure 4.10: STM images of (a) TMA step decoration with p(2×6) terraces induced by TMA, $V_s = 1.6$ V, $I_t = 0.2$ nA, 60.2 nm^2 and (b) smaller area of the same p(2×6) terrace, $V_s = -2.0$ V, $I_t = 40$ nA, 10 nm^2.

After more than five hours of continuous STM monitoring the cyclic hexamer and modulated row structures are replaced by surface terraces exhibiting a well ordered phase II structure and disordered decoration along the step edges figure 4.10(a) and (b). The bright spots decorating the step edges have been attributed to the molecules due to their size (0.65 ± 0.05 nm). They have no discernable ordering but the domain edges appear to roughly align with the ⟨011⟩ directions.

Figure 4.10(b) is an STM image taken of one of the terraces shown in figure 4.10(a) and verifies the phase II structure. These images suggest that Sn atoms have migrated from the now disordered step edges and have helped to stabilise the phase II structure observed on the terraces. Sn atom vacancies are noted within the rows of the TMA induced phase II structure. These are attributed to sites where TMA molecules bonded to the surface Cu atoms, as revealed in figures 4.6(a), (b) and (c).

As regards TMA depositions on all other Sn/Cu(100) phases no evidence for TMA absorption has been imaged with the STM, apart from occasional disordered TMA molecules at defect sites recorded for phase II. No additional Bragg spots are noted in the LEED diffraction patterns, for TMA adsorption on either phase II or III, with only a slight increase in the background intensity. The TPD results for TMA deposited on Sn/Cu(100) submonolayer phases are in good agreement with these observations.

4.2.3 TPD

Figure 4.11 shows the mass spectrum of trimesic acid. The TMA molecule has a mass of 210 amu, the strongest peak in the spectra is observed at 196 amu. Additional peaks are produced at the following masses 164, 158, 120, 105, 91, 77, 65, 51, 44 and 38 amu. Unfortunately the QMS used in this experiment was not sensitive enough to record masses above 120, so this work will concentrate on species with m/z ratios from 77 amu up to the double ionization of TMA^{++} at 105 amu.

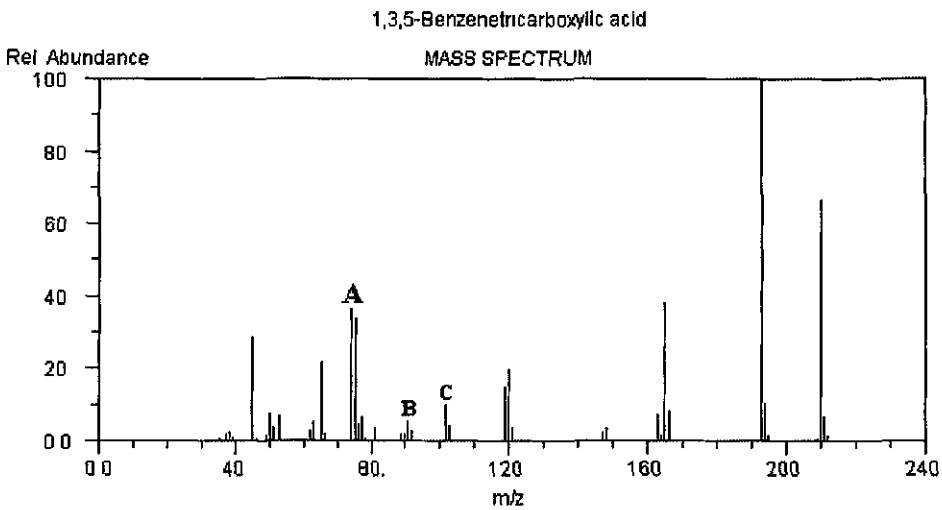

Figure 4.11: The peaks in the mass spectrum [91] of trimesic acid is shown, this is also known as the cracking pattern. The heights are made relative to the base peak of mass 196 which is given the nominal value of 100, all others are listed by their relative abundance. A, B and C were used in this study.

The decomposition of TMA, $C_6H_3(COOH)_3$ on Cu(100) is investigated by monitoring the 105, 91 and 77 amu channels as the sample temperature is ramped from room temperature. The CO_2 peak at 44 amu which is present in any UHV system was considered too close to the carboxyl end-group COOH at 45 amu to be useful in the study.

Figure 4.12(a) shows the background signal from the clean Cu(100) when the sample is brought up to a temperature of 600K. There is no significant increase in the partial pressures over this temperature range. This means any increase in the partial pressure can be attributed to the TMA molecules desorbing from the sample. When TMA desorbs from the clean copper surface, figure 4.12(b), two broad desorption peaks are observed at 400K and 570K.

Various Sn coverages were investigated using TPD following the room temperature deposition on the clean copper surface of 1L of $C_6H_3(COOH)_3$. Figure 4.13 (c),

(d) and (e) indicate the temperature programmed desorption spectra at 77, 91 and 105 amu for phases I-III. In the case of phase I (c), a small increase in the partial pressure on the trimesic acid channels are observed as broad molecular desorption peaks which begin to rise as soon as the temperature starts to increase. The initial peaks at 350K and the second broad desorption peaks at 550K are observed. For phases II(d) and III(e), no TMA desorption peaks were detected at 550K. The same small peaks at ~350K, as in the phase I spectra, appear as the temperature is ramped.

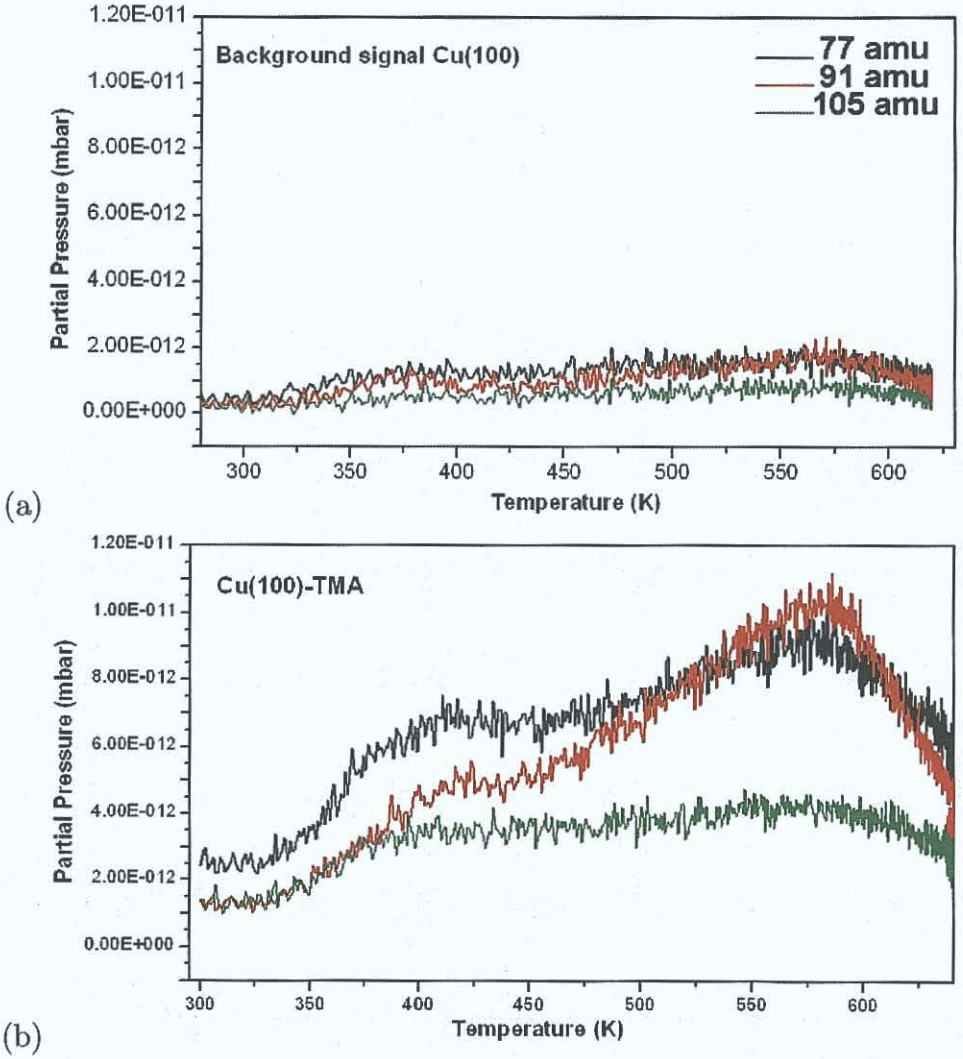

Figure 4.12: The temperature programmed desorption spectra for the (a) clean Cu(100) and (b) the Cu(100)-TMA surface. Desorption spectra at 77, 91 and 105 amu are shown.

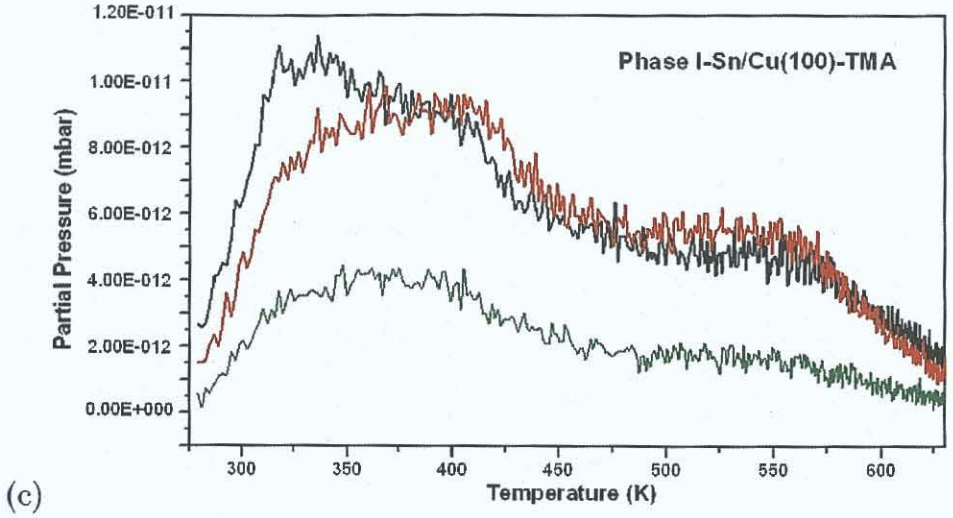

(c)

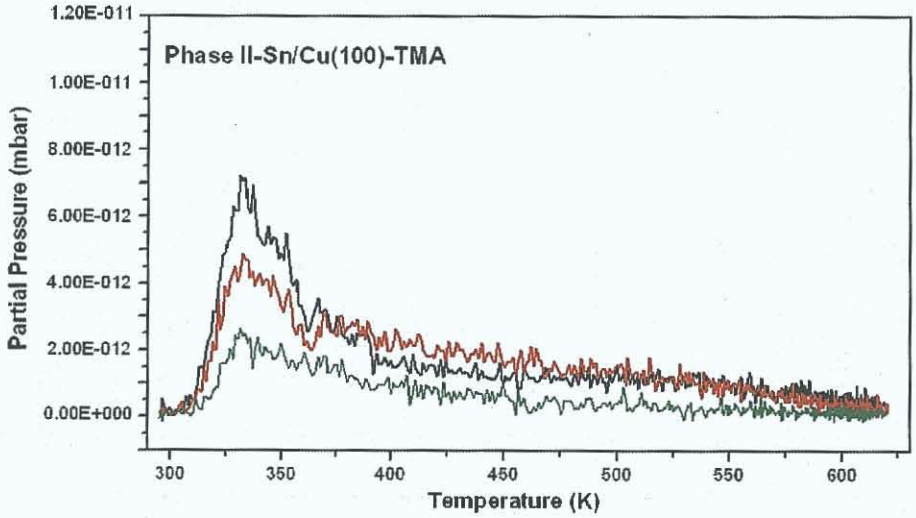

(d)

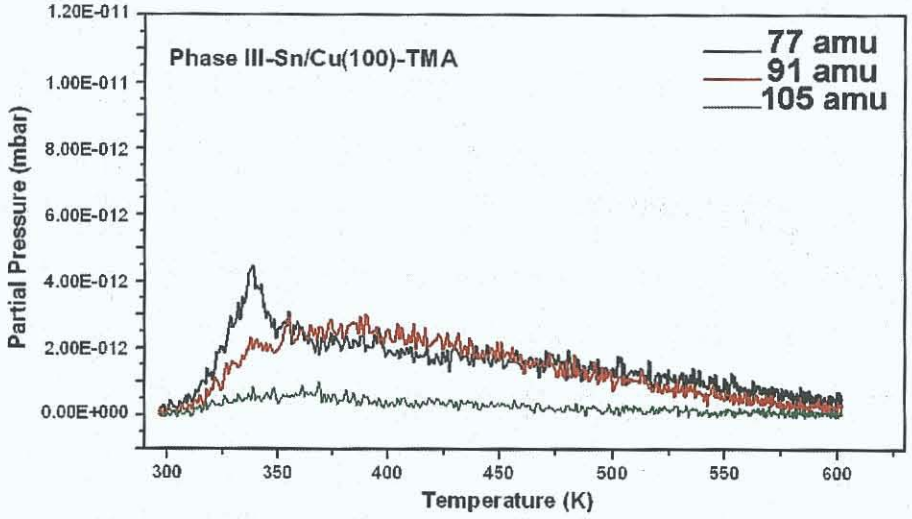

(e)

Figure 4.13: The temperature programmed desorption spectra for the (c) phases I (d) phase II and (e) phase III, Sn/Cu(100)-TMA surfaces. Desorption spectra at 77, 91 and 105 amu are shown in each case.

4.3 Discussion

4.3.1 Cu(100)-TMA

All TMA structures formed on the Cu(100) surface are unstable at room temperature including the new TMA row structure observed here for the first time. It is not unique however and the literature confirms that formic acid and PTCDA are two other molecules known to form similar structures on Cu substrates [92] [93]. Formic acid, the simplest carboxylic acid, forms a similar modulated row structure when adsorbed on Cu(110) surface at room temperature [92]. The structure consists of highly segmented domains containing short rows running along the $[1\bar{1}0]$ direction with a separation between the rows, in the [001] direction, of ~0.7 nm (i.e. two lattice spacings of the clean Cu(110)-(1×1) termination). The ragged edge of the domains observed for TMA on Cu(100) in this research was also present for formic acid, with a mean length of the rows in the $[1\bar{1}0]$ direction of 3.4 nm.

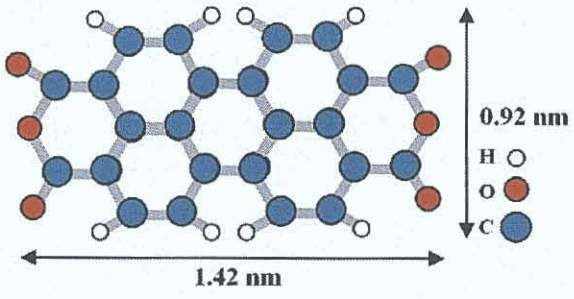

Figure 4.14: Ball and stick diagram of perylenetetracarboxylic-dianhydride (PTCDA).

The row structure of PTCDA ($C_{24}H_8O_6$) [93] [94] is observed when adsorbed on Cu(100). This is a large planar molecule of 0.92 nm by 1.42 nm, which interacts with the Cu substrate through four carbonyl end-group at either end of the planar molecule, see figure 4.14. The spacing between the rows is 0.51 nm and the rows have an average width of 1.5 nm. No LEED data was available for the PTCDA (2×1) structure and the substrate was unresolved in the STM so the direction of the rows with respect to the Cu substrate is unknown. The structure was attributed to a (2×1) with respect to the molecules dimensions.

In order to identify the bonding site of the TMA molecule on the Cu(100) surface, previous studies of the interaction of carboxylate species with Cu(100) surface were considered. The molecules were found to orientate with their planes parallel to the (011) and $(0\bar{1}1)$ planes of the Cu crystal [95]. The bridge site was identified as the most plausible adsorption site in a number of angle-scanned photoelectron

diffraction studies [95] [96] [97] [98] [99]. Density functional theory [95] [100] agree with these results confirming it to be the most stable site for chemisorption of the molecules. Based on all the results discussed, from the literature and the experiments presented in this thesis, one can confirm the interaction with the Cu substrate is through one or more of the oxygen atoms. It is also noted that the dimensions of the reconstruction of the Cu surface appear to control the modulation along the rows within the structure, which are found to be approximately 0.7 nm on the Cu(110) surface and 0.5 nm on the Cu(100) surface. This is in agreement with the spacings of the clean Cu(110) or Cu(100)-(1×1) termination respectively.

There is some evidence that the width of the molecule affects the width of the rows in the (2×1) phase of the Cu(100)-PTCDA. However for TMA and formic acid there is no correlation between the width of the rows and the size of the molecule. Also no direct correlation between the width of the rows and Cu substrate can be made. It was proposed by Poulston et al. [92] that the finite row width evident for formic acid on Cu(110) is due to a build up of repulsive intermolecular interactions. They suggest that these interactions make the addition of another formate to the row unfavourable and results in a domain boundary.

The STM results for the Cu(100)-TMA surface suggest a (2×9) to (2×12) structure which support this theory of repulsive intermolecular interactions. The LEED however reveals a (10×10) diffraction pattern. These two different results can be reconciled by considering an alternative explanation. The (10×10) diffraction pattern could be a collection of smaller (2×2), (2×4), (2×6), (2×8) and (2×10) structures. These different structures would be distributed over the entire sample. The resulting intensities of the Bragg spots would then depend on two conditions: (i) the proportion of each different domain present and (ii) if and by how much the Bragg spots from different diffraction patterns coincide. This is because the smaller the domains the more diffuse the Bragg spots appears, so coinciding Bragg spots from different structures would have a greater intensity than the other Bragg spots. The collection of (2×n), where $n < 10$ and even, domains would result in the same diffuse intensity of the Bragg spots as noted in the LEED diffraction pattern and the coinciding spots would explain the higher intensity of the $^{5}/_{10}$ and $^{6}/_{10}$ and equivalent beams.

In light of these results, TMA molecules interact with the Cu substrate through one or more of its carboxyl end-groups. This means the plane of the molecule must be orientated either perpendicular or at a tilt relative to the substrate. The model in figure 4.15 is a schematic of the bonding arrangement for TMA on the Cu(100) surface considering a single ligand bond. The plane of the molecule is aligned along the $[0\bar{1}1]$ direction and is normal to the substrate. The modulated rows formed

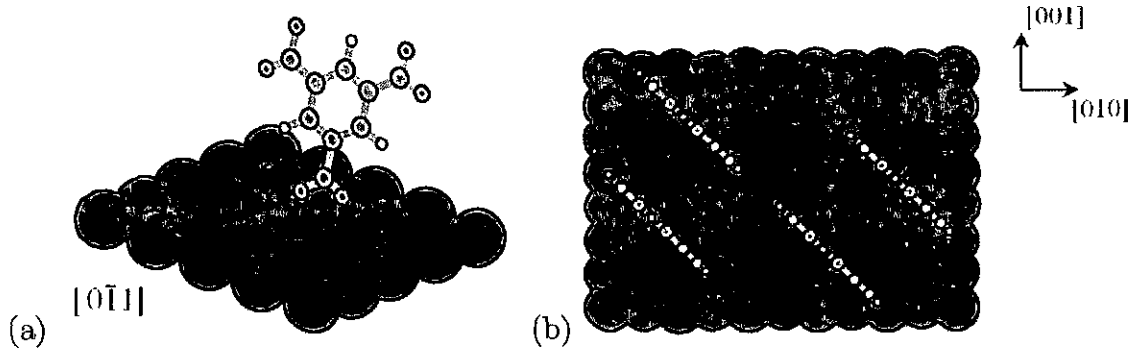

Figure 4.15: Schematic model for the bonding of TMA to the Cu(100) surface. (a) A single TMA molecule and (b) illustrates the intermolecular spacing of 0.5 nm in the [0$\bar{1}$1] direction.

by the Cu(100)-TMA eventually destabilise at room temperature and this allows TMA molecules with deprotonated carboxylate groups the freedom to move across the surface. The new quad structure is then formed between the ligands from the deprotonated carboxylate groups of four TMA molecules and a Cu adatom.

Similar quad structures are formed by Fe coordinated TMA molecules on the Cu(100) surface. The chirality in the bonding of the carboxyl ligands to the central Fe atom is explained by a unidente bond [89], this chirality is not observed in the present study with Cu adatoms. The distance between the two oxygen atoms in each of the carboxyl group is 2.2 Å. The difference in the atomic radius of the Fe (1.24 Å) and Cu (1.275 Å) [87] is not large enough to account for a bidente bond of the two oxygen atoms to a single Cu adatom and so does not explain the lack of chirality or the instability of the quad structure. It does mean however, that the bond between the ligands and the Cu atom will be unidente. A unidente Cu-carboxylate bond would require one of the oxygen atoms of the carboxylate group involved in the bonding to come significantly closer to the central Cu atom than the other. Assuming a unidente bond, and considering the rectangular shape of the quads, this suggests the carboxylate group twists with respect to the phenyl ring bonding to the Cu adatom through an oxygen atom, as illustrated in figure 4.16.

The bond strengths of the gaseous diatomic species at room temperature of FeO and CuO are equal to 390.4 $\pm$ 17.2 kJ mol^{-1} and 269.0 $\pm$ 20.9 kJ mol^{-1} respectively [101]. The strongest bond for a diatomic species is that of carbon monoxide, CO (1076.5 $\pm$ 0.4 kJ mol^{-1}). Examining these bond enthalpies shows a much stronger bond is formed between Fe and O. This helps to explain the instability at room temperature and the lack of observed chirality in the Cu-carboxylate coordinated structures.

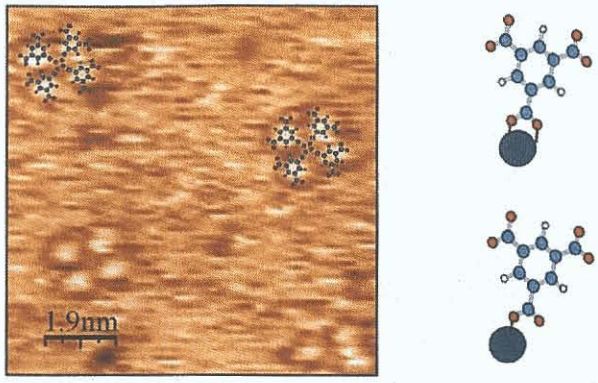

Figure 4.16: Schematic unidente bonding model of the quad structure (central Cu adatom not shown), overlayed on an STM image. Schematics of a bidente and unidente bond between a single Cu atom and TMA carboxyl end-group also shown.

4.3.2 Sn/Cu(100)-TMA

The importance of understanding surface reactivity in modern industrial catalysis has fuelled many publications in the area of reactions on Cu crystals. In the literature TPD studies concentrate on small molecules to probe surface reactivity. Formic acid (HCOOH) and carbon monoxide (CO) are the two simplest molecules most commonly used. Papers discussing the reactions of formic acid on single crystal metallic surfaces are abundant because of the molecules simple structure and the simplicity of the intermediates and products involved [102] [103].

No reference to TPD studies of trimesic acid was found in an extensive survey of the literature. The three identical (COOH) groups of TMA, expected to interact with the Cu{100} surface, have the same composition as the simplest carboxyl acid, formic acid (HCOOH). This means a limited comparison between the two molecules can be made. Bearing this in mind it is worth reviewing the available literature for formic acid reactions with single crystal Cu surfaces.

Formic acid adsorption on copper is of major chemical interest [104] because the formate intermediate has been shown to be the most stable species involved in the synthesis of methanol. Formic acid forms a strong stable bidentate formate intermediate on the copper which is easily formed from formic acid by cleavage of the O-H bond. It has been studied by different experimental techniques on Cu(100) [97] [105] [106] [107] [108] [109] [110].

Structural studies by means of photoelectron diffraction (PhD) and near-edge X-ray absorption fine structure (NEXAFS) found that formate species are adsorbed in a geometry with of the two oxygen atoms of the formate bridging two nearest

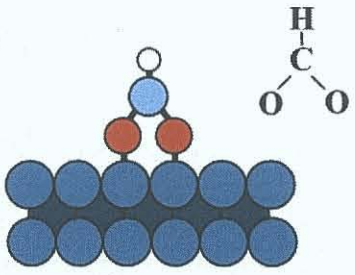

Figure 4.17: Side view geometry of formic acid in a bidentate bond between the molecule and two copper surface atoms.

neighbour copper atoms, the bridge sites of the Cu(100) surface. The oxygen atoms occupy atop positions with a Cu-O nearest neighbour distance of 1.98 ± 0.04 Å [97], as shown in figure 4.17. These results were later confirmed by theoretical studies [111] [112] [113]. The formate is stable up to 400K, after which it decomposes to yield CO_2 and H_2.

$$HCOOH \rightarrow CO_2 + H_2 \tag{4.1}$$

A formate intermediate has been proposed [50] and the following reaction mechanism has been suggested to account for HCOOH decomposition on Cu{100}:

$$HCOOH(ad) \rightarrow HCOOH(ad) + H(ad) \tag{4.2}$$

$$2H(ad) \rightarrow H_2(g) \text{ (with a TPD peak at 275K)} \tag{4.3}$$

$$2HCOO(ad) \rightarrow 2CO_2(g) + H2(g)(\text{with a TPD peak at 475K}) \tag{4.4}$$

Bearing the results for formic acid in mind, if copper atoms exist in the top layer of a surface alloy, then the TMA should behave the same as on the clean copper crystal and a TMA desorption peak is expected near 450K. No evidence for the adsorption of formate on a pure tin substrate was found in the literature. For the Sn/Cu alloy structure however TPD results were presented by McLoughlin [15], these results indicated that for phases II-IV, no formate decomposition was detected, however in the case of phase I, a small CO_2 peak was observed close to the decomposition temperature of the formate intermediate on clean Cu{100}. This indicates that TMA desorption peaks would be expected to occur in the TPD spectra for Cu sites, but not for Sn-Sn sites or Sn-Cu sites. One would expect no adsorption peaks from any surface with a Sn coverage above that of phase I, where free copper atoms have

not been observed by STM.

These expectations are confirmed in the results shown in figures 4.12 and 4.13. For phase I the peaks at 350K are attributed to loosely bound molecules The second broad peaks observed at 550K which are above the decomposition temperature of the formate intermediate observed on Cu{100}, and is attributed to the decomposition of TMA on the surface. For phases II-IV, no TMA decomposition was detected at 550K. It is evident from these observations that the carboxylic end-groups do not bond to Sn-Sn bonds or Sn-Cu bonds.

The TMA induced phase change is clearly observed in the STM and LEED results. Two observations support the role of TMA in the induced reconstructions. Firstly the step decoration suggests the Sn atoms from the step edges have migrated into the terraces because the TMA molecule do not bond to Sn atoms. These additional Sn atoms create the population of Sn required to form the phase II structure, as observed in figure 4.6(b). Secondly TMA molecules are present at the start, end and even within the rows which form the initial domains of the phase II structure, as highlighted in figure 4.6(b). Evidence of their presence in later images is attributed to Sn vacancies are observed along the rows of the Sn/Cu(100)-TMA phase II structure which were not observed for the clean Sn/Cu(100) phase II structure.

The Sn modified phase I surface produced two different co-existing TMA structures, both of which are unstable at room temperature. The first is another modulated row structure and the second is a cyclic hexamer. The modulated rows exhibit an identical spacing of 0.5 nm along their length as observed on the Cu(100)-TMA surface (see model in figure 4.15). The absence of the characteristic (10×10) diffraction pattern in the LEED results for the modulated row structure is noted. This is explained by the intensity from the beams due to the Sn reconstruction dominating the weaker TMA induced beams, both of which are aligned with the Cu substrate. The second structure, the cyclic hexamer, is similar to the arrangement of the molecules on a number of different surfaces; the passivated Ag/Si(111) surface [90], the low temperature structure on clean Cu(100) [63], structures formed on the graphite surface [10] and to the motif observed within the bulk TMA crystal structure [59], all of which are discussed in chapter 2.5.2. This hydrogen bonded structure suggests it forms over areas where the Sn coverage has prevented the carboxylic end-groups from forming bonds to exposed substrate Cu atoms. The molecules will instead be forced to form hydrogen bonded structures to stabilise. LEED and STM results give direct evidence for these hydrogen bonded structures. The LEED diffraction pattern suggests repeating units of 0.76 ± 0.03 nm and 1.39

$\pm$ 0.03 nm, compared to the 0.76 $\pm$ 0.05 nm and 1.38 $\pm$ 0.07 nm from the STM results.

One can speculate that the TMA molecules bonding to Cu substrate atoms form the seeds for both these structures. When the molecules bond through one of the three end-groups to the free copper within the phase I structure, it implies an upright molecular orientation. The phenyl ring of the molecule is then free to stabilise additional molecules into the modulated row structure by π-bond stacking between the molecules. When molecules are bonded at a step edge the carboxylic end-groups parallel to the plane of the substrate and are free to form hydrogen bonds with neighbouring molecules, forming the cyclic hexamer structure. Both of these Sn/Cu(100)-TMA structures destabilise, as with the Cu(100)-TMA structures, at room temperature (after approximately 5 hours). Eventually the molecules decorating the step edges are the only obvious indication of the presence of TMA on the surface. All the terraces then exhibit the phase II structure and the rough alignment of the disordered domains of TMA molecules at the step edges with the $\langle 011 \rangle$ directions are attributed to the phase II domain boundary edges.

4.4 Conclusions

In the Cu(100)-TMA row structure the molecular interaction with the substrate controls the spacing along the rows between the molecules. In this case the molecular spacings are consistent with two lattice spacings of the clean Cu crystal termination of the substrate. This observation is noted for other planar molecular species independent of molecular weight or length. The Cu(100)-TMA quad structure formed between four TMA molecules and a Cu adatom is not unique and similar structures are formed between TMA molecules and Fe atoms adsorbed on the Cu(100) surface [89].

The TMA molecules have been observed with STM and LEED modifying the surface in four different ways; (i) they can induce the phase I structure to reconstruct into the phase II structure, (ii) they can form a modulated row structure as on the Cu(100)-TMA surface, (iii) they can form hydrogen bonded cyclic hexamers and finally (iv) they can bond to exposed copper atoms at the step edges.

Although the Sn atoms did affect the bonding sites available to the molecules on the surface and in doing so act as a template, their mobility on the surface meant the initial templated Cu channels failed to be preserved during the interaction with the TMA molecules.

Chapter 5

The interaction of pentacene with the Bi/Si(100) surface

The creation of bismuth induced reconstructions on the Si(100) surface is discussed, in particular the novel Bi nanolines and the (2×n) Bi passivated surface. The previously unreported cross step growth of the nanolines is examined using scanning tunnelling microscopy. The (2×n) Bi reconstruction is then investigated as a stable substrates on which to build ordered organic molecular layers. The results are discussed in light of the recent publication by Sadowski et al. [114] describing the exploitation of a Bi/Si(111) surface is as a template for the growth of pentacene molecules.

5.1 The Si(100) surface

Silicon is a group IV semiconductor. The bulk material has a diamond-lattice crystal structure: a face-centred cubic lattice with a two-member primitive unit cell, such that each silicon atom is tetrahedrally bonded to four neighbours. It has a bulk lattice constant of $a_B = 5.43$Å. Cleaving a bulk silicon crystal to expose a low-index surface such as the {100} creates a highly reactive surface where each surface atom has an unpaired electron. This is due to the geometry of the {100}-truncated diamond structure. The unpaired electron is in a localised orbital directed away from the surface which is referred to as a dangling bond and may act as either a donor or acceptor. Such surfaces react readily in atmosphere, producing a layer of native oxide. Under UHV conditions, this oxide can be thermally removed. A surface reconstruction then occurs in order to minimise the number of dangling bonds and

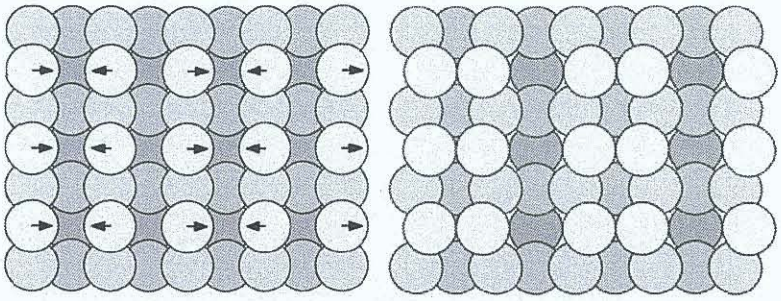

Figure 5.1: The dimerisation of the {100} truncated surface into the 2×1 surface reconstruction.

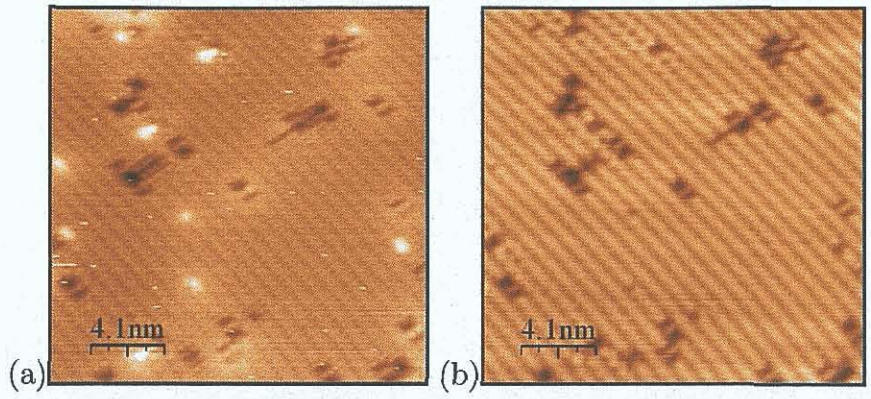

Figure 5.2: STM of the reactive Si (2×1) surface (a) filled and (b) empty states , $V_s = \pm 2.0$ V, $I_t = 0.05$ nA, 20.5 nm^2.

lower the surface free energy, figure 5.1. Neighbouring atoms dimerise by forming a σ-bond within each pair and the remaining two broken bonds move closer together forming a π-bond.

DFT energy calculations predict the lowest energy surface is make up of buckled dimers and predicts a c(2×4) reconstruction at room temperature [115]. The dimers appear symmetrical in the STM images taken at room temperature and form a (2×1) reconstruction, figure 5.2. The reason for this apparent disagreement was resolved with theory by Badziag et al. [116] and experiment by Wolkow [117] with low temperature STM measurements of the Si(100) surface. A change in the direction of buckling of the dimers occurs at a high oscillation rate ($\sim 10^{12}$ Hz [118]) at room temperature. The STM images the average position of these oscillating dimers which makes them appear symmetrical. At low temperature the dimers are frozen in place and the surface consists of virtually all buckled dimers arranged in c(4×2) domains.

The boron doped p-type silicon samples (0.05-0.1 Ωcm) used in these experiments were all prepared with an identical procedure. The sample and sample holder are degassed overnight in the preparation chamber at 723K by resistive heating. This

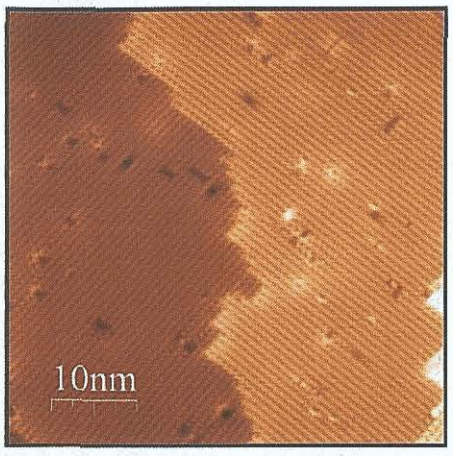

Figure 5.3: STM of double domain Si (2×1), $V_s = -1.5$ V, $I_t = 0.2$ nA, 50 nm^2.

is below the temperature required to remove the protective oxide layer. The sample is then transferred to the analysis chamber and flashed to ~1370K to remove the oxide layer. The temperature of the Si sample during flashing is monitored with an optical pyrometer (Ircon Ultimax: UX-20P). A series of flashes at this temperature is followed by a slow cool to room temperature (0.02 Watts/sec) to prepare a clean well-ordered (2×1) double domain reconstruction.

The Si(100) surface is notoriously difficult to clean due to the nature of the reactive surface and STM evidence of this is shown in figure 5.2. The filled and empty state images, are of the same sample area, and exhibit an average defect density. The zig-zag rows of buckled dimers in the upper half of the image are caused by pinning of the dimers by vacancies. Missing dimers resulting in surface vacancies can also be seen. Surface vacancies are also caused by nickel and therefore contact with stainless steel should be avoided [119]. For this reason molybdenum tools and sample holders with molybdenum and tantalum parts where used when preparing and mounting the silicon samples.

The reconstruction observed on the Si(100) surface consists of (2×1) and (1×2) domains each separated by a single atomic step, see figure 5.3. In the ideal case of a perfectly aligned crystal these steps would not exist, however even the smallest misorientation when the wafers are cut leads to step formation and a double domain structure.

5.2 Bismuth induced structures on Si(100)

The adsorption of group V elements on Si(100) has attracted much attention because of their technological importance in surface passivation [120], as a dopant in

semiconductors and for surfactant mediated epitaxy [121]. At bismuth coverages below a monolayer, several structures, which are all based on Bi dimers, have been reported; these include the (1×1) [122], the (2×1) and the (2×2) reconstructions [123]. Recently the Bi/Si(100) system has received particular attention due to two additional reconstructions: the Bi nanoline structure and the (2×n) reconstruction [124].

5.2.1 Bi nanolines

The Bi:Si(100) nanoline system is the focus of intense research as evident from a current review [125]. This system was discovered by serendipity [126] almost 10 years ago. The nanolines formed of Bi dimers, grow perfectly straight along the ⟨110⟩ directions on the Si(100) surface for hundreds of nanometres, apparently limited only by the terrace size of the substrate. They have a constant width, 1.5 nm or four Si substrate dimers, and are very stable. Below the desorption temperature of Bi they are stable against prolonged annealing and maintain the same width. The nanolines dimers induce a large reconstruction of the Si layers beneath them [126], which results in a perfect Si reconstruction either side of the Bi nanolines. Other Bi reconstructions do not produce this ordering. Besides being long, straight and defect-free, Bi nanolines are resistant to attack by atomic hydrogen, oxygen and ozone [127]. This chemical inertness and other characteristics are properties which are currently being exploited in the construction of novel nanostructures [14]. However they do not form nanowires, as the band gap of the Bi nanoline is larger than that of the surrounding silicon [126] [128].

The Bi nanolines are formed by competitive adsorption and evaporation. They can be formed by extended annealing of the Bi/Si(100)-(2×n) structure. During the course of this work this treatment of the surface was observed to lower the Si surface defect density. This can be explained in part by the relatively deep reconstruction of the Si surface under the nanoline [125] [129]. Alternatively, nanolines can be formed by depositing Bi onto the clean Si surface held at ~850K, not all the Bi evaporates and some of it remains on the surface to form the nanolines. The density of the nanolines increases with increasing deposition time and they form in perpendicular directions on neighbouring terraces. If the nanolines are annealed at ~850K for a further 30 minutes, one growth direction tends to dominate and a single-domain surface results [130], with nearly all of the Bi nanolines orientated the same direction. This Bi induced reconstruction of the top Si surface layer creates what are termed inlets and peninsulas along the silicon step edges as shown in figure 5.4.

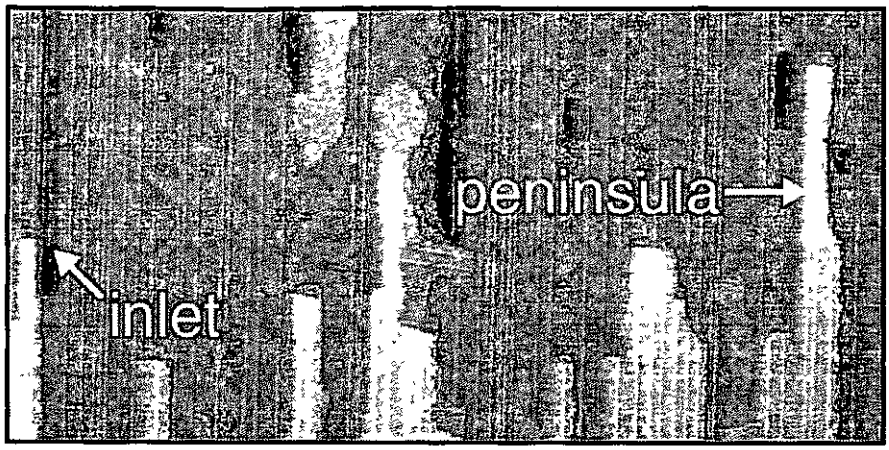

Figure 5.4: STM image of single domain surface created under the influences of bismuth nanolines, inlets and peninsula as indicated [131].

They allow the Bi nanolines to grow deep into neighbouring terraces, along the inlets into an upper terrace or along peninsulas over a lower terrace. This uneven distribution of domains is minimised by annealing the sample after the Bi deposition [130].

Seven nanolines are shown in consecutive variable voltage STM images in figure 5.5. Correlation between the images is made by comparing the defects in the silicon surface. In STM images (a), (c), (e) and (h) small notches (as indicated by arrows) in the Bi nanolines are observed, these correspond to missing Bi atoms within the structure. The nanolines have a strong bias voltage dependence, as evident in the STM images. For biases above $\pm$ 1.5 V_s the Bi nanolines appear bright compared to the surrounding Si(100), while for lower biases they image as dark trenches compared to the Si(100). This strong contrast is attributed to the low density of states near the Fermi energy [128].

To the best knowledge of the author [13] Bi nanolines have never before been observed to form across steps between different Si domains. In figure 5.6 two Bi nanolines were observed to form across a double Si step as indicated. Different bias voltages were applied to the sample to investigate the structures and confirm these findings were not the result of spurious tip effects. Consecutive STM images again display the bias voltage dependance of the Bi nanolines. A single nanoline is observed to form across a single Si step in the top right-hand corner of the STM images. Further investigation of these unusual structures was not undertaken in this work.

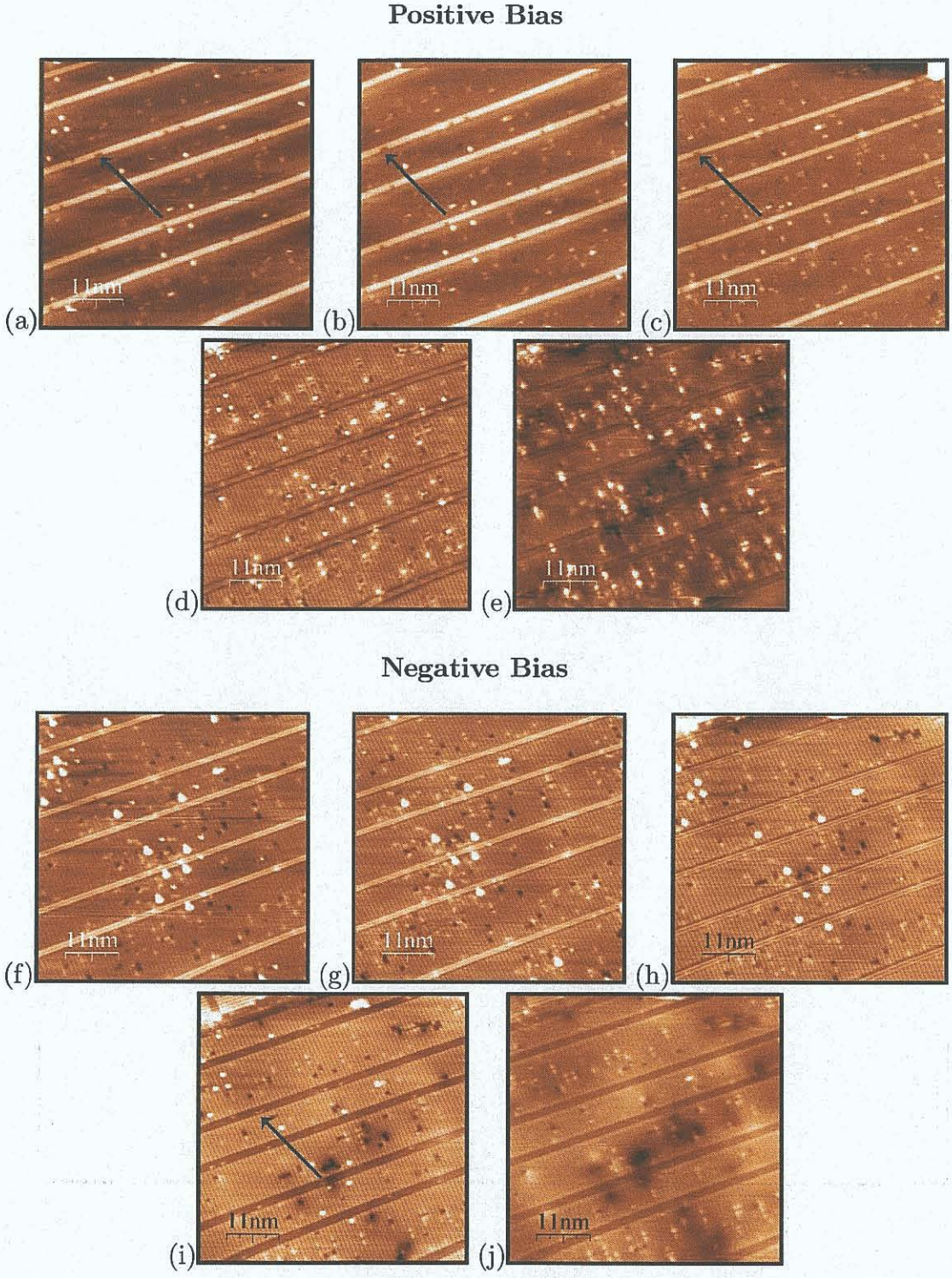

Figure 5.5: STM images of the Bi nanolines taken at different voltages and biases $I_t \approx 0.3$ nA, 60 nm^2, Positive bias (a) +2.5 V (b) +2 V (c) +1.5 V (d) +1 V (e) +0.5 V, and negative bias (f) -2.5 V (g) -2 V (h) -1.5 V (i) -1 V (j) -0.5 V. Green arrows indicate the same two missing bismuth atom site where visiable.

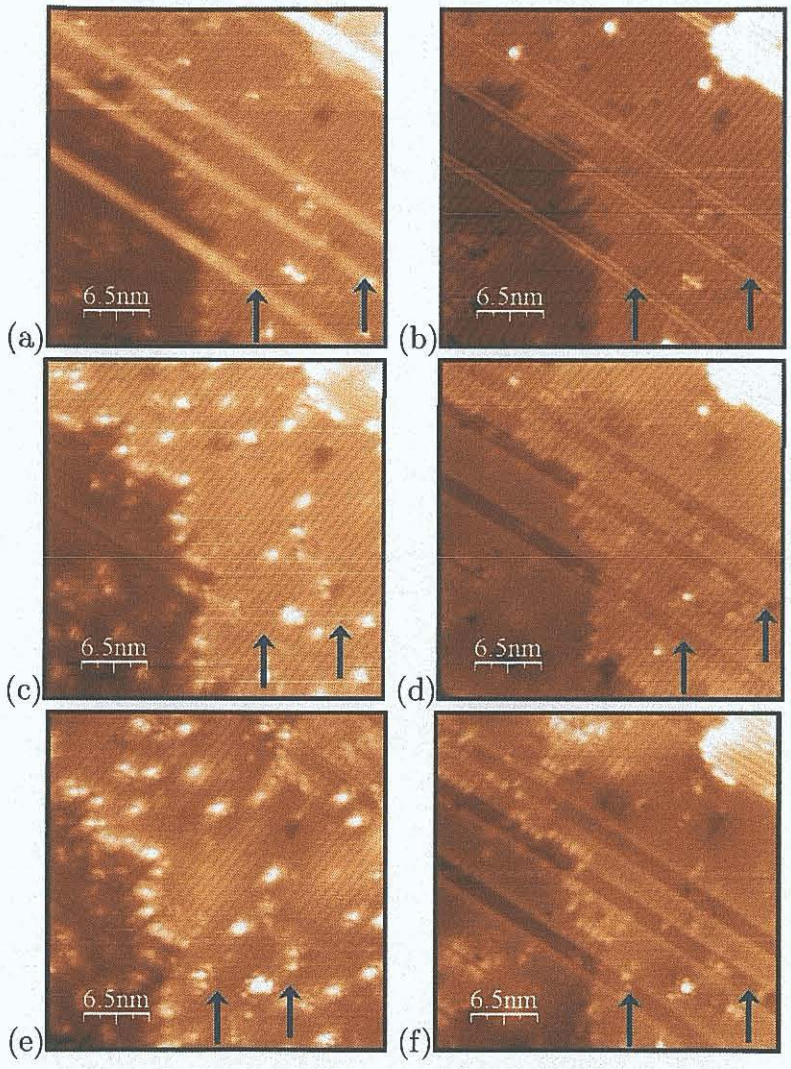

Figure 5.6: STM images of Bi nanolines crossing over single Si steps, recorded at different voltage biases, $I_t = 0.3$ nA, 33 nm^2 (a) +2 V (b) -2 V (c) +1.3 V (d) -1.3 V (e) +1 V (f) -1 V. Green arrows indicate Bi nanolines which form across double Si step.

5.2.2 The Bi/Si(100)-(2×n) reconstruction

The formation of bismuth reconstructions on the Si(100) surface is very sensitive to temperature. Deposition of a monolayer of Bi on a Si(100) surface held below the bismuth desorption temperature of ~770K forms a (2×n) surface structure [120] [132]. The (2×n) phase was first observed in a LEED diffraction pattern in 1981 [133] but not identified until 1990 [120] and later confirmed by STM [132].

The (2×n) structure is passivated, with no residual dangling bonds, as evident from the observed surface stability against O_2 [120]. The basic building block of this reconstruction is a single Bi dimer. It is formed when a Bi adatom bonds to the substrate by breaking a silicon dimer and then dimerises with a neighbouring bismuth atom [134]. Within the unit cell the 2× periodicity is a result of the orientation of the bismuth dimer formation and the n× periodicity is caused by the formation of dimer row vacancies [135] [136] [137]. LEED experiments revealed that the n periodicity, due to the vacancy rows, was dependent on both the Bi coverage and the annealing temperature [136]. The value of n ranges from 13 at temperatures around 400K down to 5 at temperatures of 800 K and above [135]. The vacancy row is expected because the covalent radii of Bi (0.146 nm) and Si (0.117 nm) are so dissimilar [138]. First principles calculations found that stress and stress anisotropy scaled almost linearly with atomic size [139] for one monolayer coverage of P, As, Sb and Bi group V atoms on the Si(001) substrate. This suggests that stress relief is responsible for the (2×n) reconstruction of Bi on the Si(001) surface.

In order to prepare the Bi/Si(100)-(2×n) surface, a Si(100)-(2×1) surface is prepared in the manner discussed in section 5.1. Two methods can be employed to create this surface: (i) deposition of multiple layers of bismuth on a room temperature surface and subsequent annealing, or (ii) holding the sample just below the Bi desorption temperature and depositing bismuth onto the surface until a monolayer coverage is reached. All results presented here use the post-anneal method (i), to form the reconstruction. Great care must be taken with the annealing temperature, too high above the desorption temperature or annealing for too long at a lower temperature and the (2×n) domains begin to desorb exposing the silicon substrate.

Conversely too low a temperature or too short an anneal and Bi islands grow on top of the (2×n) structure, with additional Bi-dimers orientated both parallel and perpendicular to the previous bismuth layers [124]. The surface is also prone to the formation of unusual defects. If the sample is heated above 770K square shaped pits are created on the surface which vary greatly in size, from less than 3.5 nm to greater than 35 nm in lateral dimension. As seen in figure 5.7 they can

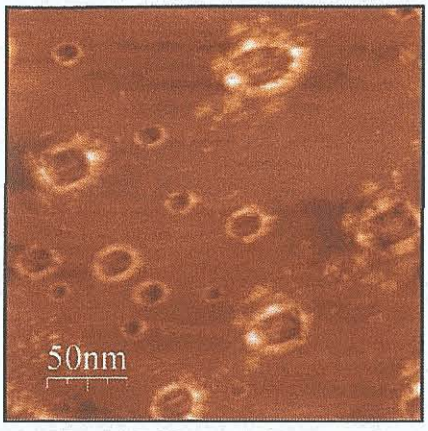

Figure 5.7: STM image of square shaped pit defects on the Bi/Si(100)-(2×n) surface, $V_s = -1.5$ V, $I_t = 0.5$ nA, 250 nm^2.

form anywhere on the surface, regardless of the atomic steps. The average depths of pits as recorded from STM images are 0.35 nm. Their density on a surface depends on the anneal temperature and defect density of the silicon substrate. Evidence of these surface pits was first published by Naitoh et al. [140] and attributed to strain relief. The nature of the pits is still unresolved and a number of different theories have been proposed. It is possible they are the manifestation of dewetting of the bismuth layer from the substrate or that they are formed by electromigration of the Bi near defects. No conclusive mechanism for their formation has been formulated.

5.3 Bi/Si(100)-(2×6) - Pentacene

The investigation of pentacene on the Si(100)-(2×6) Bi surface was motivated by the comparable width of a bismuth dimer row (1.416 nm), within the (2×6) structure, and the length of the pentacene molecule (1.41 nm). Investigations were carried out to ascertain whether this close correlation could assist in a preferential adsorption site for the pentacene molecule on a Bi-passivated surface. This study concentrated on two different coverages, the initial adsorption and thin films. They were investigated in order to assess the affect of the initial adsorption site on the structure of the thin film layer. The initial adsorption of less than a monolayer coverage of pentacene revealed the molecules aligned with the bismuth dimers across the bismuth rows. When multiple layers are deposited the molecules change their orientation and form rows aligned with the silicon substrate.

5.3.1 STM

The Bi/Si(100)-(2×6) surface with 1/12 ML coverage of pentacene is shown in figure 5.8(a) and (b). The empty state image (a) is notoriously difficult to image. It is suggested by Mark et al. [138] that this is due to the lack of unoccupied states close to the Fermi level. The empty state image reveals a strong contrast between the substrate and the adsorbed molecules. The structure of the substrate is also clearly resolved down to individual dimers. A misalignment of the Bi-dimers within a row is indicated with arrows, on both the empty and filled state images. Although figure 5.8(a) empty state and (b) filled state images are recorded at the same time in a single scan the misaligned bismuth dimers are not apparent in the filled state image.

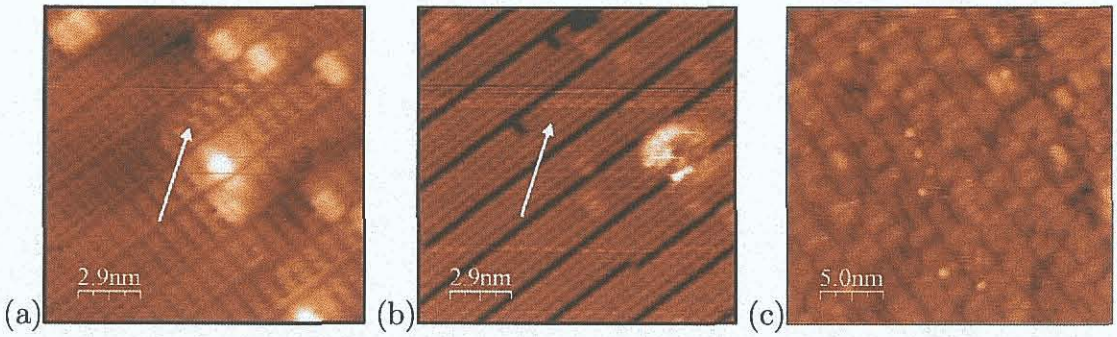

Figure 5.8: STM images of pentacene coverages below a monolayer, (a) and (b) with a 1.9×10^{-3} L pentacene coverage were taken concurrently, (a) $V_s = +1.2$ V, $I_t = 0.1$ nA, 16 nm^2 and (b) $V_s = -1.2$ V, $I_t = 0.1$ nA, 16 nm^2. STM image (c) of 0.027L pentacene coverage, $V_s = -1.2$ V, $I_t = 0.4$ nA, 25 nm^2.

The high resolution images, figure 5.9(a) and (b) show two neighbouring pentacene molecules aligned with the bismuth dimers. Each molecule measures 1.198 ± 0.05 nm in length, as indicated in the associated line profile figure 5.9(c). The molecules traverse a row of Bi dimers, in this case 1.536 nm ($4 \times a_{Si}$). The molecules continue to align in this manner up the monolayer coverage, avoiding surface defects, figure 5.8(c).

As the pentacene coverage is increased beyond a monolayer, a well ordered thin film is formed. The orientation of the pentacene molecules changes with increasing coverage, as seen by comparing figure 5.8(c) and figures 5.10(a) and (b), each bright spot is attributed to a pentacene molecule. Fourier transforms of these STM images are also included in figure 5.10(c) and (d). The distance between molecules along the rows is measured to be 0.47 ± 0.02 nm and these rows are separated by a distance of 1.18 ± 0.02 nm according to the Fourier transform measurements. If the pentacene molecules are orientated end-on to the Bi/Si(100) substrate, the area

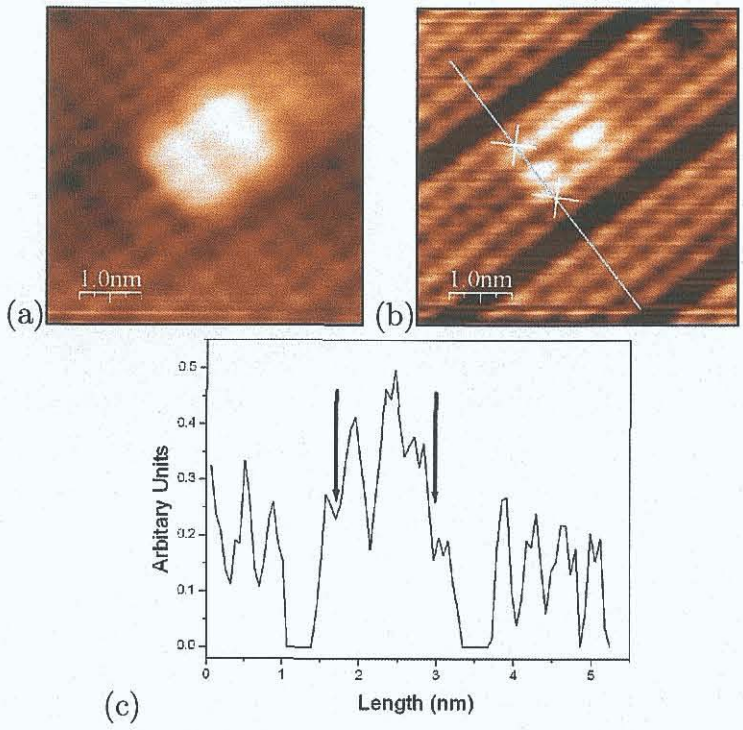

Figure 5.9: STM images taken concurrently of a 1.9×10^{-3} L pentacene coverage (a) $V_s = +1.2$ V, (b) $V_s = -1.2$ V, $I_t = 0.1$ nA, 5.5 nm^2. Line profile (c) 1.198 ± 0.05 nm taken from STM image (b) as indicated.

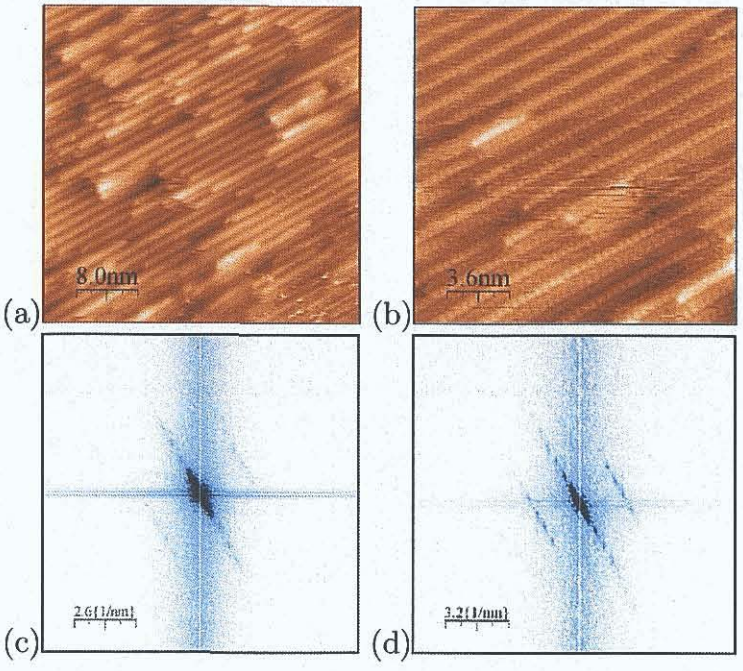

Figure 5.10: STM images with pentacene coverage of 0.32L and associated Fourier transforms. (a)$V_s = -1.0$ V, $I_t = 0.08$ nA, 40 nm^2 and (b)$V_s = +0.9$ V, $I_t = 1.2$ nA, 18 nm^2.

between the pentacene rows would contain the top of a molecular row from the layer below. This would result in a missing molecular row in every second row. However, if the molecules are tilted at an angle to the substrate the planar face or edge of the molecule would be visible. It is not clear from the STM images exactly how the molecules are orientated, i.e. with their long axis normal to the substrate or at a shallow angle. To resolve this problem additional information was obtained from LEED studies.

5.3.2 LEED

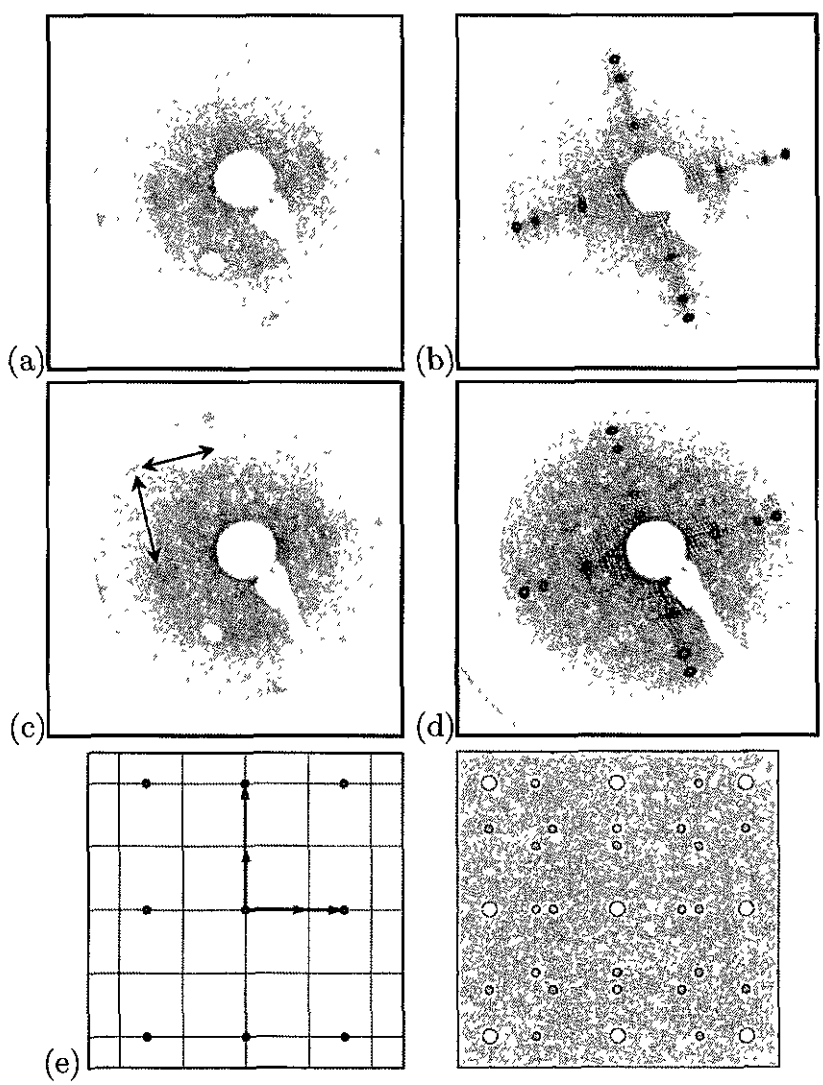

Figure 5.11: Diffraction patterns of clean Bi/Si(100) surface with n=6.2 recorded at (a) 14 eV and (b) 23 eV, and same surface with a pentacene coverage of 0.32L, recorded at (c) 14 eV and (d) 23 eV. (e) LEEDpat [17] simulated diffraction pattern, Si substrate : $a_1 = 3.84, a_2 = 3.84, \theta = 90\,°$, pentacene: $b_1 = 6.03$, $b_2 = 7.68$, θ= 90 °. Two unique domains as noted in red and blue.

The LEED pattern of Bi/Si(100)(2×6)-pentacene is only observed for a thin film coverage. The clean Bi/Si(100)(2×6) diffraction pattern is shown in figure 5.11(a) and (b). Below the monolayer coverage the only indication of the molecules is a slight increase in the background intensity of the diffraction pattern. The pentacene induced Bragg spots observed for a thin film are shown in figure 5.11 (c) and (d). They are sharp demonstrating that the film is highly ordered and they are aligned with the silicon substrate in the [011] and [01$\bar{1}$] directions. The reciprocal space distance between the ($\pm^1/_2$,0) beams equates to the 0.384 nm lattice spacing of the substrate Si atoms. Using this relationship the distances between the pentacene induced Bragg spots (as indicated with arrows on the figure) equates to lengths of 0.768 ± 0.003 nm and 0.606 ± 0.003 nm with a relative angle of 90° ± 1°. These lattice parameters compare favourably to those of the ab-plane of the triclinic structure of bulk pentacene: a = 0.790 nm, b = 0.603 nm, θ = 85.8° [58]. This implies the molecules are standing upright on the surface.

The LEEDpat program [17] is used to simulate the LEED pattern, as shown in figure 5.11(e). The parameters used are taken directly from the experimental LEED diffraction pattern, 0.768 nm and 0.603 nm with a relative angle of 90°. The registry of the pentacene Bragg spots with the substrate beams is now obvious.

5.4 Discussion

A model of the Bi/Si(100)-(2×6) structure is shown in figure 5.12, where the unit cell is outlined in red. A ball and stick arrangement of the pentacene molecule (overall size drawn to scale but not the individual atoms) in the submonolayer regime has been overlaid on the model. The registry with the underlying Bi dimers is taken from the high resolution STM images, and places the pentacene molecules lying flat on the surface and between the bismuth dimer rows. This arrangement supports the role of the bismuth dimer rows in ordering the molecules.

The molecular arrangement in the thin film is more difficult to deduce, this is due to the disagreement between the LEED diffraction pattern and the Fourier transforms of the STM images. The pentacene structure was introduced in section 2.5.1. It is triclinic in nature (a = 0.79 nm, b = 0.606 nm, c = 1.601 nm, α = 101.9°, β = 112.6°, γ = 85.8°) and features two orientations of the molecules in the bulk, as illustrated in figure 5.13. The LEED results, as previously discussed, 0.768 ± 0.003 nm, 0.603 ± 0.003 nm with a relative angle of 90° ± 1°, compare very favourably to the structure of the bulk pentacene unit cell. This implies the molecules grow in or slightly tilted away from the bulk arrangement and are orientated end on with

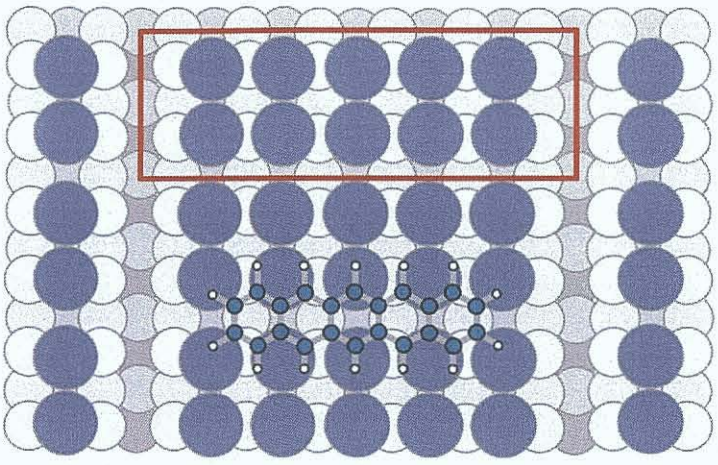

Figure 5.12: Model of the Bi/Si(100)-(2×6) with a single pentacene molecule. The silicon atoms are shown in shades of grey, the darker the shade the lower the Si layer. Bi atoms are coloured blue and atoms are drawn to scale.

respect to the substrate.

Assuming the pentacene molecules form the bulk pentacene structure albeit with a slight misalignment, the disagreement between the Fourier transforms of the STM and the LEED diffraction patterns can be resolved by comparing the Fourier transform results to the bulk structure of pentacene. To summarise, the Fourier transforms resolve distances of 1.18 ± 0.02 nm and 0.47 ± 0.02 nm, between and along the molecular rows respectively. The pentacene molecules appear to be arranged in stacked molecular rows and are tilted around their long axis out of the surface. Each new row forms between two rows in the previous layer as revealed by the STM image at high resolution figure 5.10(b). This leads to a periodic missing row structure. A plan view of the bulk structure of pentacene is shown in figure 5.14. The missing molecular row is illustrated by the uncoloured pentacene images in every second row. Using the unit cell a = 0.79 nm, b = 0.606 nm, $\gamma = 85.8°$, a simple trigonometric calculation gives bisecting diagonal distances within in the (a,b) unit cell of 0.959 nm and 1.030 nm respectively, as indicated with red lines in the figure. These distances compare favourably to the Fourier transform results. Half the diagonal distance of 0.959 nm gives 0.479 nm between the pentacene molecules which compares to the 0.47 ± 0.02 nm distance between molecules along the rows in the STM images. The 1.03 nm distance between pentacene rows compares well with the 1.18 ± 0.02 nm measured distance between rows from the Fourier transforms of the STM images.

The thickness of the π-electron cloud ca. 0.34 nm corresponds to the distance induced by the van der Waals interaction between pentacene molecules and is in

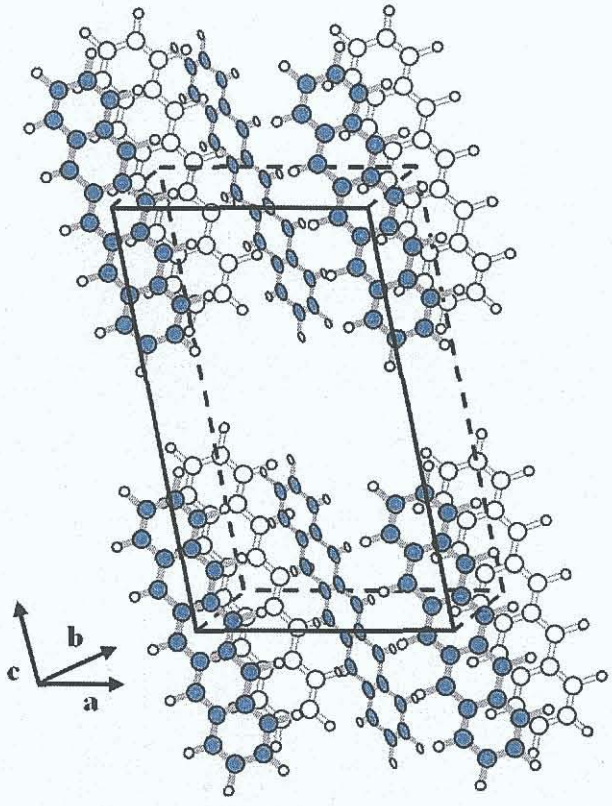

Figure 5.13: Schematic diagram of the bulk structure of pentacene. Uncoloured pentacene models indicated back row (a = 0.79 nm, b = 0.606 nm, c = 1.601 nm, $\alpha = 101.9\,°$, $\beta = 112.6\,°$, $\gamma = 85.8\,°$).

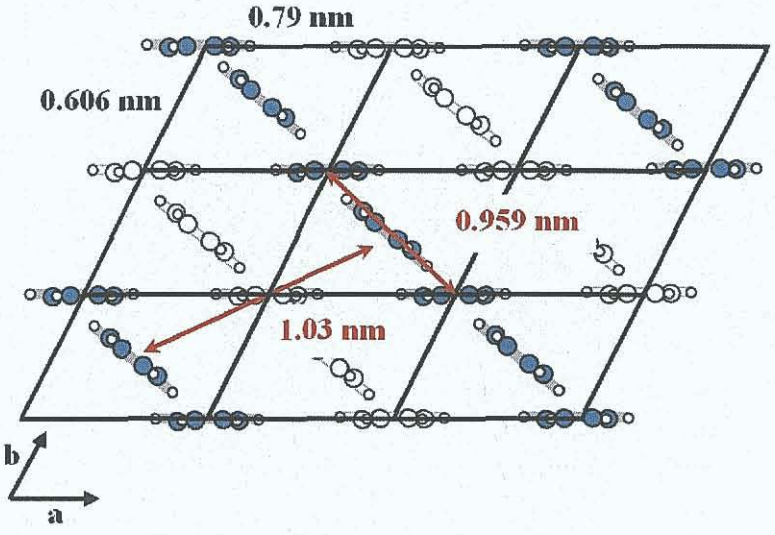

Figure 5.14: Plan view of the thin film structure of pentacene. Uncoloured pentacene molecules indicate missing rows observed in STM results. Red lines indicate diagonal bisectors of pentacene bulk unit cell.

good agreement with previous STM measurements of pentacene [141]. This means that the 0.47 nm molecular spacing recorded in the STM is larger than that expected for π-stacked molecules, but still slightly less than the side by side spacing of 0.5 nm and so the rotation of the molecules relative to each other, illustrated in figure 5.14, is speculative and corresponds to that of the bulk pentacene structure.

In addition to these experimental results, there is further evidence to support an upright orientation for the pentacene molecules in the literature. These are based on the apparent control exerted by (i) the substrate electronic structure and (ii) the molecular coverage, on the orientation of the molecule.

The apparent control of the substrate surface electronic structure on the orientation of the pentacene molecules was first noted by Thayer et al. [142]. The Au/Si(111) system produces a metallic and semi-metallic surface depending on the Au coverage. Pentacene molecules absorb in an upright orientation on the semi-metallic surface, and lie flat on the metallic surface. This observation is borne out with other examples, the pentacene molecules also lie flat on Au [143] [144] [145], Ag [146] [147] and Cu [141] [148] metallic surfaces and orient upright on semi-metallic Bi(001) [114]. The relative coverage of the molecule can also be shown to affect the orientation. Such effects have been observed for pentacene on the passivated substrate of Ag/Si(111) [149]. The molecules are initially absorbed lying flat on the surface but as the coverage is increased the molecules gradually re-orientate themselves upright on the surface, this change in orientation has been observed in consecutive STM images. Considering these results with regard to pentacene adsorbed on the passivated Bi/Si(100)-(2×n) surface, an upright orientation for the molecules would be favoured.

5.5 Conclusions

Low coverage studies of pentacene reveal flat lying molecules lying across the Bi dimer rows. A model for the bonding site as resolved with the STM is presented. The adsorption of pentacene molecules on the Bi passivated Si(100) surface is influenced by the structure of the missing Bi rows within in the (2×6) reconstruction. The LEED and STM analysis of the thin film coverage reveal a double domain commensurate unit cell of (0.768 ± 0.003 nm and 0.603 ± 0.003 nm), which is similar in dimensions to that of the bulk pentacene structure.

The initial disagreement between the LEED diffraction pattern and the Fourier transform alerts one to the fact that conclusions about the surface structure, based solely on one technique, can lead to erroneous/spurious conclusions. These experi-

ments reassert the need to use multiple techniques to investigate any surface structure. They also provide additional observational evidence for the apparent control exerted by (i) the substrate electronic structure and (ii) the molecular coverage, on the orientation of the pentacene molecule.

Chapter 6

NIXSW Imaging technique applied to Bi/Si(100)-(2×n)

The Bi/Si(100)-(2×n) single domain structure was investigated using LEED, STM and NIXSW. The LEED results are compared to those in the literature and the new STM results are discussed. NIXSW results for a number of different Bragg planes are used to test the feasibility of creating a real space image of the bismuth dimer structure from the multiple reflections in a similar manner to those reported by Cheng et al.[28].

6.1 Vicinal silicon surface

Two types of step can form on the Si(100) surface. If the dimer rows on the upper terrace are parallel to the step edge then the terrace and step are designated type "A". If the dimer rows on the upper terrace are aligned perpendicular to the step edge, it is said to be a type "B" step and terrace. These terrace and step types can be quickly identified as "A" type, where step edged are smooth and have relatively

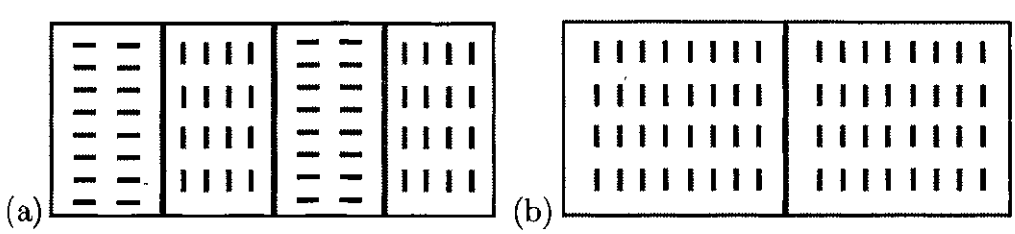

Figure 6.1: (a) (2×1) S_A step, followed by a (1×2) S_B step repeated and (b) (1×2) terraces with double step D_B between them.

straight edges and "B" type, where step edges tend to be uneven due to the dimer orientation. A Si(100) crystal with a miscut angle below 2° results in monoatomic steps, when the miscut angle is increased beyond 2° the monoatomic steps are gradually replaced with biatomic steps. When the angle exceeds 6-8° the steps become almost exclusively biatomic [150].

The misorientation of a crystal can be exploited to create a single domain (1×2) surface [151] [152], as illustrated in figure 6.1. By orienting the sample with a 5° off-cut towards the [011] direction a single domain vicinal surface can be created with the dimers rows oriented perpendicular to step edges, i.e. type "B". This off-cut produces terrace lengths of ~3 nm, corresponding to approximately 8 surface lattice constants ($a_S = a_B/\sqrt{2} = 0.384$ nm), with up to 8 dimers between biatomic step heights of 0.27 nm. In this case 12.5 % of the surface atoms belong to the step edges.

6.2 Single domain Bi/Si(100)-(2×n)

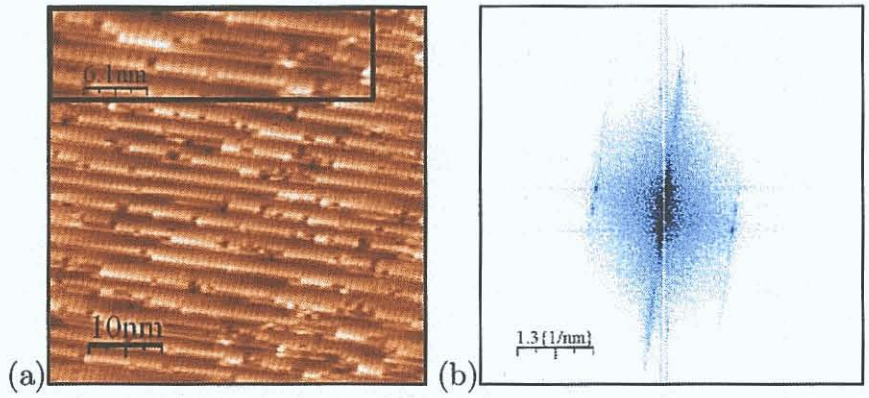

(a) (b)

Figure 6.2: (a) An STM image of the single domain Si(100)-(1×2) reconstruction, with a zoomed insert of a region of (2×1) domain. $V_s = -1.6$ V, $I_t = 0.6$ nA, 50 nm^2. (b) Corresponding Fourier transform, spot splitting relates to an average terrace width of 7 dimers.

A number of studies of the Bi/Si(100)-(2×n) single domain surface have been published [153] [154] [155] [156]. Although these reports concentrate on the interaction of the bismuth with the step topography, the same (2×n) reconstruction as seen on the double domain silicon surface, at monolayer coverage of bismuth, is reported. This conclusion was based on LEED and AES results, no STM results for the (2×n) single domain surface have been found in the literature.

The formation of the Si(100)-(2×1) double domain surface is described in section 5.1, the same procedure is applied to obtain the (1×2) single domain recon-

struction. The vicinal n-type phosphorus doped silicon (0.05-0.1 Ωcm) used in these experiments were off-cut by 5 ° towards the [011] direction. Figure 6.2 shows an STM image of the vicinal surface, and the corresponding Fourier transform gives an average terrace width of 7 dimers. The surface is not perfect as a number of small (2×1) domains are visible at step edges (insert in figure 6.2(a)). Multiple layers of bismuth were deposited from a homemade Ta evaporator, onto the Si(100)-(1×2) vicinal surface at room temperature. This was followed by an anneal at 670K to create a single domain (2×n) surface. It is noted that after bismuth was deposited on a vicinal surface the reflashing of the sample caused the substrate to develop a clean double domain Si(100) structure with very small terraces. Further annealing did not reverse this process. The single domain surface has been studied by LEED and STM.

6.2.1 LEED

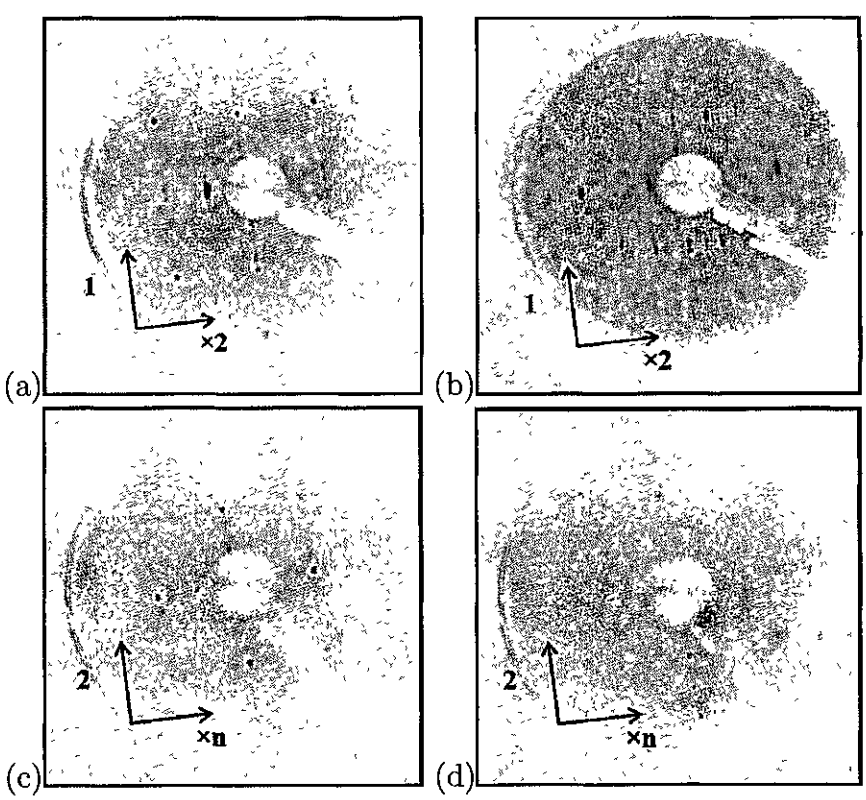

Figure 6.3: LEED diffraction patterns, (a) and (b) single domain Si(100) recorded at 62 eV and 92 eV, spot splitting relates to an average terrace width of 7 dimers, (c) and (d) Bi/Si(100)-(2×n) single domain recorded at 66 eV and 95 eV.

The diffraction pattern[1] from single domain Si(100)-(1×2) is shown in figure 6.3

[1]Contrast was altered to enhance images

(a) and (b) at 62 eV and 92 eV respectively. These diffraction patterns are in good agreement with those in the literature [156]. Arrows indicating the (1×2) single domain structure have been included as a guide. Spot splitting is observed as expected, due to the small terrace size present on the vicinal surface. An average terrace width of 7 dimers was calculated from the ratio of the diffraction spot splitting (2.61 ± 0.05 nm) to the distance between the bulk reflections (0.384 nm). This is in good agreement with the STM observation shown in figure 6.2. The deposition of several monolayers of bismuth results in a p(1×1) diffraction pattern. The sample is then annealed at 670K for ~20 minutes, this produces a (2×n) diffraction pattern, shown in figure 6.3(c) and (d). Unfortunately the intensity of the n^{th} order diffraction spots are too weak[2] to allow an accurate determination of n.

6.2.2 STM

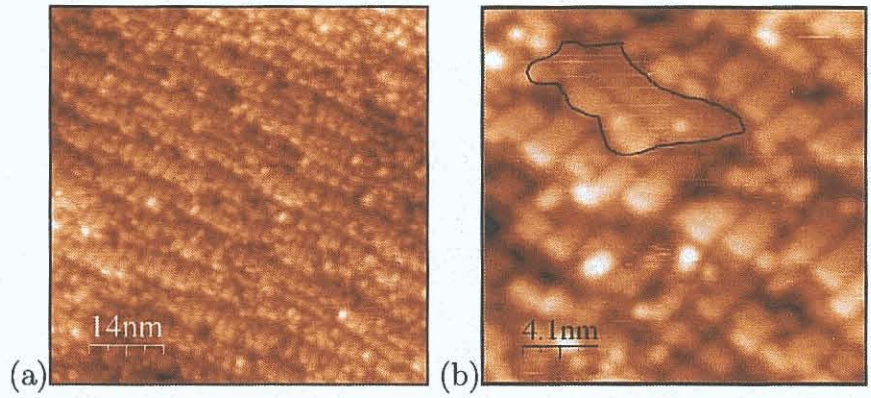

Figure 6.4: STM images of the Bi/Si(100)-(2×n) single domain reconstruction. Surface is not perfect and small areas of the other domain exist as indicated in image (b) $V_s = -2.0$ V, $I_t = 0.2$ nA, (a) 70 nm^2 and (b) 20.6 nm^2.

STM was used to investigate the surface structure and determine the periodicity of the Bi/Si(100)-(2×n) structure. Fourier transforms taken from large area STM images similar to figure 6.4(a) are used to calculate a periodicity of 2.38 ± 0.02 nm in the [0$\bar{1}$1] direction. This is equivalent to 6 silicon unit cells (to the nearest whole cell), and implies that on average five bismuth dimers align before a missing dimer break occurs, see model in section 5.12. The surface is almost entirely single domain (2×6), figure 6.4(a). However there are some small areas as indicated in figure 6.4(b), where regions of the double domain occur. These are formed when the (2×1) silicon reconstruction is exposed at poorly formed double step edged and bismuth is adsorbed on these regions. The width of the bismuth dimers on the

[2]The LEED filament was nearing the end of life during this experiment.

surface were measured by multiple line profiles on STM images similar to figure 5 9, and an average dimer width of 3.09 ± 0.03 Å was measured.

6.3 NIXSW real-space imaging technique

In order to create an image of the real-space surface from the NIXSW profiles it is necessary to measure a sufficient range of absorption profiles, apply certain symmetry rules and sum the Fourier terms [28]. In section 2.19 it was shown that the coherent fraction and coherent position define the amplitude and phase of one Fourier component of the absorber site distribution projected along a direction perpendicular to the Bragg scatterer plane. The Bi/Si(100)-(2×n) was chosen as a suitable candidate for the NIXSW imaging technique for the following reasons: (i) it has a stable structure, (ii) the passivated surface will stay clean under UHV conditions for up to three days, (iii) the bismuth dimers are of wider interest because they are the basic building blocks of the (1×1), (2×1) and (2×2) submonolayer phases [122] [123], (iv) there is a substantial body of experimental and theoretical results for the surface with which to compare the results of the imaging technique [127] [153] [154] [155] [156] and (v) a vicinal silicon substrate conveniently allows one to create a single domain (2×n) structure which allows a single bismuth dimer to be studied and therefore simplifies the resulting real-space image.

To test the feasibility of creating a real-space image of the bismuth dimer, NIXSW profiles for as many Bragg planes as possible are recorded. The NIXSW results are used to calculate the height of the bismuth dimers above the extended silicon planes before attempting to create a real-space image using the XSW imaging technique [28].

6.3.1 NIXSW Bragg reflections

The NIXSW experiments were carried out on beamline 4.2 at the SRS in Daresbury, UK. The experimental set-up is described in section 2.2.5. A fresh sample must be prepared after three days due to contamination even under UHV conditions. This is a great inconvenience as the creation of each sample surface may only be attempted once.

In order to reconstruct a real-space image from the NIXSW profiles as many reflections as possible must be recorded. There are of course limitations concerning the nature of the sample and the instrumentation that limit the number of reflections that may be obtained. In the case of the diamond lattice, the structure factor for

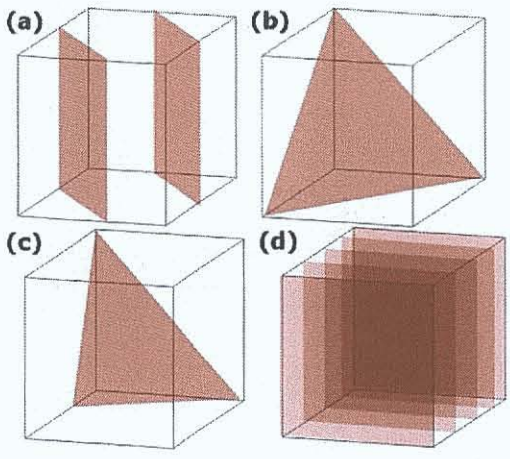

Figure 6.5: Bragg planes illustrated with 3D models and transparent planes (a) (220), (b) (111), (c) (311) and (d) (400).

a Bragg reflection is zero unless (i) the Miller indices are all odd or (ii) are all even and the sum of the indices $(h+k+l)$ is divisible by 4. The (220), (111), (311) and (400) refections, as illustrated in figure 6.5 are all permitted in a diamond crystal, however the (100), (200), (300) and (222) reflections are forbidden.

Reflections with Bragg energies higher than ~4000 eV suffer from instrumental broadening and attenuation of the XSW profiles (ΔE ~1.2 eV at E_{Bragg} = 4500 eV). For this reason the highest reflection recorded was from the (400) planes, with a calculated E_{Bragg} of 4554 eV. Another limitation is the position of the analyser with respect the synchrotron radiation entrance port. The sample must always be turned so the Bragg plane is at normal incidences to the radiation. As illustrated in section 2.8 the analyser is located ~45° clockwise about the chamber relative to the beamline entrance port. Bragg reflections can only be recorded when the sample is facing towards the analyser. Taking into account these limitations, both instrumental and inherent to the crystal structure of the sample, the following Bragg reflections were recorded; (400), (31$\bar{1}$), (11$\bar{1}$), (1$\bar{1}\bar{1}$), (20$\bar{2}$) and (220).

All NIXSW profiles were recorded by monitoring an element specific emission from the sample. The heavy bismuth atom is characterised by the large number of transitions producing photoemissions and Auger electrons. In order to record a NIXSW profile using an Auger electron emission, the energy analyser is set at a fixed kinetic energy while the photon energy is swept through the Bragg energy. For a photoemission signal the kinetic energy must be updated in step with the photon energy. This means a shrewd choice of emission signal must be made in order to avoid the crossings of photoelectron and Auger peaks. Figure 6.6 illustrates how difficult this task is. The Bragg energies of the planes are indicated by vertical red

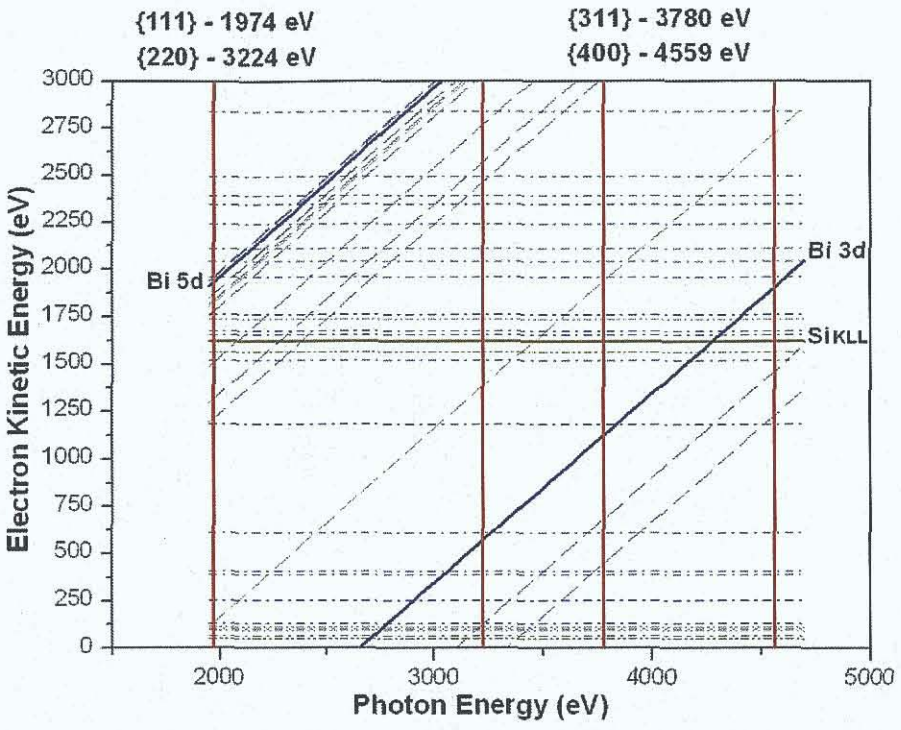

Figure 6.6: The graph shows the incident radiation versus the kinetic radiation for the Auger electrons and photoemissions from Si and Bi. The Si KLL Auger emission used in the NIXSW is represented with a bold horizontal line(yellow),and the Bi $5d_{3/2}$ and Bi $3d_{5/2}$ core levels are represented by bold diagonal lines (blue).

lines. The Auger peaks are represented by horizontal lines as they are always at a fixed kinetic energy while photoemission peaks are represented by the diagonal lines since their kinetic energy depends on the energy of the incident photons. Finally the solid lines represent the transitions used in this experiment.

The NIXSW profiles

The NIXSW profiles taken recorded from the single domain Bi/Si(100) surface are shown in figures 6.7, 6.8 and 6.9. The profiles taken from the bismuth atoms, collected for all six Bragg reflections at 300K, were measured using the photoemission yield from the highest intensity core level available. In this case, the Bi $5d_{3/2}$ and Bi $3d_{5/2}$ core levels with binding energies of 26.9 eV and 2580 eV respectively were used. The Bi $5d_{3/2}$ photoelectrons were used for the {111} reflections, while the Bi $3d_{5/2}$ were used for the {400}, {311} and {220} reflections. The Bi $5d_{3/2}$ peak is located at 1943 eV for the {111} reflections. The Bi $3d_{5/2}$ peak is located at 1970 eV for the {400} reflection, 1190 eV for the {311} reflection and 635 eV for the {220} reflection. The silicon KLL Auger electron at a kinetic energy of 1619 eV,

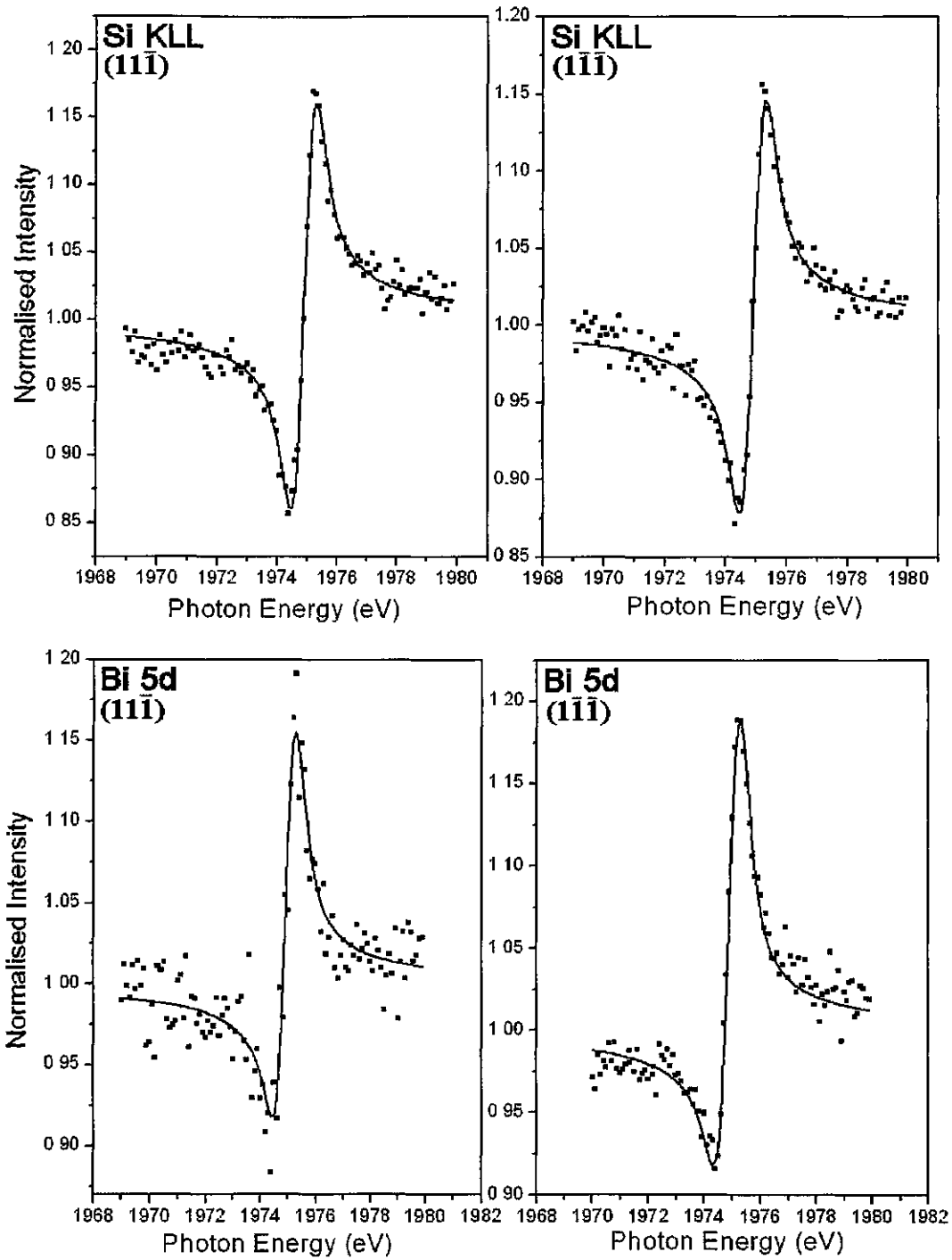

Figure 6.7: NIXSW profiles for : Silicon $p_{11\bar{1}} = 0.0 \pm 0.05$ and $f_{11\bar{1}} = 0.66 \pm 0.05$ and Bismuth $p_{11\bar{1}} = 0.05 \pm 0.05$ and $f_{11\bar{1}} = 0.55 \pm 0.05$. Silicon $p_{1\bar{1}\bar{1}} = 0.0 \pm 0.05$ and $f_{1\bar{1}\bar{1}} = 0.68 \pm 0.05$ and Bismuth $p_{1\bar{1}\bar{1}} = 0.08 \pm 0.05$ and $f_{1\bar{1}\bar{1}} = 0.63 \pm 0.05$. The solid lines show theoretical fits.

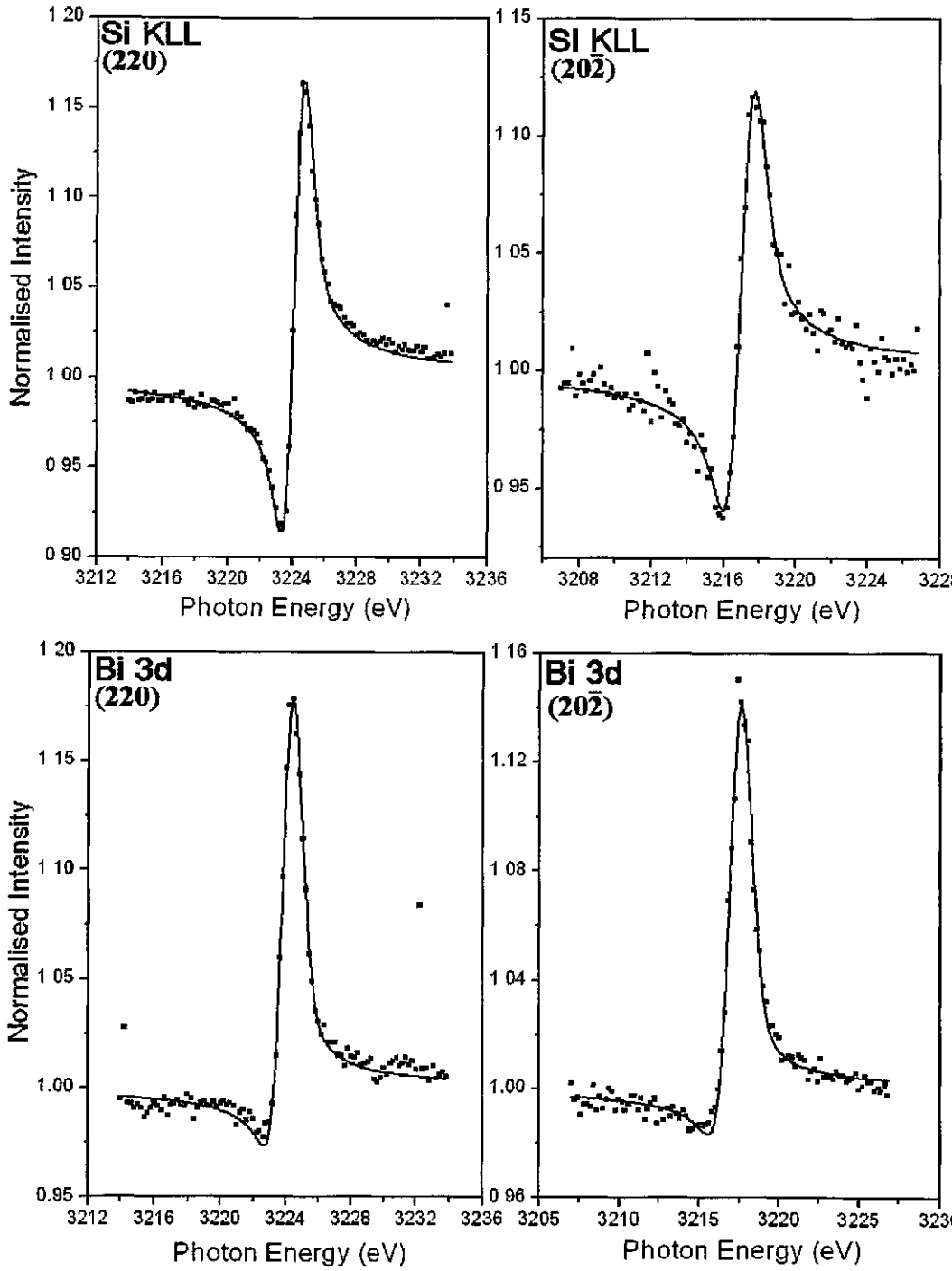

Figure 6.8: NIXSW profiles for : Silicon $p_{220} = 0.99 \pm 0.05$ and $f_{220} = 0.83 \pm 0.05$ and Bismuth $p_{220} = 1.13 \pm 0.05$ and $f_{220} = 0.64 \pm 0.05$. Silicon $p_{20\bar{2}} = 0.98 \pm 0.05$ and $f_{20\bar{2}} = 0.85 \pm 0.05$ and Bismuth $p_{20\bar{2}} = 1.14 \pm 0.05$ and $f_{20\bar{2}} = 0.50 \pm 0.05$. The solid lines show theoretical fits.

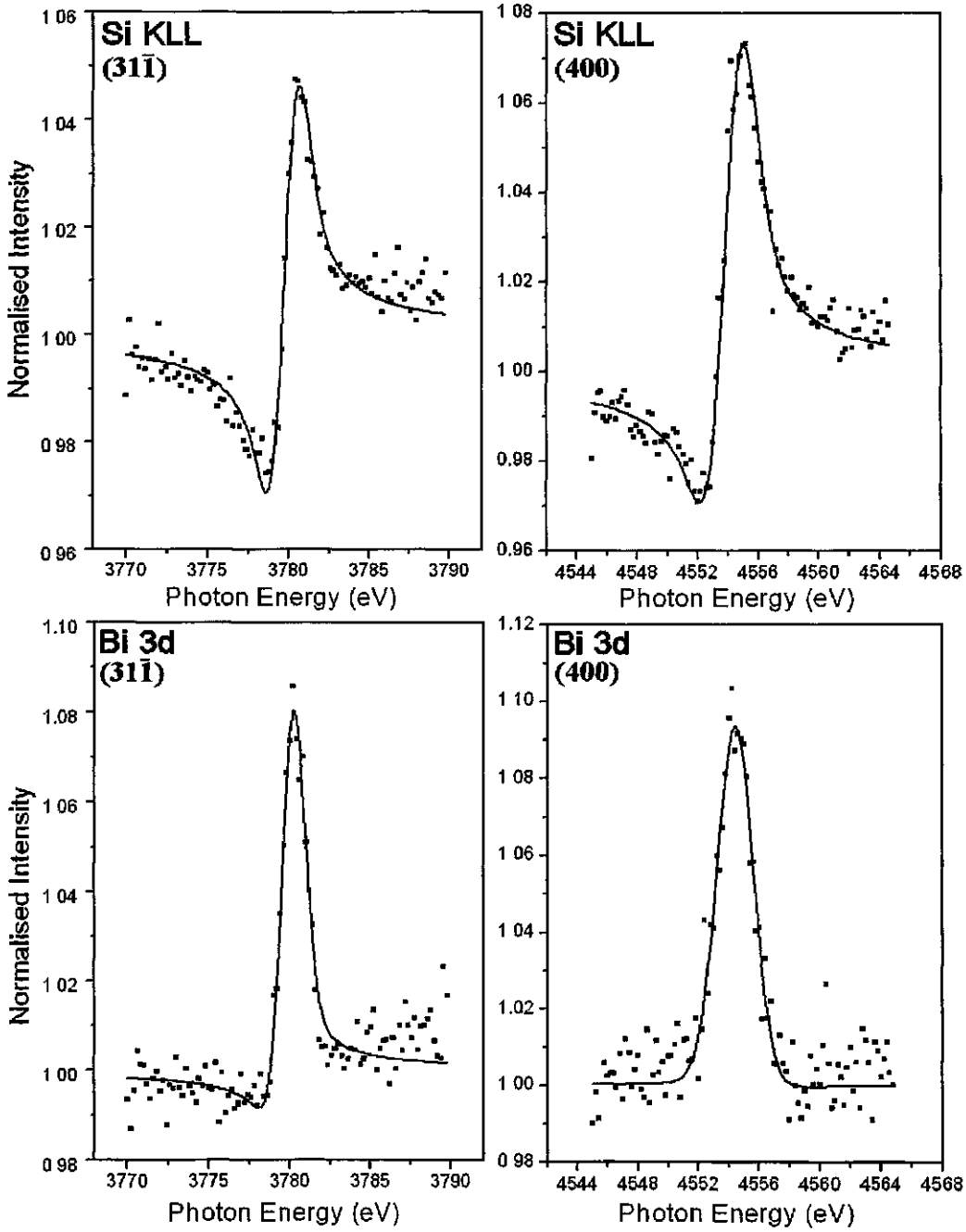

Figure 6.9: NIXSW profiles for : Silicon $p_{31\bar{1}} = 0.92 \pm 0.05$ and $f_{31\bar{1}} = 0.55 \pm 0.05$ and Bismuth $p_{31\bar{1}} = 1.13 \pm 0.05$ and $f_{31\bar{1}} = 0.38 \pm 0.05$. Silicon $p_{400} = 0.90 \pm 0.05$ and $f_{400} = 0.90 \pm 0.05$ and Bismuth $p_{400} = 0.27 \pm 0.05$ and $f_{400} = 0.79 \pm 0.05$. The solid lines show theoretical fits.

was measured for all Si(100) substrate NIXSW profiles.

The photoemission and Auger peaks sit on a background consisting of inelastically scattered secondary electrons. Correction for this background intensity was achieved by subtracting profiles measured at a kinetic energy at ~10 eV above the relevant transition.

The Bragg reflections for $(11\bar{1})$ and $(1\bar{1}\bar{1})$ planes were recorded using a InSb(111) crystal pair in the monochromator, all other reflections [(400), $(31\bar{1})$, $(20\bar{2})$, (220)],were recorded using a Ge(111) crystal pair. The profiles were fitted using a program written by Prof. R. Jones [34] in Igor Pro [35]. This program requires a procedure file with certain set parameters which are discussed in section 2.2.6. The main parameters are included in tables 6.1 and 6.2.

Bragg Reflection	**Polar angle to (100) plane**	**Interplanar distance Å** $d_H = \frac{a}{\sqrt{h^2+k^2+l^2}}$	**E_{Bragg} eV**
(111)	**54.73°**	**a/r3 = 3.13**	**1974.15**
(220)	**45°**	**a/r8 = 1.92**	**3223.77**
(311)	**25.24°**	**a/r11 = 1.63**	**3780.20**
(400)	**0°**	**a/4 = 1.35**	**4559.09**

Table 6.1: Bragg energies and angles relative to the (100) plane for reflection planes discussed, with a lattice constant 5.43 Å.

Bragg Reflection {h,k,l}	**E_{Bragg} (eV)** $E = \frac{hc}{2d_H}$	**Structure Factors**			
		$F_{(000)}$		**$F_{(hkl)}$**	
		Re	**Im**	**Re**	**Im**
{111}	**1974**	**30.07**	**21.26**	**95.52**	**47.25**
{220}	**3224**	**13.85**	**13.85**	**114.55**	**72.28**
{311}	**3780**	**10.50**	**7.45**	**115.33**	**48.57**
{400}	**4559**	**7.51**	**7.51**	**115.46**	**63.57**

Table 6.2: Calculated structure factors [36] for the Bragg reflection planes {111}, {220}, {311} and {400} of the Si crystal with a lattice constant of 5.43 Å.

A preliminary analysis of the bismuth dimer geometry can be made directly from the coherent positions and coherent fractions, table 6.3. The coherent position,

Bragg Reflection	Species	E_{Bragg} eV	$f_{(hkl)}$	$p_{(hkl)}$	$d_{(hkl)}$ Å	ΔE eV
$(11\bar{1})$	Si	1974.71	0.66	0.00	0.00	0.27
	Bi	1974.78	0.55	0.05	0.16	0.29
$(1\bar{1}\bar{1})$	Si	1974.72	0.68	0.00	0.00	0.30
	Bi	1974.77	0.634	0.08	0.25	0.32
$(20\bar{2})$	Si	3217.20	0.85	0.98	1.88	0.64
	Bi	3217.23	0.504	1.14	0.27	0.67
(220)	Si	3224.00	0.83	0.99	1.90	0.50
	Bi	3224.01	0.636	1.13	0.25	0.58
$(31\bar{1})$	Si	3779.70	0.55	0.92	1.51	0.83
	Bi	3779.89	0.376	1.13	0.21	0.71
(400)	Si	4553.80	0.90	0.90	1.22	1.06
	Bi	4554.00	0.79	0.27	0.37	1.19

Table 6.3: NIXSW coherent positions and coherent fractions for the six recorded Bragg reflections, used to fit the adsorption profiles of the $(11\bar{1})$, $(1\bar{1}\bar{1})$, $(20\bar{2})$, (220), $(31\bar{1})$ and (400) reflections.

$p_{(400)} = 1.27$ determines the height of the bismuth dimer relative to the (400) planes. It is not possible to calculate the number of (400) plane spacings between the actual silicon surface and the bismuth dimers, so it is possible for them to be at a height of 0.37 Å plus an integer number of (400) plane spacing of 1.35 Å. The coherent position of $p_{(400)} = 1.27$ place the bismuth atoms at a height of 1.72 ± 0.05 Å above a (400) plane. From the literature [156] it is accepted that the bismuth dimers are centred above the hollow sites in the silicon surface, and break the underlying silicon dimer bonds. It can easily be shown that $p_{(400)} = 2(p_{(220)})$-1. Using the coherent position obtained for the bismuth atoms relative to the (220) Bragg reflection, this suggests a $p_{(400)} = 2(1.13)$-1, which is equal to 1.26 ± 0.01, in good agreement with the $p_{(400)}$ result. The coherent fraction, $f_{(400)}$=0.79, is high considering the tight spacing between the (400) planes, and suggests a single ordered adsorption site for the bismuth. This is in good agreement with the STM evidence for symmetrical dimers of uniform height.

6.3.2 NIXSW real-space atomic-density maps

A program was implemented in MATlab [157] to sum the Fourier components of the different Bragg profiles and produce real-space atomic-density maps (appendix A). NIXSW profiles from a silicon crystal were used as a test of the code. The coherent position and coherent fractions for the six recorded Bragg planes $(11\bar{1})$, $(1\bar{1}\bar{1})$, (400), $(31\bar{1})$, $(20\bar{2})$ and (220) are the only input required, otherwise the technique is parameter independent. Atomic density images for four different slices along the [100] direction, were calculated at relative heights of 0, $^1/_4$, $^2/_4$ and $^3/_4$ through the silicon unit cell, the results of which are shown in figure 6.10.

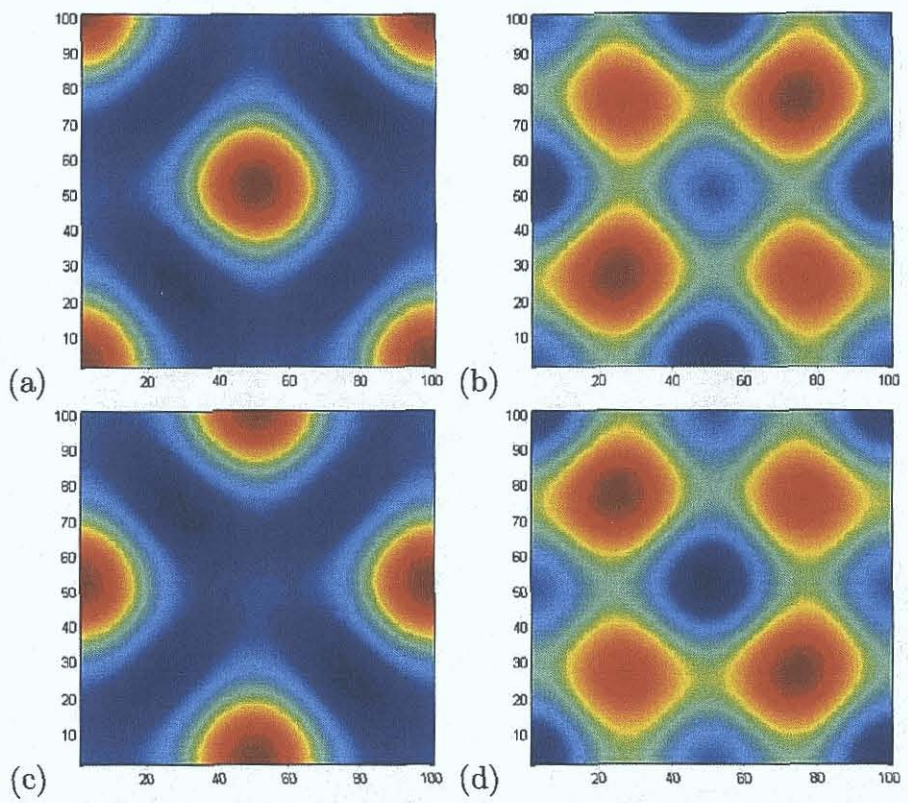

Figure 6.10: Atomic-density maps of the silicon unit cell calculated at four heights (a) 0, (b) $^1/_4$, (c) $^2/_4$, (d) $^3/_4$ along the [100] direction.

In order to interpret the results, an illustration of the position of the silicon atoms in the unit cell are shown in figure 6.11 (a) and (b). Figure 6.11(a) shows the crystal structure with the tetrahedral bonding between the atoms. Figure 6.11(b) shows the atomic positions in the [100] direction, the fraction within each atom denotes its relative height above the base of the cell. Comparing these relative heights to the NIXSW real-space atomic-density map, good agreement is observed between the NIXSW derived atomic positions and the known positions.

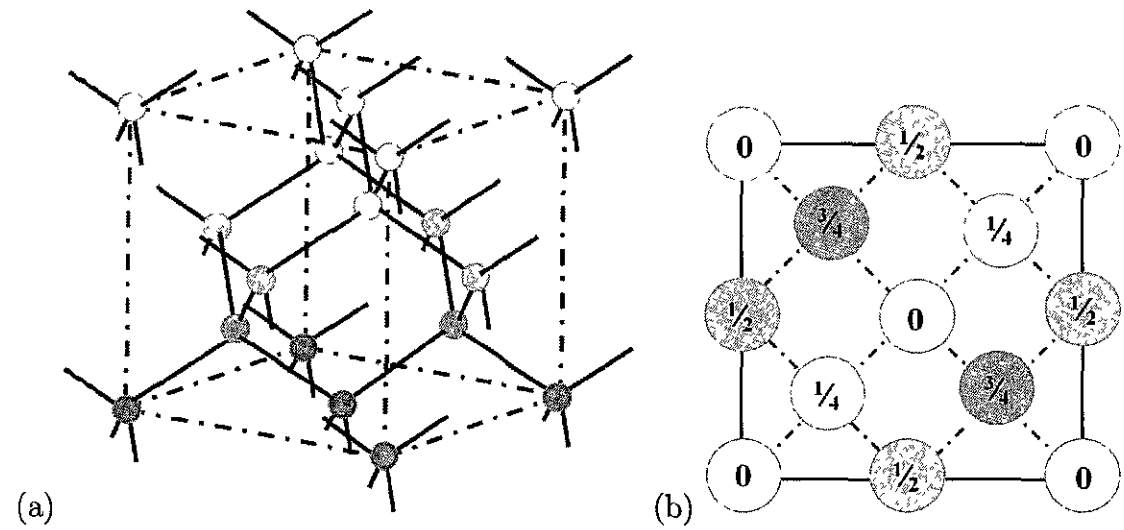

Figure 6.11: The silicon bulk unit cell with silicon atoms shaded by position within cell in (a) 3D (b) plan view.

In figure 6.10(b) and (c) atomic-density maps calculated at 25 and 75 units are shown. Four maxima are observed rather then just the two expected, however a higher intensity is noted in the correction positions. These four maxima occur because of the insufficient number of reflections available in the [100] direction. The only Bragg reflection recorded normal to the (100) surface is the (400) reflection, which can not distinguish between the silicon positions because it passes through both the $^1/_4$ and $^3/_4$ heights of the silicon unit cell.

Reviewing the symmetry of the silicon crystal, the six Bragg reflections recorded are symmetrically equivalent to another six reflections. These are the $(11\bar{1})$ plane which is equivalent to the $(1\bar{1}1)$ plane, the $(1\bar{1}\bar{1})$ plane which is equivalent to the (111) plane, similarly the $(31\bar{1})$ plane is equivalent to the $(3\bar{1}1)$ plane, and the $(20\bar{2})$ and (220) planes which are equivalent to the (202) and $(2\bar{2}0)$ planes respectively. This increases the number of Bragg planes that can be used in the analysis from 6 to 11. For the single domain Bi/Si(100)-(2×n) surface, the symmetry of the equivalent planes is also preserved.

In the case of the silicon atomic-density map the bulk structure could be retrieved from the Fourier components. For the bismuth overlayer this is not the case, a single layer of bismuth atoms cover the silicon substrate. A map of the height of the bismuth atoms above the extended silicon planes is required. In order to observe the height of the bismuth atoms directly from the recorded profiles, the program (appendix A) was altered to calculate the atomic-density map in the {110} plane.

Once again the code was verified by using the silicon NIXSW profiles. The resultant {110} atomic-density map is shown in figure 6.12(a) and (b). The density

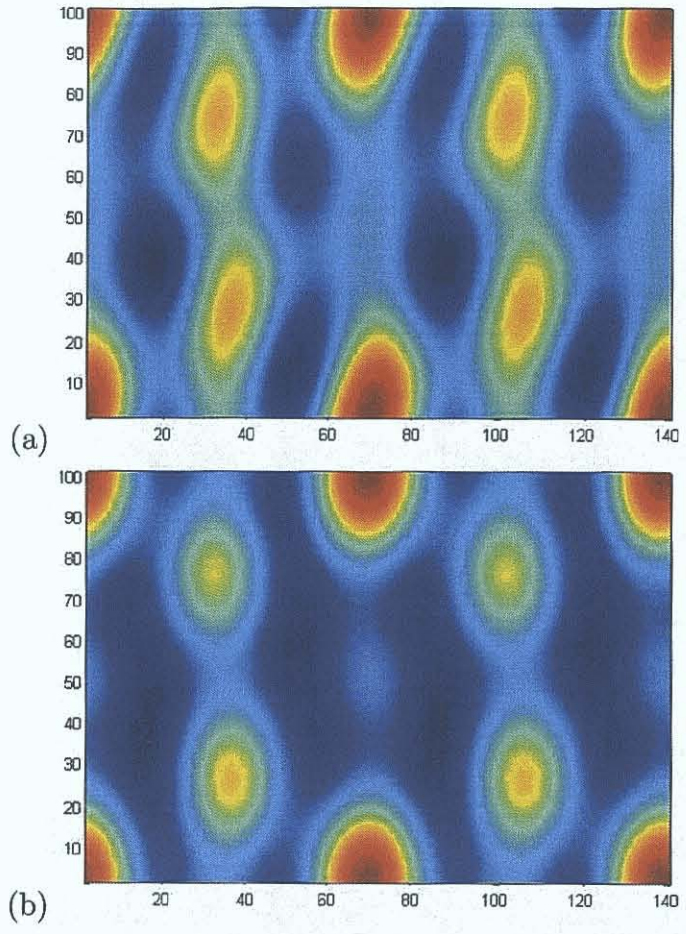

Figure 6.12: Atomic-density maps of the silicon {110} plane, 100 × 141 units (5.43 × 7.697 Å) using (a) 6 Bragg planes and (b) 11 Bragg planes in the calculation.

map shown in image (a) was created with the original six recorded Bragg planes, (b) is the result obtained using 11 Bragg planes, the additional 6 Bragg planes being the symmetry equivalent planes of the diamond structure. The silicon atoms are positioned in the base of the cell at 0 units,and the $^1/_4$ silicon atoms are observed centred at 25 units of the 100 units of the silicon unit cell. The two densities centred at 75 units, an artefact of the (400) reflection, are observed in both density maps but are weaker in the atomic-density map with 11 Bragg planes.

The same program was used to produce real-space atomic-density maps of the (110) plane, with the coherent positions and coherent fractions obtained from the Bi NIXSW profiles , figure 6.13(a). Atomic-densities are observed at heights of 6 ± 2, 31 ± 2, 56 ± 2 and 81 ± 2 units, of the unit cell. The repeating height (every 25 units) is an artefact of the (400) Bragg plane, the only plane in the [100] direction in the data set. The {110} plane has dimensions of 5.43 Å by 7.67 (5.43 $\times\sqrt{2}$) Å. The atomic-density at 6 ± 2 units converts to a height of 0.32 ± 0.1 Å (0.06 × 5.43)

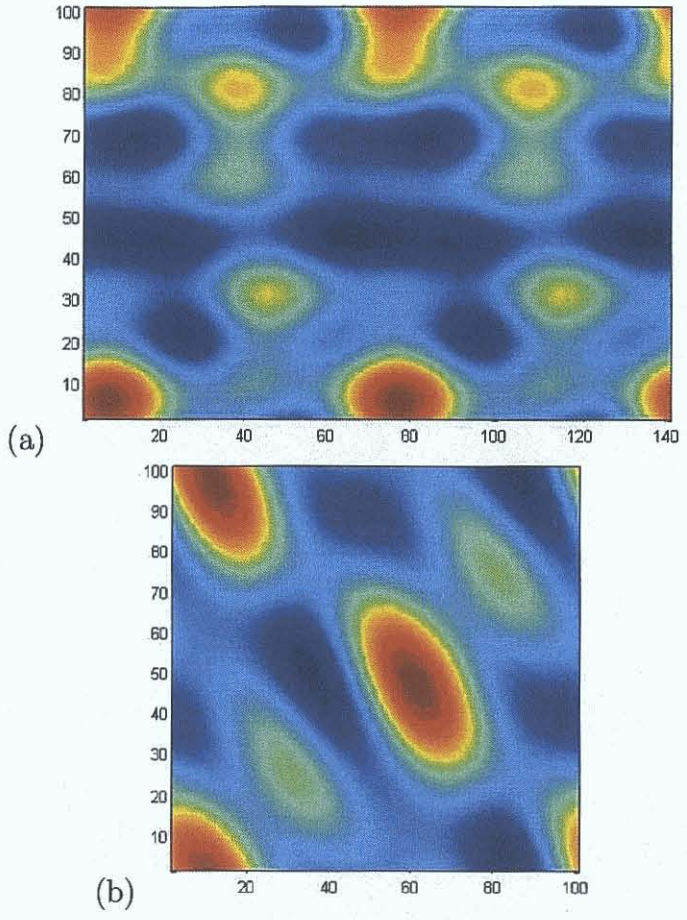

Figure 6.13: Atomic-density maps of the bismuth (a) 110 plane 100 × 141 units (5.43×7.697 Å) (b) plane at a height of (6 units) 0.32 Å above the (100) plane.

above the (400) plane. However, the actual height could be more than one plane spacing of the (400) planes. Including an additional plane spacing of 1.35 Å places the bismuth atoms at 1.67 ± 0.1 Å. This is in agreement with the reported height of 1.73 Å above the extended bulk planes [158].

The atomic-density map in figure 6.13(b) shows a plane normal to the [100] direction at a height of (6 units) 0.32 Å above the (100) plane. Measuring the distance between the atomic-densities equates to a bismuth dimer length of 3.75 ± 0.5 Å. This result appears to be an overestimation of the bismuth dimer length when compared to the STM measurement of 3.09 ± 0.03 Å.

The covalent radii for a bismuth atom is 1.46 Å which implies 2.92 Å is the lower limit on values expected for the bismuth dimer length. According to the literature the bismuth dimer length has been quoted as 2.94 ± 0.06 Å based on local-density calculations using a molecular cluster model [158], 3.4 ± 0.4 Å based on XPD data [156], 3.11 ± 0.01 Å using grazing-incidence X-ray diffraction [159], 3.1 Å based on

impact-collision ion scattering spectroscopy (ICISS) data [160] and 3.25 Å based on ab initio DFT calculations [161]. The STM results are in good agreement with these results, the NIXSW imaging is not and this is due in part to the spread of the atomic-density as apparent in the large error value. The size of the atomic-densities is dictated by the resolution of the atomic-density maps for the individual Bragg planes.

Taking into account the following observations the origin of the low resolution in the results is apparent. The (400) plane is the only phase recorded in the [100] direction because of the limits imposed by the available photon energy range and structure factor of the diamond lattice. The higher photon energy required for the $(31\bar{1})$ and (400) Bragg reflection have poor ΔE resolutions of 0.71 and 1.19 eV. There are a number of small regions of the double domain (2×n) structure which are observed in the STM but not in the LEED. Finally the strain in the Bi layer, which produces the n periodicity, results in successive dimers being pushed further away from the ideal position above the substrate hollow sites. The atomic-density map presents an average of all these slightly adjusted bismuth positions. Each of these observations contributes to a spread in the width of the bismuth dimer in the atomic density maps.

6.4 Conclusions

The structure of a (2×1) single domain of the vicinal silicon surface was discussed. The single domain Bi/Si(100)-(2×n) surface was investigated with LEED, STM and NIXSW. The LEED results are in good agreement with the literature. The STM images confirm the (2×n) structure on the single domain vicinal Si(100) surface and show careful sample preparation is vital to producing a single domain (2×n) reconstruction.

Careful consideration must be give to the choosing of a system for the NIXSW imaging technique. The favourable attributes of the Bi/Si(100) were reviewed. The coherent positions and coherent fractions from the recorded NIXSW profiles, summed together with their six symmetry equivalent planes, were enough to resolve the diamond structure of the silicon atoms within the unit cell. The height of the bismuth dimers above the extended silicon planes was accurately predicted from the atomic-density map of the {110} plane and is in agreement with results quoted in the literature. The width of the bismuth dimer was also calculated and although the accuracy is poor it has been shown that is it feasible to create a real-space image of the bismuth overlayer structure.

Chapter 7

The interaction of TMA with the Ag/Si(111) surface

In this chapter an introduction to the Si(111) and Ag/Si(111)-($\sqrt{3} \times \sqrt{3}$)R30° surfaces is given. The room temperature growth and ordering of trimesic acid (TMA), (1,3,5-benzenetricarboxylic acid) on the ($\sqrt{3} \times \sqrt{3}$)R30° (hereafter Ag/Si(111)-$\sqrt{3}$) surface is then discussed. It has been investigated using the following techniques TPD, STM and LEED. Molecules are found to initially adsorb at the step edges and defect sites but with increased coverage they begin to diffuse freely and coalesce into ordered close-packed domains. An oblique unit cell is determined and a model proposed. A missing molecule defect with short range order and a surface modulation with long range order are observed within the domain structure and are also discussed.

7.1 The clean Si(111) surface

Silicon as discussed in section 5.1 is a group IV semiconductor. It cleaves readily along the {111} planes, because each Si-Si bond is directed along one of the ⟨111⟩ axes. The cleaved surfaces react readily in atmosphere, producing a layer of native oxide. Under UHV conditions, this oxide can be thermally removed. A surface reconstruction occurs in order to minimise the number of dangling bonds lowering the surface free energy into a (7 × 7) structure or, depending on the temperature range, a metastable (5×5) periodicity [162]. The boron doped p-type silicon samples (0.1-1 Ω cm) used in these experiments are prepared as follows. The sample is degassed overnight in the sample holder in the preparation chamber at 723K by

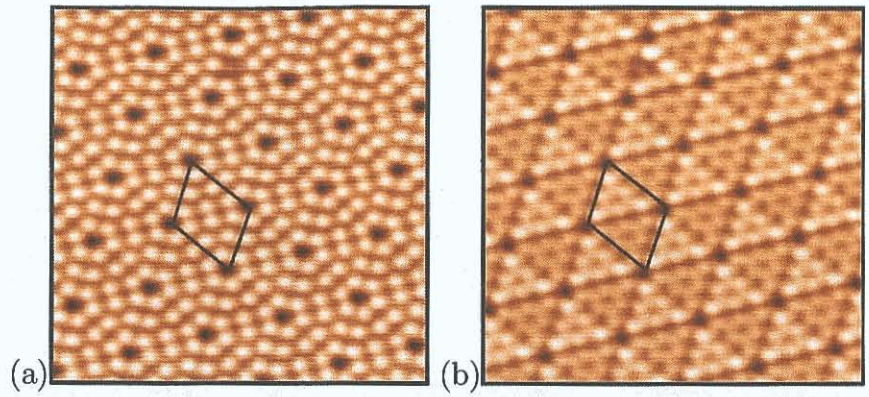

Figure 7.1: STM images of clean Si(111)-(7 × 7) surface. (a) filled and (b) empty states with the bright and dark faulted and unfaulted halves respectively, $V_s = \pm 2.0$ V, $I_t = 0.1$ nA, 13.7 nm^2.

resistive heating. This is below the temperature required to remove the protective oxide layer. The sample is then transferred to the analysis chamber and flashed to ~1273K to remove the oxide layer. The (7 × 7) reconstruction is prepared by a series of flashes at 1523K, followed by a quick cool to 1223K where the temperature is held for up to 30 minutes to encourage terrace growth, and finally allowed to cool slowly to room temperature.

The structure of the Si(111)-(7 × 7) structure was determined by Takayanagi et al. [163] through detailed analysis of transmission electron diffraction data. The reconstruction is complex with nine dimer bonds, twelve adatoms of two types and a subsurface stacking fault in each surface cell. Additional features of this Dimer-Adatom-Stacking fault (DAS) reconstruction are corner holes, each a silicon vacancy and, six unsaturated "rest atom" dangling bonds exposed in the layer below the adatoms. About the corner holes the atoms are arranged in twelvefold rings and there are also eightfold rings along each boundary between faulted and unfaulted areas. The maxima apparent in both the filled and unfilled STM images may be directly associated with the 12 top layer adatoms. These adatoms are each bonded to three second layer atoms, so eliminating three dangling bonds but introducing a new one. The unit cell is made up of two triangular sub-units of adatoms surrounded by silicon dimers. They are rendered inequivalent by a stacking fault in the left sub-unit which images with brighter contrast in the empty state image, figure 7.1. As a result of the complex (7 × 7) reconstruction only 19 of the 49 original silicon surface dangling bonds remain. This surface is metallic, with the corner adatoms on the faulted half having the highest DOS near the Fermi energy [164].

7.2 The Ag/Si(111)-$\sqrt{3}$ reconstruction

The $(\sqrt{3} \times \sqrt{3})$R30° reconstruction occurs for many of the transition metals (Au [165], Ag [166], Pt [167]), and several p-block elements (In [168], Sb [169], Bi [170], Pb [171]) on the Si(111) surface. They are all relatively simple to prepare. The Ag/Si-$\sqrt{3}$ reconstructed surface was prepared by e-beam deposition of silver (5N) from a molybdenum crucible onto unto a clean Si(111)-(7 × 7) surface held at a temperature of 770K. After deposition the sample is annealed to 870K for an additional two minutes to reduce excess silver adatoms on the silver monolayer and to minimise islanding [172]. The honeycomb-chain-trimer (HCT) model, proposed by Takahashi et al. [166], has been confirmed as the most reasonable model for the Ag/Si-$\sqrt{3}$ structure and has been studied extensively, figure 7.2. Within the unit cell of the HCT model, Ag trimers surround the Si trimers in a hexagonal ring. The Ag trimers are situated above the second-layer Si atoms, and each Ag atom participates in bonding to a member of a Si trimer. All Si dangling bonds are occupied with the exception of step edges, phase boundaries and defect sites; resulting in a passivated surface.

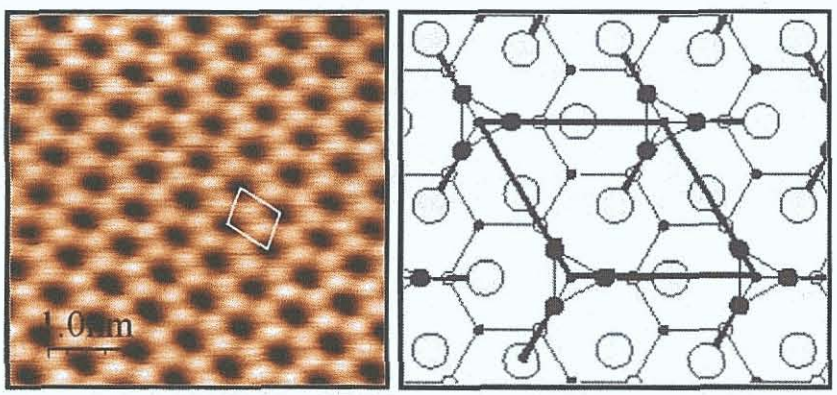

Figure 7.2: STM image of the HCT (hexagonal-chain-trimer) structure of the Ag passivated silicon. The $\sqrt{3} \times \sqrt{3}$ unit cell is marked in white. $V_s = -1.0$ V, $I_t = 0.2$ nA, 5 nm^2. HCT structure with unit cell lengths of 0.665 nm [163].

The silver passivated Si(111) surface has been used previously in studies of the ordering of molecules such as fullerenes [173][174], phthalocyanines [175] and acene molecules [176]. On the Ag/Si-$\sqrt{3}$ surface these molecules were found to diffuse freely on the surface and form islands in which the ordering is predominantly determined by intermolecular, as opposed to substrate-molecule, interactions. The energetic competitiveness of intermolecular interactions is essential for self-assembly to occur. For these reasons a study of the ordering of TMA on the silver passivated surface was undertaken.

7.3 Experimental Results

7.3.1 LEED

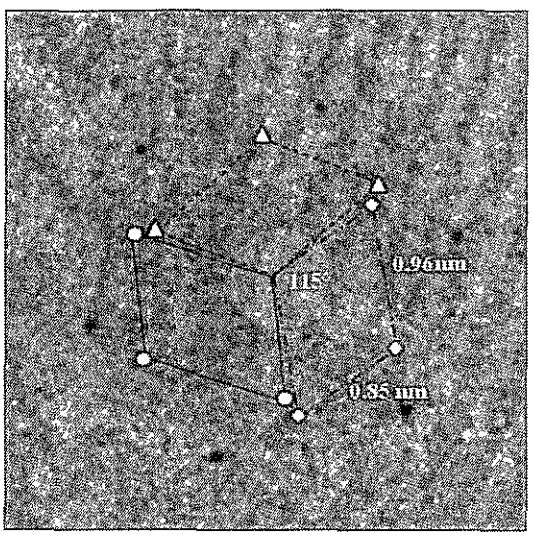

Figure 7.3: LEED image of Ag/Si-$\sqrt{3}$-TMA surface recorded at 16 eV after a deposition of ~1ML. Three oblique unit cells are indicated with circles, triangles and diamonds. The length of each unit cell is 0.85 ± 0.05 nm by 0.96 ± 0.05 nm with an interior angle of 115°.

All LEED diffraction patterns were recorded at room temperature with low emission current <20 eV using a Lanthanum Hexaboride (LaB_6) filament to minimise desorption of the molecules from the sample surface by electron bombardment. The diffraction pattern for approximately one monolayer deposition of TMA on Ag/Si-$\sqrt{3}$, shown in figure 7.3, has a p6mm two-dimensional space group. The pattern shows six intense $\sqrt{3}$ Bragg spots resulting from the hexagonal reconstruction of the

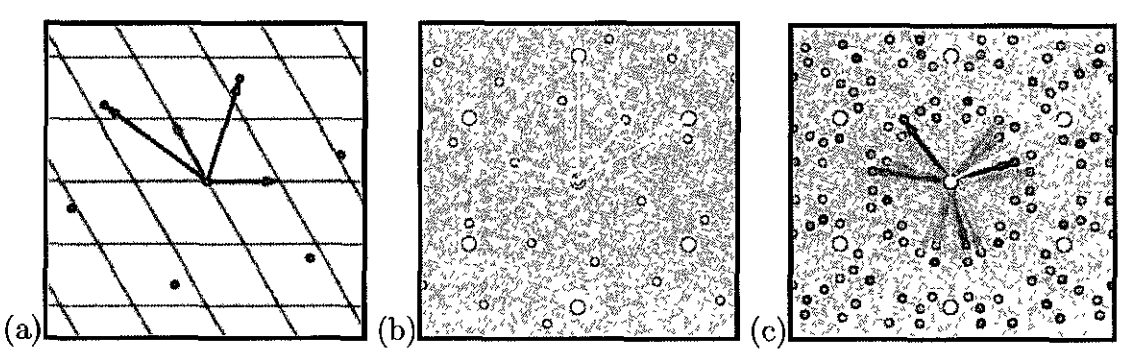

Figure 7.4: LEEDpat models of (a) real space oblique cell of 0.85 nm, 0.96 nm, $\theta = 115°$ and reciprocal space (b) single domain and (c) six domains due to the p6mm symmetry.

Ag/Si-$\sqrt{3}$ surface. All additional spots are derived from the TMA molecules, and can be removed by heating the surface up to 400K.

Twelve diffuse triangular features are observed, each of which is composed of three diffraction spots. These features can be accounted for with an oblique unit cell, three of which are indicated in figure 7.3. The distance between the $(0,0)$ diffraction spot and the TMA related features are smaller that the distance to the $\sqrt{3}$ spots, implying the oblique cell of the TMA structure is larger than the hexagonal silver cell. Taking the accepted length of the Ag/Si-$\sqrt{3}$ unit cell as 0.665 nm [177], the average lengths of the lattice vectors of the oblique cell are estimated as 0.85 ± 0.05 nm and 0.96 ± 0.05 nm with an interior angle of $115 \pm 2°$. These lengths are comparable in size to the TMA molecule (0.8 nm, see section 2.5.2).

The LEED images reveal that there are six ordered domains of TMA where each domain has three possible orientations at 120° relative to each other. The triangular features in the LEED image occur in pairs between the $\sqrt{3}$ spots. The angle between each pair is $15° \pm 1°$ and equates to the smallest angle between two TMA domains. The orientation of the TMA domains relative to the silver HCT substrate is $23° \pm 1°$ as determined from the angle between a triangular feature and the nearest $\sqrt{3}$ Bragg spot.

The experimental LEED diffraction pattern was modelled on the LEED pattern simulator, LEEDpat [17] using the dimensions recorded from the LEED data. Figure 7.4 demonstrates that the triangular features in the experimental data can be modelled with an oblique unit cell with a p6mm symmetry, which results in six rotated domains. The simulated diffraction pattern for a single domain is also shown.

7.3.2 STM

Residual dangling bonds exist on the passivated Ag/Si-$\sqrt{3}$ surface at defect sites and from the substrate silicon at step edges. These act as preferential adsorption sites where the growth of the molecular domains nucleates. For low coverage room temperature depositions, STM images (figure 7.5) show that the TMA molecules are lying flat on the surface and form a honeycomb structure. The Ag/Si-$\sqrt{3}$ substrate images as the smaller hexagonal structure with silicon trimers imaging as dark spots between the brighter silver trimers.

Streaking occurs in the STM images and is consistent with the presence of loosely bound molecules on the surface. The diameter of the holes in this structure is measured as 1.35 ± 0.05 nm and is comparable to the value of 1.4 nm observed in the cyclic hexamer crystal structure of TMA [59]. By annealing the sample up to

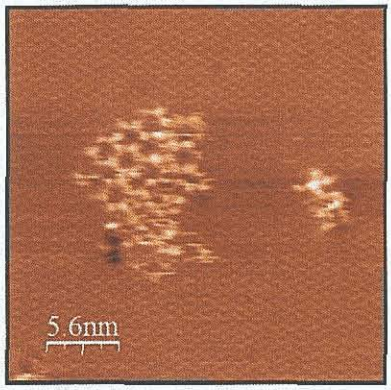

Figure 7.5: An STM image, recorded at low TMA coverage, reveals the flat lying molecules forming a honeycomb structure. The diameter of the holes in this structure is measured as 1.35±0.05 nm. $V_s = -1.5$ V, $I_t = 0.5$ nA, 28 nm^2.

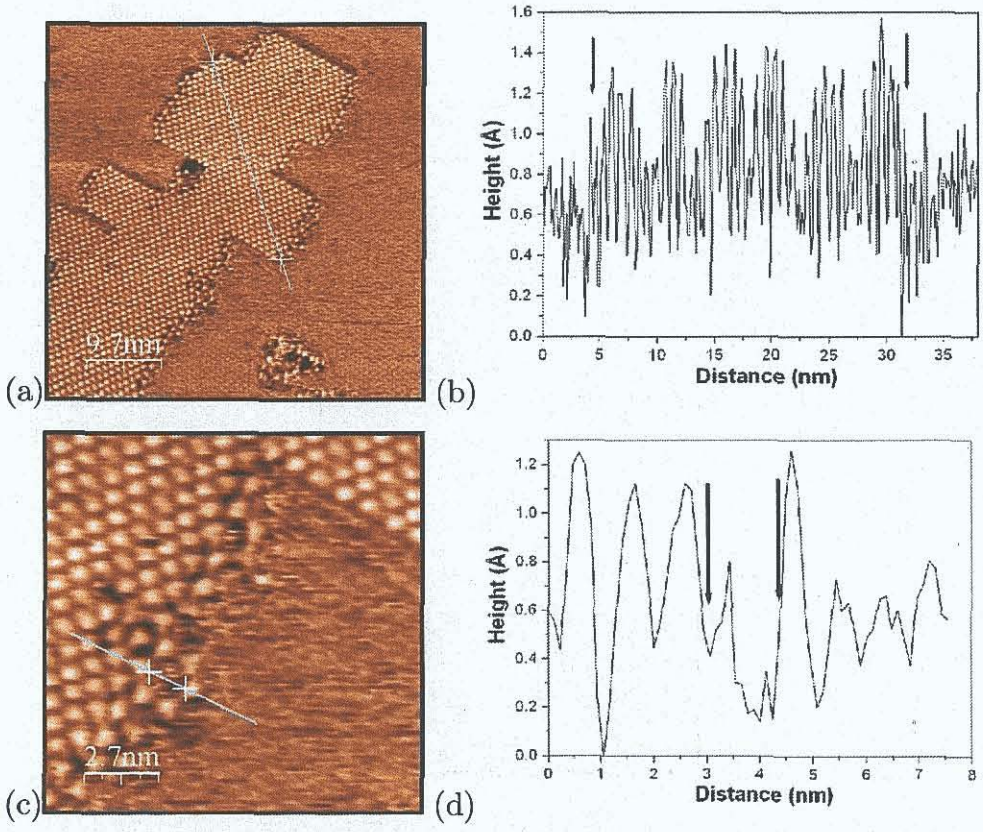

Figure 7.6: STM image of single TMA domain (a) $V_s = -1.5$ V, $I_t = 0.3$ nA, 48.7 nm^2. (b) Height profile along line indicated on image (a) showing modulation along a molecular row. (c) Zoomed area showing cyclic hexamer composed of flat lying TMA molecules, $V_s = -1.5$ V, $I_t = 0.5$ nA, 14 nm^2. The island edges parallel to the modulation are uneven, with flat lying molecules decorating the edge. Perpendicular to the modulation the edges are straight and well ordered. (d) Line profile across hexamer as indicated on image (c).

370K the molecules desorb from the surface except at defect sites and the step edges where they are chemisorbed through exposed silicon dangling bonds.

Further depositions at room temperature transform the flat lying molecular islands into an ordered array of bright features, as imaged by the STM. Each bright feature in the array is associated with a single TMA molecule. The higher packing density and improved stability of STM imaging suggests a lateral intermolecular attraction within the ordered arrays.

An example of such an array is shown in figure 7.6(a) and (c) a magnified region of the same image. In these figures several triangular shaped features can be seen along the island edge. The characteristic shape and size of these features is consistent with those of flat lying TMA molecules with the phenyl ring parallel to the substrate. The magnified area in figure 7.6(c) shows a cyclic hexamer with a diameter of 1.45 nm which compares well with the 1.4 nm of the bulk crystal structure [59].

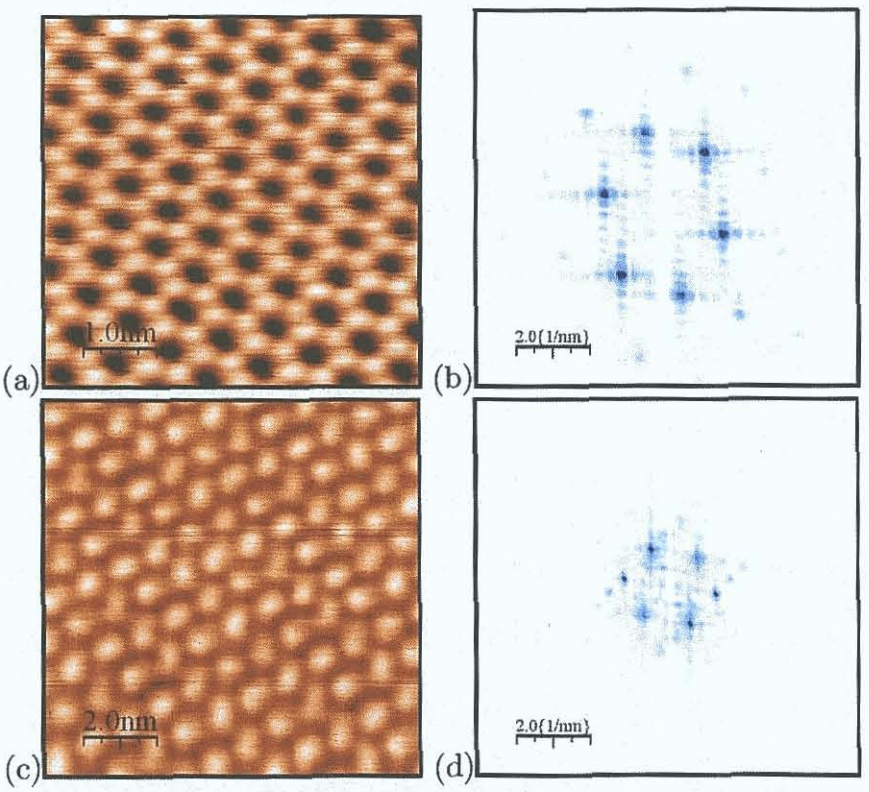

Figure 7.7: (a) An STM image, $V_s = -1.0$ V, $I_t = 0.2$ nA, 10 nm^2 and (b) associated Fourier transform of the Ag passivated surface. (c) An STM image of a single domain of TMA, $V_s = -2.0$ V, $I_t = 0.1$ nA, 10 nm^2 and (d) associated Fourier transform.

A Fourier transform of the STM images was preformed using the WXSM analysis software [38]. The Fourier transforms are comparable to the LEED images of the same surfaces as both represent the reciprocal space features of the structures.

From the Fourier transform of the clean Ag/Si-$\sqrt{3}$ STM image the hexagonal $\sqrt{3}$ reconstruction of the silver passivated Si(111) is evident, figure 7.7(b). A second Fourier transform was preformed on a STM image of a single domain of TMA figure 7.7(d). The TMA structure is not perfectly hexagonal in nature, and is best described by an oblique cell. The distances between the $(0,0)$ position and the TMA diffraction spots are smaller than that of the Ag/Si-$\sqrt{3}$ surface Bragg spots, so the unit cell of the TMA is larger than the unit cell of the silver passivated substrate. Half the inverse distance between opposite Ag/Si-$\sqrt{3}$ spots in the Fourier transform can be equated to the length of the silver unit cell, which has an accepted value of 0.665 nm. Similarly this inverse relationship can be used to calculate the average TMA unit cell length, which was estimated at 0.90 ± 0.05 nm. These results concur with the LEED diffraction patterns.

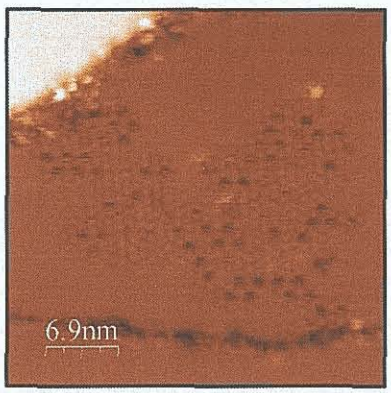

Figure 7.8: STM image of a TMA domain in which the short range order of the missing molecule defect is present. Step decoration occurs through exposed dangling bonds at step edges. $V_s = -1.5$ V, $I_t = 0.5$ nA, 34 nm^2.

A modulation is observed within the molecular domains present in the STM images. Line profiles (figure 7.6(b)) taken along a molecular row show that the modulation has a periodicity of 2.4 ± 0.1 nm. The island edges parallel to the modulation are uneven with flat lying molecules decorating the edge. Perpendicular to the modulation the edges are straight and well ordered. This modulation is not present on all TMA domains. In its absence a missing-molecule defect is observed, as shown in figure 7.8. The modulation and the defect are mutually exclusive features of the domains. When imaged with the STM the missing-molecule defects appear as dark regions in both positive and negative bias. The defects are isolated from each other by six nearest-neighbour TMA molecules and exhibit a short range-order.

In high-resolution images it is possible to image both the molecules and the substrate. The image in figure 7.9 shows where, as a result of a tip change while scanning, the molecules and the substrate are observed in the same image. From

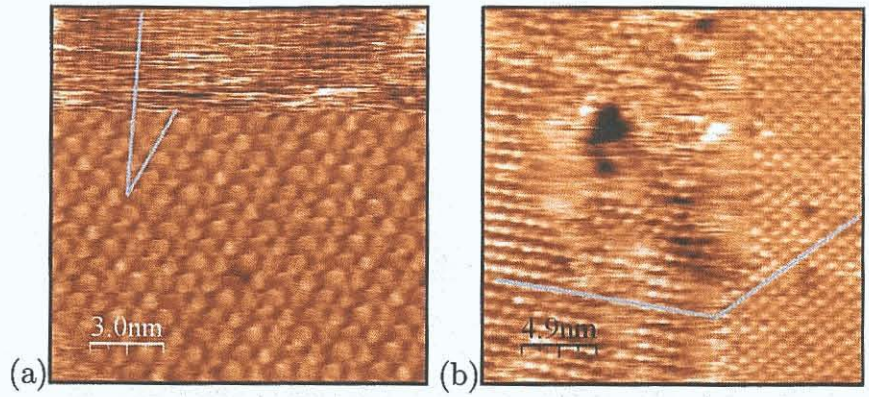

Figure 7.9: (a) Molecules and the substrate are observed in the same STM image, with a relative rotation of 23° ± 1°, $V_s = -2.0$ V, $I_t = 0.06$ nA, 15 nm^2. (b) STM image shows two of the six possible molecular domains. These domains have a relative orientation of 135° ± 1°. $V_s = -2.0$ V, $I_t = 0.06$ nA, 25 nm^2.

this and similar images the registry of the oblique unit cell of the organic overlayer with respect to the hexagonal unit cell of the Ag/Si-$\sqrt{3}$ surface is determined to be 23°±1°. The STM analysis also reveals the existence of six molecular domains, three orientated at 120° to each other with three additional domains rotated by 15° ± 1° relative to the first. Figure 7.9 shows two domains with a relative orientation of 135° ± 1°, this confirms the previous results determined from the LEED images. There is also good agreement with the values obtained from the LEED (0.85 ± 0.05 nm and 0.96 ± 0.05 nm) and STM (0.87 ± 0.05 nm and 0.93 ± 0.05 nm) measurements of the oblique cell, all of which are comparable to the actual width of a single TMA molecule 0.805 nm [59].

7.3.3 TPD

A TPD study was carried out on the high coverage Ag/Si(111)-TMA surface. The experimental procedure is the same as that discussed in section 2.4. The decomposition of trimesic acid, $C_6H_3(COOH)_3$, is investigated by monitoring the 105, 91 and 77 amu channels as the sample temperature is ramped from room temperature. A broad desorption peak is observed at 400K as shown in figure 7.10. No other TMA desorption peaks were detected above 400K for the Ag/Si(111)-TMA surface. Similar results are observed for Sn/Cu(100) at a coverage greater than $\theta_{Sn} = 0.3$ ML. This is an indication that no strong bonds form between the molecules and the substrate. Once the TPD experiment was completed the same sample was then investigated using the STM and LEED techniques. No evidence of the molecules on the sample terraces were detected with the STM however an increase in the defects

observed at step edges is noted, and a slight increase in the background intensity was observed in the LEED.

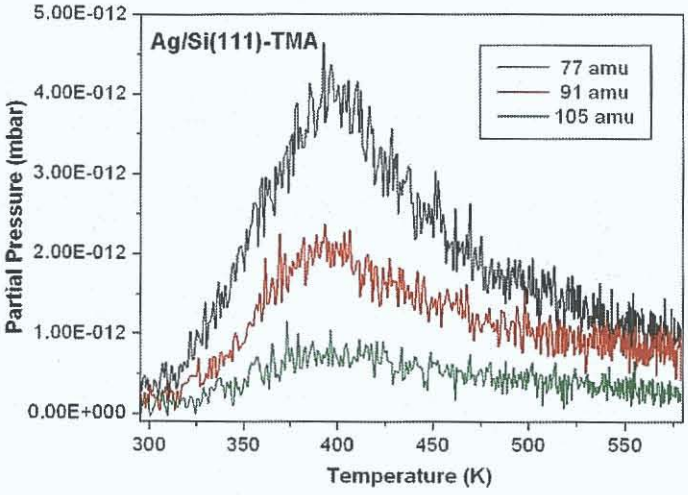

Figure 7.10: TPD spectra for the Ag/Si-$\sqrt{3}$-TMA surface.

7.4 Discussion

From differences noted between the STM images recorded at low and high molecular coverage it is evident that there is a change in the orientation of the molecules relative to the Ag/Si-$\sqrt{3}$ substrate. At low coverage the molecules adopt a flat lying orientation with the plane of the molecule parallel to the surface, whereas at coverages approaching one monolayer, STM images show the molecules in an upright or tilted position within islands. Bonding between the TMA molecules and the substrate may occur through interaction with the π-electrons of the phenyl ring producing a flat lying geometry or deprotination of either one or two of the equivalent carboxyl end-groups for an upright geometry.

The substrate electronic structure may also have a critical role in the upright and flat lying orientation of the molecules. As discussed in section 5.4 the electronic structure of the substrate affects the orientation of adsorbed pentacene molecules. The TMA molecules adsorb in an upright orientation on metallic Cu(100) [63] and Au(111) [64] surfaces but lies flat when adsorbed on a semimetallic graphite surface [10].

The bonding between the TMA molecules and the passivated surface appears to be weak. The molecules desorb from the surface at 400K, as observed in the TPD spectra. After the desorption no molecules were observed on the substrate with

the STM and the TMA induced Bragg spots are absent from the LEED diffraction pattern. This mean the LEED, STM and TPD results all support a weak molecular substrate interaction.

The close correspondence between the hexagonal formations observed at low coverage and at island edges to the crystal structure of TMA confirms the importance of intermolecular hydrogen bonding in the ordering of the molecules. At higher TMA coverages these formations coalesce into ordered domains.

A modulation is evident within some of the molecular domains. The cause of this modulation has not been unambiguously determined, however evidence suggests it is due to different upright bonding geometries. For example, when TMA molecules are adsorbed on the Cu(100) surface [63], STM images show a modulation in the height of the molecules which is attributed to a difference in bonding configuration. Also, in situ STM and cyclic voltammetry measurements of TMA adsorption on Au(111) in aqueous electrolytes reveals different orientations of the molecules [64]. Where bonding occurs through a single carboxyl group better conductivity is observed in comparison to that of molecules with two carboxyl groups bonded to the surface. Again, this difference in conductivity is reflected in the modulation observed in the STM images of this interface.

Figure 7.8 shows an STM image of a domain in which missing molecule defects are observed. The average diameter of these defects is 1.2 ± 0.05 nm, consistent with a single missing molecule. A similar missing molecule defect is observed for a monolayer of C_{60} on the Ag/Si-$\sqrt{3}$ surface [178]. The C_{60} orders into six incommensurate domains with respect to the substrate. Two types of domains are observed; a defect free hexagonal arrangement of the molecules, with an intermolecular distance of 1.016 nm and a second strained arrangement which exhibits missing-molecule defects. The strained domains have intermolecular distances of 1.071, 0.995 and 0.947 nm. The defects are attributed to the strain field generated by this arrangement of the C_{60} molecules within the domain. The missing-molecule defect for the C_{60} system exhibits a similar ordering to that of the TMA. Each defect has six filled nearest neighbour sites and forms a short range periodic ordering.

STM line profiles of the TMA molecules on the Ag/Si-$\sqrt{3}$ surface have an average height of 0.2 ± 0.05 nm above the substrate, which is inconsistent with the expected size of the upright molecule. However this is consistent with results obtained for TMA on Cu (100) [63] where molecular height was found to be $0.13 - 0.15$ nm. This discrepancy is rationalised by the fact that the STM images reflect the electronic density and not the true topography of the surface. For example, the apparent height of maleic anhydride $C_4O_3H_2$ on silicon exhibits a strong dependence on the

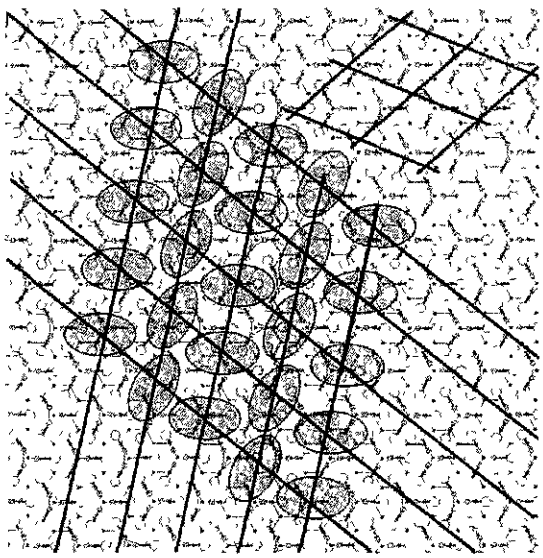

Figure 7.11: Proposed model showing possible end-group bonding sites (shaded ovals), with a lattice of oblique unit cells superimposed. A second lattice with a relative orientation of 15° is shown in upper right hand corner.

bias voltage and is significantly smaller than the true molecular height [179].

From a detailed analysis of the STM and LEED data a model has been constructed of oblique unit cells for the TMA-Ag/Si(111)-$\sqrt{3}$ interface, shown in figure 7.11. The oblique cells are orientated at 23° relative to the substrate unit cell. A second smaller domain is also shown (in red). This domain is aligned at an angle of 15° to the first domain but also, in agreement with the LEED and STM data, at 23° relative to the Ag/Si-$\sqrt{3}$ substrate.

Bonding of the molecules to the surface in an upright configuration must take place through one or two of the carboxyl end-groups of the molecule. The phenyl ring can rotate freely about the C-C bond. This means the aromatic ring can orientate and tilt in any direction regardless of the orientation of a bond between the carboxyl group and the substrate. It is also possible for the molecule to bond though two of the end-groups, this permits a tilting of the molecule but does not allow rotation of the phenol ring about the C-C bond. Resolution of the individual molecules within the island domains has been achieved but no submolecular detail is observed. The orientation of the carboxylate bond between the molecule and the substrate within each oblique unit cell is as yet undetermined because of these bonding and resolution complications. A tentative model of the position of the molecule within the oblique cells is proposed with the relative orientation of the aromatic rings of the molecules taken from STM images. This arrangement of the molecules is indicated with shaded ovals in figure 7.11.

Based on the LEED diffraction patterns, the domains are incommensurate with the substrate, so similar but non-identical bonding sites will be available at the corners of each cell. Limiting the bonding of the molecule to one end-group there are two possible bonding sites available. The distance of 0.22 nm [59] between the two oxygen atoms of the carboxyl end-group allow the molecule to bond to two silver atoms on the same trimer ($\sim$ 0.33 nm), or between the silicon trimer and a silver atom ($\sim$ 0.39 nm) [166]. At the corner of each oblique unit cell one of these bonding sites is available to the molecule. The bonding sites do not align perfectly with the unit cell and this could provide a mechanism for the strain detected in the molecular domains.

7.5 Conclusions

TMA molecules are found to diffuse freely on the Ag/Si(111)-$\sqrt{3}$ surface and form islands in which the ordering is predominantly determined by intermolecular, as opposed to substrate-molecule interactions. Low coverage studies of TMA molecules reveal the nucleation of flat lying molecules at defect sites on the surface. With increased coverage the molecules diffuse freely to coalesce into highly ordered close-packed domains. LEED and STM reveal two domains with 3-fold symmetry with $15° \pm 1°$ rotation relative to each other. This leads to six incommensurate domains each of which are orientated at $23° \pm 1°$ with respect to the substrate hexagonal cell. A surface modulation and a missing molecule defect are mutually exclusive features of the domains. From the analysis it is concluded that both are strain relief mechanisms present in the TMA overlayer. An oblique unit cell is determined by LEED (0.85 ± 0.05 nm and 0.96 ± 0.05 nm) and STM (0.87 ± 0.05 nm and 0.93 ± 0.05 nm) analysis. A tentative bonding configuration for the molecules between two silver trimers or between a silver and silicon trimer within each oblique cell is proposed.

Chapter 8

Conclusions and Future work

8.1 Conclusions

The purpose of this work was to investigate the ordering of organic molecules on templated substrates. A metal was deposited onto the clean Cu(100), Si(100) and Si(111) substrates to create an initial reconstruction which was then used as a template to influence the ordering of a chosen organic molecule. Each substrate was investigated to record what effect the template had on the ordering of the organic molecule, and the stability of the features.

The surface alloy Sn/Cu(100) system was investigated with LEED and for the first time by STM and NIXSW. These new results confirmed the current phase III model structure, altered and further refined the phase I, phase II and phase IV structural models reported in the literature and lead to the discovery of a new structure, phase IIH. The surface alloy formation of the four submonolayer phases I, II, IIH and III was confirmed and phase IV was shown to posses an overlayer structure.

The new STM and NIXSW results for phase I confirmed the model, based on LEED data proposed by McLoughlin et al. [75] as the optimum structure. The modulation of Cu atoms within the Cu channels was noted. A new LEED analysis revealed glide plane symmetries in the phase II structure and in combination with STM and NIXSW results lead to a new model for this phase. The NIXSW results confirmed the different bonding environments of the Sn atoms as a result of the glide plane restrictions on the Sn atom positions within the unit cell.

The new submonolayer phase IIH was reported for the first time. LEED and STM results were used to propose a surface alloy model for this structure. Two different unit cells were proposed for the structure. The model for the phase III structure,

determined from IV LEED measurements by Pussi et al. [78] was confirmed. It was shown to be in excellent agreement with the new experimental results presented in this work, in regard to both the compression of the Sn rows and surface corrugation. A dealloyed structure for phase IV was proposed based on the new STM and NIXSW results. The model of McLoughlin et al. [15] was altered to place the first layer of Sn atoms in the bridge site between substrate Cu atoms. The growth of a second Sn layer on this structure was confirmed.

The carboxylic acid, TMA, was studied on both the clean Cu(100) and the Sn/Cu(100)-phase I surfaces after the in-depth analysis of the Sn/Cu(100) submonolayer phases revealed copper channels were only present in the phase I structure. The TMA structures formed on Cu(100) are unstable at room temperature. The substrate controls the spacing between the molecules leading to the formation of an ordered molecular row structure. This observation is supported by results for other planar molecular species on the low index (110) and (100) Cu substrates [92] [94]. The molecular row spacings are consistent with two lattice spacings of the clean Cu crystal termination. The observed TMA quad structure, formed between four TMA molecules and a Cu adatom, is not unique and similar structures are reported for TMA molecules and Fe atoms co-adsorbed on Cu(100) [89].

The TMA molecules have been observed with STM and LEED modifying the surface in four different ways (i) they induced the phase I structure to reorder into the phase II structure, (ii) they formed molecular rows as they did on the clean Cu(100) surface, (iii) they formed hydrogen bonded cyclic hexamers similar to the motif present in the bulk TMA structure and finally (iv) they bonded to exposed copper atoms at the step edges.

The Sn/Cu(100) surface alloy phase I template was successful in limiting the bonding of the TMA molecules to the Cu substrate atoms. It was not ideal however, as the Sn atoms restructured themselves on the surface and the initial Cu channels in the phase I structure were lost. This clearly shows that the stability of the substrate reconstruction in the presence of the organic molecule is required before any templating will be entirely successful.

The Bi/Si(100)-(2×6) experiments were motivated by the comparable width of the bismuth dimer rows (1.416 nm), within the (2×6) structure, and the length of the pentacene molecule (1.41 nm). An STM study of the pentacene coverage up to a monolayer reveal flat lying molecules lying across the Bi dimer rows. A model for the bonding site was proposed. The LEED and STM analysis of the thin film coverage concluded a double domain commensurate structure was formed with a unit cell of similar dimensions to that of the bulk pentacene structure.

The adsorption of pentacene molecules on the Bi passivated Si(100) surface is influenced by the structure of the missing Bi rows within in the (2×6) reconstruction. However there is strong additional observational evidence for the apparent control exerted by (i) the substrate electronic structure and (ii) the molecular coverage, on the orientation of the pentacene molecule.

Before the NIXSW imaging technique should be applied, careful consideration must be give to the choice of sample. The favourable attributes of the single domain Bi/Si(100)-(2×n) surface were reviewed and the surface was initially investigated with LEED and STM before NIXSW experiments were performed.

The coherent positions and coherent fractions from the recorded NIXSW profiles, summed together with an additional five symmetry equivalent planes, were sufficient to resolve the diamond structure of the silicon atoms within the unit cell. The height of the Bi dimers above the extended silicon planes was predicted from the atomic-density map of the (110) plane and is in agreement with results quoted in the literature [158]. The width of the bismuth dimer was also calculated and although the resolution is poor it has been shown that it is feasible to create a real-space atomic-density map of the bismuth dimer structure.

In a third series of experiments, the Ag/Si(111) passivated surface provided a substrate upon which the TMA intermolecular interaction dominated the molecular-substrate interactions. Both the surface and the molecules possess a high degree of symmetry and it was hoped to produce a network of cyclic hexamers in an overlayer which would be commensurate with respect to the substrate.

STM studies revealed an initial nucleation of unstable flat lying molecules at defect sites on the surface and confirmed the molecules did diffuse freely over the surface. However instead of lying flat and forming cyclic hexamers as observed on the semi-metallic graphite surface [10], with increasing coverage they coalesced into highly ordered close-packed domains, with the molecules in an upright orientation. From the data analysis it was concluded that strain relief mechanisms are present at the TMA overlayer. A tentative bonding configuration for the TMA molecules within an oblique cell was proposed. Further evidence for the apparent control exerted by (i) the substrate electronic structure and (ii) the molecular coverage, on the orientation of molecules is noted.

The observational evidence presented suggests planar acene molecules will adsorb in an upright orientation on semi-metallic surfaces, and conversely lie flat on metallic surfaces. In contrast to this the carboxylic acid adsorbed in an upright orientation on metallic surfaces but lies flat when adsorbed on the semi-metallic graphite surface.

The passivated Ag/Si(111) surface is a good candidate as a substrate for tem-

plates formed from organic molecules, once the possible upright or flat lying orientations of the molecules is considered. This surface along with the passivated Bi/Si(100) surface have applications as substrates for thin film growth as both surfaces produce well-ordered initial molecular growth. Although the active copper channels on the phase I Sn/Cu(100) surface were lost after the adsorption of TMA, the surface did eventually form stable ordered terraces with disordered step edges.

As a general result of these experiments the following attributes should be considered before a templated surface will be successful in exercising control over the ordering of organic molecules, (i) the initial templating must be stable in the presence of the organic molecule (ii) the induced ordering of the organic molecules should be stable at room temperature, (iii) the effect of the electronic structure of the surface on the orientation of the molecules, (iv) where molecule-molecule interactions dominate the size and shape of the molecule and the positions of the end-groups should be considered, (v) where molecular-substrate interaction dominates the bonding sites on the surface should compliment the bonding groups of the molecule.

8.2 Future work

The observational evidence collected here from both the literature and the experiments presented suggest that orientation can indeed be controlled by an astute choice of substrate and molecular coverage. Further work with other molecules containing carboxylic end-groups and other acene molecules, could test these observations.

The coverage dependant orientation of molecules should be investigated further. To this end the Bi/Si(100)-(2×n) surface provides a template for further research into acene molecules. The flat orientation of other acene molecules on passivated surfaces indicated by this work could be confirmed. Tuning the spacing between the bismuth dimer rows with the annealing temperature and then observing what effect this has on the pentacene adsorption is another avenue for future research. The observed coverage dependent orientation of the pentacene molecule would also benefit from further investigation.

The observation that Bi nanolines can form across Si(100) steps requires further study. This might provide the insight required to determine the properties that lead to the formation of the nanolines. This better understanding would give researchers a more educated guess as to which other systems could form similar structures rather than relying on serendipity.

Apart from forming other metallic nanolines on top of the Bi nanolines it would be of interest to consider using the Bi nanolines as a mask. The surrounding Si

surface could be passivated and then the Bi nanolines could be selectively removed to leave clean Si dimers lines on a passivated surface. Preliminary work involving passivating the silicon with an organic molecule and then annealing the sample to remove the Bi nanolines without disrupting the passivated silicon regions has shown very limited success and further study is recommended.

Applying the NIXSW imaging technique to an adsorbed layer has only been reported for the Sn/Ge(111) [16] and Sn/Si(111) [180] surfaces, which is unsurprising considering how challenging the experiments are [181]. It is concluded from this work that the NIXSW imaging technique is more suitable for the analysis of multiple element crystal structure such as muscovite mica [28] or at crystal liquid interface [29]. In relation to adsorbed layers the future of the NIXSW technique appears to be in providing the structural characterisation of surfaces to the complimentary chemical state characterisation provided by photoemission as outlined in a recent publication by Lee et al. [182] for the Sn/Ge(111) surface.

It is hoped the conclusions that have emerged from this study will provoke discussion and prompt further investigations in this area.

Appendix A

NIXSW-Imaging MATLAB analysis code

The MathWorks program MATLAB was used to write a program that would calculate an atomic-density map of the (100) plane from the Fourier component of all the Bragg reflection.

```
% program to process NIXSW data
% Bismuth on silicon 100 surface daresbury data
% test principle on Silicon results for all 12 Bragg planes
clear all
%Miller indices of the planes
HA = [1 -1 -1]; HB = [2 0 -2]; HC = [2 2 0]; HD = [1 1 -1]; HF = [4 0 0]; HG = [3
1 -1]; HI = [1 1 1]; HJ = [1 -1 1]; HK = [3 -1 1]; HL = [2 -2 0]; HM = [2 0 2];
% coherent positions
pA = [0.08]; pB = [1.14]; pC = [1.13]; pD = [0.05]; pF = [0.27]; pG = [1.126]; pI =
[0.08]; pJ = [0.05]; pK = [1.126]; pL = [1.13]; pM = [1.14];
%coherent fractions
fA = [0.634]; fB = [0.504]; fC = [0.636]; fD = [0.55]; fF = [0.79]; fG = [0.376]; fI =
[0.634]; fJ = [0.55]; fK = [0.376]; fL = [0.636]; fM = [0.504];
%coorindates over plane of interest
x=0; y=0; z=0;
k=0; %loop counter outer
for y = 0:.01:1
k = k+1;
l=0; %loop counter inner
```

```
for x = 0:.01:1
z = 0.06;%height above plane in [100]
l = l+1;
r=[x;y;z];
dA = 2*fA*cos(2*pi*(pA-HA*r)); dB = 2*fB*cos(2*pi*(pB-HB*r));
dC = 2*fC*cos(2*pi*(pC-HC*r)); dD = 2*fD*cos(2*pi*(pD-HD*r));
dF = 2*fF*cos(2*pi*(pF-HF*r)); dG = 2*fG*cos(2*pi*(pG-HG*r));
dI = 2*fI*cos(2*pi*(pI-HI*r)); dJ = 2*fJ*cos(2*pi*(pJ-HJ*r));
dK = 2*fK*cos(2*pi*(pK-HK*r)); dL = 2*fL*cos(2*pi*(pL-HL*r));
dM = 2*fM*cos(2*pi*(pM-HM*r));
rhoA(k,l)=(dA); rhoB(k,l)=(dB); rhoC(k,l)=(dC);
rhoD(k,l)=(dD); rhoF(k,l)=(dF); rhoG(k,l)=(dG);
rhoI(k,l)=(dI); rhoJ(k,l)=(dJ); rhoK(k,l)=(dK);
rhoL(k,l)=(dL); rhoM(k,l)=(dM);
end
end
%plot output of Fourier summation
figure
pcolor(1+rhoA+rhoB+rhoC+rhoD+rhoF+rhoG+rhoI+rhoJ+rhoK+rhoL+rhoM)
shading interp axis square
```

This code was altered to produce atomic-density maps of the bismuth dimers in the same plane by simply replacing the coherent positions and coherent fractions of the silicon with those of the bismuth. The code implemented in MATLAB was also used to investigate the {110} plane for both the silicon and bismuth atom positions by simply altering the loops as noted.

```
%coordinates over plane of interest
x=0; y=0; z=0; k=0; %loop counter outer
for z = 0:.01:1
k = k+1;
l=0; %loop counter inner
for x = 0:.01:1
l = l+1;
y=x%hold to 110 plane
r=[x;y;z];
```

References

[1] G. Binnig, H. Rohrer, C. Gerber, and E. Weibel, "Surface studies by scanning tunneling microscopy," *Phys. Rev. Lett.*, vol. 49, p. 57, 1982.

[2] G. Binnig, C. F. Quate, and C. Gerber, "Atomic force microscope," *Phys. Rev. Lett.*, vol. 56, p. 930, 1985.

[3] J. Lehn, *Supramolecular Chemistry: Concepts and Perspectives.* Wiley-VCH, 1995.

[4] Z. Alferov, "Nobel Lecture: The double heterostructure concept and its applications in physics, electronics, and technology," *Rev. Mod. Phys.*, vol. 73, p. 767, 2001.

[5] C. Joanchim, J. K. Gimzewski, and A. Aviram, "Electronics using hybrid-molecular and mono-molecular devices," *Nature*, vol. 408, p. 541, 2000.

[6] S. F. Bent, "Organic functionalization of group iv semiconductor surfaces: principles, examples, applications, and prospects," *Surf. Sci.*, vol. 500, p. 879, 2002.

[7] M. Böhringer, K. Morgenstern, W.-D. Schneider, R. Berndt, F. Mauri, A. D. Vita, and R. Car, "Two-dimensional self-assembly of supramolecular clusters and chains," *Phys. Rev. Lett.*, vol. 83, p. 324, 1999.

[8] J. V. Barth, G. Costantini, and K. Kern, "Engineering atomic and molecular nanostructures at surfaces," *Nature*, vol. 437, pp. 671–679, 2005.

[9] S. K. Ghose, I. K. Robinson, P. A. Bennett, and F. J. Himpsel, "Structure of double row quantum wires in Au/Si(553)," *Surf. Sci.*, vol. 581, pp. 199–206, 2005.

[10] S. Griessl, M. Lackinger, M. Edelwirth, M. Hietschold, and W. M. Heckl, "Self-assembled two-dimensional molecular host-guest architectures from trimesic acid," *Single Molecules*, vol. 3, p. 25, 2002.

[11] J. A. Theobald, N. S. Oxtoby, M. A. Phillips, N. R. Champness, and P. H. Beton, "Controlling molecular deposition and layer structure with supramolecular surface assemblies," *Nature*, vol. 424, pp. 1029–1031, 2003.

[12] F. Rosei, M. Schunack, P. Jiang, A. Gourdon, E. Lgsgaard, I. Stensgaard, C. Joachim, and F. Besenbacher, "Organic molecules acting as templates on metal surfaces," *Science*, vol. 296, pp. 328–331, 2002.

[13] J. H. G. Owen, "Early investigator and author of the latest Bi nanoline review." 2006, private communication.

[14] J. H. G. Owen and K. Miki, "1-D Epitaxial Growth of Indium on a Self-Assembled atomic-scale Bismuth template," *Nanotechnology*, vol. 17, pp. 430–433, 2006.

[15] E. McLoughlin, "Structural investigations of metal and semiconductor interfaces," Ph.D. dissertation, Dublin City University, 2000.

[16] J. S. Okasinski, C. Y. Kim, D. A. Walko, and M. J. Bedzyk, "X-ray standing wave imaging of the $^1/_3$ monolayer Sn/Ge(111) surface," *Phys. Rev. B*, vol. 69, p. 041401, 2004.

[17] K. Hermann and M. A. Van Hove, *LEEDpat Version 2.0*, 2006. [Online]. Available: http://electron.lbl.gov/software/intsoftware.html

[18] C. Davisson and L. H. Germer, "Diffraction of electrons by a crystal of nickel," *Phys. Rev. B*, vol. 30, p. 705, 1927.

[19] L. J. Clarke, *Surface Crystallography, An Introduction to Low Energy Electron Diffraction.* Wiley, 1985.

[20] Omicron NanoTechnology GmbH, *Users manual*, 2002. [Online]. Available: http://www.omicron.de

[21] J C. Vickerman (Editor), *Surface Analysis - The Principal Techniques.* John Wiley & Sons, 2003.

[22] M. A. Van Hove and W. H. Weinberg and C. M. Chan, *Low-Energy Electron Diffraction.* Springer Verlag Berlin Heidelberg, 1986.

[23] C. Kittel, *Introduction to Solid State Physics* 7^{th} *Edition.* John Wiley & Sons, 1996.

[24] D. P. Woodruff, "Surface structure determination using X-ray standing waves," *Rep. Prog. Phys.*, vol. 68, pp. 743–98, 2005.

[25] J. Zegenhagen, "Surface structure determination with X-ray standing waves," *Surf. Sci. Reports*, vol. 18, pp. 199–271, 1993.

[26] D. P. Woodruff, "Normal incidence X-ray standing wave determination of adsorbate structures," *Prog. Surf. Sci.*, vol. 57, 1988.

[27] R. Miller, G. T. Deditta, R. Jones, D. A. Lang, C. M. Weeks, and H. A. Hauptmann, "On the application of the minimal principle to solve unknown structures," *Science*, vol. 259, p. 1430, 1993.

[28] L. Cheng, P. Fenter, M. J. Bedzyk, and N. C. Sturchio, "Fourier-expansion solution of atom distributions in a crystal using X-Ray Standing Waves," *Phys. Rev. Lett.*, vol. 90, p. 255503, 2003.

[29] Z. Zhang, P. Fenter, L. Cheng, N. C. Sturchio, M. J. Bedzyk, M. L. Machesky, and D. J. Wesolowski, "Model-independent X-ray imaging of adsorbed cations at the crystalwater interface," *Surf. Sci. Lett.*, vol. 554, p. L95, 2004.

[30] H. Wiedemann, *Synchrotron Radiation.* Springer, 2003.

[31] V. R. Dhanak, *Daresbury Synchrotron Radiation Source,* 2006. [Online]. Available: http://www.srs.ac.uk/srs/stations/station4.2.htm

[32] G. Van Der Laan and B. T. Thole, "Determination of glitches in soft X-ray monochromator crystals," *Nuclear Inst. and methods in physics research*, vol. A263, p. 515, 1988.

[33] J. C. Woicik, T. Kendelewicz, K. E. Miyano, P. L. Cowan, M. Richter, B. A. Karlin, C. E. Bouldin, P. Pianetta, and W. E. Spicer, "Extended X-ray absorption fine structure and X-ray standing wave study of the clean InP(110) surface relaxation," *J. Vac. Sci. Technol. A*, vol. 10, p. 2041, 1992.

[34] R. G. Jones, "Nixsw99#1," 2006, XSW analysis program, Dept. of Chemistry, University of Nottingham, Nottingham, UK.

[35] Wavemetrics Ltd., *Igor Pro Version 4.0*, 2006. [Online]. Available: http://www.wavemetrics.com/

[36] M. S. del Rio (ESRF) and R. J. Dejus (APS), *X-ray Oriented Programs (XOP)*, 2006. [Online]. Available: http://www.esrf.fr/computing/scientific/xop2.1/

[37] J. J. Lee, C. J. Fisher, D. P. Woodruff, M. G. Roper, and R. G. Jones, "Non-dipole effects in photoelectron-monitored X-ray standing wave experiments: characterization and calibration," *Surf. Sci.*, vol. 494, pp. 166–182, 2001.

[38] Nanotec Electronica, 2006. [Online]. Available: http://www.nanotec.es

[39] H. C. O'Hanian, *Modern Physics, 2nd Edition.* Prentice Hall International, 1987.

[40] A. Rae, *Quantum Mechanics, 3rd Edition.* Institute of Physics Publishing, 1992.

[41] R. Wiesendanger, *Scanning Probe Microscopy and Spectroscopy Methods and Applications.* Cambridge University Press, 1998.

[42] J. Tersoff and D. R. Hamann, "Theory and application for the scanning tunneling microscope," *Phys. Rev. Lett.*, vol. 50, p. 1998, 1983.

[43] J. Tersoff and D. R. Hamamn, "Theory of the scanning tunneling microscope," *Phys. Rev. B.*, vol. 31, p. 805, 1985.

[44] D. A. Bonnell, *Scanning Tunneling Microscopy and Spectroscopy Theory, Techniques, and Applications.* VCH Publishers, 1993.

[45] J. A. Stroscio (Editor) and W. J. Kaiser (Editor), *Scanning Tunneling Microscopy (Experimental Methods in the Physical Sciences).* Academic Press, 1994.

[46] J. P. Ibe, P. P. Bey, S. L. Brandow, R. A. Brizzolara, N. A. Burnham, D. P. DiLella, K. P. Lee, C. R. K. Marrian, and R. J. Colton, "On the electrochemical etching of tips for scanning tunneling microscopy," *J. Vac. Sci. Technol. A*, vol. 8 (4), p. 3570, 1990.

[47] G. Sheerin, "An etching apparatus for the preparation of tungsten tips for scanning tunnling microscopy," 2002, Department of Physical Sciences.

[48] W. A. Hofer, "Challenges and errors: interpreting high resolution images in scanning tunneling microscopy," *Prog. Surf. Sci.*, vol. 71, p. 147, 2003.

[49] L. R. Apker, "Surface phenomena useful in vacuum technique," *Ind. Eng. Chem*, vol. 40, pp. 846–847, 1948.

[50] G. Attard and C. Barnes, *Surfaces.* Oxford University Press, 1998.

[51] R. Nix, *An Introduction to Surface Chemistry*, 2006. [Online]. Available: http://www.chem.qmul.ac.uk/surfaces/scc/

[52] C. D. Dimitrakopoulos, J. Kymissis, S. Purushothaman, D. A. Neumayer, P. R. Duncombe, and R. B. Laibowitz, "Low-voltage, high-mobility pentacene transistors with solution-processed high dielectric constant insulators," *Adv. Mater.*, vol. 11, p. 1372, 1999.

[53] C. D. Dimitrakopoulos, A. R. Brown, and A. Pomp, "Molecular beam deposited thin films of pentacene for organic field effect transistor applications," *J. Appl. Phys.*, vol. 80, p. 2501, 1996.

[54] F.-J. M. zu Heringdorf, M. C. Reuter, and R. M. Tromp, "Growth dynamics of pentacene thin films." vol. 412, p. 517, 2001.

[55] P. G. Schroeder, C. B. France, J. B. Park, and B. A. Parkinson, "Energy level alignment and two-dimensional structure of pentacene on Au(111) surfaces," *J. Appl. Phys.*, vol. 91, p. 3010, 2002.

[56] L. Casalis, M. F. Danisman, B. Nickel, B. Bracco, T. Toccoli, S. Ianotta, and G. Scoles, "Hyperthermal molecular beam deposition of highly ordered organic thin films," *Phys. Rev. Lett.*, vol. 90, p. 206101, 2003.

[57] Q. Chen, A. J. McDowall, and N. V. Richardson, "Ordered Structures of Tetracene and Pentacene on Cu(110) Surfaces," *Langmuir*, vol. 19, p. 10164, 2003.

[58] R. B. Campbell, J. M. Robertson, and J. Trotter, "The crystal and molecular structure of pentacene," *Acta. Crystallogr.*, vol. 14, p. 705, 1961.

[59] D. J. Duchamp and R. E. Marsh, "The crystal structure of Trimesic Acid (Benzene-1,3,5-tricarboxylic Acid)," *Acta. Cryst.*, vol. B25, p. 5, 1969.

[60] S. V. Kolotuchin, P. A. Thiessen, E. E. Fenlon, S. R. Wilson, C. J. Loweth, and S. C. Zimmerman, "Self-assembly of 1,3,5-benzenetricarboxylic (trimesic) acid and its analogues," *Chem. Eur. J.*, vol. 5, p. 2537, 1999.

[61] S. Chatterjee, V. R. Pedireddi, A. Ranganathan, and C. N. R. Rao, "Self-assembled four-membered networks of trimesic acid forming organic channel structures," *J. Mol. Struct.*, vol. 520, p. 107, 2000.

[62] S. C. Zimmerman, "Putting molecules behind bars," *Science*, vol. 276, p. 543, 1997.

[63] A. Dmitriev, N. Lin, J. Weckesser, J. V. Barth, and K. Kern, "Supramolecular Assemblies of Trimesic Acid on a Cu(100) surface," *J. Phys. Chem. B*, vol. 106, pp. 6907–6912, 2002.

[64] G. J. Su, H. M. Zhang, L. J. Wan, C. L. Bai, and T. Wandlowski, "Potential-induced phase transition of Trimesic acid adlayer on Au(111)," *J. Phys. Chem. B*, vol. 108, pp. 1931–1937, 2004.

[65] A. Dmitriev, N. Lin, J. Weckesser, J. V. Barth, and K. Kern, "Supermolecular assemblies of trimesic acid on Cu(100) surfaces," *J. Phys. Chem. B*, vol. 106, pp. 6907–6912, 2002.

[66] J. Tersoff, "Surface-Confined Alloy Formation in Immiscible Systems," *Phys. Rev. Lett.*, vol. 74, p. 434, 1995.

[67] J. A. Venables, "Atomic processes in crystal growth," *Surf. Sci.*, vol. 299/300, p. 798, 1994.

[68] G. E. Rhead, C. Argile, and M. G. Barthes, "Quantitative auger electron spectroscopy of metal monolayers on metals: Evidence for adsorbate/substrate interface effects," *Surf. Interf. Anal.*, vol. 3, p. 165, 1981.

[69] U. Bardi, "The atomic structure of alloy surfaces and surface alloys," *Rep. Prog. Phys.*, vol. 57, p. 939, 1994.

[70] G. A. Somorjai, *Introduction to Surface Chemistry and Catalysis.* John Wiley and Sons, 1994.

[71] P. D. Woodruff (Editor), *The Chemical Physics of Solid Surfaces: Surface Alloys and Alloy Surfaces.* Elisevier, 2002.

[72] D. Ghaleb and B. Perraillon, "Anisotropy of surface diffusion of silver on (331) and (110) clean copper surface at low temperature," *Surf. Sci*, vol. 162, p. 103, 1985.

[73] C. Argile and G. E. Rhead, "Growth of metal monolayers and ultrathin films on copper: simple and bimetallic layers of lead and tin," *Thin Solid Films*, vol. 87, p. 265, 1982.

[74] F. Abel, C. Cohen, J. A. Davies, D. Moulin, and D. Schmaus, "Thin-film growth of Sn on Cu(100)," *Appl. Surf. Sci.*, vol. 44, p. 17, 1990.

[75] E. McLoughlin, A. A. Cafolla, E. AlShamaileh, and C. J. Barnes, "A re-interpretation of the Cu{100}/Sn surface phase diagram," *Surf. Sci.*, vol. 428-485, pp. 1431-1439, 2001.

[76] H. L. Meyerheim, M De Santis, W. Moritz, and I. K. Robinson, "Domain-wall interactions in Bi/Cu(001)," *Surf. Sci.*, vol. 418, p. 295, 1998.

[77] G. Sheerin, "Bi/Cu(100)," 2003, unpublished STM and STS results.

[78] K. Pussi, E. McLoughlin, E. AlShamaileh, A. A. Cafolla, and M. Lindroos, "Determination of the structure of Cu{100}-p($3\sqrt{2}\times\sqrt{2}$)R45 °-Sn," *Surf. Sci.*, vol. 549, pp. 24–30, 2004.

[79] M. A. Hove, W. Mortiz, H. Over, P. J. Rous, A. Wander, A. Barbieri, N. Materer, U. Starke, and G. A. Somorjai, "Automated determination of complex surface structures by LEED," *Surf. Sci. Rep.*, vol. 19, p. 191, 1993.

[80] E. McLoughlin, 2003, private communication.

[81] H. H. Farrell and G. A. Somorjai, "Properties of the Nonspecular Low-Energy Electron Diffraction Beams Scattered by the (100) Face of Face-Centered-Cubic Metal Single Crystals," *Phys. Rev.*, vol. 182, p. 751, 1969.

[82] J. R. Noonan and H. L. Davis, "1979 LEED analysis of Cu(100)," *J. Vac. Sci. Technol.*, vol. 17, p. 194, 1980.

[83] F. Besenbacher, "Scanning tunnelling microscopy studies of metal surfaces," *Rep. Prog. Phys.*, vol. 59, p. 1737, 1996.

[84] B. Aufray, H. Giordano, and D. N. Seidman, "A scanning tunneling microscopy study of surface segregation of Sb at a Cu(111) surface," *Surf. Sci.*, vol. 447, p. 180, 2000.

[85] G. Gilarowski and H. Niehus, "Iridium on Cu(100): Surface Segregation and Alloying," *Phys. Stat. Sol*, vol. 173, p. 159, 1999.

[86] C. Argile and G. E. Rhead, "Adsorbed layer and thin film growth modes monitored by Auger electron spectroscopy," *Surf. Sci. Rep.*, vol. 10, p. 1794, 1989.

[87] Atomic radius: radius of the maximum distance that an e- (charge density) can exist in the outermost shell. Referred to as metallic radii, based on $^1/_2$ bond length in pure metals.

[88] B. C. Cowie, "Argand diagram representation of the coherent fraction and coherent position," 2003, Excel spreadsheet which exploits the Argand diagram to interpret multiple adsorption sites.

[89] P. Messina, A. Dmitriev, N. Lin, H. Spillman, M. Abel, J. V. Barth, and K. Kern, "Direct observation of chiral metal-organic complexes assembled on a Cu(100) surface," *J. Am. Chem. Soc.*, vol. 124, pp. 14 000–14 001, 2002.

[90] G. Sheerin and A. A. Cafolla, "Self-assembled structures of trimesic acid on the Ag/Si(111)-($\sqrt{3} \times \sqrt{3}$)R30° surface," *Surf. Sci.*, vol. 577, pp. 211–219, 2005.

[91] NIST Mass Spec Data Center, *Mass Spectrum of 1,3,5-Benzenetricarboxylic acid*, 2006. [Online]. Available: http://webbook.nist.gov/

[92] S. Poulston, R. A. Bennett, A. H. Jones, and M. Bowker, "STM study of formic acid adsorption on Cu(110)," *Phys. Rev. B*, vol. 55, p. 12888, 1997.

[93] T. Wagner, A. Bannani, C. Bobisch, M. Fendrich, H. Karacuban, and R. Möller, "Adsorption of PTCDA on Cu(100)," *Ecoss 23, Berlin*, 2005.

[94] T. Wagner, "Adsorption of PTCDA on Cu(100)," 2005, private communication.

[95] M. Sambi, G. Granozzi, M. Casarin, G. A. Rizzi, A. Vittandini, L. Caputi, and G. Chiarello, "Surface carboxylate species on Cu(100) studied by angle-scanned photoelectron diffraction and LCAO-LDF calculations," *Surf. Sci*, vol. 309, p. 322, 1994.

[96] L. S. Caputi, G. Chiarello, M. G. Lancellotti, G. A. Rizzi, M. Sambi, and G. Granozzi, "Azimuthal orientation of formate and acetate on Cu(100) studied by angle-resolved photoelectron diffraction," *Surf. Sci. Lett.*, vol. 291, pp. L756–L758, 1993.

[97] D. P. Woodruff, C. F. McConville, J. Somers, M. Surman, A. L. D. Kilcoyne, T. Lindner, G. Paolucci, and A. M. Bradshaw, "Photoelectron diffraction from oxygen containing species on Cu(100)," *Surf. Sci.*, vol. 201, pp. 228–244, 1988.

[98] D. P. Woodruff, C. F. McConville, A. L. D. Kilcoyne, T. Lindner, J. Somers, M. Surman, G. Paolucci, and A. M. Bradshaw, "The structure of the formate species on copper surfaces: new photoelectron diffraction results and SEXAFS data reassessed," *Surf. Sci*, vol. 201, p. 228, 1988.

[99] K. U. Weiss, R. Dippel, K. M. Schindler, P. Gardner, V. Frietzsche, A. Bradshaw, A. Kilcoyne, and D. Woodruff, "Chemical shift photoelectron diffraction from molecular adsorbates," *Phys. Rev. Lett.*, vol. 69, 1992.

[100] S. P. Mehandru and A. B. Anderson, "Formate adsorption and azimuthal orientation of Cu(100) from molecular orbital theory," *Surf. Sci.*, vol. 68, p. 76, 1989.

[101] J. A. Kerr, *CRC Handbook of Chemistry and Physics 1999-2000 : A Ready-Reference Book of Chemical and Physical Data.* CRC Press, 2000.

[102] R. J. Madix and J. Benziger, "Kinetic Processes on Metal Single-Crystal Surfaces," *Annual Review of Physical Chemistry*, vol. 29, pp. 285–306, 1978.

[103] C. M. Friend and X. Xu, "Reactions on Transition Metal Surfaces," *Annual Review of Physical Chemistry*, vol. 42, pp. 251–278, 1991.

[104] J. R. B. Gomes and J. A. N. F. Gomes, "Adsorption of the formate species on copper surfaces: a DFT study," *Surf. Sci.*, vol. 432, pp. 279–290, 1999.

[105] B. A. Sexton, "Surface vibrations of adsorbed intermediates in the reaction of alcohols with Cu(100)," *Surf. Sci.*, vol. 88, p. 319, 1979.

[106] L. H. Dubois, T. H. Ellis, B. R. Zegarski, and S. D. Kevan, "New insights into the kinetics of formic acid decomposition on copper surfaces," *Surf. Sci.*, vol. 172, p. 385, 1986.

[107] J. Stohr, D. Outka, R. J. Madix, and U. Dobler, "Evidence for a Novel Chemisorption Bond: Formate (HCO_2) on Cu(100)," *Phys. Rev. Lett.*, vol. 54, p. 1256, 1985.

[108] D. Outka, R. J. Madix, and J. Stohr, "Structural studies of formate and methoxy groups on the Cu(100) surface using NEXAFS and SEXAFS," *Surf. Sci.*, vol. 164, p. 235, 1985.

[109] M. D. Crapper, C. Riley, and D. P. Woodruff, "Normal Versus Anomalous Formate-Copper Surface Bonding and the Application of X-Ray-Absorption

Fine-Structure Studies to Molecular Adsorption," *Phys. Rev. Lett.*, vol. 57, p. 2598, 1986.

[110] M. D. Crapper, C. E. Riley, and D. P. Woodruff, "The structure of formate on Cu(100) and Cu(110) surfaces," *Surf. Sci.*, vol. 184, p. 121, 1987.

[111] A. Wander and B. W. Holland, "The structure of formate on Cu(100)," *Surf. Sci.*, vol. 199, p. L403, 1988.

[112] S. P. Mehandru and A. B. Anderson, "Formate adsorption and azimuthal orientation on Cu(100) from molecular orbital theory," *Surf. Sci.*, vol. 219, pp. 68,, 1989.

[113] M. Casarin, G. Granozzi, M. Sambi, and E. Tondello, "A LCAO-LDF study of formate chemisorption on Cu(100)," *Surf. Sci.*, vol. 307, p. 95, 1994.

[114] J. T. Sadowski, T. Nagao, S. Yaginuma, Y. Fujikawa, A. Al-Mahboob, K. Nakajima, T. Sakuraki, G. E. Thayer, and R. M. Tromp, "Thin bismuth film as a template for pentacene growth," *App. Phys. Lett.*, vol. 86, p. 073109, 2005.

[115] Z.Zhu, N. Shima, and M. Tsukdad, "Electronic states of Si(100) reconstructed surfaces," *Phys. Rev. B*, vol. 40, p. 11868, 1989.

[116] P. Badziag and W. S. Verwoerd and M. A. Van Hove, "Prediction of the effect of the sample biasing in scanning tunneling microscopy and of surface defects on the observed character of the dimers in the Si(001)-(2×1) surface," *Phys. Rev. B*, vol. 43, pp. 2058–2062, 1991.

[117] R. A. Wolkow, "Direct observation of an increase in buckled dimers on Si(001) at low temperature," *Phys. Rev. Lett.*, vol. 68, pp. 2636–2639, 1992.

[118] K. Hata, Y. Sainoo, and H. Shigekawa, "Atomically resolved local variation of the barrier height of the flip-flop motion of single buckled dimers of Si(100)," *Phys. Rev. Lett.*, vol. 86, no. 14, pp. 3084–3087, 2001.

[119] J. Koo, J. Yi, C Hwang, D. Kim, and S. Lee, "Dimer-vacancy defects on the Si(001)-2×1 and the Ni-contaminated Si(001)-2×n surfaces," *Phys. Rev. B*, vol. 52, p. 17269, 1995.

[120] T. Hanada and M. Kawai, "Surface structure and oxidation of Si(001) single bond - Bi," *Vacuum*, vol. 41, p. 650, 1990.

[121] K. Sakamoto, K. Kyoya, K. Miki, H. Matsuhata, and T. Sakamoto, "Which surfactant shall we choose for the heteroepitaxy of Ge/Si(001)?-Bi as a surfactant with small self-incorporation-," *Jpn. J. Appl. Phys.*, vol. 32, p. L204, 1993.

[122] W. C. Fan, N. J. Wu, and A. Ignatiev, "Determination of a Bi-induced (1×1 structure of the Si(100) surface," *Phys. Rev. B*, vol. 45, p. 14167, 1992.

[123] H. P. Noh, C. Park, D. Jeon, K. Cho, T. Hashizume, Y. Kuk, and T. Sakurai, "Adsorption of Bi on Si(001) surface: An atomic view," *J. Vac. Sci. Technol. B*, vol. 12, pp. 2097–2099, 1994.

[124] K. Miki, J. H. G. Owen, D. R. Bowler, G. A. D. Briggs, and K. Sakamoto, "Bismuth-induced structures on Si(100) surfaces," *Surf. Sci.*, vol. 421, p. 397, 1999.

[125] J. H. G. Owen and D. R. Bowler, "Self-assembled nanowires on semiconductor surfaces," *J. Mat. Sci.*, vol. In press, 2006, dOI:10.1007/s10853-006-0246-x.

[126] K. Miki, D. R. Bowler, J. H. G. Owen, G. A. D. Briggs, and K. Sakamoto, "Atomically perfect bismuth lines on Si(001)," *Phys. Rev. B*, vol. 59, p. 14868, 1999.

[127] J. H. G. Owen, D. R. Bowler, and K. Miki, "Bi nanoline passivity to attack by radical hydrogen or oxygen," *Surf. Sci.*, vol. 499, pp. L124–L128, 2002.

[128] R. H. Miwa and G. P. Srivastava, "Self-organised Bi lines on the Si(100) surface: A theoretical study," *Phys. Rev. B*, vol. 66, p. 235317, 2002.

[129] J. M. MacLeod, C. P. Lima, R. H. Miwa, G. P. Srivastava, and A. B. McLean, "Bismuth nanolines on Si(001) and their influence on mesoscopic surface structure," *Mat. Sci. Technol.*, vol. 20, p. 951, 2004.

[130] J. M. MacLeod and A. B. McLean, "Single 2×1 domain orientation on Si(001) surfaces using aperiodic Bi line arrays," *Phys. Rev. B*, vol. 70, p. R041306, 2004.

[131] A. McLean, *Bismuth nanolines on Si(001) and their influence on mesoscopic surface structure*, 2006, 78Fig4.pdf reproduced with kind permission of author. [Online]. Available: http://physics.queensu.ca/~nanophys/papers.html

[132] C. Park, R. Z. Bakhtizin, T. Hashizume, and T. Sakurai, "Ordering of missing-row-defects forming (2×n)-Bi phases on the Si(100) 2×1 surface studied by the Scanning Tunneling Microscopy," *Jpn. J. Appl. Phys.*

[133] A. Kawazu, T. Otsuki, and G. Tominaga, "Growth of bismuth layers on Si(100) surfaces," *Jpn. J. Appl. Phys.*, vol. 20, p. 553, 1981.

[134] L. Gavioli, M. G. Betti, and C. Mariani, "Electronic properties of $(2\times n)$-Bi reconstructions on Si(100)," *Surf.Sci.*, vol. 377-379, p. 215, 1997.

[135] T. Hanada and M. Kawai, "Study of successive phase transitions of the Si(001)-Bi surface by RHEED," *Surf. Sci.*, vol. 242, p. 137, 1991.

[136] C. Park, R. Z. Bakhtizin, T. Hashizume, and T. Sakurai, "Strain relief and ordering of (2×n)-Bi structure on Si(100)," *J. Vac. Sci. Technol. B*, vol. 12, p. 2049, 1994.

[137] M. Naitoh, H. Shimaya, S. Nishigaki, N. Oishi, and F. Shoji, "Scanning tunneling microscopy observation of bismuth growth on Si(100) surfaces," *Surf. Sci.*, vol. 377-379, p. 899, 1997.

[138] A. G. Mark, J. A. Lipton-Duffin, J. M. MacLeod, R. H. Miwa, G. P. Srivastava, and A. B. McLean, "The electronic properties of Si(001)Bi$(2 \times n)$," *J. Phys. Condens. Matt.*

[139] Y. He and J. G. Che, "Stress relief from missing dimers on Bi/Si(001)," *Surf. Sci*, vol. 569, p. 176, 2004.

[140] M. Naitoh, M. Takeia, S. Nishigakia, N. Oishib, and F. Shojic, "Scanning tunneling microscopy observation of Bi-induced surface structures on the Si(100) surface," *Surf. Sci.*, vol. 482-485, p. 1440, 2001.

[141] S. Lukas, G. Witte, and C. Wöll, "Novel mechanism for molecular self-assembly on metal substrates: Unidirectional rows of pentacene on Cu(110) produced by a substrate-mediated repulsion," *Phys. Rev. Lett.*, vol. 88, pp. 028 301–1, 2002.

[142] G. E. Thayer, J. T. Sadowski, F. M. zu Heringdorf, T. Sakuraki, and R. M. Tromp, "Role of surface electronic structure in thin film molecular ordering," *Phys. Rev. Lett.*, vol. 95, p. 256106, 2005.

[143] J. H. Kang and X.-Y. Zhu, "π-stacked pentacene thin films grown on Au(111)," *Appl. Phys. Lett.*, vol. 82, p. 3248, 2003.

[144] P. G. Schroeder, C. B. France, J. B. Park, and B. A. Parkinson, "Energy level alignment and two-dimensional structure of pentacene on Au(111) surfaces," *J. Appl. Phys.*, vol. 91, p. 3010, 2002.

[145] G. Beernink, T. Strunskus, G. Witte, and C. Wöll, "Importance of dewetting in organic molecular-beam deposition: Pentacene on gold," *Appl. Phys. Lett.*, vol. 85, p. 398, 2004.

[146] Y. L. Wang, W. Ji, D. X. Shi, S. X. Du, C. Seidel, Y. G. Ma, H.-J. Gao, L. Chi, and H. Fuchs, "Structural evolution of pentacene on a Ag(110) surface," *Phys. Rev. B*, vol. 69, p. 075408, 2004.

[147] L. Casalis, M. F. Danisman, B. Nickel, G. Bracco, T. Toccoli, S. Iannotta, and G. Scoles, "Hyperthermal molecular beam deposition of highly ordered organic thin films," *Phys. Rev. Lett.*, vol. 90, p. 206101, 2003.

[148] S. Lukas, S. Sahnchen, G. Witte, and C. Wall, "Epitaxial growth of pentacene films on metal surfaces," *ChemPhysChem*, vol. 5, p. 266, 2004.

[149] P. Guaino, D. Carty, G. Hughes, P. Moriarty, and A. A. Cafolla, "Scanning tunneling microscopy study of pentacene adsorption on Ag/Si(111)-$(\sqrt{3} \times \sqrt{3})$R30°," *Appl. Surf. Sci.*, vol. 212-213, p. 537, 2003.

[150] J. Dabrowski, *Silicon surfaces and formation of interfaces : basic science in the industry.* World Scientific, 2000.

[151] E. Pelhke and J. Tersoff, "Nature of the step-height transition on vicinal Si(001) surfaces," *Phys. Rev. Lett.*, vol. 67, p. 465, 1991.

[152] E. Pehlke and J. Tersoff, "Phase diagram of vicinal Si(001)," *Phys. Rev. Lett.*, vol. 67, p. 1290, 1991.

[153] Y. J. Lee, S. Y. Lee, and S. Kim, "Reconstructions and step structures on vicinal Si(001) surfaces by interaction with Bi," *J. Phys.: Condens. Matt.*, p. 1953, 1990.

[154] K. S. Kim, Y. Takakuwa, Y. Mori, and S. Kono, "Reflection high energy electron diffraction and Auger electron spectroscopy (RHEED-AES) observation of Bi desorption from a single-domain Si(001)2×1-Bi surface," *Jpn. J. Appl. Phys.*, vol. 35, pp. L1695–L1698, 1996.

[155] J. Wasserfall and W. Ranke, "Step topography of Si(001) vicinal, clean and after deposition of As, Sb and Bi," *Surf. Sci.*, vol. 331-333, pp. 1099–1104, 1995.

[156] M. Shimomura, K. Miki, T. Abukawa, and S. Kono, "Structures of the "nanowire" and 2×n of Bi/Si(001)," *Surface Science Letters*, vol. 447, pp. L169–L174, 2000.

[157] The MathWorks, *Matlab, The language of technical computing. Version 7*, 2004.

[158] G. E. Franklin, S. Tang, J. W. Woicik, M. J. Bedzyk, A. J. Freeman, and J. A. Golovchenko, "High-resolution structural study of Bi on Si(001)," *Phys. Rev. B.*, vol. 52, p. R5515, 1995.

[159] N. Jedrecy, L. Gavioil, C. Mariani, V. Corradini, M. G. Betti, B. Croset, and C. de Beauvais, "Structure and missing-dimer probability distribution of the (2×n) bi-induced Si(001) surface," *Surf. Sci.*, vol. 433-435, pp. 367–372, 1999.

[160] N. Oishi, N. Saitho, M. Naitoh, S. Nishigaki, F. Shoji, S. Nakanishi, and K. Umezawa, "A structural analysis of Bi/Si(100) 2×n surfaces by iciss," *Appl. Surf. Sci.*, vol. 212-213, pp. 373–377, 2003.

[161] K. Chuasiripattana and G. P. Srivastava, "Progressive changes in atomic structure and gap states on Si(001) by Bi adsorption," *Surf. Sci.*, vol. 574, pp. 43–51, 2005.

[162] W. Monch, *Semiconductor Surfaces and Interfaces, 2nd Edition.* Springer Verlag: Berlin, 1987.

[163] K. Takayanagi, Y. Tanishiro, M. Takahashi, and S. Takahashi, "Structural analysis of Si(111)-(7 × 7) by UHV-transmission electron diffraction and microscopy," *J. Vac. Sci. Technol. A*, vol. A3, p. 1502, 1984.

[164] M. Fujita and H. Nagayoshi, "Electronic structure of the DAS model for the Si(111) (7 × 7) reconstructed surface by energy band calculations," *Surf. Sci.*, vol. 242, p. 229, 1991.

[165] J. Quinn, F. Jona, and P. M. Marcus, "Atomic structure of Si{111} ($\sqrt{3} \times \sqrt{3}$)R30°-Au," *Phys. Rev. B*, vol. 46, pp. 7288–7291, 1992.

[166] T. Takahashi, S. Nakatani, N. Okamoto, T. Ichikawa, and S. Kikuta, "A study of the Si(111)($\sqrt{3} \times \sqrt{3}$)-Ag surface by transmission X-ray diffraction and X-ray diffraction topography," *Surf. Sci.*, vol. 242, pp. 54–58, 1991.

[167] P. Morgen, M. Szymonski, J. Onsgaard, B. J rgensen, and G. Rossi, "Formation of the Pt/Si(111) interface," *Surf. Sci*, vol. 197, pp. 347–362, 1988.

[168] H. Öfner, S. L. Surnev, Y. Shapira, and F. P. Netzer, "In overlayers on Si(111) 7×7: Growth and evolution of the electronic structure," *Phys. Rev. B*, vol. 48, pp. 10 940–10 949, 1993.

[169] V. K. Paliwal, A. G. Vedeshwar, and S. M. Shivaprasad, "Residual thermal desorption study of the room temperature formed Sb/Si(111) interface," *Phys. Rev. B*, vol. 66, p. 245404, 2002.

[170] K. J. Wan, T. Guo, W. K. Ford, and J. C. Hermanson, "Initial growth of Bi films on a Si(111) substrate: Two phases of $\sqrt{3} \times \sqrt{3}$ low energy electron diffraction pattern and their geometric structures," *Phys. Rev. B*, vol. 44, pp. 3471–3474, 1991.

[171] H. H. Weitering and D. R. Heslinga, "Structure and growth of epitaxial Pb on Si(111)," *Phys. Rev. B*, vol. 45, pp. 5991–6002, 1992.

[172] R. I. G. Uhrberg, H. M. Zhang, T. Balasubramanian, E. Landemark, and H. W. Yeom, "Photoelectron spectroscopy study of Ag/Si(111)$\sqrt{3} \times \sqrt{3}$ and the effect of additional Ag adatoms," *Phys. Rev. B.*, vol. 65, p. 081305 R, 2002.

[173] M. D. Upward, P. Moriarty, and P. H. Benton, "Double domain ordering and selective removal of C_{60} on Ag/Si(111)- ($\sqrt{3} \times \sqrt{3}$)R30°," *Phys. Rev. B*, vol. 56, p. R1704, 1997.

[174] M. J. Butcher, J. W. Nolan, M. R. C. Hunt, P. H. Beton, L. Dunsch, P. Kuran, P. Georgi, and T. J. S. Dennis, "Orientationally ordered island growth of higher fullerenes on Ag/Si(111)- ($\sqrt{3} \times \sqrt{3}$)R30°," *Phys. Rev. B*, vol. 64, p. 195401, 2001.

[175] M. D. Upward, P. H. Beton, and P. Moriarty, "Adsorption of cobalt phthalocyanine on Ag terminated Si(111)," *Surf. Sci.*, vol. 441, p. 21, 1999.

[176] P. Guaino, A. A. Cafolla, D. Carty, G. Sheerin, and G. Hughes, "An STM investigation of the interaction and ordering of pentacene molecules on the Ag/Si(111)-($\sqrt{3}\times\sqrt{3}$)R30° surface," *Surf. Sci.*, vol. 540, p. 107, 2003.

[177] E. J. van Loenen, J. E. Demuth, R. M. Tromp, and R. J. Hamers, "Local electron states and surface geometry of Si(111)-$\sqrt{3} \times \sqrt{3}$ Ag," *Phys. Rev. Lett.*, vol. 58, p. 373, 1987.

[178] T. Nakayama, J. Onoc, and K. Takcuchi, "Weakly bound and strained C_{60} monolayer on the Si(111)$\sqrt{3}\times\sqrt{3}$-Ag substrate surface," *Phys. Rev. B*, vol. 59, p. 12627, 1999.

[179] T. Bitzer, T. Rada, and N. V. Richardson, "Inhibition of the [2+2] cycloaddition: Maleic anhydride on Si(100)-2 × 1," *J. Phys. Chem. B*, vol. 105, p. 4535, 2001.

[180] A. A. Escuadro, D. M. Goodner, J. S. Okasinski, and M. J. Bedzyk, "X-ray standing wave analysis of the Sn/Si(111) -$\sqrt{3} \times \sqrt{3}$ surface," *Phys. Rev. B*, vol. 70, p. 235416, 2004.

[181] D. Walko, 2006, private communication.

[182] T. Lee, S. Warren, B. C. C. Cowie, and J. Zegenhagen, "Chemically-resolved Structural Analysis of Sn/Ge(111) Surface," *Phys. Rev. Lett.*, vol. 96, p. 046103, 2006.